UNIVERSITY OF GLASGOW

Statistical modelling of the near-Earth magnetic field in space weather

by

Qingying Shu

A thesis submitted in partial fulfillment for the
degree of Doctor of Philosophy

in the

College of Science and Engineering
School of Mathematics and Statistics

February 2018

Declaration of Authorship

I, Qingying Shu, declare that this thesis titled, 'Statistical modelling of the near-Earth magnetic field in space weather' and the work presented in it are my own. I confirm that:

- This work was done wholly or mainly while in candidature for a research degree at this University.
- Where any part of this thesis has previously been submitted for a degree or any other qualification at this University or any other institution, this has been clearly stated.
- Where I have consulted the published work of others, this is always clearly attributed.
- Where I have quoted from the work of others, the source is always given. With the exception of such quotations, this thesis is entirely my own work.
- I have acknowledged all main sources of help.
- Where the thesis is based on work done by myself jointly with others, I have made clear exactly what was done by others and what I have contributed myself.

Signed: _____

Date: _____

Abstract

Space weather refers to electromagnetic disturbances in the near-Earth environment as a result of the Sun-Earth interaction. Severe space weather events such as magnetic storms can cause disruption to a wide range of technologies and infrastructure, including communications systems, electronic circuits and power grids. Because of its high potential impact, space weather has been included in the UK National Risk Register since 2011. Space weather monitoring and early magnetic storm detection can be used to mitigate risk in sensitive technological systems. The aim of this project is to investigate the electromagnetic disturbances in the near-Earth environment through developing statistical models that quantifies the variations and uncertainties in the near-Earth magnetic field.

Data of the near-Earth magnetic field arise from in-situ satellite measurements and computer model outputs. The Cluster II mission (Escoubet et al., 2001a) has four satellites that provide in-situ measurements of the near-Earth magnetic field at time-varying locations along their trajectories. The computer model consists of an internal part that calculates the magnetic field sourced from Earth itself and an external part that estimates the magnetic field resulting from the Sun-Earth interaction. These magnetic fields, termed as the *internal field* and the *external field*, add up to the total magnetic field. Numerical estimates of the internal field and the external field are obtained respectively from the IGRF-11 model (Finlay et al., 2010) and the Tysganenko-96 (T96) model (Tsyganenko, 2013) given the times and the locations as inputs. The IGRF model outputs are invariant to space weather conditions whereas the T96 model outputs change with the input space weather parameters. The time-varying space weather parameters for T96 model include the solar wind ram pressure, the y and the z-components of the interplanetary magnetic field, and the disturbance storm time index. These parameters are the estimated time series of the solar wind conditions at the magnetopause, i.e. the boundary of the magnetosphere on the day-side, and the disturbance level at the Earth's surface. Real-time values of the T96 model input parameters are available at hourly resolution from `https://omniweb.gsfc.nasa.gov/`.

The overall aim of the thesis is to build spatio-temporal models that can be used to understand uncertainties and constraints leveraged from 3D mathematical models of space weather events. These spatio-temporal models can be then used to help understand the design parameters that need to be varied in building a precise and reliable sensor network. Chapter 1 provides an introduction to space weather in terms of the near-Earth magnetic field environment. Beginning with an overview of the near-Earth magnetic field environment, Chapter 2 describes the sources for generating in-situ satellite measurements and computer model outputs, namely the Cluster II mission, the IGRF model,

and the T96 model. The process of sampling the magnetic field data from the different data sources and the space-time dependence in the hourly sampled magnetic field data are also included in this Chapter. Converting the space-time structure in the magnetic field data into a time series structure with a function relating the position in space to time, Chapter 3 explores the temporal variations in the sampled in-situ satellite measurements. Through a hierarchical approach, the satellite measurements are related to the computer model outputs. This chapter proposes statistical methods for dealing with the non-stationary features, temporal autocorrelation, and volatility present in the time series data.

With the aim of better characterising the electromagnetic environment around the Earth, Chapter 4 develops time-series models of the near-Earth magnetic field utilising in-situ (CLUSTER) magnetic field data. Regression models linking the CLUSTER satellite observations and two physical models of the magnetic field (T96 and IGRF) are fit to each orbit in the period 2003-2013. The time series of model parameter estimates are then analysed to examine any long term patterns, variations and associations to storm indices. In addition to explaining how the two physical models calibrate with the observed satellite measurements, these statistical models capture the inherent volatility in the magnetic field, and allow us to identify other factors associated with the magnetic field variation, such as the relative position of each satellite relative to the Earth and the Sun. Mixed-effect models that include these factors are constructed for parameters estimated from the regression models for evaluating the performance of the two computer models. Following the calibration of the computer models against the satellite measurements, Chapter 5 investigates how these computer models allow us to investigate the association between the variations in near-Earth magnetic field and storms. To identify the signatures of storm onsets in different locations in the magnetosphere, change-point detection methods are considered for time series magnetic field signals generated from the computer models along various feasible satellite orbits. The detection results inform on potential sampling strategies of the near-Earth magnetic field to be predictive of storms through selecting achievable satellite orbits for placing satellite sensors and detecting changes in the time series magnetic signals.

Chapter 6 provides of a summary of the main finding within this thesis, identifies some limitations of the work carried out in the main chapters, and include a discussion of future research. An Appendix provides details of coordinate transformation for converting the time and position dependent magnetic field data into an appropriate coordinate system.

Acknowledgements

First of all, I would like to thank all my supervisors Prof. Marian Scott, Prof. Lyndsay Fletcher, Prof. Peter Craigmile, and Dr. Matteo Ceriotti for their invaluable support and guidance through my Ph.D. It has be a great pleasure and an invaluable experience for me to work with and to learn from them. I am extremely grateful for their advices, encouragement, and patience, without which the completion of this thesis would not have been possible.

I would like to acknowledge University of Glasgow, Science and Engineering College Sensor Studentship, for funding my Ph.D. and to the School of Mathematics and Statistics, College Mobility Scholarship, and STATMOS, for funding my academic travels and visits.

I would also like to thank my parents for inspiring me to pursue my Ph.D. study and showing care and support in the meantime.

Finally, I would like to express my gratitude to everyone in the School of Mathematics and Statistics (especially Mengyi for her company from the very beginning and Tushar for being ally in the final writing-up stage) for creating a friendly and supportive working environment, to people I spent quality time with during my short visit at The Ohio State University, and to all my friends back-home and in Glasgow for providing mental support.

Contents

List of Figures

List of Tables

Abbreviations

ACF	Autocorrelation function
AR	Autoregressive
ARCH	Autoregressive conditionally heteroscedastic
ARL	Average Run Length
CIR	Co-rotating Interaction Regions
CME	Coronal Mass Ejection
CUSUM	Cumulative sum control chart
CvM	Cramer-von-Mises
EM	Expectationmaximization
ESA	European Space Agency
FGLS	Feasible Generalized least squares
GLR	Generalized likelihood ratio
GLS	Generalized least squares
GSE	Geocentric solar ecliptic
GSM	Geocentric solar magnetospheric
IGRF	International Geomagnetic Reference Field
IMF	Interplanetary Magnetic Field
KS	Kolmogorov-Smirnov
MHD	Magnetohydrodynamics
ML	Maximum likelihood
MLE	Maximum likelihood estimation
QMLE	Quasi-maximum likelihood estimation
T96	Tsyganenko model 1996

Chapter 1

Introduction

"Weather on Earth, such as wind, snow and rain, has different terrestrial impacts and different meteorological causes. Similarly, space weather, including geomagnetic storms, radiation storms and solar radio noise, has different terrestrial impacts and is the result of different types of solar phenomena. "

UK National Risk Register of Civil Emergencies 2013

Space weather is a rapidly growing field within space sciences that studies the electromagnetic variations in the complex Sun-Earth system and their consequences on human society (Moldwin, 2008). The term space weather refers to time-variable conditions in the space environment that can influence the performance and reliability of space-borne and ground-based technological systems, and can endanger human life and health (US National Space Weather Program Strategic Plan, 2010). The space environment consists of the Sun, the solar wind, and the Earth's magnetosphere, ionosphere, and atmosphere. As the development of modern technology facilitates research into plasma physics processes in space, it is now well understood that space weather is driven by the Sun. The Sun interacts with the Earth via the continuously emitted high-speed plasma streams that propagate across interplanetary space and envelop the Earth (Hapgood, 2017). The sequence of physics processes associated with the Sun-Earth interaction generates various space weather phenomena.

One key phenomenon of space weather is the space storm (Daglis, 2001) which, if it arrives at Earth, can give rise to a *magnetic storm* or *geomagnetic storm* (Loewe and Prölss, 1997). The storm interconnects the Sun, interplanetary space, and the Earth. Magnetic storms that last from days to weeks are mainly triggered by the Sun's coronal

mass ejections (CMEs), the mechanism of which is explained in Section 1.1. In the near-Earth space environment, a storm can be recognized as temporary disturbances in the electromagnetic field preceded by the arrival of a solar wind shock wave. On the surface of the Earth, a storm can be observed as a sharp decrease in the magnetic field strength followed by a gradual recovery to its original level. Magnetic storms have profound influence on the Earth. An example of severe space weather can be found in Eastwood (2008), where a recent major space storm in October-November 2003 was discussed. Records of the 2003 Halloween storm show that a series of solar flares and CMEs occurred from mid-October to early November, satellite-based systems and communications were affected, aircraft were advised to avoid high altitudes near the polar regions, a one-hour-long power outage happened in Sweden, and aurorae were observed in countries at different latitudes (NASA/SOHO, 2008, United States Geological Survey: Science Features, 2013). These facts suggest that this space storm affected the Earth in a global manner. Prior to 2003, there are notable major events in 1967, 1972, 1989, and 2000, but at the present time there have been no significant events for over a decade (Hapgood, 2017). Further back in history, the Carrington event recorded in September 1859 when the English astronomer Richard Carrington observed a white light flare on the solar disk, is thought to have been the most severe on record, and marked the beginning of extreme space weather studies (Cliver and Dietrich, 2013, Cliver and Svalgaard, 2004). A recent threat tantamount to the Carrington storm appeared in July 2012 when a non-Earth-directed CME was measured in-situ by the STEREO-A spacecraft (Baker et al., 2013, Ngwira et al., 2013). It was argued that the CME would have generated a Carrington-class geomagnetic storm if it had been Earth-directed.

Magnetic storms and other space weather phenomena under severe conditions have numerous adverse impacts on human activities, especially when our society becomes more and more dependent on advanced technology. Everyday technological systems, such as power grids, pipelines, transoceanic communication cables, satellites, aviation, and global navigation satellite systems, can be easily disrupted by severe space weather, as large variations in the terrestrial magnetic field induce currents that affect the normal operation of electrical conductor systems. Odenwald (2012) gave a detailed description of space weather impacts. Eastwood et al. (2017) reviewed the economic impacts of space weather among other literature detailing the likelihood and statistics of different types of space weather phenomena. The threat that space weather poses to our modern

society has been in included in the UK National Risk Register (NRR) for Civil Emergencies (Cabinet Office, 2015), where severe space weather is ranked highly, ahead of explosive volcanic eruptions and alongside extreme weather (Hapgood, 2012).

The societal needs of understanding and forecasting space weather has increased tremendously. Early detection of space storms can be used for mitigating risks in sensitive technological systems. This thesis is motivated by the possibility of using a space-based network of sensors for monitoring the near-Earth magnetic field, with each sensor carried on a CubeSat-like spacecraft. The core question of this Ph.D. project is to design an optimal monitoring network consisting of moving sensors for sampling the magnetic field at desired frequency, subject to the physical constraints of satellite orbits, to guarantee that certain statistical design objectives are met. The project involves statistical modelling, changepoint detection, and network design for monitoring the 3D spatio-temporal electromagnetic disturbances in the near-Earth environment.

So far this chapter has provided an overview of this Ph.D. project with a brief introduction to space weather. Section 1.1 gives the research background of the project, with a sketch of the physics behind space weather, a description of important space weather features, and a summary of recent advances in space weather studies. Section 1.2 states the aims and objectives of statistical modelling, change-point analysis, and sensor network design in three stages, and Section 1.3 closes this chapter with an outline of the thesis structure.

1.1 Research Background

Space weather exists both as a type of natural hazard and a scientific discipline. Since the risks of space weather gained rising awareness in the past few decades, space weather, as a discipline, has been developed along with the need for forecasting and prediction of extreme space weather events. Space weather as a discipline studies the state and dynamics of the Earth's space environment in response to variable solar activity (Watermann, 2007), and the task of forecasting space weather requires the integration of solar physics, interplanetary physics, magnetospheric physics and ionospheric physics (Saiz et al., 2013). Efforts of space weather modelling in different aspects have been

made accordingly. Tsagouri et al. (2013) summarized the recent progress in understanding space weather phenomena with the focus on solar activity (Messerotti et al., 2009), the radiation environment of the Earth (Vainio et al., 2009), solar wind variations and their interaction with the geomagnetic field (Watermann et al., 2009), and the upper atmosphere response to space weather events (Belehaki et al., 2009).

This project concerns primarily the near-Earth magnetic field environment, since the near-Earth field is influenced by the solar-terrestrial interaction, and variations in this field reflects sophisticated space plasma processes associated with space weather. Adverse space weather conditions that directly or indirectly affect human and technology systems merges in the near-Earth field in the form of electromagnetic disturbances. Large electromagnetic disturbances that occur occasionally have detrimental effects, and early detection of such events can be achieved through developing a monitoring network that recognizes abrupt changes of magnetospheric behaviours in the near-Earth space. This requires the knowledge of the magnetospheric behaviours under different space weather conditions, i.e. the dynamics of the near-Earth magnetic field in space plasma physics.

As a matter of fact, physics processes that govern the transport of energy, momentum and mass in the complex Sun-Earth system during electromagnetic disturbances have only been partially understood by scientists. Hultqvist and Treumann (1999) acknowledged that the contribution of solar plasma to the Earth's magnetosphere has only been tenuously understood due to inseparable plasma condition in the ionosphere, which is the ionized component in the Earth's upper atmosphere that forms the inner edge of the magnetosphere. Welling et al. (2015) summarized the advances in understanding the near-Earth plasma environment and provided an up-to-date review. An accurate understanding of the near-Earth magnetic field and its spatio-temporal variations is crucial in many aspects of solar-terrestrial physics and applications. Therefore a quantitative approach that fuses the known facts from established magnetospheric physics and direct observations from operational services would contribute to the knowledge of the near-Earth space environment. Tools available for this study include Earth-orbiting satellites that provide in-situ measurements of the field and semi-empirical models that are based on mathematical equations and historical observations of the near-Earth magnetic field.

This section introduces a framework for a statistical formulation of the space weather

monitoring problem, namely design of the best sampling strategies for recognizing the spatio-temporal disturbances related to space storms in the near-Earth environment. Subsection 1.1.1 describes the near-Earth space environment, covering the formation, structure, and dynamics of the Earth's magnetosphere. Subsection 1.1.2 presents the main features of magnetic storms, shedding light on the storm-time disturbances in the near-Earth magnetic environment. Section 1.1.3 reviews recent development of space weather monitoring based on the study of the near-Earth magnetic field.

1.1.1 Space weather in the near-Earth environment

Space weather arises from the Sun (Bothmer and Daglis, 2007, Kivelson and Russell, 1995, Koskinen, 2011), from where streams of high-speed hot plasma continuously flow outward. The variable plasma stream, known as *the solar wind*, is supersonic with velocity ranging from 300 to 800 km/s, and forms shock waves when diverted around a planetary obstacle. Alfvén's frozen-in theorem (Alfvén, 1942) states that in a fluid with infinite electric conductivity, magnetic field lines are frozen into the fluid and have to move along with it. Since the solar wind is highly electrically conducting, the solar magnetic field is considered to be frozen into the flow of the solar wind. As the Sun rotates, the solar wind carries the solar magnetic field outward in a spiral pattern (Parker, 1965). Transient disturbances in the solar wind, such as erupting "ropes" of magnetised plasma caused by CME, and their effects will be elaborated in subsection 1.1.2. Structure in the solar magnetic field modulates the flow of the solar wind. With the fast flows overtaking the slow ones, the interaction of solar wind with different velocities compresses the solar wind plasma, distorting the magnetic fields and the flow directions (Russell, 1991). The *Interplanetary Magnetic Field (IMF)* is the magnetic field of the solar wind that carries the effects of solar activity towards the Earth and other planets in the solar system. The Earth has a dipole magnetic field with the axis tilted at an angle of 11.7 degrees with respect to its rotational axis. The solar wind interacts with the terrestrial magnetic field, compressing it on the day-side and stretching it on the night-side. The huge cavity in the solar wind created by the solar-terrestrial interaction is called *the magnetosphere* (Russell, 2007).

The Earth's magnetosphere responds to solar activity and and functions as a reservoir of energy and particles. As a result of the interaction between the magnetized solar

wind and Earth's magnetic field, the magnetosphere is shaped by a series of current systems and filled by a variable mixture of ionospheric and solar wind plasma. Figure

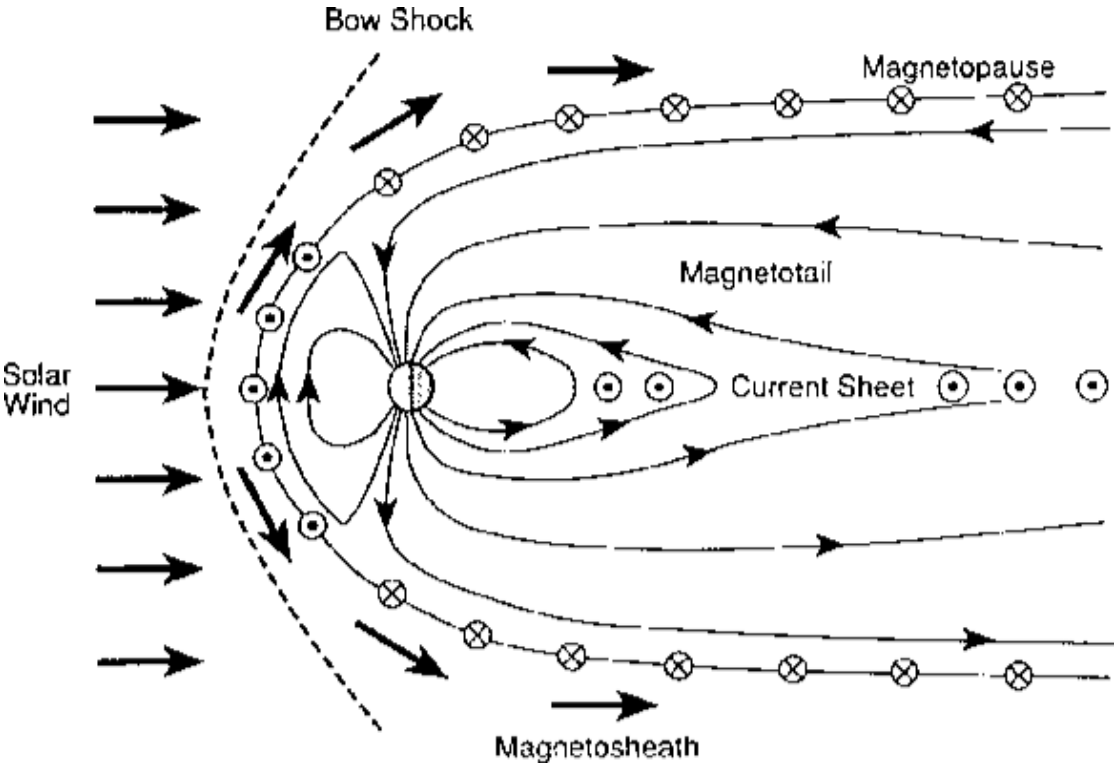

FIGURE 1.1: Cross section of the magnetosphere. Source: Hughes (1995). The arrows show the magnetic field directions. The circles with an X represent currents flowing into the page and the circles with a dot represent outward flowing currents.

1.1 shows the magnetopause current system and the magnetotail current sheet in the cross section of the magnetosphere. A bow shock is formed as indicated by the dashed curve. The bow shock slows down and deflects the solar wind flow before it reaches the magnetopause (De Pater and Lissauer, 2015). The magnetopause is the boundary separating the magnetosheath, the zone of shocked solar wind plasma, from the plasma of the magnetosphere. Inside the magnetopause, plasma motion is dominated by the terrestrial magnetic field. The distance of the magnetopause from the centre of the Earth varies with solar wind ram pressure, i.e. the product of plasma density and squared relative speed of the plasma, and typically ranges from 6 to 15 Earth radii (r_E). Lines and arrows in the figure represent the magnetic field lines and their directions. Figure 1.2 provides an illustration of magnetospheric currents in 3D. The ring current flowing westward around the Earth is carried by charged particles trapped in the inner magnetosphere. It is the most essential element in the study of magnetic storms and

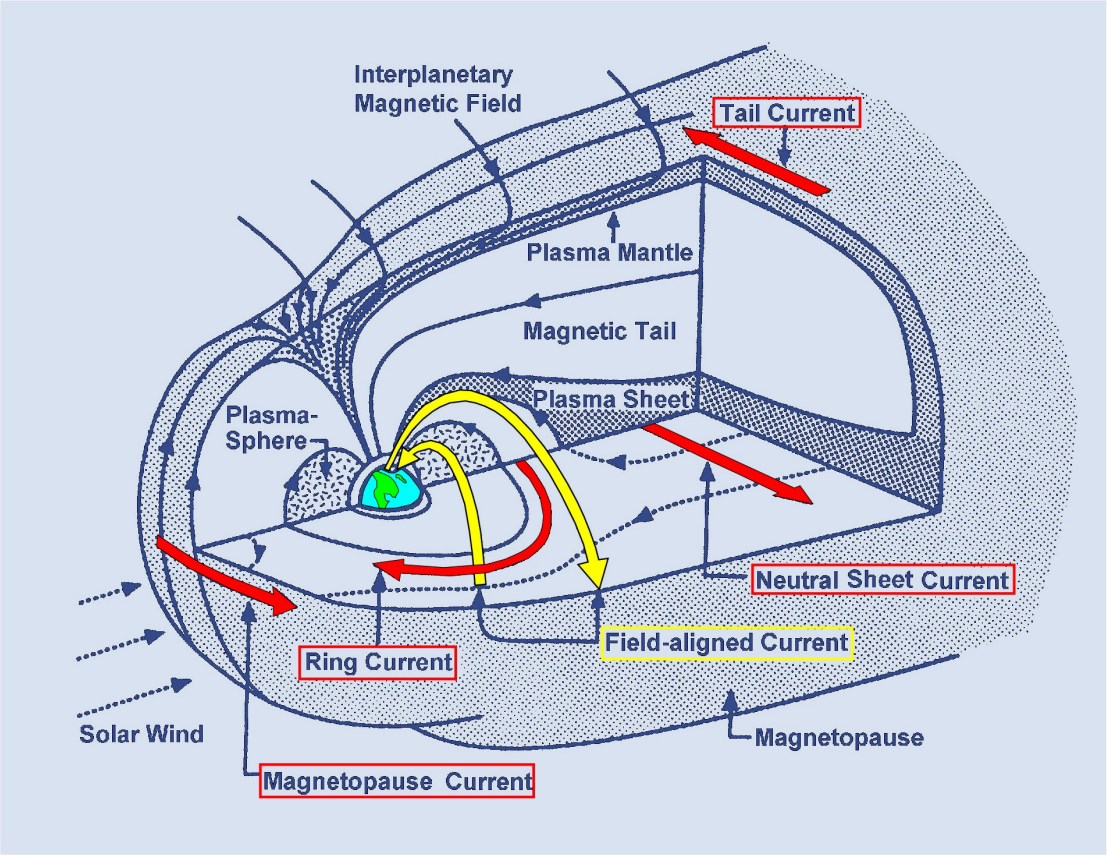

FIGURE 1.2: A sketch of the magnetosphere. Source: Kivelson and Russell (1995). The Sun-Earth interaction generates a complex system of magnetospheric and ionospheric current systems.

magnetospheric substorms. During a magnetic storm, the number of particles in the ring current will increase, resulting in a decrease in the geomagnetic field. The decrease of the geomagnetic field due to the ring current is measured by the *disturbance storm time (Dst) index* available from `http://wdc.kugi.kyoto-u.ac.jp/dstdir/`. The field-aligned currents in coexistence with the ring current flow along magnetic field lines and connect the magnetosphere to the ionosphere. Radiation belts where the magnetic field traps high-energy plasma were discovered in the inner magnetosphere, or the plasmasphere, by Van Allen et al. (1959). The inner belts extend from 1.1 to 2 r_E and the outer belts extend from 3 to 9 r_E (Daglis, 2001). The region between the belts is considered as an ideal location for spacecraft operation as it is normally devoid of particles, however, during storms the region would turn into location of high particle radiation intensity and could become harmful to space-based assets (Baker et al., 2004).

In the near-Earth space, the magnetic field comes from the magnetospheric currents and the Earth's dipole magnetic field. The overall magnetic field has diurnal and annual

variations in an Earth-fixed reference frame. The daily variations are caused by the Earth's rotation and the orientation of the rotational axis (Maus and Lühr, 2005). The magnetospheric fields sourced from the magnetospheric currents under quiet conditions would appear steady in the Geocentric Solar Magnetospheric (GSM) coordinate system, which has its x-axis pointing from the Earth to the Sun and the z-axis being the projection of the dipole axis on the plane perpendicular to the x-axis. The GSM coordinate system is the mostly commonly used reference frame in studies of the Sun-Earth interaction. The IMF should also be considered in the GSM system (Russell and McPherron, 1973). Conversions between the GSM system and other Earth-fixed coordinate systems (Russell, 1971), such as GEI, GEO, or GES, are included in Appendix A. However, the magnetopheric fields do not appear stationary in the GSM frame. A fundamental process that limits the field being stationary in magnetospheric dynamics is *magnetic reconnection*.

The magnetic field lines inside the magnetosphere continuously join or merge with magnetic field lines of the interplanetary magnetic field. The process transfers plasma and energy from the solar wind into the magnetosphere and drives particle acceleration and convection (Kuijpers et al., 2015). Reconnection occurs when magnetic field lines of opposite directions get compressed together. Dungey (1961) proposed that the dynamics of the magnetosphere are driven by magnetic reconnection and the reconnection is regulated by the orientation of the IMF. The Dungey model in Figure 1.3 shows reconnection in the noon-midnight meridian in two scenarios: the northward IMF on the left panel and the southward IMF on the right panel. During northward IMF, the reconnection occurs symmetrically away from the magnetopause; During southward IMF, the reconnection occurs first at the day-side magnetopause and then at the night-side magnetotail. For IMF that involves an east-west component, reconnection would still occur and the reconnection site locate at points where the internal magneto-spheric field is anti-parallel to the external shocked solar-wind field. As the IMF changes, the reconnection site moves on the magnetopause.

In general, southward IMF is expected to produce a much stronger effect than northward IMF. Figure 1.4 shows an example of reconnection during southward IMF. The processes can be summarized as follows: southward IMF triggers reconnection at day-side magnetopause in stage 1, creating open magnetic field lines that allow solar wind plasma to enter the magnetosphere along the open field in stage 2 and 3; solar wind

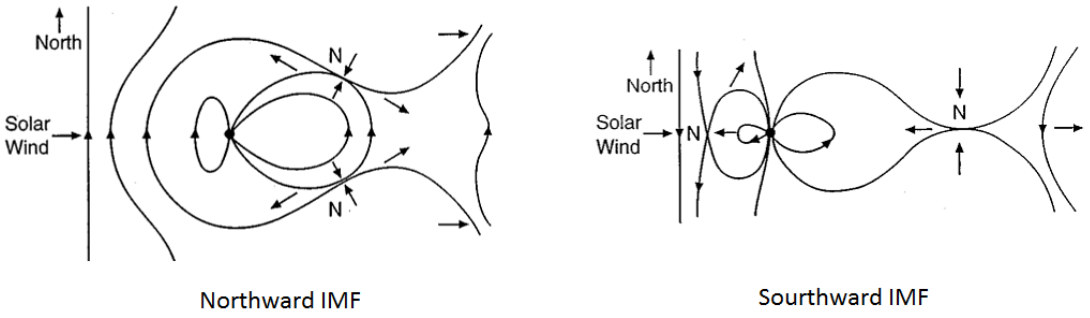

FIGURE 1.3: Dungey models of the reconnecting magnetosphere. Source: Russell (2007). The left panel shows the noon-midnight meridian (the x-z plane in the GSM frame) for northward IMF and the right panel the southward IMF. The points labelled "N" are neutral points at which the magnetic field is zero. The arrows show the flowing directions.

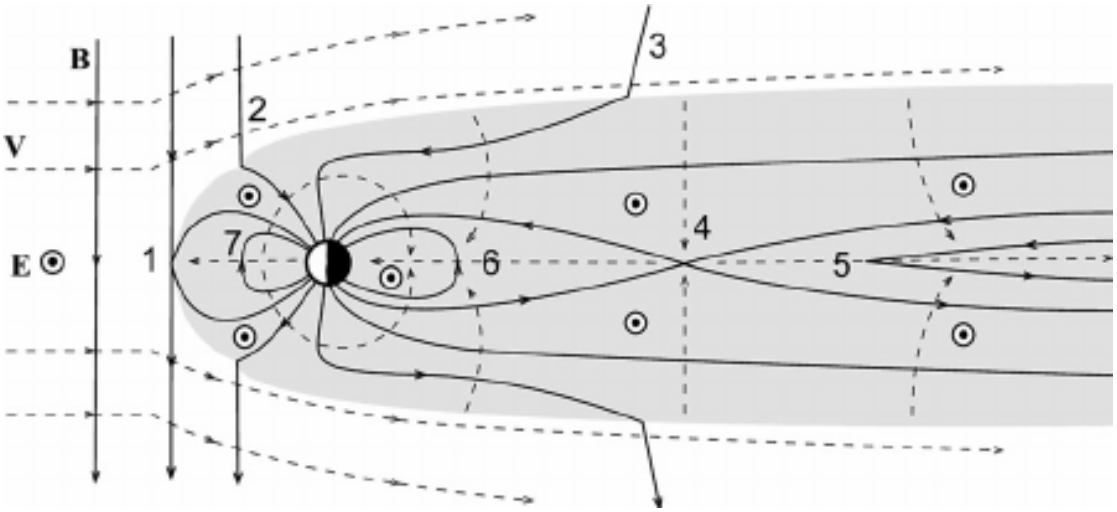

FIGURE 1.4: Diagram showing the stages of the Dungey cycle. Source: Seki et al. (2015). **E** - the electric field; **V** - the velocity vector; **B** - the magnetic field. The solar wind plasma and IMF impose on the Earth's magnetopshere: $\mathbf{E} = -\mathbf{V} \times \mathbf{B}$. The dashed lines are the flow streamlines and the solid lines are the magnetic field lines. The stages of reconnection are numbered from 1 to 7 in time order.

mass, momentum and energy transferred and stored in the magneto-tail subsequently cause reconnection between open lobe field lines at the cross-tail current sheet in stage 4; the reconnection ends with closed magnetic field lines in stage 5 and 6 and convects back to day-side magnetic field or IMF in stage 7. In short, day-side reconnection at the magnetoapuse opens closed magnetic flux; nightside reconnection at a distant location ($\sim$ 100 rE) in the magnetotail closes open magnetic flux. Time scales of these stages from the opening of the field lines at the day-side to the closing of the field lines on the nightside are 1-hour (Cowley, 1982), or equivalently, the propagation time of the solar wind from the magnetopause to the magnetotail can be several tens of minutes (Milan

et al., 2007).

The Dungey cycle was once considered as a steady-state process where the rates of day-side and nightside reconnection were assumed equal. It is now understood that reconnection at day-side and night-side can happen independently and the reconnection rates do not need to be balanced at any instant. Sotirelis et al. (2017) demonstrated the linkage of magnetic reconnection to the polar cap behaviour. It has been found that day-side reconnection causes the polar cap to expand while night-side reconnection causes the polar cap to contract. Depending on the reconnection rates at the two sides, the response of the Earth's magnetosphere to the solar wind can be recognized as steady and non-steady states. However, it has been argued that the solar-wind-magnetospheric system never reaches a steady state but keeps oscillating with a period of roughly an hour, and the oscillation may be driven by intermittent magnetic reconnection (You-Qiu et al., 2005).

Whether the reconnection is intrinsically intermittent or continuous has long been a discussion. Frey et al. (2003) reported continuous reconnection at the Earth's high-latitude magnetopause under northward IMF, or stable solar wind conditions, based on observation of day-side proton aurora spot, as variable solar wind would input energy into the magnetosphere and cause radiation belt particles to spiral into the atmosphere thus creating aurorae. The reconnection rate at the magnetopause could be intermittent if the IMF changes. During southward IMF, the day-side reconnection leads to a build up of magnetic energy in the magnetotail, and a subsequent tail reconnection results in an explosive release of magnetic energy, termed a *magnetospheric substorm* (Baker et al., 1996). The intervals where the dayside reconnection is balanced by nightside reconnection are recognized as *steady magnetic convection events* (DeJong et al., 2008). There exists *auroral electrojets*, i.e. two broad sheets of electric current flowing in the auroral ovals, and auroral observations in the form of auroral electrojet indices AE, AL, and AU (See Table 1.1 for definitions of these indices) (Davis and Sugiura, 1966, Gjerloev et al., 2004, Kamide and Akasofu, 1983) were considered the most accurate way of timing and locating magnetospheric events (Sergeev et al., 2012). McWilliams et al. (2008) details the selection criteria of magnetospheric events using AE index. The auroral indices together with in-situ spacecraft observations advance understanding of substorm dynamics.

The study of what factors control the rate of reconnection has been an active field. Connor et al. (2014) recently found that sudden enhancements of solar wind dynamic pressure increases the reconnection rates at the day-side and night-side within an hour. The temporal behaviour of IMF and solar wind pressure control the time-varying reconnection rate. The hourly variation of IMF leads to magnetospheric events such as substorms, but when the solar wind apply a coherent stress to the magnetosphere over many hours, i.e. prolonged southward IMF, the response of the magnetosphere would involve into a *magnetic storm* under such conditions. (Bothmer and Daglis, 2007)

1.1.2 Magnetic storm and its main features

A *magnetic storm* or *geomagnetic storm* refers to large global disturbances in the near-Earth environment under the influence of the solar wind and the interplanetary magnetic field. As the magnetosphere is controlled by the solar wind, magnetic storms begin when disturbances in the solar wind reach the Earth's magnetosphere. CMEs, the massive transient eruptions of solar coronal material into space, and solar flares, the rapid release of energy from the coronal magnetic field, are the most energetic phenomena among various types of solar disturbances. Figure 1.5 provides photos of a CME taken by two

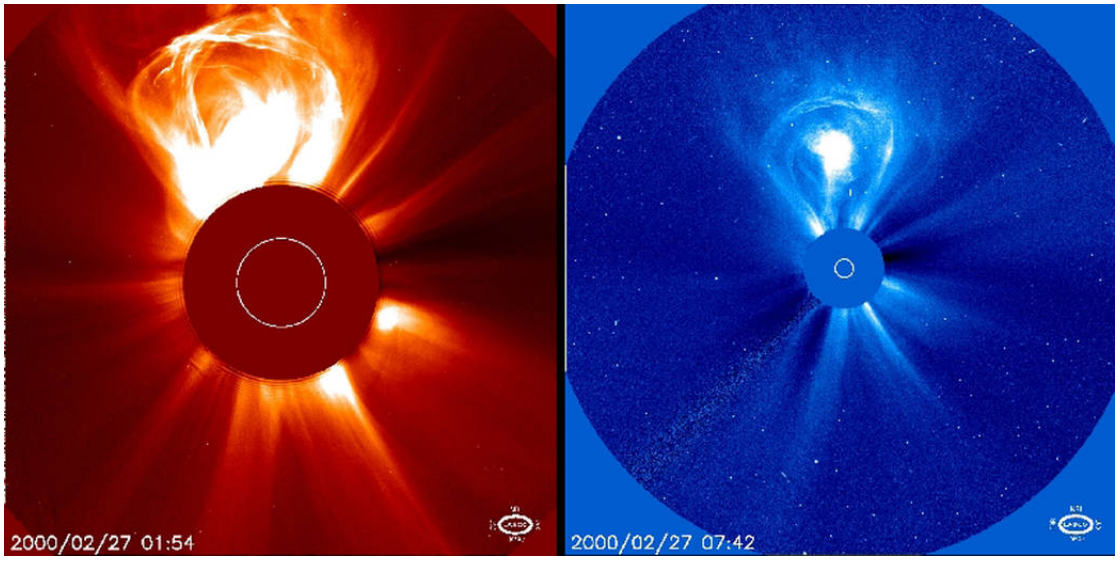

FIGURE 1.5: A coronal mass ejection on Feb 27th, 2000 taken by SOHO LASCO C2 and C3. Credit: SOHO ESA NASA

coronagraphs on SOHO. A large CME blast a billion tons of particles into space and the particles can be accelerated to millions of miles per hour. These solar phenomena are more likely to occur during solar maximum, marked by the maximum number of

sunspots in a solar cycle that lasts 11 years on average. A magnetic storm would happen if a CME strikes the Earth's magnetosphere. As a result, a peak in geomagnetic activity occurs around the solar maximum (Richardson et al., 2000). Another source contributing to the occurrence of geomagnetic storms but out of solar maximum is the Corotating Interaction Regions (CIRs), which are formed because the Sun's dipole tilt and irregular shape of solar coronal holes, lead fast solar wind to run into slow solar wind further ahead.

Chapman and Bartels (1940) described the typical behaviour of the geomagnetic storm in four stages: the sudden commencement signalled by an increase in the horizontal component of the Earth's magnetic field within a few minutes, the initial phase lasting a few hours during which the horizontal component stays higher than its normal value, the main phases characterized by a sharp decrease, and the recovery phase consisted of a slow relaxation of the horizontal component back to its normal value. This description was based on magnetic field measurements at ground observatories. Parker (1962) summarized the dynamical process of geomagnetic storm as follows: The solar wind exerts force on the boundary of the magnetosphere, resulting in a compression of the geomagnetic field, and the field then exerts force outward into space, causing an expansion and a decrease of the magnetic field around the equatorial regions. This phenomenon can be interpreted as a deformation of the geomagnetic field by external stresses. This interpretation is that the phenomena are a deformation of the geomagnetic field by external stresses. Gonzalez et al. (1994) defined a geomagnetic storm as

"an interval of time when a sufficiently intense and long-lasting interplanetary convection electric field leads, through a substantial energization in the magnetosphere-ionosphere system, to an intensified ring current sufficiently strong to exceed some key threshold of the quantifying storm time (Dst) index".

Figure 1.6 gives an example of the Dst index during the Oct-Nov 2003 storm, with quiet-time behaviour on the left side of the plot and the super storm on the right. The activity levels are indicated by the shaded regions in the plot and the typical cut-off for studying the storm effects on power grids and satellites is Dst less than -200 to -300 nT. During solar cycle 23, beginning in May 1996 and ending in January 2008, 90 intense storms (Dst $\leq$ 100 nT) have been identified out of the 220 storms (Dst $\leq$ 50 nT) (Rathore et al., 2011), and the 2003 Halloween storm driven by CMEs was the largest storm in

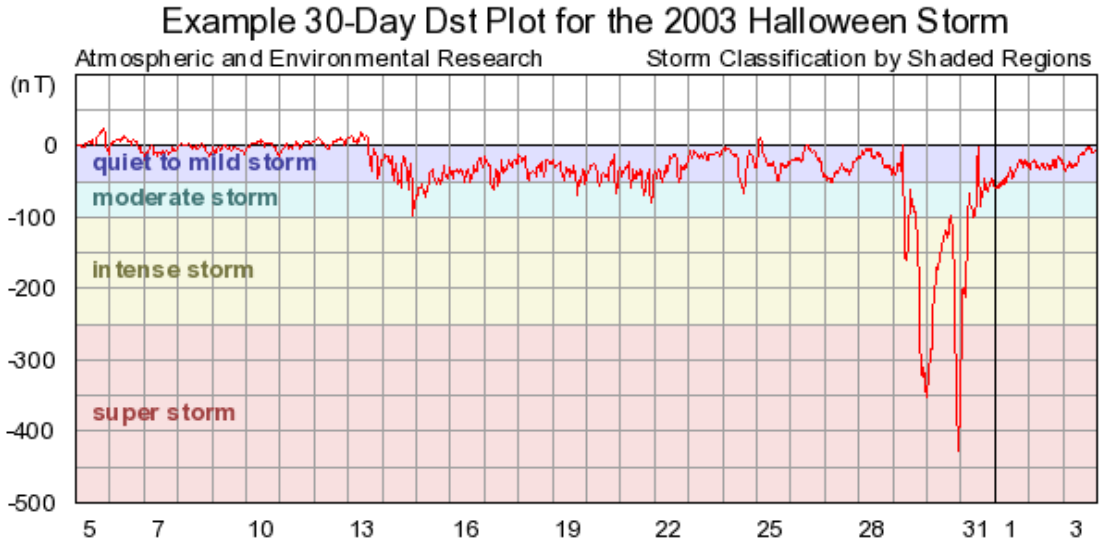

FIGURE 1.6: Illustration of geomagnetic storm classifications. Source http://www.aer.com/science-research/space/space-weather/space-weather-index

that solar cycle (Gopalswamy et al., 2005). Echer et al. (2008) investigated these intense storms with the interplanetary data from the ACE and WIND satellites and classified the storms into different interplanetary causes. It was found that all the intense storms were caused when the IMF was southwardly directed in the GSM coordinate and the four most common interplanetary structures responsible for intense storm development were sheath fields (Sh), magnetic clouds which drove fast shocks (sMC), combined sheath and MC fields (Sh+MC), and CIRs, in decreasing order with the highest being 24% and the lowest 13%. Sh and MC are both possible manifestation of a CME: MCs are defined by strong magnetic field and large-angle smooth rotation of the field; sheath fields are recognized as highly turbulent solar wind plasma and fields (Tsurutani et al., 1988).

Dst is one of the most widely used geomagnetic indices partly because it is motived by a specific physical theory – the enhancement of equatorial ring current. The Dst is derived from ground-based observations at low-latitude magnetometer stations as an estimate of the storm-time magnetic disturbances at the Earth's equator. It reflects the variation of the ring current, and other currents including the day-side magnetopause and the night-side tail current also contribute to the Dst during highly disturbed storm periods (Turner et al., 2000). However, the Dst has some biases mostly because of the geographic location of measurements (Häkkinen et al., 2003) and CIR-driven and CME-driven storm differs in their Dst representation in that a corrected Dst, excluding the effects of the quiet-time currents, is more under-predicted for CIR-driven storms than

TABLE 1.1: Summary of important geomagnetic indices

AE,AU,AL	1-, 2.5-min, or hourly auroral electrojet indices
Dst	Hourly index mainly related to the ring current
K	3-hr local quasi-logarithmic index
Kp	3-hr and hourly quasi-logarithmic planetary index

for that of CME-driven storms (Cramer et al., 2013). Table 1.1 summarizes some of the important geomagnetic indices. There are other geomagnetic indices that function as more generic measurements such as the range indices K and Kp (Love and Remick, 2007). The 3-hour K integer index was first introduced by Bartels et al. (1939) as a measure of the range of irregular and rapid, storm-time activity, and the Kp index (Menvielle and Berthelier, 1991) measures the planetary-scale magnetic activity based on the average of fraction K indices at 13 sub-auroral observatories. The auroral electrojet indices AU, AL, and AE measure the auroral zone component of the currents at different temporal scales.

All these indices are indicators of geomagnetic activity. The Dst and Kp are used to study magnetic storms, whereas the auroral electrojet indices are used to study magnetospheric substorms. The storm-substorm relationship does not seem to be fully understood yet. An earlier view by Akasofu and Chapman (1961) believed that magnetic storms are caused by frequent occurrence of intense substorms, and a modern view by Kamide (1992) proposed that the magnetic storms are driven by the enhanced magnetospheric convection from sustained southward IMF. McPherron (1997) concluded that magnetospheric substorms occur regardless of magnetic storm and substorms are more frequent and stronger during the main phase of magnetic storms.

1.1.3 A review of recent developments

The Earth's magnetosphere has time-varying configurations and exhibits non-linear fluctuations over a wide range of spatial and temporal scales. The magnetospheric variations are produced by the interaction of the solar conditions with the near-Earth space environment and can be detected from observations in the magnetosphere and on the surface of the Earth. Solar activity such as CMEs could provide warnings for severe space weather events, however, forecasting magnetopsheric disturbances based on solar observations are not accurate enough for practical purposes (Saiz et al., 2013).

The challenge of the forecasting task is to predict magnetic storms accurately and as soon as possible based on the understanding of the near-Earth space environment. It is understood that the large-scale variability of the magnetosphere is produced both by the changing external solar conditions and by non-equilibrium internal dynamics (Vasyliūnas, 2011). The coupling of the solar-wind to the magnetosphere and the internal physical processes have been modelled by the magnetohydrodynamics (MHD) equations. Global MHD models provide a physics-based understanding of magnetospheric structure and dynamics (Lopez et al., 2001). Magnetospheric research has advanced from the early days of considering primarily electrodynamics and plasma physical processes by the MHD equations to the present-day realization of the real complexity of the magnetosphere (Lui, 2002). Data-based modelling of the Earth's dynamic magnetosphere has been developed from the aspects of the mathematical methods, spacecraft databases, and parametrization of the magnetospheric models by the solar wind drivers and ground-based indices (Tsyganenko, 2013). The semi-empirical magnetic field models are now capable of producing the magnetospheric response to variable solar wind and interplanetary conditions. On the other hand, in-situ satellites such as Cluster mission (Escoubet et al., 2001a) and the Solar Terrestrial Probes mission Magnetospheric Multiscale (MMS) provide an improved perspective of the micro-physics of magnetospheric phenomena, contributing to the knowledge in the driving mechanisms in the magnetosphere (Angelopoulos et al., 1998).

Development of the lower-cost CubeSat (Woellert et al., 2011) makes an in-situ monitoring sensor network plausible. The UK Space Agency performed a preparatory study of CENTINEL, a magnetospheric space weather constellation mission consisting of 100+ CubeSats (Eastwood, 2015). The study examined key technical challenges - deployment, communications and debris mitigation - in the context of space weather observation. A statistical design of sensor network of CubeSats will provide space weather monitoring system for recognizing storms and contribute to better space weather mitigation strategies in the cases of extreme space weather events.

1.2 Aims and Objectives

This Ph.D. project aims at developing statistical designs of a sensor network of small satellites moving through space, and measuring space weather conditions, including the

magnetic field, semi-continuously. The project involves research in data analysis, spatio-temporal statistical methodology, visualization, and computational inference.

The overall aim of the thesis is to build spatio-temporal models that can be used to understand uncertainties and constraints leveraged from 3D mathematical models of space weather events, and from typical measurement and error values derived from existing single-spacecraft sensors. These spatio-temporal models can be then used to help understand the design parameters that need to be varied in building a precise and reliable sensor network. The required network parameters must then be set against what is achievable in terms of sensor quality and satellite numbers (i.e. cost), satellite orbits and formations (i.e. sensor positions) and satellite communication restrictions (i.e. temporal sampling) to arrive at an optimal sensor network solution. This is primarily a modelling project that requires advanced statistical methods of general applicability, basic aspects of the physics of space weather and its measurements, and the real world constraints of practical engineering.

The space weather monitoring problem of developing a sensor network that can provide reliable estimates of the near-Earth magnetic field for detecting and predicting space storm has three stages. The first stage explores the variations in the near-Earth magnetic field utilizing in-situ satellite measurements and physics-based empirical models. The main objectives of spatio-temporal statistical modelling are to characterise the magnetic field variation in near-Earth space, compare storm and non-storm behaviour, and calibrate the physical models with real magnetic field data. The second stage investigates the best sampling strategies for recognizing storm signals based on results from stage one. The objectives are to develop a detection algorithm for recognizing changes along a satellite orbit and identify feasible satellite orbits along which storm signal can be captured in time. The final stage is devoted to the construction of a storm warning system, i.e. an achievable CubeSat constellation for monitoring space weather, with the proposed detection algorithms and the planned satellite orbits from stage two. The objective is to optimize statistical design of a sensor network consisting of small satellites moving through space and continuously measuring space weather conditions for early space storm detection, when informed by space-weather physical models, the character of the sensed data and the achievable satellite orbits. With spacecraft and telemetry resources at a premium, it is necessary to ensure that the network is configured and the

data sampled in an optimal way. Statistical techniques will be extended for application to the design of space weather monitoring network.

In summary, this research project tackles general questions of spatial-temporal modelling of sensor data, optimal sensor positioning, sampling and data selection in constrained, dynamic 3D sensor networks.

1.3 Thesis Outline

This thesis consists of 6 chapters including this introductory chapter. Chapter 1 has defined the space weather monitoring problem in the context of the near-Earth magnetic field environment and identified magnetic storms as the event of interest for monitoring space weather.

Chapter 2 describes the data sources for the study of the near-Earth magnetic field environment. The data sources include satellite measurements and computer models of the near-Earth magnetic field. The Cluster II satellites provide in-situ measurements of the near-Earth magnetic field at time-varying locations along their trajectories. Two computer models are available for producing estimates of the internal and the external magnetic fields. IGRF the internal field model calculates the Earth's magnetic field and takes times and locations as inputs; T96 the external field model outputs the magnetospheric field from the Sun-Earth interaction and requires space weather parameters as additional inputs. The space weather parameters are derived from satellite-based observations in the interplanetary space and ground-based observations at the surface of the Earth. These parameters have an one-hour resolution. Sampling from the satellite measurements and the computer model outputs generate near-Earth magnetic field data that are dependent in space and time. The data consists of three magnetic field vectors, which are the Cluster satellite measurements, the IGRF model outputs, and the T96 model outputs, sampled at one-hour time interval along the motion of the Cluster satellites.

Chapter 3 explores the variations in the hourly-sampled magnetic field data. The magnetic field data has a space-time dependency for which the location in space can be regarded as a function of time. The chapter presents the space-time structure of the magnetic field data in the GSM coordinate frame and visualizes the Cluster satellite

trajectories. The GSM frame is considered the most appropriate reference frame for describing the solar-terrestrial magnetic field interaction, which plays a key role in the near-Earth magnetic field environment. In the GSM frame, magnetic field vectors are represented by magnetic field strengths in the x-, y- and z-components of the GSM frame. The satellite measurements and the computer model outputs are collected along the each of the four Cluster satellites and consist of field strengths in the three components. A simple regression model relates the satellite measurements to the IGRF and the T96 model outputs, since the observations of the near-Earth magnetic field are correlated with the estimates of the internal and the external fields. Such models are fitted to the data of the three components across the four satellites. Residuals of the regression model exhibit non-stationarity and time series methods are applied to piecewise stationary residuals for dealing with the temporal autocorrelation and the changing variances.

Chapter 4 evaluates the overall performance of the two computer models through developing a time-series-based regression model that incorporates the Cluster satellite data and the computer model outputs. The statistical model regresses the satellite measurements on the two computer model outputs and allows its parameters to vary across satellite orbits. Within each satellite orbit, the error term of the regression model appears to be stationary. The autocorrelation and the changing variance identified in the regression errors are captured by a time series structure. The time series structure for errors that quantifies the uncertainties in the regression modelling is individually defined for each orbit. These structures are taken into account in the estimation of the regression model parameters. The estimated parameters in the regression model characterize the relationship between the satellite measurements and the computer model outputs, thus calibrating the computer models against the Cluster satellite data. The Chapter then assesses the calibration results using a mixed-effects model. Potential fixed and random effects are considered in the mixed effects model for explaining the variations in the estimated regression parameters.

Chapter 5 focuses on recognizing the patterns of magnetic storm onset in the near-Earth space environment through generating estimates of the magnetic field at times and locations in space under storm and non-storm conditions and creating spatial maps of the near-Earth magnetic field on selected 2-dimensional grids with the estimates. Magnetic storms disturb the near-Earth magnetic field environment on a global scale and

such disturbances reach the surface of the Earth. The geomagnetic storm indices derived from observations at the surface of the Earth are used to select the storm periods. Space weather parameters under storm and non-storm conditions are input to the T96 model for generating estimates of the external magnetic field under both conditions, given that the external field responses to space weather and, based on the results from Chapter 4, the T96 models provide fairly good estimates of the external magnetic field regardless of the space weather conditions. Change-point detection approaches are considered for recognizing the magnetic storm patterns in time series magnetic field data collected along different satellite orbits. Comparison of change-point methods will be made based on the detection results. The detection results inform on potential sampling strategies of the near-Earth magnetic field to be predictive of storms through selecting achievable satellite orbits for placing the sensors and detecting changes in the time series magnetic signals.

Chapter 6 summarizes the main finding of these thesis and closes with a discussion of this work, as well as areas for future research.

Chapter 2

Space-weather data sources

Space weather is concerned with studying the natural variability of the near-Earth space environment, the region of which encompasses the Earth's upper atmosphere, ionosphere, and magnetosphere. The near-Earth space environment is a complex system of magnetic fields that responds to solar-terrestrial interaction. This magnetic environment is considered as being *quiet* if it exhibits regular small variations. A quiet magnetic environment is essential to the operation of our modern society, since an increasing number of sensitive technological systems on Earth or in near-Earth space rely on it. However, the magnetic environment can be disturbed by solar activity and sometimes undergoes sharp changes when magnetic storms occur. The mechanism of magnetic storms was reviewed in Section 1.2. It is understood that the onset of magnetic storms depends on the solar wind condition and the IMF orientation external to the Earth's magnetosphere. We also learned that storms are powered by magnetic reconnection and are identified by intensification of the equatorial ring current inside the magnetosphere. The storm-time magnetic disturbances, on time-scales ranging from minutes to a few days, result from changes in the ionospheric and magnetospheric electric currents driven by the Sun-Earth interaction.

The magnetic environment surrounding the Earth is systemically monitored by geomagnetic observatories on the ground. Ground-based surveys, quantifying the level of disturbances with geomagnetic indices, suggest that the amplitude and the time derivative of magnetic field are the main two sources of geomagnetic effects on technological systems, as they distort the magnetic field reference and induce electric currents.

The magnetic environment has also been explored by numerous satellites orbiting in near-Earth space. The in-situ investigation has revealed some key mechanisms of space weather phenomena and provided a large set of magnetic field measurements in near-Earth space. The NASA's Magnetospheric Multiscale mission recently witnessed the process of magnetic reconnection happening in the magnetosphere and confirmed that the reconnection powers various events in space (Burch et al., 2016). The availability of the large set of magnetic data provided by past and currently-flying missions together with ground observatories led to the development of data-based modelling of the magnetic fields in near-Earth space.

We study the magnetic field resulting from two sources: (*i*) the *main* or *internal field*, generated from the Earth's core; and (*ii*) the *magnetospheric field*, also known as *external field*, originating from the Sun-Earth interaction. This leads to modelling each source separately (see, e.g., Tsyganenko (2013)): the main-field models only take time and position as inputs, whereas the magnetospheric models are parametrized by solar wind drivers and ground-based index as their inputs.

This chapter describes the process of collecting magnetic data in near-Earth space for the study of the near-Earth space magnetic environment and its variability in relation to space weather. Near-Earth space is conventionally defined as the region of space starting 50 -70 km above the Earth's surface and extending tens of Earth radii, and as introduced by Hargreaves (1992), it refers to the space close enough to affect human activities but remote enough to be beyond everyday experience. In near-Earth space there are interactions between the terrestrial magnetic field and the solar magnetic field. Magnetic data in near-Earth space are available in the form of satellite measurements and computer model outputs. The difference of collecting magnetic data from the two sources lies in the fact that satellite measurements are made at time-varying locations with the motion of the satellite while computer model outputs can be generated at arbitrary time and location from the main-field and the magnetospheric models.

The chapter is organized as follows. Section 2.1 introduces the near-Earth space magnetic environment with the physical properties of magnetic fields and the origins of the Earth's magnetic fields. Section 2.2 presents the sources of the near-Earth space magnetic data. The Satellite measurements come from the Cluster II mission and the computer model includes an internal part IGRF-11 and an external part T96. Section

2.3 details the sampling procedure for collecting magnetic data from the two data sources and Section 2.4 summarizes the structure of the magnetic data and discusses the limits and complexity of the data sets.

2.1 Introduction

The near-Earth space environment is a complex region, which can be modelled in a number of different physical approximations. However, the complexity is such that a complete physical description of its dynamics is still lacking. Instead of gaining a physical knowledge of the space plasma, the research project is oriented towards a statistical understanding of near-Earth space dynamics, in particular, the variations in the electromagnetic fields. As already mentioned, the variations observed in near-Earth electromagnetic fields are separated into variations in the internal field and the magnetospheric field. The variations of internal origins is relevant to the study of geomagnetism (De Michelis et al., 2005), while the variations of external origins shed light on space weather. The central physical quantity of interest is the magnetic field from the space weather effects point of view (Bowe and McCulloch, 2007, Menvielle and Marchaudon, 2007, Thomson, 2014). In addition, electric fields are more difficult to measure in space than on the Earth, give that the intensities of electric fields in space can be relatively small (Parks, 1991).

As shown in the previous chapter, the Earth's magnetic field interacts with the solar wind and the solar-terrestrial interaction forms the terrestrial magnetosphere, resulting in various kinds of phenomena in space. With the beginning of scientific satellite investigations in 1958, many phenomena of space plasma have been directly observed (Stern, 1989). This includes disturbances in the magnetosphere, which is the subject of our research project. It has been gradually revealed that the Earth's magnetic field traps charged particles and the magnetosphere has a changing boundary and configuration. We now provide a review of the science underlying magnetic fields.

2.1.1 The basic science of magnetic fields

A magnetic field is a mathematical tool used to describe the magnetic effect of electric currents and magnetic materials. In the near-Earth space environment, the magnetic

field can be regarded as the total magnetic effect of the magnetospheric currents and the Earth itself. At a given point in time and space, the magnetic field can be specified by a direction and a magnitude. The symbol $\mathbf{B}$ is often used to represent the vector field that has three components in a Cartesian coordinate system. A magnetic field can be written as

$$\mathbf{B} = B_x\mathbf{x} + B_y\mathbf{y} + B_z\mathbf{z}, \tag{2.1}$$

where $\mathbf{x}$, $\mathbf{y}$, and $\mathbf{z}$ are unit vectors in a chosen reference frame, and B_x, B_y, and B_z are strengths of the magnetic field measured in each component. The strengths and the magnitude of $\mathbf{B}$ are measured in nano-Tesla (nT), e.g. 10^{-9} Tesla (T), in the near-Earth space environment. The equivalence of Tesla in SI units is newtons per meter per ampere, where $\mathbf{B}$ is defined in terms of the Lorentz force it exerts on moving electric charges. The Lorentz force law states that a particle of charge q moving with velocity $\mathbf{v}$ in the presence of an electric field $\mathbf{E}$ and a magnetic field $\mathbf{B}$ experiences a force $\mathbf{F}$ such that

$$\mathbf{F} = q\mathbf{E} + q\mathbf{v} \times \mathbf{B}, \tag{2.2}$$

in SI units. The force $\mathbf{F}$ in (2.2) is named the electromotive force (*emf*). The electric field $\mathbf{E}$ and the magnetic field $\mathbf{B}$ are both vector fields, and each has a time and location *dependence*. The Lorentz force and Maxwell's equations form the foundation of electromagnetism, i.e. the interaction between charged particles and electromagnetic fields,

$$\nabla \cdot \mathbf{E} = \frac{\rho}{\epsilon_0}; \tag{2.3}$$

$$\nabla \cdot \mathbf{B} = 0; \tag{2.4}$$

$$\nabla \times \mathbf{E} = -\frac{\partial \mathbf{B}}{\partial t}; \tag{2.5}$$

$$\nabla \times \mathbf{B} = \mu_0 \left(\mathbf{J} + \epsilon_0 \frac{\partial \mathbf{E}}{\partial t} \right); \tag{2.6}$$

where ϵ_0 and μ_0 are the universal constants representing the permittivity and permeability of free space, ρ and $\mathbf{J}$ denotes the electric charge and current density, and $\mathbf{E}$ and $\mathbf{B}$ are the electric and magnetic fields. The above equations from the top to bottom are Gauss's law, Gauss's law for magnetism, Maxwell-Faraday equation, and Ampere's Law with Maxwell's addition. Gauss's law (2.3) means the electric flux leaving a volume is proportional to the charge inside. Gauss's law for magnetism (2.4) shows the total

magnetic flux through a closed surface is zero. Ampere's Law with Maxwell's addition (2.5) states that magnetic fields can be generated by electric current, i.e. flow of electric charge, and by changing electric fields. The Maxwell-Faraday equation (2.6) describes how a time-varying magnetic field induces an electric field. Following Faraday's law of induction, the electromotive force, *emf*, drives the induced electric current, as described by

$$emf = -\frac{d\phi}{dt} \tag{2.7}$$

where ϕ is the magnetic flux through the loop defined as

$$\phi = \int_{\mathbf{S}} \mathbf{B} \cdot d\mathbf{S}. \tag{2.8}$$

In the above sentence, **B** denotes the magnetic field and **S** denotes the loop. Equations (2.7) and (2.8) show that the electric field and current can be induced by a time-varying magnetic field. It is important to note the magnetic field **B** in (2.8) comes from both the external and internal magnetic sources, the external field originating in the magnetosphere and ionosphere, and the internal field generated by the Earth. The induced current at the surface of the Earth can be thought as the end link of the chain interaction in space weather, and the geomagnetic indices derived from the rate of change in the magnetic field on the Earth are reliable indicators for the space weather effects on ground-based technological systems (Pulkkinen, 2007, Viljanen et al., 2001).

The electromagnetic fields and the charged particles obey the fundamental Maxwell's equations and the Lorentz equation of motion in a vacuum, and some of the magnetic storm effects are associated with the electromotive force. The behaviour of near-Earth space is in principle described by Maxwell's equations and the Lorentz force equation, however the coupling between the macroscopic **E** and **B** fields, and the microscopic behaviour of particles, and the range of space and time scales involved, means that analytical solutions are impossible and numerical solutions are only approximations. Although the near-Earth space is a tenuous medium, the number of equations involved in the plasma dynamics is still large in number, making analytical solution to all of the coupled equations impossible (Parks, 1991). Thus historical observations and empirical studies are invaluable in understanding the behaviour of the near-Earth space environment.

2.1.2 Earth's magnetic field

As previously stated the magnetosphere refers to the space dominated by the Earth's magnetic field, or the so-called *geomagnetic field*. Since the Earth is composed of solid crust, semi-solid mantle, liquid iron outer core, and solid iron inner core, the geomagnetic field is a combination of magnetic fields generated by three different sources (Gunnarsdóttir, 2012). First, the *main field* is generated by a magnetic dynamo in the Earth's liquid core. Secondly the *crustal field* is generated by magnetized rocks on the Earth's crust. Finally, the *induced field* is produced by the induced currents from the ionized particles above the Earth. Thus changing magnetic field in the crust, mantle and oceans, the *magnetospheric field* is generated by electric currents flowing in the ionosphere and the magnetosphere. On the surface of the Earth, the main field constitutes 97-99 percent of the total field and the other fields make up the rest of the total field (`https://denali.gsfc.nasa.gov/research/mag_field/conrad/explain.html`).

The main field and the crustal field have internal origins, and the magnetospheric field and the induced field have eternal origins. In a word, the geomagnetic field comprises an internal field originated from the Earth and an external field resulting from the solar-terrestrial interaction. Hence a decomposition of the geomagnetic field divides it into an internally generated field and an externally driven field. Separating the external field from the overall magnetic field is essential for the study of space weather phenomena. Olsen et al. (2010) reviewed methods developed for the separation of external and internal source contributions. In the regions without electric currents, the magnetic field can be expressed as the negative gradient of a scalar potential, and the potential can be expanded into a series of spherical harmonics (Gauss et al., 1839). The Gauss algorithm has been proven to be sufficient for describing the internal field that resembles a magnetic dipole field, and Finlay et al. (2010) present numerical modelling of the internal field using this method. In the region with electric currents, knowledge of the distribution of currents in space is required for separating the external field from the measured magnetic field. In the widely used models by Tsyganenko and Stern (1996a), the external field of magnetospheric origin is described as the sum of the currents flowing in the near-Earth environment. Magnetic contributions of the currents can be analytically derived from solar wind dynamic pressure, IMF, and geomagnetic index in the externally parametrized model.

The geomagnetic field has been measured at various locations over hundreds of years, with devices ranging from ancient compass to modern magnetometers. Historical study of the geomagnetic field suggests that the main field can be approximated by a magnetic dipole that is tilted at an angle of about 10 degrees with respect to the Earth's rotational axis. On the surface of the Earth, the magnitude of the geomagnetic field ranges from $23,000$ nT to $62,000$ nT (Matzka et al., 2010). Figure 2.1 shows a map of an international network of about 160 observatories. The geomagnetic field has also been

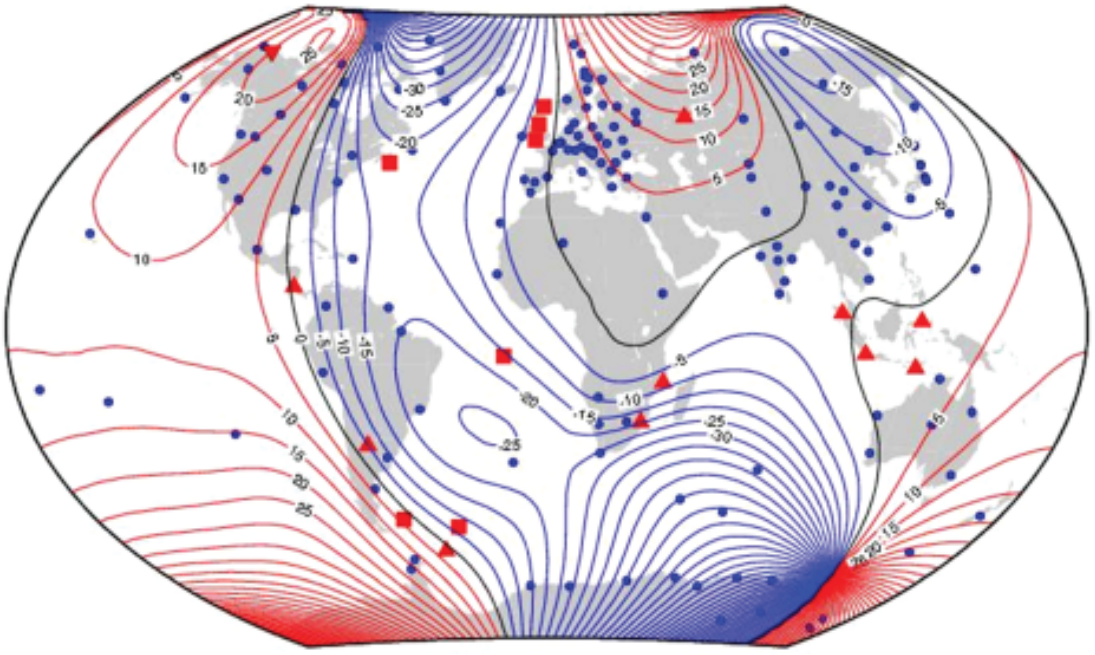

FIGURE 2.1: Worldwide distribution of geomagnetic observatories in 2013. Source: Thomson (2014). Squares, triangles, and dots indicate locations of observatories. Blue/red contours represent the west/east direction of magnetic north from true (geographic) north; black contours show where magnetic and true north match.

investigated by satellites for several decades, and in-situ measurements of the geomagnetic field in the near-Earth space has revealed that the dipole field becomes distorted by the time-variable solar wind when the field reaches outward into space. The internal field dominates the geomagnetic field from the Earth's surface up to around four r_E, beyond which the geomagnetic field is increasingly affected by the external field.

Both the internal field and the external field change with time. Temporal variations in the overall magnetic field have time scales from seconds up to millions of years. The variations include changes in direction and magnitude, the strength of which can vary from a few nT to thousands of nT, and can be periodic or completely random. For example, the main field varies in strength from approximately $30,000$ nT near the

equator to 60,000 nT at the poles. The secular variation or amount of change is about 10 per year as a result of the geomagnetic pole reversal, during which the north and south pole undergo a reversal i.e. change in direction, that happens every 500,000 years on average; the external field varies on time scales of seconds to days, primarily due to solar interactions. These fields result from current systems and range in intensity from fractions of a nT to thousands of nT.

It is generally believed that the long-term variations, i.e variations with time scales of a year or more, come from the internal field, whereas short-term variations are associated with the external field. The short-term variations can be traced to irregular changes that happen during magnetic storms and regular changes due to the rotation or orbital motion of the Earth, Sun and Moon. The storm-time disturbances that are rapid and intense involve the magnetospheric currents and induced currents in the Earth's crust and oceans, and pose a natural hazard to technological systems that rely on a stable magnetic environment. The long-term variations can be divided into the variations in the Earth's dipole field and its non-dipole field. The non-dipole variations come from electric currents flowing at the core-mantle boundary while the dipole variations are attributed to the Earth's core (Lanza et al., 2006). Another kind of variation that is non-dipole but originates from the core is called the *geomagnetic jerks*, which are relatively sudden changes in the second derivative of the Earth's magnetic field with respect to time (De Michelis et al., 2005). Geomagnetic jerks are observed every one or two years, on average.

To sum up, the geomagnetic field observed at a location in space within the region of the magnetosphere can be regarded as the sum of the internal field $\mathbf{B}_I$ and the external field $\mathbf{B}_E$, i.e. $\mathbf{B} = \mathbf{B}_I + \mathbf{B}_E$, where $\mathbf{B}$ denotes the total observed magnetic field. Both the internal and the external magnetic fields have a time-varying spatial structure, however, the dynamics differs in the two fields. The fields $\mathbf{B}_I$ and $\mathbf{B}_E$ can be regarded as functions of time and location, respectively. The internal field $\mathbf{B}_I$ undergoes slow secular variations and is almost static with respect to the Earth; The external field $\mathbf{B}_E$ is highly variable under the influence of solar wind and IMF conditions and is relatively fixed with respect to the Sun. In the data-based modelling of the magnetic fields, the internal field $\mathbf{B}_I$ is viewed as the negative gradient of the Earth's magnetic potential and the external field $\mathbf{B}_E$ is considered as the overall effects of the major magnetospheric currents, including the ring current, tail current sheet, field-aligned current systems, and the magnetopause

currents. The next section will present computer models of the magnetic fields, together with other magnetic data sources, in further details.

2.2 Sources of near-Earth magnetic data

The geomagnetic field has been routinely measured in a number of ways. At the surface of the Earth, observatories around the world monitor the geomagnetic field at fixed locations. Temporal variations in the ground data are summarized through geomagnetic indices, such as Kp and Dst, for quantifying the global magnetic activity (Menvielle and Marchaudon, 2007). In the near-Earth space, satellite missions sample the magnetic field at time-varying locations restricted to orbital trajectories. Current multi-satellite missions include Cluster II (Escoubet et al., 2001b) and Swarm (Friis-Christensen et al., 2008, Macmillan and Olsen, 2013) launched in 2013. The near-Earth magnetic field is measured by flux-gate magnetometers carried on the spacecraft. Further away from the Earth, the ACE satellite (Smith et al., 1998) records the IMF, a component of the solar magnetic field, carried outward from the Sun by the solar wind, and the solar wind ram pressure in the interplanetary space around the L1 Lagrangian point (The L1 Lagrangian point is the point between the Sun and the Earth at a distance of approximate 1.5 million kilometres). ACE lies outside the magnetosphere, while Earth-orbiting satellites and ground observatories investigate mostly the field within the magnetosphere.

Numerical simulations of the geomagnetic field from computer-based models complement satellite measurements for the study of the near-Earth space environment. The computer models used in the work presented in this thesis are the IGRF model that approximates the internal field, and the Tsyganenko model T96 that approximates the external field. The T96 model requires external conditions, such as the solar wind, IMF, and Dst, to be input. The solar wind and IMF are being measured by satellite in the interplanetary space and the Dst index is derived from ground-based observations. All these input parameters are available on an hourly basis. This section focuses on the Cluster mission that provides magnetic field vector measurements at a high resolution.

2.2.1 Satellite investigations

The Cluster mission (Escoubet et al., 1997) directed by ESA and NASA investigates the small-scale plasma structure in the key magnetospheric regions. The multi-spacecraft mission consists of four identical satellite orbiting around the Earth in a tetrahedral formation. The four Cluster II satellites C1-C4 were launched in pairs in July and August 2000 after the first launch of Cluster I satellite failed in 1996. The mission was declared operational in February 2001 and has been extended until December 2018.

Each Cluster satellite carries the same set of eleven instruments, a complete list of which is given in Table 2.1. The Flux-gate Magnetometer (FGM) (Balogh et al., 2001) listed

TABLE 2.1: The instrumental complement of each Cluster spacecraft

Instrument	Purpose
ASPOC	Spacecraft potential control
CIS	Ion velocity distribution
EDI	Electric field drift velocity
FGM	Magnetometer
PEACE	Electron velocity distribution
RAPID	High energy electron and ion velocity distribution
DWP	Wave processor
EFW	Electric field and waves
STAFF	Magnetic and electric fluctuations
WBD	Electric field and wave forms
WHISPER	Electron density and waves

among the eleven instruments samples the magnetic field as the satellite travels along its orbit, so that the FGM sensor measures the magnetic field at time-varying location in space. Consequently, the in-situ measurements of the magnetic field are constrained by the satellite orbits.

The Cluster satellites were initially launched into similar elliptical polar orbits, within which the satellites reach variable altitude and speed. At or near apogee, i.e. the point of highest altitude, a satellite moves slowly; at or near perigee, i.e. the point of lowest altitude, a satellite travels rapidly. These orbits have a perigee of roughly 4 r_E, an apogee of roughly 19.6 r_E, and orbital periods of 57 hours (Zhang et al., 2010). The plane of the orbits is fixed with respect to the inertial space, and with the Sun-Earth rotation, the plane sweeps through the magnetosphere completing a full scan every year (Escoubet et al., 1997). There is a day-side season from November to June, during which

the satellite spend most of their time investigating the day-side magnetosphere, and a tail season between June and November, when the satellite investigate the night-side magnetotail region. Figure 2.2 shows the two seasons in the left and right panels with a sketch of the magnetosphere as the background. The red ellipses indicate the initial orbit of 2001 and the orbit in 2009 in the two seasons.

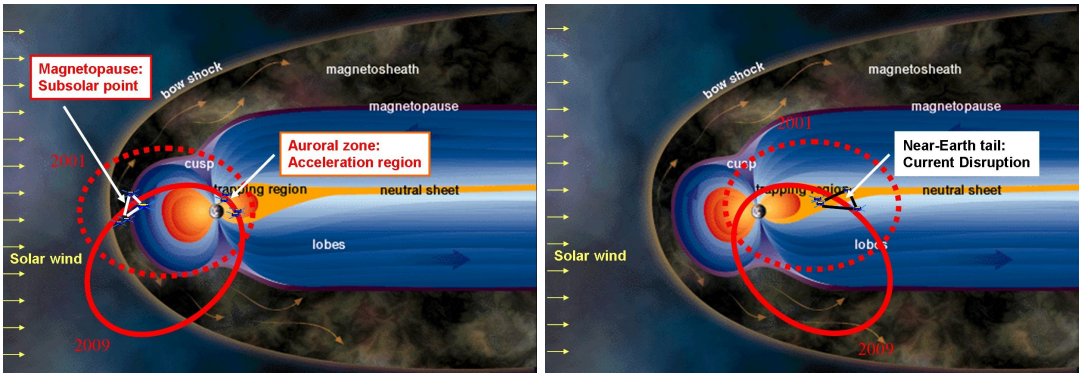

FIGURE 2.2: The sketch of the Earth's magnetosphere with the orbits of Cluster satellite. source: ESA.

The inter-satellite distance varies with time. Figure 2.3 shows that the separations of the satellites within the tetrahedron have changed throughout the mission, from 2001 up to 2018. The separation distance is relatively small in comparison with the distance from the Earth to the satellite. The ESA website at http://sci.esa.int/cluster/

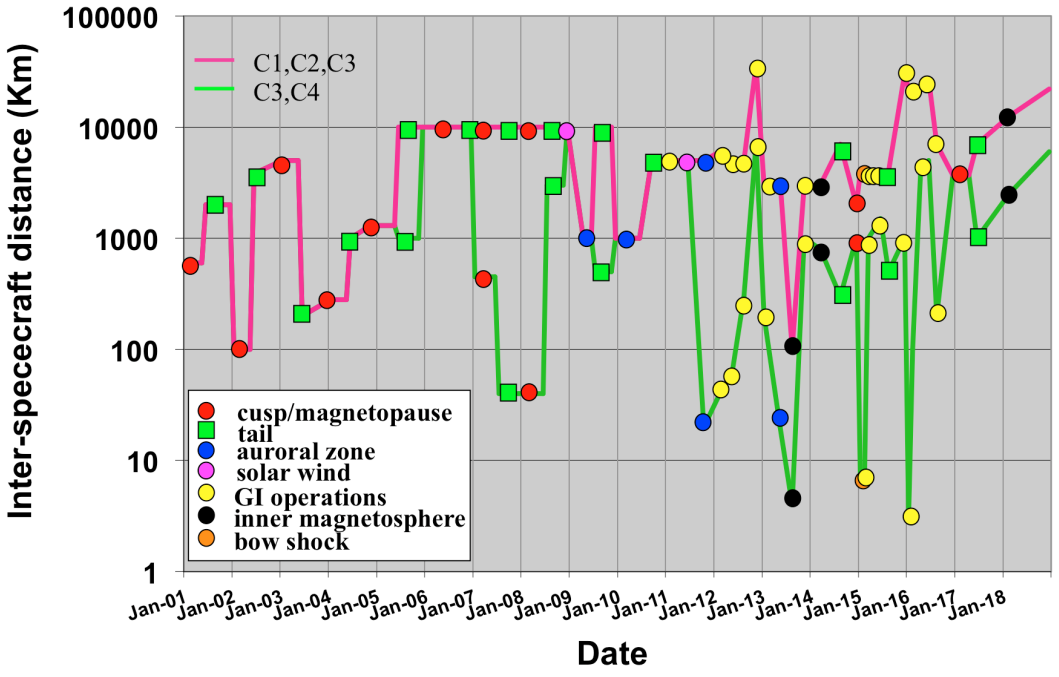

FIGURE 2.3: The inter-satellite separation during the mission. Source: ESA

23160-constellation-geometry-over-time/ also provides a detailed description of satellite operation in relation to Figure 2.3.

The Cluster magnetic field investigation provides provide the magnetic field vector and the position vector in the GSE coordinate system. The FGM instrument carried on Cluster satellite has two tri-axial flux-gate sensors, with one designated as the primary sensor. The sensors can be operated in several ranges, covering the magnetic strength from less than 1 nT to over 65000 nT (Alconcel et al., 2014). The procedures of calibration, validation and archiving the Cluster FGM parameters are described in Gloag et al. (2010). It is important to note that the Cluster data are calibrated by the data centre from 2001 to 2007 but not afterwards. It was claimed by Balogh et al. (1997) that the Cluster magnetic-field investigation provides accurate, hi-resolution, inter-calibrated four-point measurements of the magnetic-field vector in the magnetosphere and in the upstream solar wind along the Cluster orbit. After more than ten years in operation, Alconcel et al. (2014) investigated the long-term trends in the Cluster FGM calibration, and concluded that the calibration parameters of the Cluster FGM sensors are stable, with offset being around 0.2 nT per year in sensors on C1 and negligible on C2, C3 and C4.

The calibrated FGM magnetic data along with the satellite trajectory data for C1-C4 are available in ASCII format from the CDAWeb data service in the Space Physics Data Facility (SPDF) at NASA's Goddard Space Flight Centre https://cdaweb.sci.gsfc.nasa.gov/index.html/.

2.2.2 Computer models

The International Geomagnetic Reference Field (IGRF) (Finlay et al., 2010) is an established numerical model for calculating $\mathbf{B}_I$ the internal magnetic field. The IGRF is based on Gauss's harmonic expansion which has the following expression in spherical coordinates:

$$U(r,\theta,\phi) = R_E \sum_{n=1}^{N} \left(\frac{R_E}{r}\right)^{n+1} \sum_{m=1}^{n} \left(g_n^m \cos m\phi + h_n^m \sin m\phi\right) P_n^m \left(\cos\theta\right), \tag{2.9}$$

where $U(r,\theta,\phi)$ represents the scalar potential of the main field, r denotes the radial distance from the centre of the Earth in units of km, $R_E = 1r_E$ is the Earth radius,

θ denotes the geocentric co-latitude and ϕ denotes east longitude. $P_n^m(\cos\theta)$ are the Schmidt semi-normalized associated Legendre functions of degree n and order m (Winch et al., 2005). g_n^m and h_n^m are the Gaussian coefficients.

The IGRF models the geomagnetic field as a gradient of a magnetic scalar potential and fits the parameters using measured magnetic field from a global network of ground-based observatories and a huge volume of marine, airborne, and satellite data. The IGRF describes the large-scale structure of the main field and its secular variations and updates every five years, as the main field undergoes slow but noticeable variations. The 11-th version of the IGRF, IGRF-11, specifies the numerical coefficient of a truncated spherical harmonic series up to 10th order in n, with 120 coefficients. The coefficient values are give by linear interpolation. IGRF-11 is the internal field model that spans the time interval from 1900.0 to 2015.0. The model coefficients are available at `http://www.ngdc.noaa.gov/IAGA/vmod/igrf.html`, along with software to compute the model output given times and locations as input.

The IGRF model serves as a reasonable approximation in the space near or above the Earth's surface. However, there might be contributions on the surface of the Earth that not taken into account in the model, e.g. man-made sources such as buildings, parked cars, and etc. and natural sources such as the magnetization of crustal rocks. The IGRF model aims to capture the secular variations of the internal magnetic field; hence its estimates should not be very much affected by man-made sources as mentioned above. Other limitations of the IGRF model include errors in the numerical coefficients and omissions as a result of the truncation.

The semi-empirical Tsyganenko magnetic field models (Tsyganenko, 2013) are considered as the best-fit representations for the external magnetic field. The Tsyganenko model has been updated from its earliest version T89 (Tsyganenko, 1989), a simple empirical approximation for the global magnetosphere for different ground disturbance levels, to T96 (Tsyganenko and Stern, 1996a), a variable configuration that has an explicitly defined realistic current systems the response to the different solar wind condition. A few more recent versions of Tsyganenko models are T01, T04S and TS07D (Tsyganenko and Sitnov, 2007). T01 is different from T96 in that T01 requires a one-hour time history of external inputs. T04S and TS07D absorbed more satellite data such as Cluster in determining its dynamical structure. As previous research by Woodfield et al. (2007),

Zhang et al. (2010) suggests, the T96 model among the series of Tsyganenko models is adequate for studying the storm-time disturbances in this project.

The T96 model includes a few modules representing the principal magnetospheric current systems:

- Chapman-Ferraro current confining the dipole field inside the magnetopause;
- the tail current closed via the magnetopause;
- symmetric ring current and partial ring current;
- Birkeland currents, connecting the ionosphere with the solar wind (Region 1 currents) or with the partial ring current (Region 2).

A rough sketch of how the currents flow in space can be found at Figure 1.2 in Chapter 1.

Since the external field is associated with flowing currents that are widely distributed over the space, the external field model cannot be derived from spatially localized observations but extensive sets of spacecraft data that covers the magnetosphere with a sufficient density (Tsyganenko and Sitnov, 2007). Figure 2.4 shows projections of measurement locations on the equatorial plane in the GSM frame for subsets of data taken from five different satellites indicated by different colours. The magenta represents the locations of Cluster satellite.

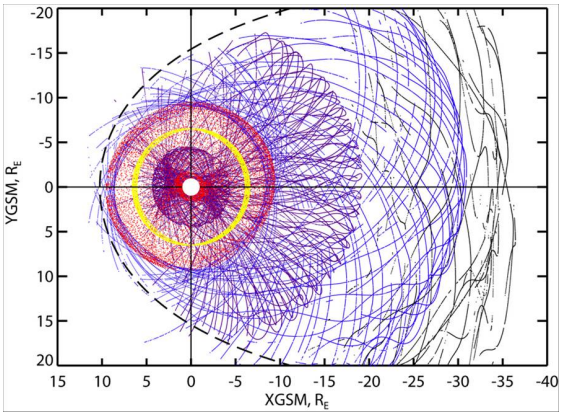

FIGURE 2.4: Distribution of magnetic field data measurements in the magnetosphere. Source: http://rbspgway.jhuapl.edu/geomag_field/model/index.html

Figure 2.5 shows plots of the magnetospheric field lines generated from the Tsyganenko model. The left and right panel plots can be regarded as two snapshots of the magnetic

field line inside the magnetosphere on the x-z plane. In this case, the two plots together illustrate change in magnetic configuration as a result of a southward turn in IMF, where the z-component of IMF goes from 2 nT in the left figure to −8 nT in right figure.

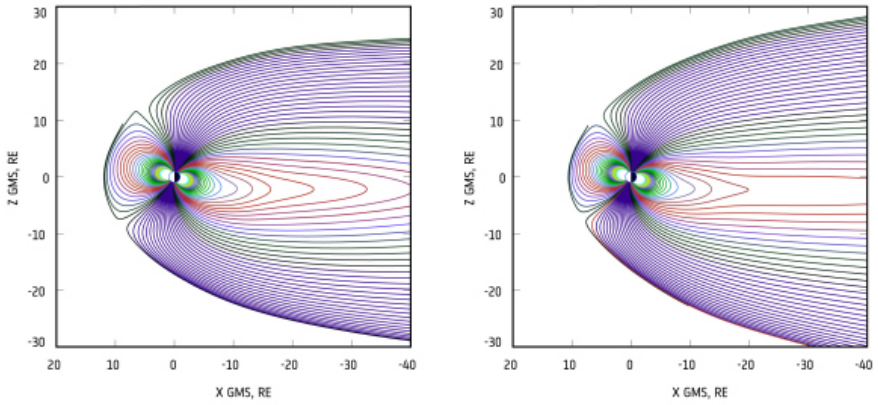

FIGURE 2.5: Examples of magnetosphere field model plots. The left and the right panel show snapshots of magnetic field lines in side the Earth's magnetosphere at two adjacent time points. Source: ESA by N.Tsyganenko (https://directory.eoportal.org/web/eoportal/satellite-missions/content/-/article/cluster)
The figure are plotted in units of r_E in the x-z plane of the GSM coordinate system.

The Tsyganenko model is parametrized by the solar wind ram pressure, Dst index, and the transverse components of the IMF. The input parameters can be obtained from OMNIWeb at https://omniweb.gsfc.nasa.gov/form/dx1.html. The OMNIWeb contains an almost 50-year record of hourly-averaged solar wind magnetic field and geomagnetic activity indices. The solar wind data are derived from 15 geocentric spacecraft and 3 solar spacecraft.

2.3 Sampling from the data sources

High-resolution magnetic field $\mathbf{B}(t, \mathbf{s})$ at time t and location $\mathbf{s}$ has been directly measured by the flux-gate magnetometers (FGM) carried on Cluster satellites. The times and locations at which the magnetic field is measured is determined by the trajectory of the satellites. Numerical estimates of the internal field $\mathbf{B}_I(t, \mathbf{s})$ and the external field $\mathbf{B}_E(t, \mathbf{s})$ can be simulated from mathematical and empirical models, namely the IGRF-11 model and the T96 model, given the time t and the location $\mathbf{s}$ as inputs.

The sampling methods used in this work are designed to pair up the in-situ satellite measurements and the two model-based outputs and carry out regression analysis using

the satellite measurements as the reponse and the two outputs as explanatory variables. For a set of $\{t, \mathbf{s}\}$, there will be corresponding $\mathbf{B}(t, \mathbf{s})$ measured by a Cluster satellite, $\mathbf{B}_I(t, \mathbf{s})$ estimated by the IGRF model, and $\mathbf{B}_E(t, \mathbf{s})$ generated from the T96 model given appropriate input parameters including the transverse components of IMF, solar wind ram pressure, and Dst index. The input parameters for T96 model are all time-dependent and are be obtained from OMNIWeb, as discussed already in Section 2.2.2.

The data available for the Cluster satellites are the trajectories (i.e., time points t and positions $\mathbf{s}$) along with the recorded magnetic vector field, $\mathbf{B}(t, \mathbf{s})$. Hourly values of the observed magnetic vector fields are obtained by sampling at one hour intervals from the Cluster dataset. For the simulated internal and external field outputs, we use the hourly trajectories from each Cluster satellite as inputs. The sampling of the magnetic field vector from the magnetic field models requires simulation in a FORTRAN package GEOPACK (Tsyganenko, 2008). The GEOPACK has 19 subroutines for transformation between various geophysical coordinate systems and calculations of the geomagnetic field model in the Earth's magnetosphere using the numerical model IGRF-11 or the empirical model T96. The time restriction for IGRF-11 is from 1900 to 2015 and for T96 is the recent fifty years during which solar wind and geomagnetic input parameters are recorded.

2.4 Examples of satellite-based and model-based data

This section closes the chapter with a summary of the magnetic data in the near-Earth space at time-varying locations. The satellites and the computer models are producing estimates of the magnetic field $\mathbf{B}$ in three components, X, Y, and Z at times $t \in T$, for some time index set T, at locations $\mathbf{s} \in D$ in a given three dimensional coordinate system $D \subset \mathbb{R}^3$. Given regular hourly measurements in time we have assumed that $T \subset \mathbb{Z}$, the time domain is a subset of the integer set. t takes positive integer values and $\mathbf{s}$ can be vectors restricted to the space covered by the satellite orbits. t stands for number of hours since the first observation and can be converted to the format of "yyyy-mm-dd hh"; $\mathbf{s}$ represents position vector with its x-, y-, and z- components, measured in km or r_E, in GSM coordinate system.

For a component d, $d = X, Y, Z$, let $S_d(\mathbf{s}, t)$ denote the satellite measurement of the magnetic field component d, $I_d(\mathbf{s}, t)$ denote the IGRF model calculation of the internal magnetic field component d, and $T_d(\mathbf{s}, t)$ denote the Tsyganenko (T96) model calculation of the external magnetic field component d.

TABLE 2.2: An example of a magnetic field data subset (1)

Index No.	time (hour) yyyy-mm-dd hh	position (r_E) X	Y	Z	orbit No.
1	2003-01-01 01	5.39	13.15	8.31	1
2	2003-01-01 02	5.87	13.94	7.46	1
3	2003-01-01 03	6.33	14.71	6.37	1

TABLE 2.3: An example of a magnetic field data subset (2)

Index	Satellite (nT)			IGRF (nT)			T96 (nT)		
No.	S_x	S_y	S_z	I_x	I_y	I_z	T_x	T_y	T_z
1	-14.88	7.94	15.24	-5.12	-4.65	2.99	5.19	10.35	-0.47
2	-3.71	12.90	0.98	-4.53	-3.15	3.73	4.59	4.73	-4.22
3	12.75	18.65	-4.09	-3.90	-1.73	4.26	3.95	7.51	-2.74

The sampled magnetic field dataset has a structure illustrated by Table 2.2 and 2.3, which together form a subset of the hourly observations. Table 2.2 lists variables of time, position, and orbit; Table 2.3 lists variables of the sampled observed and modelled magnetic field vectors corresponding to the information in Table 2.2. The magnetic field vectors from different sources have three components in the GSM coordinate frame and the three field strengths are measured in units of nano-Tesla (nT). In the data set, missing values are represented by the symbol NA.

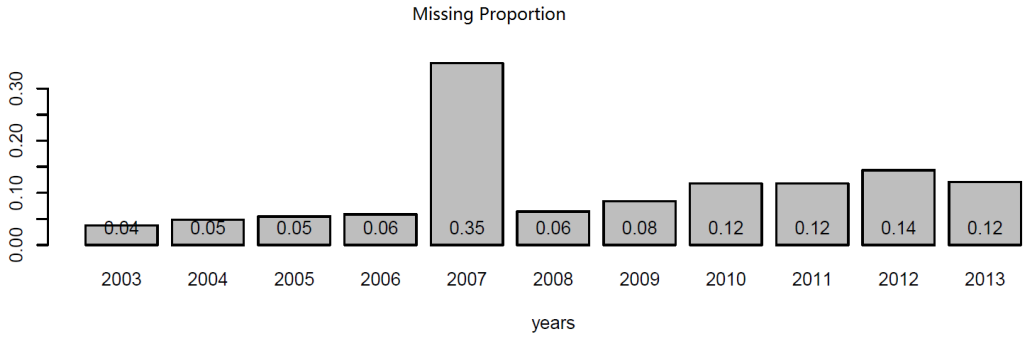

FIGURE 2.6: Missing proportion in years

The dataset contains hourly samples of 11-years from 2003 to 2013, during which Cluster satellites are operative and have rather complete measurements. There are 8760 or 8784 hourly observations for normal or leap years. The 11-year dataset contains 96432

observations in 1663 orbits and roughly ten percent of the observations (10482) are missing. Missing data occur when Cluster satellite measurements are not recorded. There are different amount of data missing every year and especially in 2007, where 35 percent of the observations are missing, as Figure 2.6 suggests. The data do not appear to be missing at random. It has been mentioned that data loss is mainly due to satellite manoeuvre, which happens in the case of satellites changing orbit or storm occurrences to avoid damaging devices carried on the satellite. Further analysis of trajectory data and solar wind data would be required to identify the reason for missing data at particular time.

Previous study suggests that these empirical models provide realistic results in general. Woodfield et al. (2007) surveyed the contributions of ionospheric and magnetospheric current systems to the Earth's magnetic field, by using perigee pass data from the Cluster spacecraft, based on predictions of the Tsyganenko 2001 (T01) global field model. The results showed that the T01 model performs very well in a global sense, although absolute residuals between the data and the model can reach 20 nT near perigee, often with stable bipolar signatures, which repeat on the phase period of the Cluster orbit and were assumed to be observed field-aligned currents (FACs). Zhang et al. (2010) extended the study of Woodfield to compare eight years magnetic field data from the 4-spacecraft Cluster array with the Tsyganenko (T89, T96, T01, T04) models. It has been found that the Tsyganenko models perform better during weaker geomagnetic activity. There are particular deviations from the models associated with the ring current. It also has been concluded that during the ring current crossings through perigee, at around 4 r_E, the T96 model always overestimates the ring current.

Chapter 3

Characterizing the magnetic variations

The aim in this chapter is to derive statistical properties of the observed magnetic fields sampled from the Cluster satellite FGM measurements and compare these properties with the properties of the simulated magnetic fields generated by the IGRF-11 and the T96 models. As mentioned in Chapter 2, the IGRF-11 and the T96 models provide estimates of the internal and the external magnetic fields and the two model outputs are subject to different biases and uncertainties as indicated by reviews of the two models by Macmillan and Finlay (2011) and Tsyganenko (2013). Likewise, the Cluster satellite FGMs, although the general performance of which are considered to be satisfactory, nonetheless, measure the magnetic field with errors, that needs to be quantified. A recent evaluation of Cluster FGM magnetic data can be found in Alconcel et al. (2014). Thus it is necessary to develop a scientific understanding of the near-Earth space magnetic environment in the presence of possible biases and uncertainties.

This chapter serves as an exploratory data analysis chapter and is organized as follows. Section 3.1 presents the space-time dependence of the magnetic field data and demonstrates how it is possible to analyse the spatio-temporal structure in terms of a simpler time series structure. Section 3.2 explores the temporal variations in the time series magnetic data and addresses the relevant statistical issues, such as temporal correlation and changing variances. Section 3.3 performs regression analysis of the magnetic data while accounting for its temporal structure, using the Cluster satellite measurements as

the response and the two computer model outputs as the predictor variables. Section 3.4 closes this chapter with a summary of the exploratory analysis.

3.1 Space-time dependence

The magnetic data are sampled across time as well as space and the spatio-temporal dataset consists of 9 variables that are the satellite measurements and estimates of the internal and the external magnetic field components of the x-, y-, and z- directions in the GSM coordinate frame. For any variable in the dataset, let $\{Y(\mathbf{s},t) : \mathbf{s} \in D_s, t \in D_t\}$ denote the sequence of observations made at spatial position $\mathbf{s}$ and time t with the spatial domain being $D_s \subset \mathbb{R}^3$ and the temporal domain being $D_t \subset \mathbb{R}^1$. If the time t varies discretely (as in our case – the data is sampled hourly), the sequence can be written as $\{Y_t(\mathbf{s}) : \mathbf{s} \in D_s, t \in D_t\}$ where $D_t \subset \mathbb{Z}$. In addition, if a set of time-dependent observations is fixed in space, the spatial components can be discarded and $\{Y_t : t \in D_t\}$ forms a time series.

The sampling processes in space and time is constrained by the motion of Cluster satellites, so that the location in space $\mathbf{s}$ is determined by the time t and the range of the spatial domain D_s becomes the coverage of the satellite in space. We can introduce an *orbital function*, $f : D_t \mapsto D_s$, that maps the time t from the temporal domain D_t to the location in space $\mathbf{s}$ in the spatial domain, and the function should be bijective. The spatio-temporal process $\{Y_t(\mathbf{s}) : \mathbf{s} \in D_s, t \in D_t\}$ with the space-time constraint $\mathbf{s} = f(t)$ can be written as $\{Y_t(f(t)) : t \in D_t\}$, or simply $\{Y_t : t \in D_t\}$. Thus the spatio-temporal process becomes a discrete time series process with the temporal domain being $D_t = \{1, 2, \cdots, n\}$. The spatial information, though not included in the modelling of the data in terms of the time t, can be accessed through the orbital function.

This section explores the space-time dependency in the hourly sampled magnetic field data through visualizing the motion and spatial coverage of the Cluster satellites, and then transforms the spatio-temporal data into time series data, embedding the spatial information into time for later analysis in the following sections. Subsection 3.1.1 introduces the concept of orbit and trajectory for describing the motion of the Cluster satellites. Subsection 3.1.2 relates the space to the time via an orbital function and

presents the magnetic data as a time series with spatial information incorporated in an orbital factor.

3.1.1 Satellite trajectories

Trajectory data consists of the times t and the locations $\mathbf{s}$ at which the Cluster satellites measure the magnetic field. The locations $\mathbf{s}$ are 3-dimensional vectors originally recorded in the GSE frame and then transformed in the GSM frame (see details of coordinate transformation in Appendix A). The GSM frame is a non-inertial reference frame which, by definition, is a frame of reference that is undergoing acceleration with respect to an inertial frame (Tocaci, 2012). The GSM frame is converted from an inertial frame, the GEI frame with time defined in the rotational matrix. This makes space and time interdependent in the GSM frame, apart from the fact that the data are collected at time-varying locations constrained by the motion of Cluster satellites. In other words, the reference frame itself and the location of sampling in the reference frame are both determined by time. The orbits of the satellite can be visualized and understood based on the trajectory information.

As previously mentioned in Chapter 2, the four Cluster satellites, C1, C2, C3 and C4, are flying in a tetrahedron shape, and the size of this tetrahedron varied through time from 200 km up to about 19,000 km. Despite the separation in distance, the four satellites have similar orbital features in the same time periods, as operation of the four identical satellites are controlled simultaneously by European Space Operation Centre (ESOC). Figure 3.1 provides a visualization of the trajectory of C1 in the year 2003. The sub-plots show the satellite positions in the x-z planes in the GSM coordinate system for every month, with yellow curves showing the effects on an orbit which is elliptical in the inertial frame of the transformation to GSM. Assuming no perturbations or manoeuvres in a short time period, the satellite orbit is fixed in the inertial system. When projected into the GSM system, however, the satellite orbit wobbles and its plane gradually sweeps through space. The wobbling effect is caused by the Earth rotating about its rotational axis, as the Earth's magnetic dipole is tilted roughly at an angle of about 10 degrees with respect to the Earth's rotational axis and the GSM frame has the projection of the magnetic field dipole as its z-axis while the inertial frame has the rotational axis as its z-axis. The rotation of the Earth around the Sun causes the satellite to cross the various

near-Earth plasma regions. Every year, the satellite orbit plane should complete a 360 degree scan in the GSM system.

The trajectory of C1 in year 2003 was chosen as C1 is the first satellite and 2003 was the first year in the dataset. Figure 3.1 and 3.2 show the typical variations in the satellite trajectories. Other satellites of other years have similar trajectories.

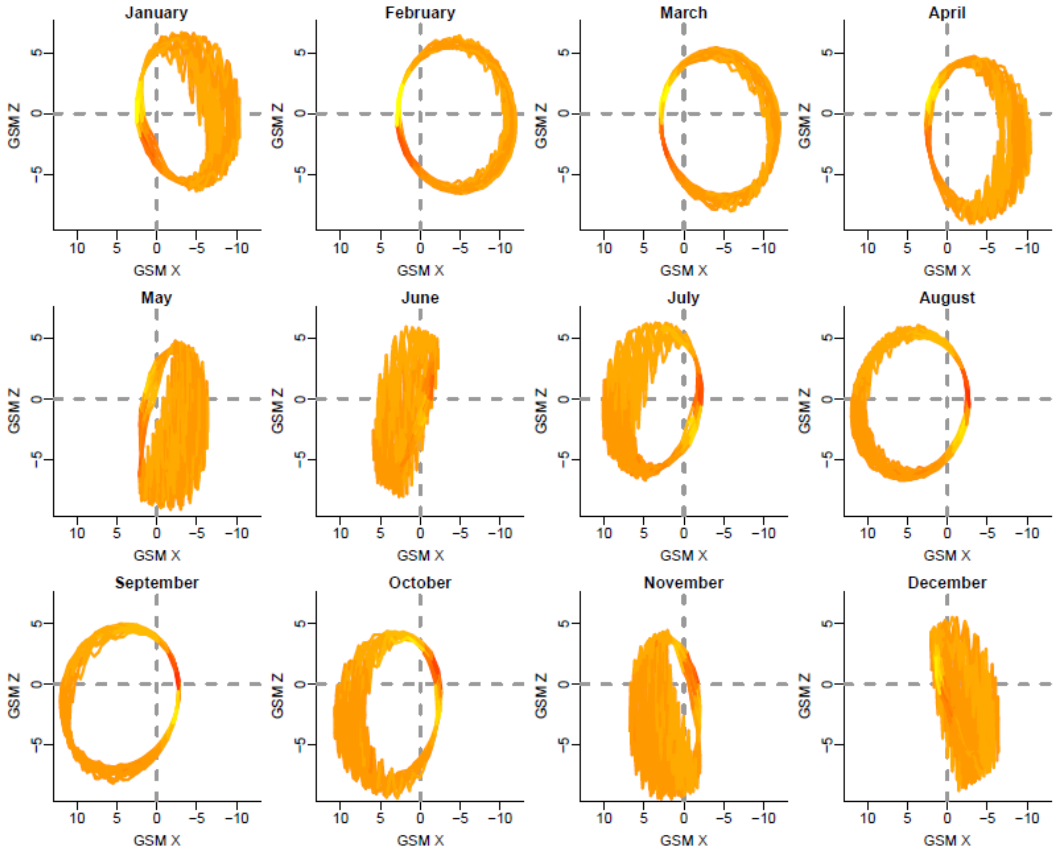

FIGURE 3.1: Orbital variations of satellite by month in 2003
The axis unit is km.The centre of the Earth is at the origin of the reference frame

In the year 2003, the highly elliptical orbits (HEO) of the Cluster satellite reached a perigee of around 4 Earth radii (r_E) and an apogee of 19.6 r_E. Each orbit took approximately 57 hours to complete. We visualise the perigee and apogee positions of C1 of the 2003 orbits in Figure 3.2. Orbits are numbered from 1 to 154 in 2003. The starting point of an orbit is chosen to be the location at time half way through an apogee to a perigee, and the end point lies roughly at the same position as its starting point after an orbit period. The orbits are defined in this way so that it is easy to split one orbit into two halves, the perigee-crossing half and the apogee-crossing half, for later investigation. The plot is given on the x-y plane in GSM system. Dots on the inner circle

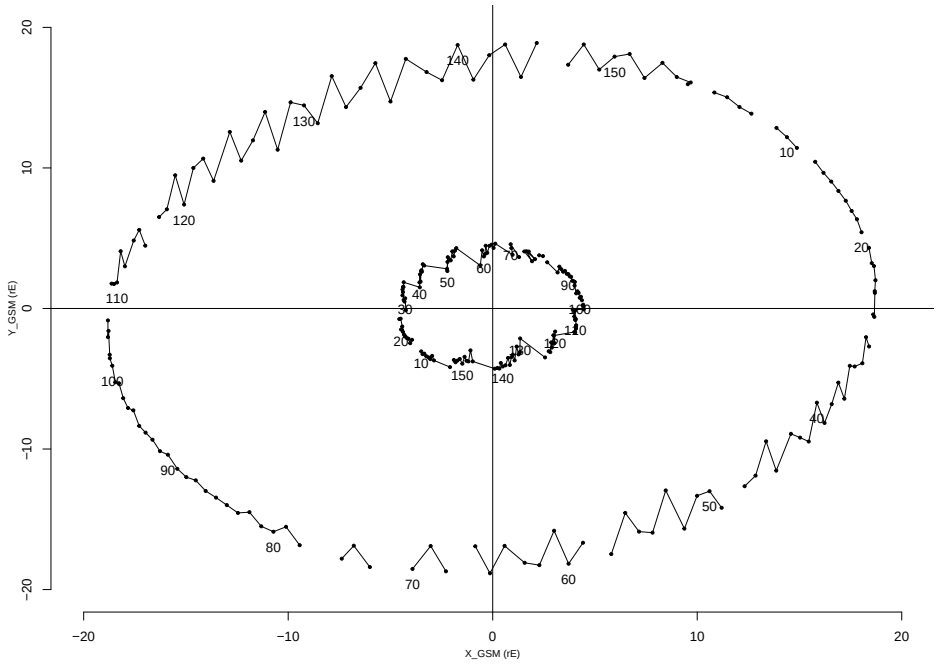

FIGURE 3.2: Perigee and apogee locations of C1 in 2003 on the GSM x-y plane

mark the perigee locations, and dots on the outer circle mark the apogee locations. The perigees and apogees are labelled for selected orbits from 10 to 150 at a separation of 10 orbits. As the number indicates on the x-y plane in GSM system, the projected axis of the satellite orbit goes clockwise. Along the two circles, there are dots along the curve that are disconnected. This suggests that there are discontinuities in the observation. Data are missing in these disconnected areas around perigees and apogees and at other locations where satellite positions are not recorded. The missing data problem will be addressed in a later section.

The example of the trajectory of the C1 satellite in 2003 has shown orbital variations in the GSM coordinate system. When elements of the orbit remain unchanged, or the orbit is fixed in the inertial system, the orbital variations in the GSM system come from the Earth's rotation, which generates wobbling features, and the rotation of Earth around the Sun, causing the orbit plane to sweep through the magnetosphere.

Apart from the short-term orbital variations described in the above example, there exists long-term orbital variations resulting from artificial and natural forces, such as manoeuvres and gravitational perturbations. Satellite manoeuvres change the semi-major axis of the orbit, apogee and perigee altitudes, orbital period, orbit plane inclination etc. Data are not available during or shortly after manoeuvres. The satellite orbit also changes

over time due to gravitational perturbations by other objects. It is impossible to describe satellite orbits precisely using only fixed orbital parameters, commonly known as Keplerian elements, throughout the whole Cluster mission, as Keplerian elements only describe the orbit at any given instant of time, and they are time-varying.

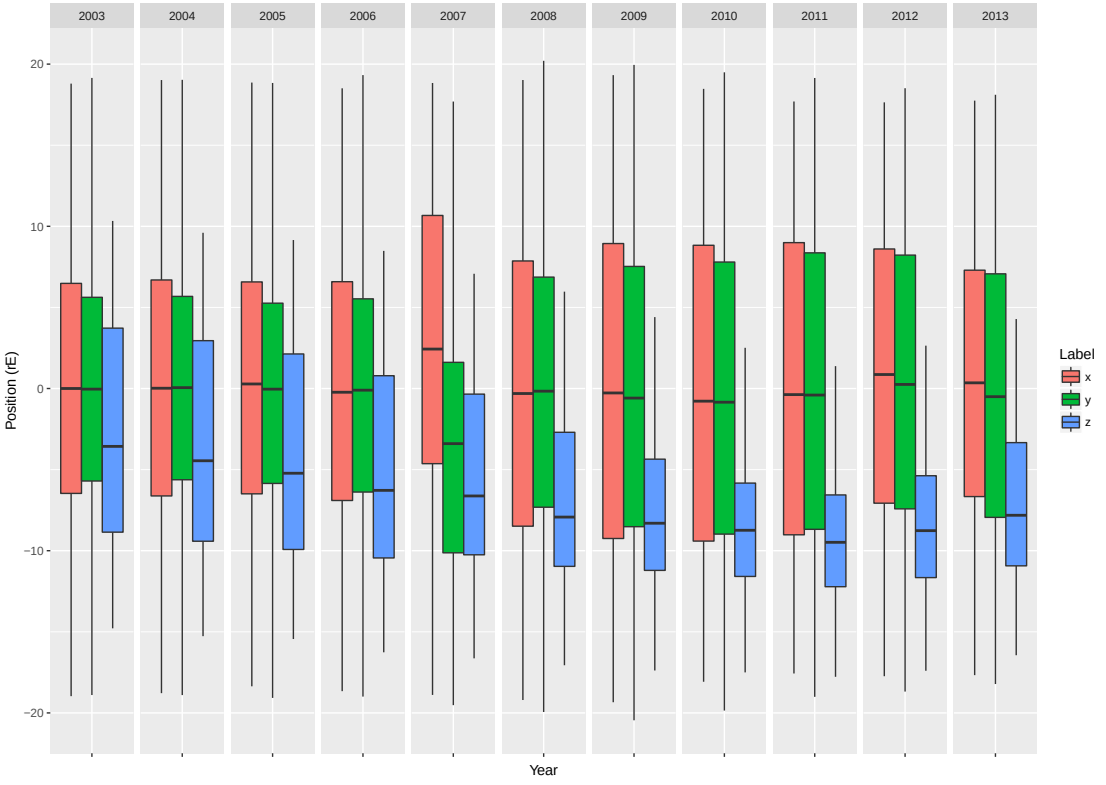

FIGURE 3.3: Boxplot of the C1 satellite locations from 2003 to 2013

Figure 3.3 roughly assesses the long term orbital variations in C1 satellite using box-plot of the satellite locations. From 2003 to 2013, box-plots are given for satellite positions in the x-, y-, and z-direction in the GSM system. From the z-component, shown by boxes coloured in blue, it can be observed that gravitational effects of the Earth impose a long term cycle of change in the mean distance, which reduced to a minimum in 2011 before beginning to rise again. The sudden change in the 2007 trajectory data for the x- and y-component was mainly due to missing observations and satellite manoeuvre. In later analysis of magnetic field data, orbits along which large proportion of missing values occurred were removed hence the sudden change in the trajectory data wouldnt affect the modelling of the magnetic field data. The gradual change in the z-component can be explained by the fact that polar orbit tends to cartwheel as it need fuel to maintain apogee in equatorial plane. Similar results have been obtained from trajectory analysis of the other Cluster satellites.

3.1.2 Time dependence

Let $\{Y_t(\mathbf{s}) : \mathbf{s} \in D_s, t \in D_t\}$ denote a sequence of magnetic field strengths recorded at time t and space $\mathbf{s}$. There exists a function $f : D_t \mapsto D_s$ assigning the time t to the space $\mathbf{s}$. The function f specifies the movement of the satellite in space and time and can be regarded as an orbital function. It is difficult to define the motion of the satellites in an explicit function since the motion is being affected by a number of unexpected conditions such as the cumulative effects of gravitational perturbation or the satellite manoeuvre. To simplify this problem, the orbit numbers, i.e. the labels of the perigees, are considered as the orbital factor in the later analysis of the magnetic data. Hence the orbital factor together with the time index takes account of the proximity in time and space in the non-inertial GSM reference and the orbital factor will used be in statistical modelling in the later section to allow variations in the parameters across orbits.

Setting aside the orbital factors, the spatio-temporal magnetic data becomes time-dependent only, with spatial information incorporated in time. The datasets of each individual satellite can be regarded as a multivariate time series of 9 components, namely the satellite measurements and the two model outputs of the magnetic field strengths in the $\{x, y, z\}$ direction in the GSM frame. The datasets contain $\{S_x, S_y, S_z, I_x, I_y, I_z, T_x, T_y, T_z\}$ for each of the four satellites $\{C1, C2, C3, C4\}$. For a given component $d \in \{x, y, z\}$, a subset of three variables $\{S_d, I_d, T_d\}$ is of interest and the subscript d can be omitted for simplicity. To include the time-dependency, the notation of the subset becomes $\{S_t, I_t, T_t\}$ for $t \in \mathbb{Z}$. The next section explores the temporal variations in $\{S_t, I_t, T_t : t \in \mathbb{Z}\}$ of all three components $\{x, y, z\}$ and the four satellites $\{C1, C2, C3, C4\}$.

3.2 Temporal features

3.2.1 Trends, seasonal, and cyclic patterns

We start by visualizing the temporal variations in the magnetic field data in a short time period. Figure 3.4 gives time plots of a single satellite (C1) measurements and the two model outputs within an orbit period of 57 hour. The top panel (a) has the position vectors decomposed into three components in the GSM coordinate frame. The grey dotted vertical lines indicate the time at which the satellite reaches perigee in the orbit.

Panel (b) plots C1 measurements of the magnetic field. The x-, y-, and z- components of the field vectors are represented by the black, blue, and red curves. The field strengths lies in the range of −400 to 400 nT. The field curves take a bipolar shape as the satellite sweeps across the geomagnetic equator around the perigee and are flat at both ends. As the magnetic field strength drops off rapidly with distance from the Earth, the field strengths have values close to zero when the location of sampling is far from the perigee. Around the perigee, the field strengths deviate from each other in magnitude. Panel (c) plots IGRF outputs along the same orbit of C1 obtained by calculating IGRF at the C1 positions and times. The patterns in (c) are almost identical to (b). Panel (d) plots the T96 outputs within the range of −100 to 100 nT, where the model has been generated from the appropriate solar wind and other inputs. The variation in T96 outputs is much smaller but more spread out compared to IGRF outputs. This means that the internal field is more variable than the external field in scale and the large variations in the satellite measurements mainly come from the internal field with in this time period.

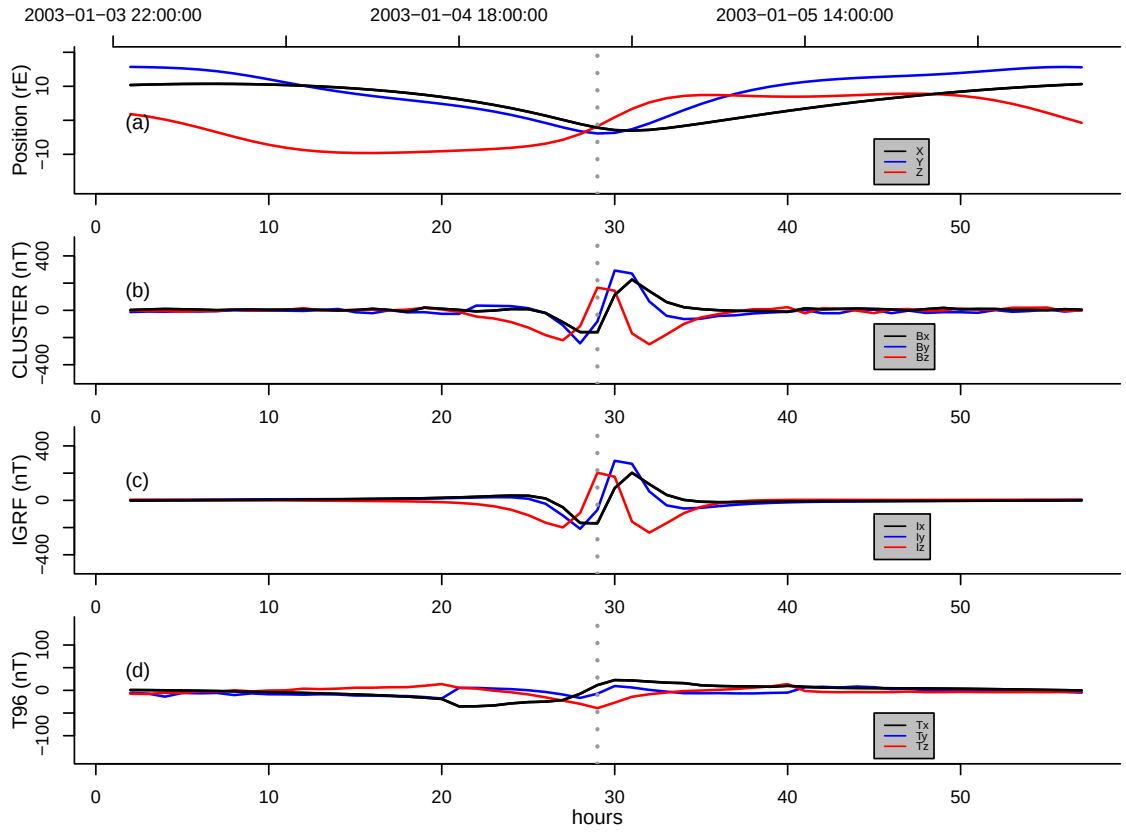

FIGURE 3.4: temporal variations within an orbit

We visualize the variations on a longer time scale by taking a full year of satellite data.

Figure 3.5 plots the satellite measurements of the field strengths against time in the year 2003. From top to bottom rows the figure has the x-, y-, and z- components of the magnetic field. The figure shows, on the left column, time plots of the three components in the full year. All three components seem to have mean values centred around zero. Cyclic features can be observed in the x- and y- component. The z-component has changing variance as well. Between the two blue vertical lines are data in March, the time plot of which is given in the middle column for further examination. The right column plots the data in June, corresponding to the interval between the red vertical lines in the left column plots. There are periodic patterns in the month time plot. The length of the period approximates to the orbital period of 57 hours. The spikes in the magnetic fields values are due to perigee crossing. The magnitude of the spike varies over the three components, and over time. When the satellite is not crossing the perigee, the magnitude of the magnetic field is closer to zero.

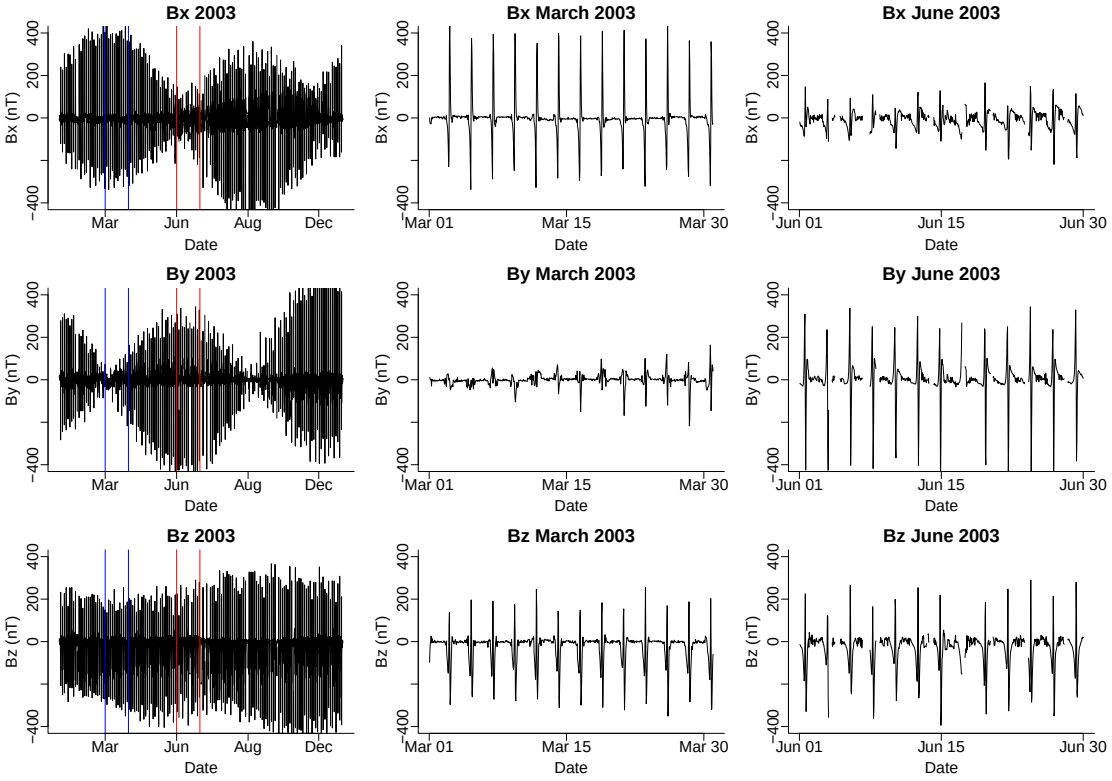

FIGURE 3.5: Time plot of hourly sampled satellite data in 2003

Figure 3.6 provides a better visualization of the monthly variations in the magnetic data and associates the variations to the shifting locations in space. The left panels are box plots of the magnetic field strengths, from top to bottom, in the x, y, and z components; the right panels are the box-plots of the satellite position vectors, from top to bottom,

in the x-, y-, and z- components. The plots show that there are notable cyclic patterns in the x- and y- components of both the satellite measurements and positions.

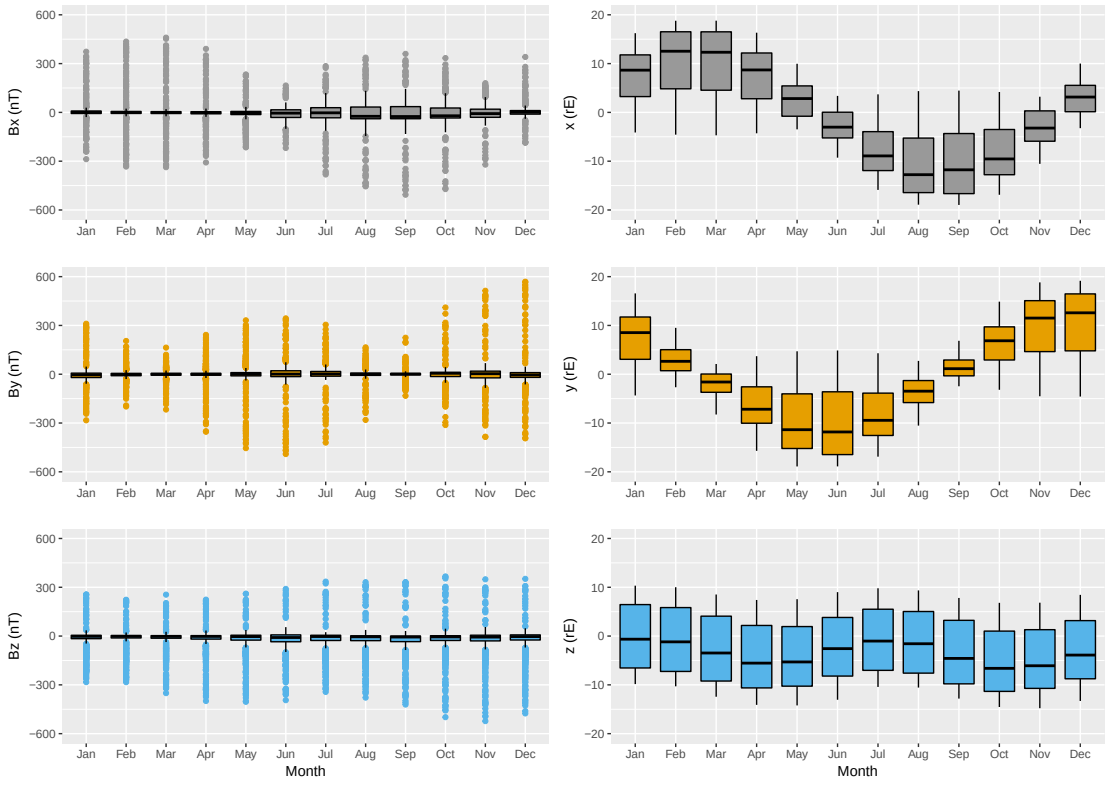

FIGURE 3.6: Box plots of the satellite measurements and positions by month

Figure 3.7 provides the time series plots of C1 measurements and position from 2003 to 2013. From top to bottom are the x-, y- and z- component of the measured magnetic field vectors and the x-, y- and z- component of the satellite position vectors. The vectors are recorded in the GSM frame and have one-hour resolution. The behaviour of the magnetic data in the first half of the plot is quite different from its behaviour in the second half. Up to the year 2007, the magnetic field strengths in the x- and y- components have a seasonal pattern, however, the pattern changes dramatically after 2007 and missing values as indicated by the blank regions in the plot occur more frequent in the later years. This could be a results of satellite manoeuvre. The time plots of the position vectors in the bottom three panel suggested that the orbital inclination changes as the z-component has a decreasing trend when the x- and y- component remain the same. This is a demonstration of one satellite data and the other three satellites data have similar features since the satellite are staying relatively close to each other and are thus investigating the same regions at the same time.

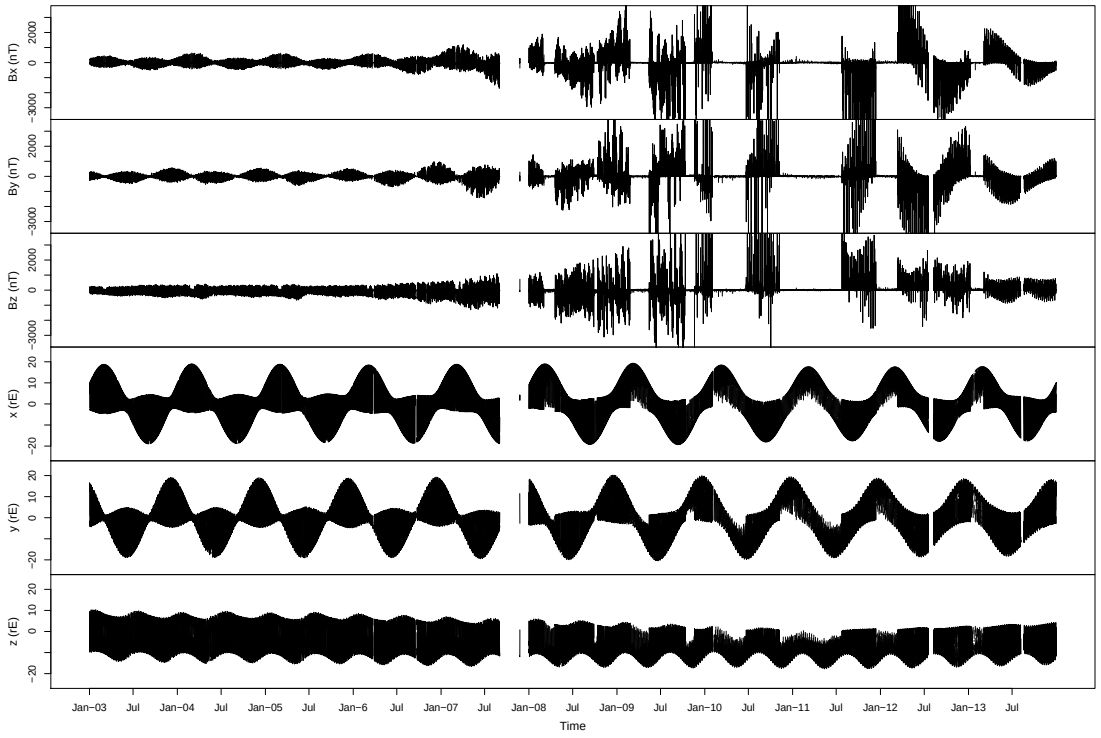

FIGURE 3.7: Time plot of satellite measurements and positions from 2003-2013

3.2.2 Missing data

Missing values occur when satellite measurements are not recorded in the exact hours that the data are being sampled at. The four Cluster satellites appear to have missing values at the same times and locations, hence the missingness in the satellite data is considered to be a results of satellite manoeuvres. Figure 3.7 give us a rough idea of where and when the data are missing. The blank space in the time plots indicates missing values. The plot suggests a large portion of data are missing in the second half of the year 2007 when the satellites were shifting orbits and in the later years there are noticeable missing values as well. The dataset from 2003 to 2006 seems to be rather complete compared with the dataset of other years. However, there is a small portion of missing values which are not observable in the time plots in all these years. The time plots in Figure 3.7 also tells us that the satellite records of the magnetic field vectors and the position vectors are consistent in that missing values occurs at the same time in both. This is important because the IGFR and T96 models would not generate outputs if the position vectors are not available. Therefore in the magnetic field dataset $\{S_t, I_t, T_t\}$ across the three components and the four satellite are missing at the same time.

Most statistical methods for discrete-time series assume that values are observed at all the regularly sampled time point. When data is missing we have to impute the missing values (while carefully accounting for the uncertainty of imputed non-observed values) or modify the statistical procedure to account for the missingness. The pattern in the missingness needs to be identified before analysing incomplete data. Little and Rubin (2014) provides a comprehensive discussion of exploring and processing datasets with missing values. The mechanisms that leads to missing data, or the relationship between missingness and the underlying values in the dataset, can be summarized as follows:

- Missing completely at random (MCAR) means the probability of a value being missing is not related to the observed or missing values;
- Missing at random (MAR) means the probability of a value being missing is only related to the observed values but not the unobserved values;
- Missing not at random (MNAR) means there are systematic and informative reasons why data are missing and should be carefully evaluated.

As mentioned above, it seems that missing satellite observations are due to orbital manoeuvre. It is evident that missing observations are unrelated to the magnetic field values themselves, since satellite manoeuvres tend to happen around the same time very year while extreme values occur under magnetic storm on rare occasions. The missingness caused by the manoeuvres was removed by discarding orbits along which over one third of satellite observations are missing. The new dataset of satellite observations along selected orbits no longer has a missing pattern. Therefore it is safe to carry on with the assumption of MAR; i.e., the patterns of missingness do not depend on the unobserved values. The modification of statistical methods for dealing with the magnetic data with the MAR assumption will be included in the next chapter, Data imputation would be achievable for satellite position vectors, and subsequently, the magnetic field vectors once the relationship between the satellite measurements and the model outputs has been established and the model outputs have been generated given imputed position vectors.

3.2.3 Limits of detection

Data can be recorded as the minimum or the maximum of the detection level of an equipment when true values of the observations are below or above the limit of detection. Limits of detection exists as a problem not for the satellite data but the T96 model outputs, since the T96 model requires external input parameters and some of which are out of the range of detection.

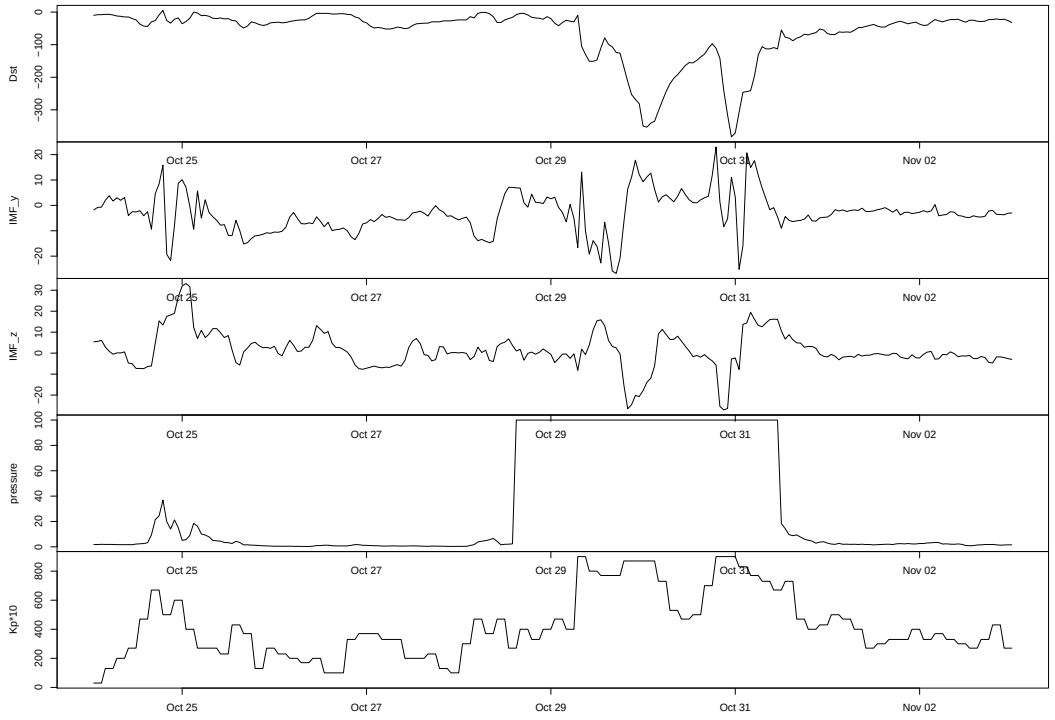

FIGURE 3.8: Time plot of T96 model input parameters in Oct 2003

Figure 3.8 shows an example in which one of the T96 input parameters is saturated. From top to bottom the figure presents time plots of the Dst index, the y- and z-component of IMF, the solar wind ram pressure, and the Kp index. The first four variables are inputs parameters for the T96 models and the last variable quantified the level of disturbances during a magnetic storms. The time range of these plots are spanning over the 2003 Oct storm. The solar wind ram pressure shown in the fourth panel are saturated at the values of 100, meaning the data are recorded as above the limit of detection. This happens when the magnetic environment is highly disturbed as indicated by the Kp index being over 8 (Kp*10 $>$ 80). As a result, the T96 model outputs could be compromised or biased given a saturated input parameter. Whether

the T96 model outputs are still true representation of the external magnetic field under the storm conditions will be examined in the next chapter.

Further analysis of the T96 input parameters suggests that the solar wind ram pressure becomes saturated during long-lasting and highly disturbed storms and such storms only happen on very rare occasion. For most of the major storms, for example the May 2003 storm with time-dependent inputs parameters given in Figure 3.9, there is no such problem when the disturbances level is high in a shorter time span.

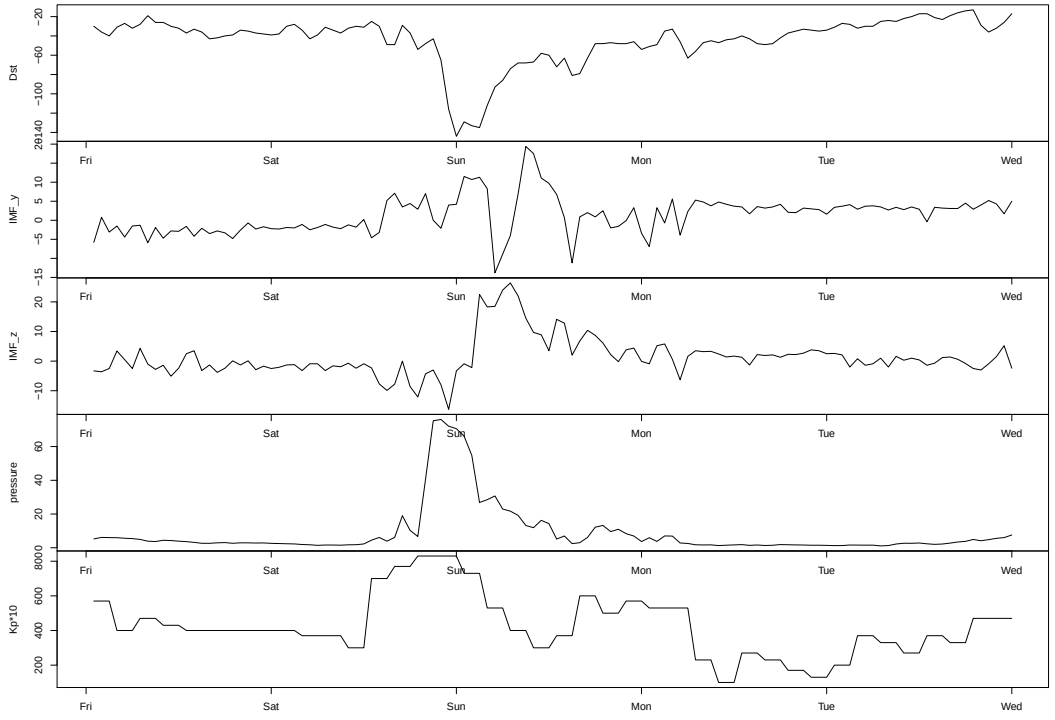

FIGURE 3.9: Time plot of T96 model input parameters in May 2003

Conventional methods for dealing with this problem is to assume that the data values are censored, and to adjust the statistical analysis to account for possible censoring. A detailed discussion of statistical methods for censored data can be found at Helsel (2012). In this thesis, the problem will not be discussed further as it is not a major concern given that the limits of detection are not on the direct observations and only apply for certain extreme events. The biases of T96 model engendered by the limits of detection on the input parameters will be attributed to the overall performance of the model in the later chapters. Extreme value theory deals with the stochastic behaviour of the extreme values in a process and has been investigated for quantifying extreme

behaviour in geomagnetic activity. However, the non-stationary nature of magnetic field data poses a problem for making extreme value analysis assumptions (Thomson et al., 2011).

3.3 A hierarchical statistical modelling approach

This section describes a hierarchical modelling approach that links the satellite measurements to the two model outputs for each individual Cluster satellite. The approach provides a structure that allows the bias and uncertainties of the magnetic data to be incorporated and quantified in a statistical model. We start with simple regression models that take the satellite measurements as the response and the two computer model outputs as the explanatory variables, and then through careful diagnostics of the residuals we make the model progressively more complicated to handle the time series dependence that we observed in the regression errors.

The section is organized as follows: Subsection 3.3.1 introduces the model structure in the time series context and states the assumptions of a regression model for the satellite measurements of the magnetic field. Subsection 3.3.2 analyses the regression residuals using time series methods and explores statistical properties of these residuals, such as time series dependence in the mean and in the variance of the residuals. Subsection 3.3.2 then summarizes the regression modelling results and the time-series properties of the regression residuals and comments on the relationship between the satellite measurements and the model outputs as informed by the statistical model.

3.3.1 Regression in the time series context

For any Cluster satellites $C \in \{C1, C2, C3, C4\}$ and any component $d \in \{x, y, z\}$ in the GSM frame, our magnetic field dataset contains a subset of three time series variables. Let B_t denote the latent magnetic field component d at the position of C at time t, and B_t can be decomposed into an internal field and an external field. The magnetic dataset $\{S_t, I_t, T_t\}$ at every time point t, for $t \in \{1, 2, \cdots, n\}$ where n denotes the length of each variable in the dataset, has a satellite measurement S_t that estimates the magnetic field strength B_t and two model outputs I_t and T_t that estimate, respectively, the internal

and external components of B_t. It is reasonable to assume that S_t measures B_t with an error ϵ_{1t}, i.e.

$$S_t = B_t + \epsilon_{1t}, \qquad t \in \{1, 2, \cdots, n\}, \tag{3.1}$$

and B_t is linearly dependent on the I_t and T_t, i.e.

$$B_t = \mu_t + \alpha_t I_t + \beta_t T_t + \epsilon_{2t}, \qquad t \in \{1, 2, \cdots, n\} \tag{3.2}$$

where μ_t, α_t, β_t are time-dependent coefficients and ϵ_{2t} is an error. Thus, through a hierarchical approach, the satellite measurements can be related to the model outputs via the latent magnetic field,

$$S_t = \mu_t + \alpha_t I_t + \beta_t T_t + \epsilon_t, \qquad t \in \{1, 2, \cdots, n\} \tag{3.3}$$

where for each t, ϵ_t can be regarded as the sum of ϵ_{1t} and ϵ_{2t}.

We will show that the measurements of the magnetic fields from the satellites has a linear relationship with the two model outputs and that the two outputs can be considered to be independent from each other, as they were generated from computer models that represent separate magnetic fields of different origins (see Chapter 2).

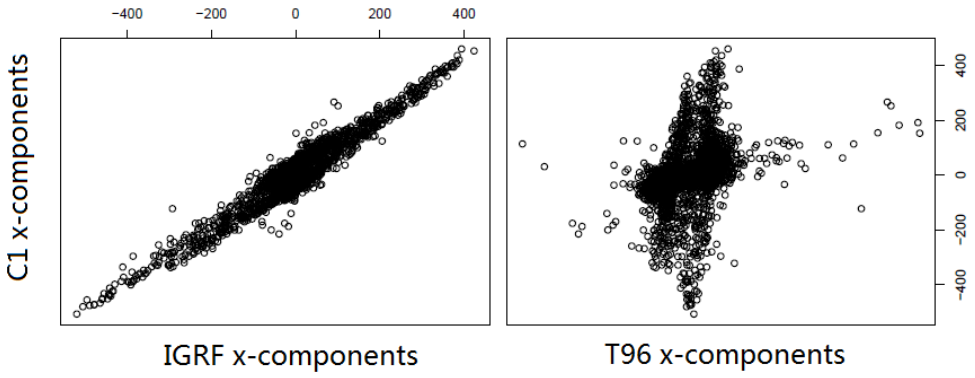

FIGURE 3.10: Scatter plots of the satellite measurements against the two model outputs of the x-components in C1 2003

Figure 3.10 plots the x-components of the satellite measurements against the x-components of the IGRF and T96 model outputs. The figure displays the pairwise relations among the three variables as labelled. The dataset is taken from the satellite C1 in 2003. The scatterplots suggest a strong linear relationship between the satellite measurements and

the IGRF model outputs and a weak linear relationship between the satellite measurements and the T96 model outputs.

We start with a simple regression model and set the time-varying parameters μ_t, α_t, and β_t in model 3.3 to fixed parameter μ, α, and β in model 3.4,

$$S_t = \mu + \alpha I_t + \beta T_t + \epsilon_t, \qquad t \in \{1, 2, \cdots, n\}. \tag{3.4}$$

The model in Equation 3.4 can be expressed in a matrix form

$$\mathbf{y} = \mathbf{X}\boldsymbol{\theta} + \boldsymbol{\epsilon}, \tag{3.5}$$

where $\mathbf{y}$ is a $n \times 1$ vector of observations, $\mathbf{X}$ is a $n \times 3$ matrix of rank 3, $\boldsymbol{\theta}$ is a 3×1 vector of unknown parameters, and $\boldsymbol{\epsilon}$ is a $n \times 1$ vector of observational errors, i.e.

$$\mathbf{y} = \begin{pmatrix} S_1 \\ S_2 \\ \vdots \\ S_n \end{pmatrix}, \quad \mathbf{X} = \begin{pmatrix} 1 & I_1 & T_1 \\ 1 & I_2 & T_2 \\ \vdots & \vdots & \vdots \\ 1 & I_n & T_n \end{pmatrix}, \quad \boldsymbol{\theta} = \begin{pmatrix} \mu \\ \alpha \\ \beta \end{pmatrix}, \quad \boldsymbol{\epsilon} = \begin{pmatrix} \epsilon_1 \\ \epsilon_2 \\ \vdots \\ \epsilon_n \end{pmatrix}.$$

Assuming that the components of $\boldsymbol{\epsilon}$ are uncorrelated and have a mean value of zero and a constant variance, say σ^2, the estimator of $\boldsymbol{\theta}$ can be obtained by the least squares method which minimize $(\mathbf{y} - \mathbf{X}\boldsymbol{\theta})^T(\mathbf{y} - \mathbf{X}\boldsymbol{\theta})$ with respect to $\boldsymbol{\theta}$. The *Gauss-Markov Theorem* states that in a linear regression model in which the errors have expectation zero and are uncorrelated and have equal variances, the best linear unbiased estimator (BLUE) of the coefficients is given by the ordinary least squares (OLS) estimator. The OLS estimator has the form $\widehat{\boldsymbol{\theta}} = (\mathbf{X}^T\mathbf{X})^{-1}\mathbf{X}^T\mathbf{y}$.

To apply the Gauss-Markov Theorem in a time series context, the following assumptions must hold:

1. Linearity: there exists a relationship between the response y_t and two explanatory variables x_{t1} and x_{t2};

2. No perfect collinearity: no explanatory variables can be expressed as a linear function of other explanatory variables;

3. Strict exogeneity: the explanatory variables are strictly exogenous with respect to the error term,

$$\mathrm{E}(\epsilon_t|\mathbf{X}) = 0, \quad t = 1, 2, \cdots, n.$$

4. No serial correlation: the errors are uncorrelated,

$$\mathrm{Cov}(\epsilon_t, \epsilon_{t-\tau}|X) = 0, \quad \tau = 1, 2, \cdots, n-1.$$

5. Homoskedasticity: the conditional variance of the error term is constant, i.e.

$$\mathrm{Var}(\epsilon_t|\mathbf{X}) = \sigma^2, \quad t = 1, 2, \cdots, n.$$

When conditions $1-3$ hold, the OLS coefficient estimator is unbiased, i.e. $\mathrm{E}(\widehat{\boldsymbol{\theta}}_{OLS}) = \boldsymbol{\theta}$. When conditions 4 and 5 are added, the unbiased of the standard OLS estimator of the variance of the OLS coefficients estimator can be obtained so that the standard tools of OLS can be used for inference. The Gauss-Markov Theorem assures that OLS is BLUE under the conditions $1-5$. If an additional condition that the error term is normally distributed and has mean zero, $\epsilon_t \sim \mathcal{N}(0, \sigma^2)$, hold, then the OLS coefficient vector has a normal distribution and the ratio of each coefficient to its standard error has a t distribution.

In our analysis of the magnetic data, condition $1-3$ are self-evident so that $\widehat{\boldsymbol{\theta}}_{OLS} = \{\hat{\mu}, \hat{\alpha}, \hat{\beta}\}$, the OLS estimates of the regression coefficients in Equation 3.4 must be unbiased. Regression residuals obtained through the OLS estimation, $\hat{\boldsymbol{\epsilon}} = \mathbf{y} - \mathbf{X}\widehat{\boldsymbol{\theta}}$, can be used to check condition 4 and 5.

Model 3.4 was fitted to one-year (2003) magnetic field data of the C1 satellite in three components so that three models with the same regression structure were developed for C1 satellite measurements in the x-, y-, and z-components in the GSM coordinate frame. Table 3.1 shows the parameters estimated from the regression models for the three components. All the coefficients in the regression model are highly significant. The models of the x-, y-, and z- components have the R-squared as 0.9667, 0.9744 and 0.9798, respectively. This indicates that the linear models explain about 96-97 percent of the variability of the satellite measurements with the IGRF and T96 model outputs. The intercepts $\hat{\mu}$ are negative for all three components. The IGRF coefficients are estimated

to be very close to 1 and the T96 coefficients are estimated to be slightly lower than the values of the IGRF coefficients. Confidence intervals can be constructed for $\hat{\mu}$, $\hat{\alpha}$,

TABLE 3.1: OLS estimates of the regression coefficients

	the x- components	the y- components	the z-components
$\hat{\mu}$	-0.703	-0.226	-1.774
$\hat{\alpha}$	0.992	1.002	1.001
$\hat{\beta}$	0.943	0.814	0.818

and $\hat{\beta}$ for assessing the regression parameters and quantifying the relationship between the satellite measurements and the computer model outputs if the variance-covariance structure of $\widehat{\boldsymbol{\epsilon}}_t$ is known. However, the information is unavailable since condition 4 and 5 have not been validated.

Figure 3.11 shows the time plots of the OLS residuals $\{\hat{\epsilon}_t\}$ of the models. Panel (a) plots the residuals $\{\epsilon_t\}$ estimated from the GSM x-component against time t, $t \in \{1, 2, \cdots, n\}$, where n represents the total number of discrete hours in the year and has the values of $24 \times 365 = 8760$. Panel (b) gives the time plot of $\{\epsilon_t\}$ from the y-component and Panel (b) gives the time plot of $\{\epsilon_t\}$ from the z-component. The residuals of the three

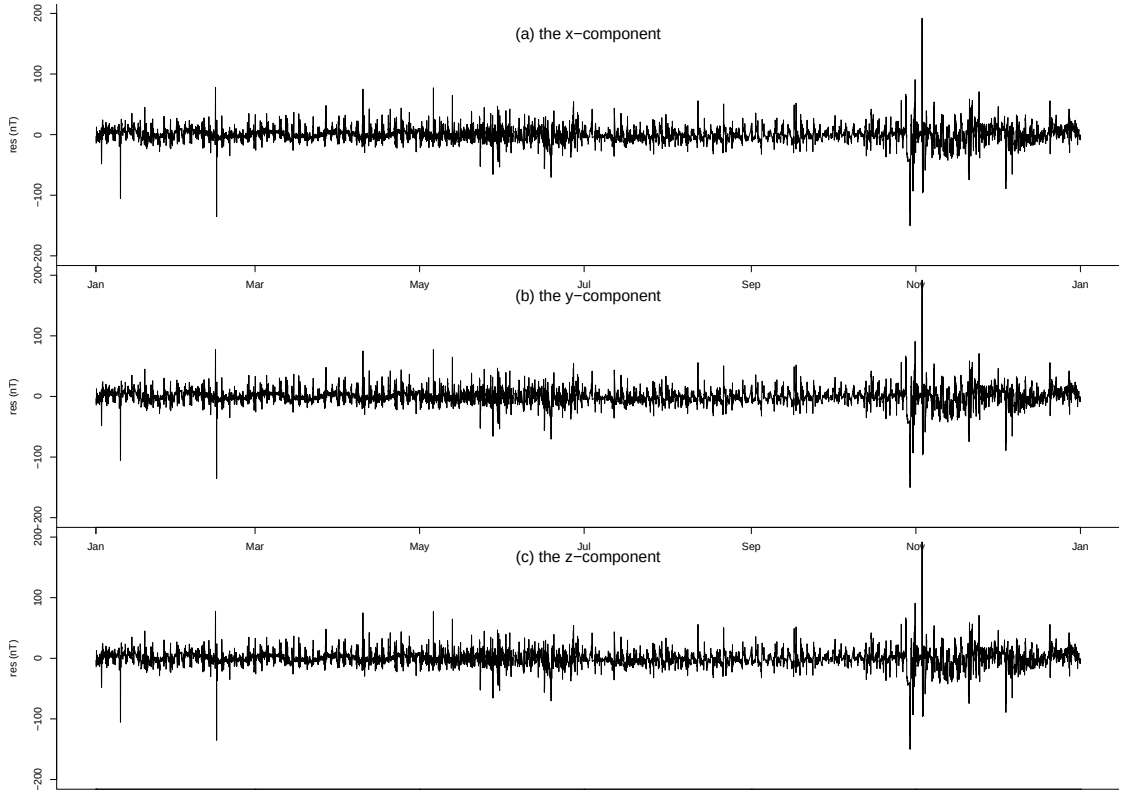

FIGURE 3.11: Residual plots of the regression model (C1, 2003)

components seem to have mean zero but non-constant variance and serial correlation

is difficult to assess in the residuals plots. We extend the regression analysis to other datasets and the model fitted to magnetic field data of different satellite in other years including 2004, 2005 and 2006 produce residuals of similar features.

In applying the OLS estimation, it has been assumed that the error term has mean zero, constant variance, and no serial correlation. The assumptions of no serial correlation and homoskedasticity look dubious for the satellite-based observations of the magnetic field and need to be dealt with carefully. Residuals from the OLS regression can be regarded as a univariate time series, since $\widehat{\boldsymbol{\epsilon}} = \{\hat{\epsilon}_t : t = 1, 2, \cdots, n\}$ is a sequence of observations of the same variable collected at regular interval over time. In the following subsection, time series analysis will be used for understanding the temporal dependence in the mean and in the variance of the regression residuals.

3.3.2 Time series analysis of the residuals

Analysis of time series that takes temporal dependence into account is referred to as time series analysis. Shumway and Stoffer (2010) provided a review of two approaches in time series analysis, namely frequency-domain and time-domain approaches. The main difference between the two approaches is that the former analyses a mathematical function or a signal with respect to the frequency while the latter is based on observing the autocorrelation of the time series. For investigating the behaviour of the time-indexed regression residuals, the time-domain approach would be appropriate. This subsection will provide the procedure to analyse and model the regression residuals from the magnetic field data using the time-domain approach, which involves the use of AutoRegressive Integrated Moving Average (ARIMA) models (Box et al., 2015), (generalized) autoregressive conditional heteroscedasticity (ARCH/GARCH) (Engle, 2001), or the combined ARIMA-GARCH models. ARIMA models that analyse time series linearly are often used together with ARCH/GARCH models, the method of which measures volatility of the time series and can be used to describe the error term of ARIMA models. Theses time series models will be briefly introduced in terms of their assumptions, parameter estimation methods, and selection criteria in this subsection.

3.3.2.1 Stationarity

A time series is often denoted as $\{x_t\}$ or $\{X_t\}$, since x_t the observations of sequence can be regraded as a set of random variables X_t. A common assumption in time series methods is that the data are stationary. A time series being stationary means that there is no systematic change in the mean or covariance properties of the series over time. Strictly speaking, the property of stationarity is not defined for a time series but for a model. If a time series data exhibits characteristics that resemble a stationary process, a stationary model would be appropriate to be fitted. A transformation of a non-stationary series into a stationary series is often required in the analysis of time series. This often involves removing trend and seasonal and cyclic patterns by differencing or regression modelling (Chatfield, 2016). Loosely speaking, a time series is said to be stationary if it shows no long-term, has constant mean and variance. Two definitions of stationarity, namely *strictly stationary* and *weakly stationary*, are given as follows:

Definition 3.1. A time series $\{X_t, t \in \mathbb{Z}\}$, where $\mathbb{Z}$ is the integer set, is said to be *strictly stationary* if the joint distribution of $X_{t_1}, \cdots, X_{t_k}$ is the same as the joint distribution of $X_{t_1+\tau}, \cdots, X_{t_k+\tau}$.

Definition 3.2. A time series $\{X_t, t \in \mathbb{Z}\}$ is called *second-order stationary*, or *weakly stationary* if it has finite variance, constant mean, and autocovariance function (acv.f) that depends only on the lag, i.e.

1. $\mathrm{E}(X_t^2) < \infty \quad \forall t \in \mathbb{Z}$,
2. $\mathrm{E}(X_t) = \mu \quad \forall t \in \mathbb{Z}$,
3. $\gamma(t, t+\tau) = \gamma(\tau), \quad \forall t, \tau \in \mathbb{Z}$.

The acv.f is given by $\gamma(t, t+\tau) = \mathrm{Cov}(X_t, X_{t+\tau}) = \mathrm{E}[(X_t - \mathrm{E}(X_t))\mathrm{E}(X_{t+\tau} - \mathrm{E}(X_{t+\tau})]$.

Strictly stationarity 3.1 means that the shifting the time series by a time lag τ has no effect on its joint distribution. The assumption of strictly stationary is very restrictive, and in practice a time series process is often assumed to be weakly stationary 3.2. This implies that the time series process has constant mean and variance over time and the acv.f and the *autocorrelation function* (ac.f) specified in Equation 3.6 do not depend on

the time t but only the lag τ.

$$\rho(\tau) = \frac{\text{Cov}(X_t, X_{t-\tau})}{\sqrt{\text{Var}(X_t)\text{Var}(X_{t-\tau})}} \tag{3.6}$$

Thus, under the stationary assumption, for a time series the acv.f. $\gamma(t, t+\tau)$ can be written as $\gamma(\tau)$. Standardizing the acv.f. by the variance of X_t, which is $\gamma(0)$ for a stationary process, produces the ac.f, which is defined as

$$\rho(\tau) = \gamma(\tau)/\gamma(0).$$

A fundamental stationary process is the so-called *white-noise process*, from which many other stationary processes can be derived. A white-noise process process consists of a sequence of uncorrelated random variables, each with a zero mean and the same finite variance, i.e. $\{X_t\}$ is a white-noise process if, given a constant σ^2,

$$\text{E}(X_t) = 0 \quad \forall t, \quad \text{Var}(X_t) = \sigma^2 \quad \forall t, \quad \gamma(\tau) = 0 \quad \forall \tau \neq 0.$$

A white noise process is a stationary process but not necessarily strict stationary, however a Gaussian white noise process is strictly stationary.

The regression residuals $\{\hat{\epsilon}_t\}$ of model 3.4 for magnetic field data of the three components are not stationary, as time plots in Figure 3.11 suggested the variances of $\{\hat{\epsilon}_t\}$ for all three directional components are clearly changing over time, and this invalidates the weakly stationary assumption.

One way of carrying the stationary assumption forward is to assume *locally stationary* or *piecewise stationary* for $\{\hat{\epsilon}_t\}$. Segmenting the regression residuals by satellite orbits generates piecewise residuals of each orbit. Figure 3.12 shows that the regression residuals of the three components within each satellite orbit appear to be stationary and there are missing values in some orbits. In this case, time series models will be considered for regression residuals within each satellite orbits so that the assumption of stationarity holds. A discussion of fitting stationary time series models with missing value will follow.

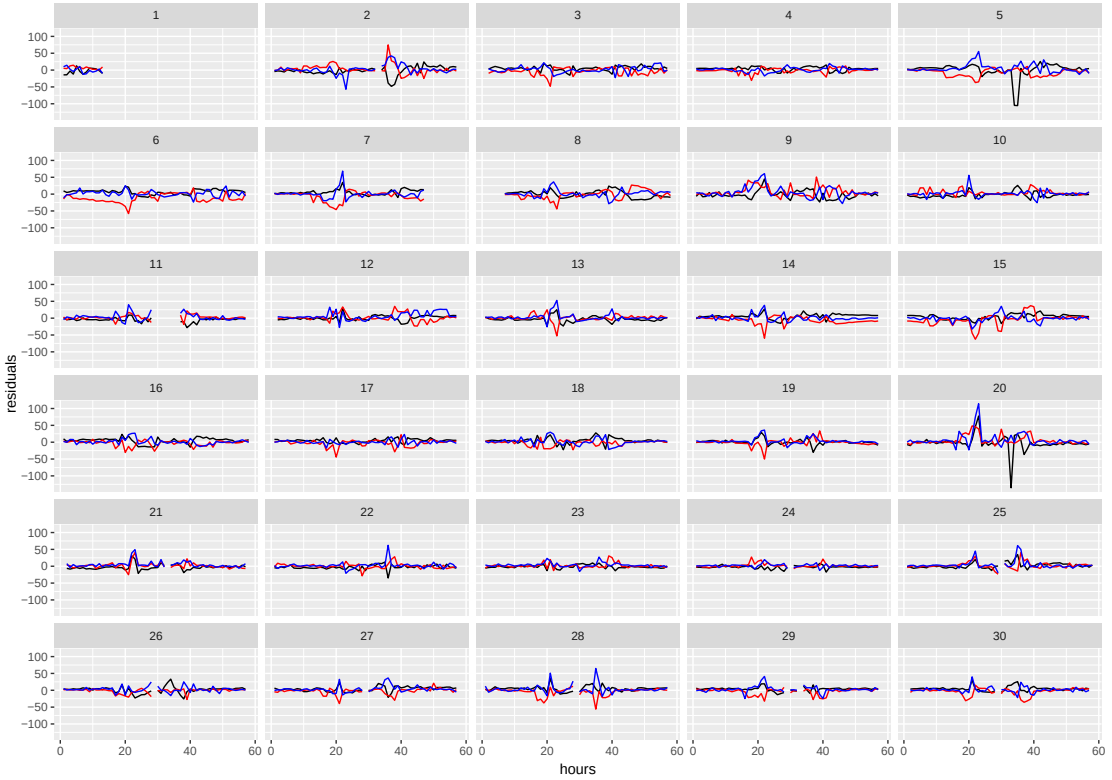

FIGURE 3.12: Plots of regression residuals against time within orbits across the first 30 orbits of C1 satellite in 2003. The black, red, and blue lines represents the residuals of the x-, y-, and z-components.

3.3.2.2 Autocorrelation

Spatio-temporal data are often correlated in time and space. It is important to take correlation into account when analysing spatio-temporal data as failing to do so would result in underestimation of standard errors of model parameters (Cressie and Wikle, 2015). It is also of interest to use the correlation structure for predictive purposes. As discussed earlier, the spatio-temporal magnetic field data can be viewed as time series data using the orbital function. Within an orbit, the spatial dependence has been reparametrized in terms of the temporal dependence. Spatial correlation will not be discussed in this thesis, for the following reasons:

- There is not sufficient data for us to to investigate the spatial structure, as there is one point of observation at one time rather that a snapshot of a large spatial domain from the satellite measurements;
- The intrinsic spatial structure, i.e. the time-based sampling at time-varying locations, as demonstrated in the earlier sections, has been converted to temporal

structure through relating the locations at which the observation to the time via an orbital function.

Hence our analysis focuses on capturing the temporal correlation in regression residuals within each orbital level using time series stationary process models.

Commonly used stationary process models include the AutoRegressive (AR), Moving Average (MA), and AutoRegressive Moving Average (ARMA) model. These models constitute a class of AutoRegressive Integrated Moving Average (ARIMA) models which were developed by Box et al. (1970) to handle autocorrelation. An ARIMA model has parameters of three components, autoregressive parameters p, number of differencing d, and moving average parameters q. For stationary time series, d is set to be zero when there is no constant or time-varying trend that needs to be dealt with by differencing the time series. Hence for a stationary time series $\{x_t\}$ which has no trend or seasonality, the following ARIMA models would be considered:

- In AR models, the current value of the series x_t is expressed as a linear combination of its p values. An autoregressive model of order p, AR(p), has the form:

$$x_t = \sum_{\tau=1}^{p} \phi_\tau x_{t-\tau} + \epsilon_t,$$

  where ϕ_τ, $\tau = 1, \cdots, p$ are auto-regression coefficients to be estimated and ϵ_t is a white noise random error;

- In MA models, the current value of the series x_t is expressed in terms of its current and past q errors. A moving average model of order q, MA(q), can be written as:

$$x_t = \sum_{\tau=1}^{q} \theta_\tau \epsilon_{t-\tau} + \epsilon_t,$$

  where θ_τ, $\tau = 1, \cdots, q$ are coefficients of the lagged errors to be estimated and ϵ_t is a white noise random error;

- An AutoRegressive Moving Average model is denoted by ARMA(p,q), where p is the order of the autoregressive part and q is the order of the moving average part,

and the model has the following form:

$$x_t = \sum_{\tau=1}^{p} \phi_\tau x_{t-\tau} + \sum_{\tau=1}^{q} \theta_\tau \epsilon_{t-\tau} + \epsilon_t.$$

The order of the ARMA model, p or q, can often be determined by the sample autocorrelation function (ac.f.) and the sample partial autocorrelation function (pac.f.), which are the ac.f. and pac.f. estimated from an observed time series.

The theoretical ac.f. was defined in Equation 3.6 and the theoretical pac.f is given as

$$\pi_(\tau) = \text{Cov}(X_t, X_{t-\tau} | X_{t-1}, \cdots, X_{t-\tau+1}). \tag{3.7}$$

The sample ac.f. is a sequence of auto-correlation coefficients computed at the different time lags and a coefficient at lag h can be calculated from the sample covariance function at lag h and 0 with the sample mean $\bar{y}$,

$$\hat{\rho}_\tau = \frac{\hat{\gamma}(\tau)}{\hat{\gamma}(0)} = \frac{\sum_{t=1}^{n-1}(x_t - \bar{x})(x_{t+\tau} - \bar{x})}{\sum_{t=1}^{n}(x_t - \bar{x})^2}.$$

The sample pac.f. is the sequence of autocorrelation coefficients calculated between different time lags with the observations in between the lags removed. The calculation of the sample pac.f. of lag τ is given in Equation 3.8,

$$\hat{\pi}_\tau = \frac{\hat{\rho}_\tau - \sum_{j=1}^{\tau-1} \pi_{\tau-1,j} . \hat{\rho}_{\tau-j}}{1 - \sum_{j=1}^{\tau-1} \pi_{\tau-1,j} . \hat{\rho}_{\tau-j}}, \quad \tau > 1. \tag{3.8}$$

If $\tau = 0$, then $\hat{\pi}_0 = 1$. If $\tau = 1$, then $\hat{\pi}_1 = \hat{\rho}_1$.

Shumway and Stoffer (2010) provides a detailed description of identifying and modelling the autocorrelation structure. For example, an AR(p) model can be identified if a time series has an exponentially decaying pattern in its ac.f. plot and spikes to lag p in its pac.f. plot. General rules of to identify ARIMA model can be summarized as follows:

- a MA(q) can be identified if the ac.f. plot cut off after lag q and the pac.f. plot exponentially decays;
- if the ac.f. plot exponentially decays and the pac.f. plot cut off after lag p, an AR(p) can be identified;

- if both ac.f. plot and pac.f. plot die down, a mixed ARIMA model would be considered.

Another way of checking and identifying the model is to use model selection criteria. This approach finds the number of parameters that minimises the model selection criteria. Common selection criteria include Akaike's Information Criterion (AIC) (see Akaike (1973)), Akaike's Information Criterion (corrected) (AICc) (see Hurvich et al. (1998)), and Bayesian Information Criterion (BIC) (see Schwarz et al. (1978)). These criteria represent a trade-off between the complexity of the model and its goodness of fit.

In addition, statistical tests can be used to check if a fitted ARMA model is appropriate. Ljung-Box test (Ljung and Box, 1978), for example, tests whether the autocorrelations of a time series are different from 0 by setting up a testing hypothesis. The test can be applied to the residuals of an ARMA model to check if the ARMA model selected using the general rules or selection criteria is adequate for describing the autocorrelation in a time series. The hypothesis will be rejected if the time series is independent and uncorrelated; otherwise , the ARMA model needs modification due to remaining correlation in the series of the ARMA model residuals.

Assuming stationarity for this regression residuals within each satellite orbit, we fit ARMA models to $\{\epsilon_t : t = 1, 2, \cdots n_o\}$, where t denotes the hour within the orbit o and n_o denotes the length of the orbit o. Figure 3.13 shows the sample ac.f. and the sample pac.f. plots of the residuals within a selected orbits and the residuals are obtained from OLS estimation. The panel (a), (c), and (e) show the ac.f. plots of the residuals in the x-, y- and z-components and the panels (b), (d), and (f) show the pac.f. plots of the residuals in the three components. For all three components, the ac.f. plots are decaying and the pac.f. plots have a spike at lag 1. This suggests that an AR(1) model can be fitted to each of the three series. Analysis of regression residuals within other orbits shows similar patterns for the ac.f. plot and the pac.f plot across the three components. Hence for the regression residuals $\{\epsilon_t : t = 1, 2, \cdots n_o\}$ of any orbit o in any component d, $d \in \{x, y, z\}$, we propose

$$\epsilon_t = \phi_o \epsilon_{t-1} + z_t, \tag{3.9}$$

where ϕ_o is the AR(1) parameter that varies across orbits and z_t denotes the AR(1) model residuals. z_t is assumed to be a white noise process, the observations within which has no correlation or dependence. The models are fitted by calling the function

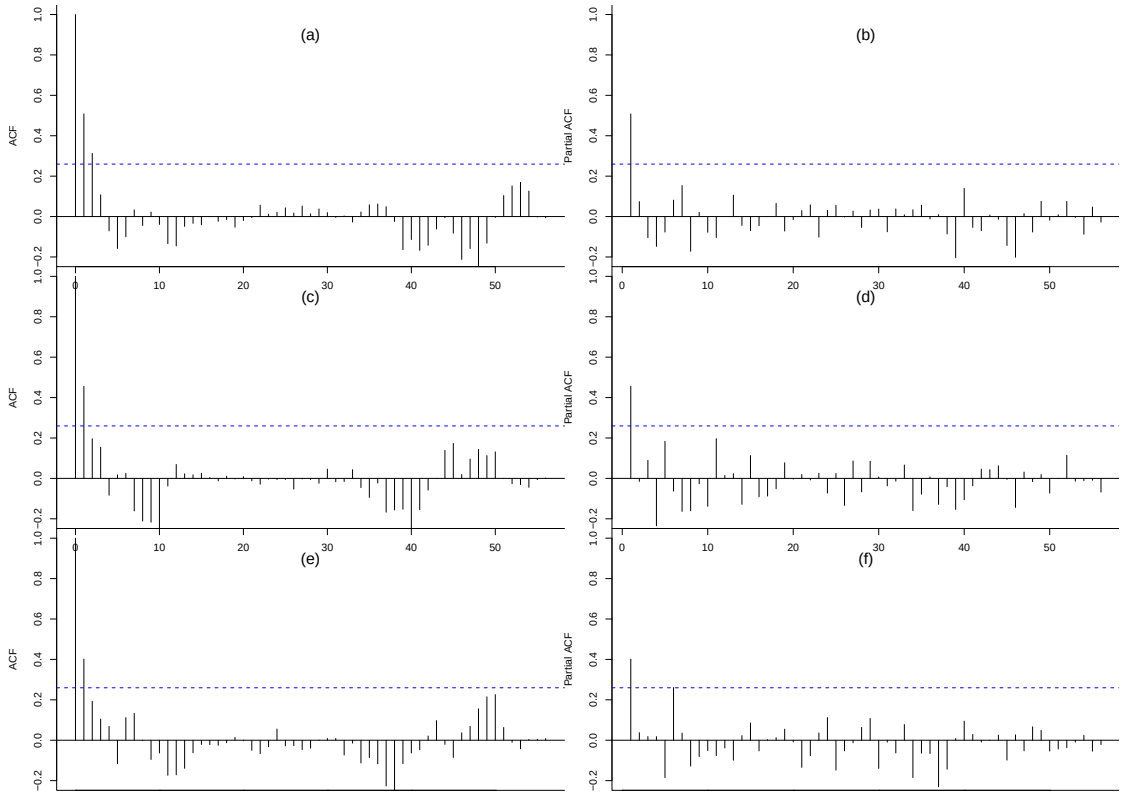

FIGURE 3.13: Ac.f. and pac.f. plots of the regression residuals

$ar()$ in R. Fitting an AR model to the data by selecting the complexity by AIC also identifies the order 1. The AIC developed by Akaike (1973) is a measure of the relative quality of statistical models for a given set of data. The AIC has a definition that given a statistical model M of data x, let k be the number of estimated parameters in the model, $\hat{L}$ be the maximum value of the likelihood function for the model, i.e. $\hat{L} = P(x|\hat{\theta}, M)$, where $\hat{\theta}$ are the parameter values that maximize the likelihood function, then the AIC value of the model is $AIC = 2k - 2ln(\hat{L})$. The model with the minimum AIC value would be preferred. AR(1) models have been identified for regression residuals within each orbit by the Jenkins-Box rules and the AIC criteria. Therefore we discuss methods of parameter estimation for $AR(p)$ assuming the order p is known to be 1.

In general, estimation of AR models can be done with simple regressions using OLS estimator. However, estimating an AR(p) model by OLS does not use information contained in the first p observation and thus causes a loss of efficiency. The method of Yule-Walker estimation calculates the approximate confidence intervals for the model parameters, but the Yule-Walker estimator has poor asymptotic efficiency and unnecessarily high variance. Maximum Likelihood Estimator (MLE), which often assumes Gaussian white noise for the AR model residuals, is the optimal since the maximum

likelihood estimates have the smallest asymptotic variance. The approach of using an approximate (typically Gaussian) likelihood function for estimation is called quasi-MLE (QMLE). The likelihood function is calculated from a transformed set of data instead of all data.

MLE evaluates the sample joint distribution, also called the likelihood function, and search for the parameters that maximize the likelihood function. The likelihood function can be regarded as the product of marginal density of individual sample in the case of identical and independent sample. In time series analysis where dependence structure of observations is specified, conditional density must be used in replacement of marginal density for evaluating the sample likelihood. Let $\{\epsilon_t, t = 1, 2, \cdots, N\}$ denote the N observations of the variables $\{E_t, t = 1, 2, \cdots, N\}$ that follows an AR(1) process,

$$E_t = \phi E_t + z_t, \tag{3.10}$$

with $z_t \sim \mathcal{N}(0, \sigma^2)$ and $|\phi| < 1$ (the condition for the process to be stationary). The parameters to be estimated are denoted by a vector $\boldsymbol{\theta}$, $\boldsymbol{\theta} = (\phi, \sigma^2)^T$. Since $\{z_t\}$ is a Gaussian white noise, E_1 must be Gaussian,

$$E_1 \sim \mathcal{N}(0, \frac{\sigma^2}{1-\phi^2}). \tag{3.11}$$

For $t > 1$,

$$E_t | E_{t-1} = \epsilon_{t-1} \sim \mathcal{N}(\phi\epsilon_{t-1}, \sigma^2), \tag{3.12}$$

The likelihood of the complete sample can thus be calculated as

$$f_{E_N, E_{N-1}, E_{N-2}, \cdots, E_1}(\epsilon_N, \epsilon_{N-1}, \epsilon_{N-2}, \cdots, \epsilon_1; \boldsymbol{\theta}) = f_{E_1}(\epsilon_1; \boldsymbol{\theta}). \prod_{t=2}^{N} f_{E_t|E_{t-1}}(\epsilon_t|\epsilon_{t-1}; \boldsymbol{\theta}).$$

The conditional densities $f_{E_1}(\epsilon_1; \boldsymbol{\theta})$ and $f_{E_t|E_{t-1}}(\epsilon_t|\epsilon_{t-1}; \boldsymbol{\theta})$ for $t >$ are specified by their distributions in Equation 3.11 and 3.12.

The log likelihood function, denoted as $\mathcal{L}(\boldsymbol{\theta})$, is therefore

$$\mathcal{L}(\boldsymbol{\theta}) = \log f_{E_1}(\epsilon_1; \boldsymbol{\theta} + \sum_{t=2}^{N} \log f_{E_t|E_{t-1}}(\epsilon_t|\epsilon_{t-1}; \boldsymbol{\theta}),$$

and can be used for the computation of the MLE estimates for $\boldsymbol{\theta}$. (The numerical computation is omitted here).

Using the MLE method, we fit AR(1) models to the regression residuals of individual orbits, $\{\hat{\epsilon_t}; t = 1, 2, \cdot, n_o\}$. $\hat{\epsilon_t}$ was obtained using OLS estimation from the regression model 3.4 and for missing observations of the response, the residuals are recorded as NA. Hence the time series datasets $\{\hat{\epsilon_t}; t = 1, 2, \cdot, n_o\}$. $\hat{\epsilon_t}$ contain missing values whenever the satellite measurements are missing. In *R*, the function *na.action*() deals with missing values. Setting *na.action*() to *na.pass*, we skip the missing values when estimating the AR(1) model parameters in our exploratory analysis. The missing values will be reconsidered in the Chapter 4.

Table 3.2 lists the AR(1) model parameters estimated with MLE for regression residuals of a single orbit across the three component. The coefficients ϕ estimated from this particular orbit have similar values (around 0.5) for the x-, y-, and z-components. The variances σ^2 have its lowest value of 44.34 in the x-component and its highest value of 93.34 in the y-component. Both parameters, the coefficients and the variances, change over satellite orbits since the AR(1) models are fitted to different orbital datasets. The AR(1) parameter estimation results from other orbits will be included in the summary of this section.

TABLE 3.2: MLE estimates of the AR(1) coefficients

	the x- component	the y- component	the z-component
$\hat{\phi}$	0.5638	0.5220	0.4058
$\hat{\sigma}^2$	44.34	93.34	85.42

Diagnostic procedure of the fitted AR(1) models includes observing residual plot and the AR(1) model residual ac.f. and pac.f. diagrams or checking Ljung-Box result.

Figure 3.14 shows the ac.f. and pac.f.plots of the AR(1) model residuals of a single orbit in the three components. Panel (a) and (b) are for the ac.f. and pac.f.plots of the x-component; Panel (c) and (d) are for the y-component; Panel (e) and (f) are for the z-component. These plots show no significant lags (the 0 lag ac.f. is always 1 as it calculates the autocorrelation between an observation and itself.), indicating the selected models are appropriate for capturing the autocorrelation in the regression errors, i.e. AR(1) models are adequate models to represent the regression residuals.

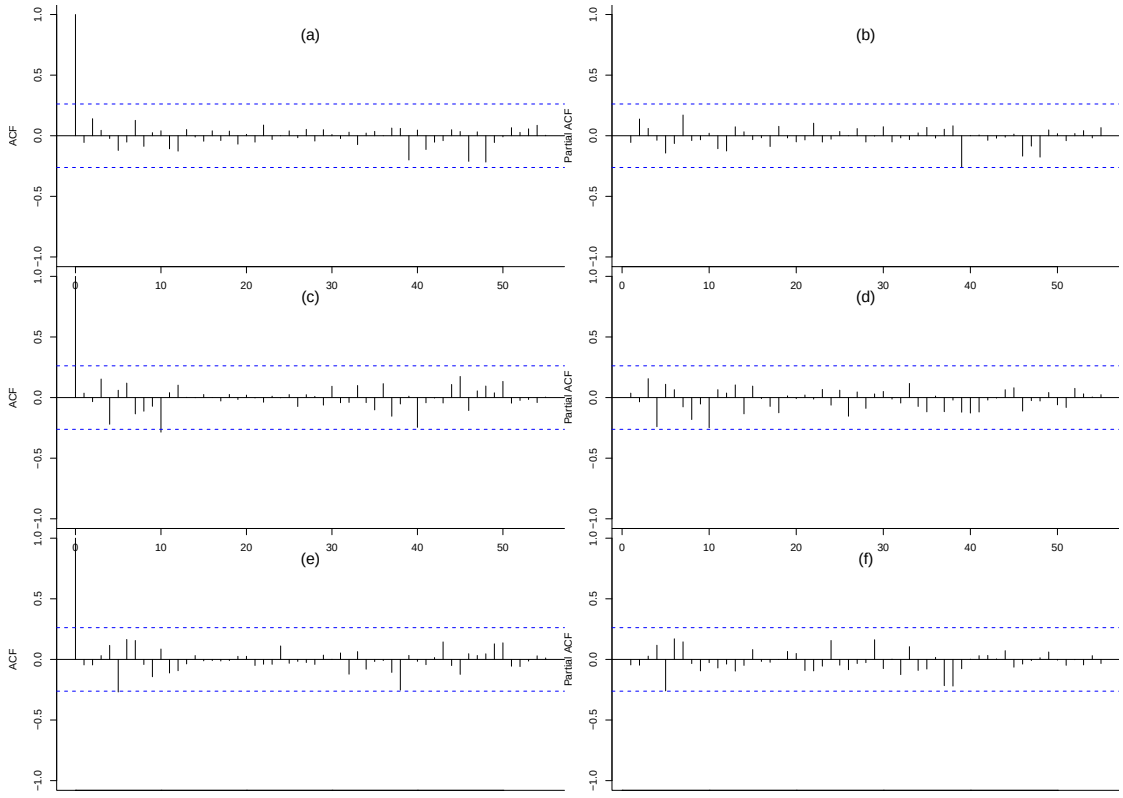

FIGURE 3.14: Ac.f. and pac.f. plots of the AR(1) model residuals

Although the ac.f. and pac.f.plots of the AR(1) model residuals have no significant lags, the time series plot of residuals and squared residuals, shown in Figure 3.15, display some cluster of volatility. Panels (a), (c), (e) on the left-hand side give the AR(1) residual plot in the x-, y- and z-components; Panels (b), (d), (f) on the right-hand side give the squared residual plots. This violates the AR(1) model assumptions that $\{z_t\}$ has constant variances, and needs to be dealt with in the subsequent section.

3.3.2.3 Heteroscedasticity

Heteroscedasticity, as opposed to homoscedasticity, refers to changes in variance in a model. White test proposed by White (1980) is the best test for heteroskedasticity. Model for changing variance would provide better estimates of the local variance, and such estimates can be used to produce more reliable prediction intervals. Such models are often considered for residuals, referred to as the error terms, of regression or ARMA models. Engle (1982) introduced ARCH models, assuming the variance of the current error term is related to the size of the past error terms. Such dependence in the error terms gives rise to volatility clustering, the behaviours of which are commonly observed

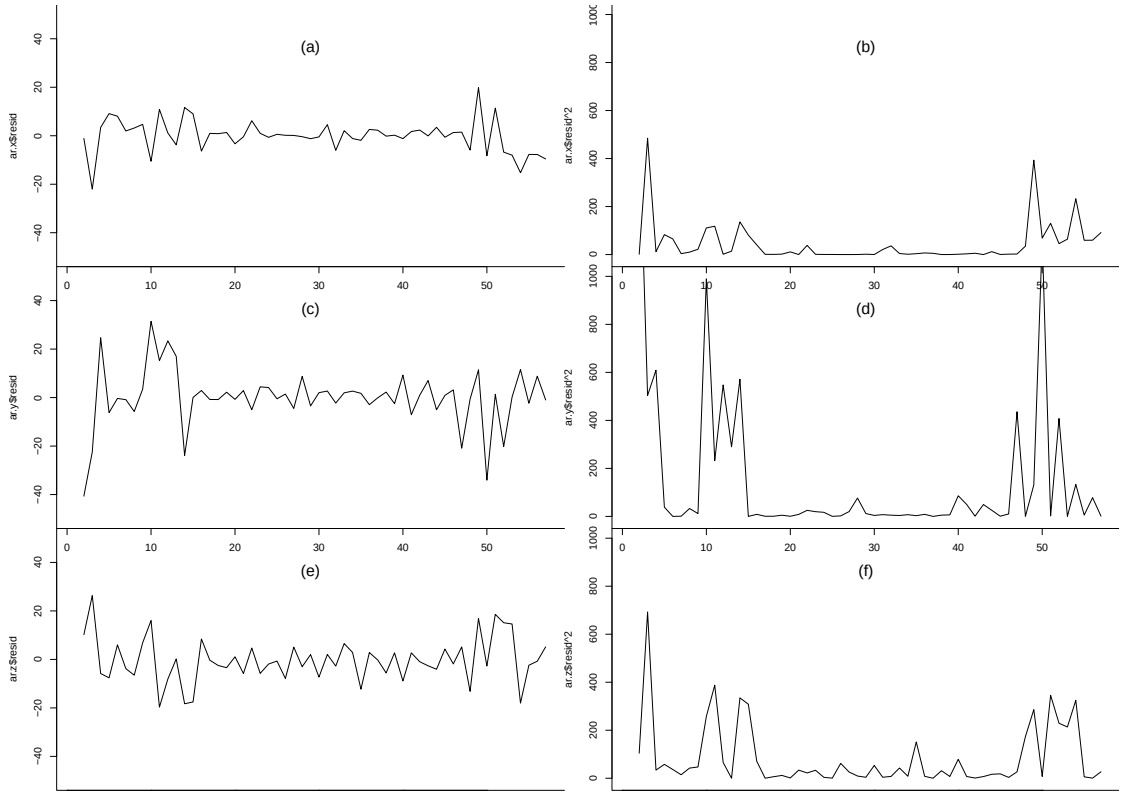

FIGURE 3.15: Time series plots of AR(1) residuals and squared residuals of the three components

in financial time series, e.g. return series of market-priced assets. Bollerslev (1986) generalized the ARCH model into GARCH models that account for the volatility clustering. Changing variance is evident in the time plot of the AR model residuals, as shown in Figure 3.15, and ARCH or GARCH methods, which concerns with the conditional variance of the time series, will be used to model the volatility clustering of the AR model residuals.

Let $\{z_t\}$ denote the error terms. In our case the error terms are the AR(1) model residuals. In an ARCH process, z_t can be split into two components, a stochastic piece η_t and a time-dependent standard deviation σ_t, so that

$$z_t = \sigma_t \eta_t, \tag{3.13}$$

$\{\eta_t\}$ follow a standard normal distribution and are independently and identically distributed while $\{\sigma_t\}$ are described as

$${\sigma_t}^2 = \omega + \sum_{i=1}^{q} \lambda_i z_{t-i}^2, \tag{3.14}$$

where $\omega > 0$ and $\lambda_i \geq 0$.

In a GARCH(p, q), σ_t has a different description,

$$\sigma_t^2 = \omega + \sum_{i=1}^{q} \lambda_i z_{t-i}^2 + \sum_{i=1}^{p} \delta_i \sigma_{t-i}^2. \tag{3.15}$$

The steps for fitting an ARCH/GARCH model are similar to those for fitting an ARIMA model. We start with checking the clusters of volatility in the AR residual plot and then the squared residual plot. Then ac.f. and pac.f. plots of squared residual will suggest if the squared residuals from the AR model are independent. If the ac.f. and pac.f. plots of squared residuals display significant lags, then the residuals should not be independent. The lag length p of a GARCH(p, q) process can be obtained through estimating the ac.f. and pac.f. of $\{z_t^2\}$.

Figure 3.16 plots the ac.f and pac.f of the squared AR(1) model residuals. Since there is no significant spike in the plot, we drop the p component in GARCH(p, q) and consider an ARCH(q) model. The Lagrange multiplier test proposed by Engle (1984) determines the lag length q of ARCH(q) models. Likewise, selection criteria can be used to determine the order of an ARCH model.

For the AR(1) model residuals, we identify $q = 1$ and assume an ARCH(1) process for $\{z_t\}$ in Equation 3.9,

$$z_t = \sigma_t \eta_t, \qquad \eta_t \overset{i.i.d.}{\sim} \mathcal{N}(0, 1) \tag{3.16}$$

$$\sigma_t{}^2 = \omega + \lambda z_{t-1}^2, \qquad \omega > 0, \quad \lambda_i \geq 0. \tag{3.17}$$

The ARCH(1) model parameters ω and λ can be estimated using OLS or MLE. Given an estimate of the parameters for the ARCH(1) model, we use Ljung-Box test to check the model adequately explains the variance process.

3.3.3 Summary and results

Regression analysis has been performed on magnetic field data of the four Cluster satellites of the three components in the GSM frame over 11 years (2003-2013). For a single satellite measurements of one component in a year, there exists such a relationship that

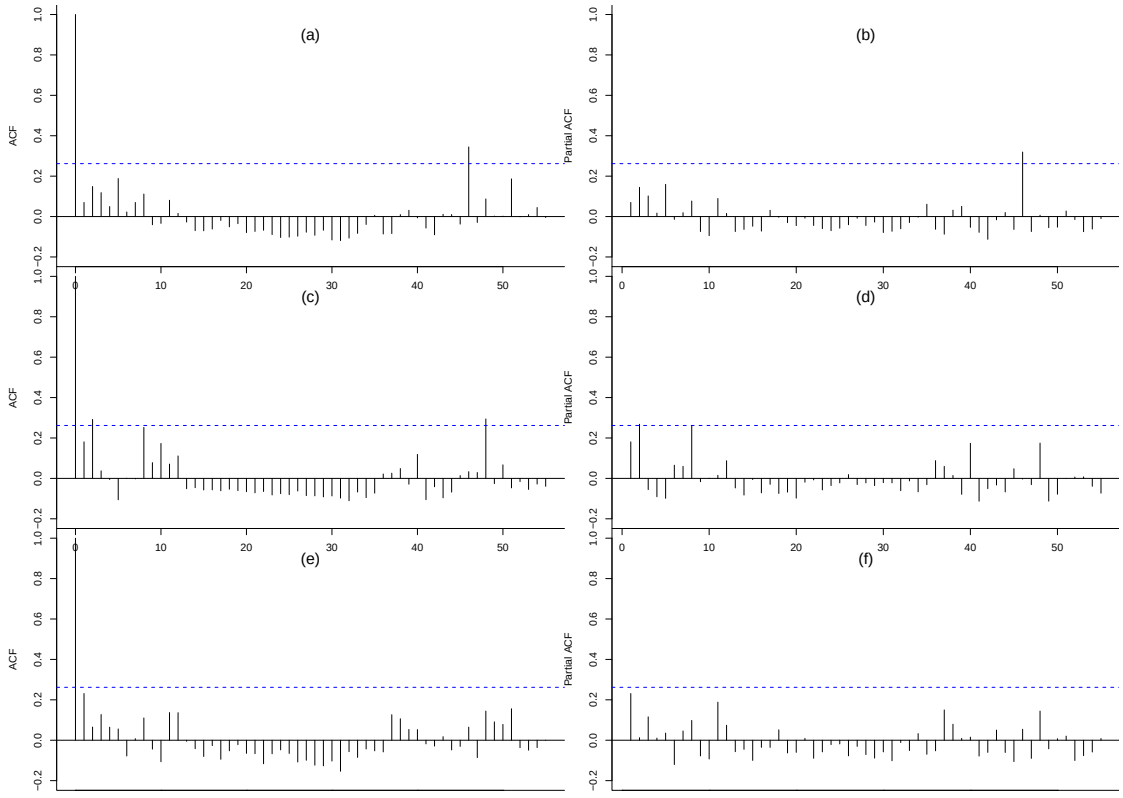

FIGURE 3.16: Ac.f. and pac.f. plots of the squared AR(1) model residuals

the satellite measurements are linearly dependent on the IGRF and the T96 model outputs, i.e.,

$$S_t = \mu + \alpha I_t + \beta I_t + \epsilon_t, \quad t = 1, 2, \cdots, n. \tag{3.18}$$

In Equation 3.18, μ, α, and β are the regression coefficients fixed over time, $\{\epsilon_t, t = 1, 2, \cdots, n\}$ are the error terms, and n denotes the total number of observations in the year.

OLS estimation provides estimates of the regression parameters, $\hat{\mu}$, $\hat{\alpha}$, and $\hat{\beta}$, and a series of regression residuals $\{\hat{\epsilon}_t, t = 1, 2, \cdots, n\}$. Time plot of $\{\hat{\epsilon}_t\}$ suggests that the regression errors are not stationary. Splitting the series $\{\hat{\epsilon}_t, t = 1, 2, \cdots, n\}$ by the satellite orbit o lead to piecewise stationary time series, $\{\hat{\epsilon}_t, t \in \mathcal{O}_{o(t)}\}$, where $\mathcal{O}_{o(t)}$ denotes the set of times within the satellite orbit o.

Time analysis of $\{\hat{\epsilon}_t, t \in \mathcal{O}_{o(t)}\}$ for individual orbit o suggested the errors are correlated in time and have changing variance. An AR(1) model has been identified for capturing autocorrelation in the regression errors and an ARCH(1) model has been incorporated to the AR(1) model for accounting changing volatility in the AR(1) model errors. The method of MLE was used to obtain parameters in the the AR and the ARCH models.

The combine AR(1)-ARCH(1) can be written as, for the regression error term ϵ_t of any satellite orbit o at times $t \in \mathcal{O}_{o(t)}$,

$$\epsilon_t = \phi\epsilon_{t-1} + z_t, \quad |\phi| < 1 \tag{3.19}$$

$$z_t = \sigma_t\eta_t, \qquad \eta_t \overset{i.i.d.}{\sim} \mathcal{N}(0,1) \tag{3.20}$$

$$\sigma_t^2 = \omega + \lambda z_{t-1}^2 \qquad \omega > 0, \quad \lambda_i \geq 0. \tag{3.21}$$

The AR(1)-ARCH(1) model parameters are estimated in two steps using MLE. We fitted an AR(1) model to the piecewise regression residuals $\{\hat{\epsilon}_t, t \in \mathcal{O}_{o(t)}\}$, assuming equal variance for the AR(1) errors, and obtained the AR(1) model residuals $\{\hat{z}_t, t \in \mathcal{O}_{o(t)}\}$ for which we then fitted an ARCH(1) model. Missing values were ignored in estimating parameter in the AR and the ARCH models. The parameters $\{\phi, \omega, \lambda\}$ can be subscripted by the orbit o, since they are estimated from regression residuals of different satellite orbits and are allowed to vary across the orbits.

Initial results from the regression analysis give OLS estimates of regression model parameters across satellites and directional components by year. Figure 3.17 plots the estimates obtained from the four satellites and the three components against the time by year. Panel (a) plots $\hat{\mu}$ the estimated intercepts, Panel (b) plots $\hat{\alpha}$ the estimated coefficients of the IGRF model, and Panel (c) plots $\hat{\beta}$ the estimated coefficients of the T96 model. The three colours, black, red and blue, represent x-, y- , and z- components and the four lines of the same colour in each plot represent the estimates from the four satellites. Panel (a) and (c) show a difference in the estimated parameters $\hat{\mu}$ and $\hat{\beta}$ across the three components while Panel (b) shows $\hat{\alpha}$ estimated from the three components and the four satellites are almost identical since the 12 lines overlay with each other. The x-component of C1 in 2003, for example, have $\hat{\alpha}$ and $\hat{\beta}$ close to 1 and $\hat{miu}$ close to 0. This implies that in 2003 the IGRF and the T96 model well represent the x-component of C1.

The OLS estimates are believed to be unbiased since the residuals of each regression model appear to have the expectation of zero. However, the variance-covariance structure of the residuals within each model changes over time. The variance-covariance structure of the regression residuals are parametrized by the AR(1)-ARCH(1) models fitted to every single orbit period whereas the regression parameters are estimated from magnetic field data of every single year. Hence condolence intervals can not be computed

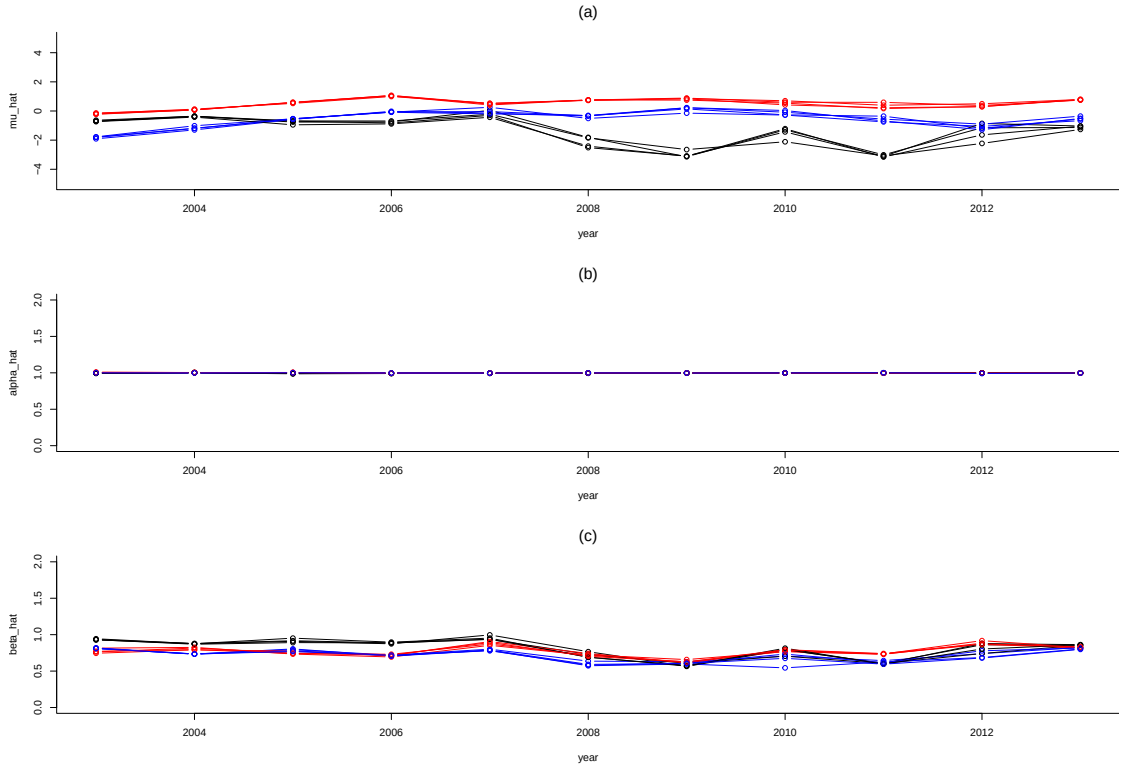

FIGURE 3.17: Time plots of the OLS estimates over 11 years of three components and four satellites. Panel (a), (b), and (c) show the plots of $\hat{\mu}$, $\hat{\alpha}$, and $\hat{\beta}$

for the yearly estimated regression parameters at this stage for assessing the relationship between the satellite measurements and the two computer model outputs.

3.4 Comments and discussion

It has been demonstrated in this chapter that in-situ observations of the near-Earth magnetic field provided by the Cluster satellite measurements poses various challenges to statistical analysis and modelling.

To begin with, the magnetic field data has an unusual dependence in space and time, as the data were collected at regular time intervals but at time-varying locations. The space-time dependence is govern by the Cluster satellites orbiting around the Earth, the motion of which depicts the satellite trajectories, and the trajectories are subject to non-quantifiable changes, such as changes resulted from satellite manoeuvre and gravity. The locations and the times at which the magnetic field are being sampled are contained in the satellite trajectory data. Through mapping the locations to the times via an orbital

function, we simplified the problem by converting the spatio-temporal data into time series data while keeping the spatial information accessible.

Secondly, the magnetic field data has three dimensions since the data were recorded as vectors in the GSM coordinate frame. Temporal variations, as illustrated in time plots of the magnetic field data, are engendered by a change of sampling locations and space weather conditions, and patterns of the variations appeared to be different in the magnetic field strengths measured in different components. Hence the behaviour of the three magnetic field components will be considered individually.

Thirdly, time plots of the in-situ Cluster measurements along the satellite orbits exhibit seasonal and cyclic variations. This because the time-varying magnetic field is being sampled at time-varying location. Temporal variations in the observed magnetic field can be attribute to changes in the sampling locations and the space weather conditions. Decomposing the magnetic field by its source of origin produces an internal field which is invariant to the space weather conditions and an external field that responses to the Sun-Earth interaction. Estimates of the internal and the external fields are obtained from the computer models, the IGRF and the T96 models. The time and the sampling location of each Cluster measurements are input into the computer models. We regress the satellite data on the two model outputs, assuming the relationship between the satellite data and the model outputs is constant in time. A simple regression model was fitted to the magnetic field strengths in each components and of each satellite. Estimates of the regression parameters differs in components but do not seem to change much across satellite. Statistical properties of in the magnetic field data, such as non-stationarity, autocorrelation, and heteroskedasticity, have been derived from the time-series of the regression residuals. This suggest the errors are correlated and have clustering volatility when modelling the satellite measurements in terms of the two model outputs. To hand the time series dependence, we assume locally stationarity for orbital errors, i.e. regression residuals within each orbits and apply the ARIMA and ARCH methods using MLE estimation. MLE can be used to deal with missing data, problem of which will be address in the next chapter. A two stage fitting procedure has been used for describing the autocorrelation and the heteroskedasticity. An AR process is fitted to the regression residuals and then an ARCH process is fitted to the AR residuals. Again this was preformed on residuals of every single orbit.

The work in this chapter was a preliminary assessment of the calibration of the magnetic field models with the satellite data by looking at the yearly estimated regression parameters. The fact that regression residuals are piecewise stationary and the pieces were segmented by the satellite orbits suggest that the properties of the magnetic field data changes over orbits. We also recognize that the spatial information and the space weather condition changes across the satellite orbits as well. It can be deduced from the exploratory analysis that the relationship between the satellite measurement and the two model outputs might not stay constant across the orbit. We will include time-varying effects in our models in terms of satellite orbit to include space and characterized the near-Earth magnetic field through calibrating the physical models using Cluster satellite observations Orbit-varying coefficients models will be developed in the next chapter to account for the magnetic field variations in satellite orbits and the models will be fitted to the data of different satellites and directional components. Confidence intervals for orbital parameters can be constructed through parametrizing the variance-covariance structure of each orbit in an AR-ARCH model. Estimates of orbital parameters in the time-series-based model quantifies the relationship between the satellite measurements and the two model outputs and can be used to calibrate the computer models with the satellite measurements made in different regions of space and under variable space weather conditions.

Chapter 4

Time-series-based modelling of the magnetic field

Previous analysis in Chapter 3 has showed a regression model with time series errors can be used to link the measurements of individual Cluster satellites to the IGRF and T96 model outputs for hourly sampled magnetic field vectors of their x-, y- and z-components. Parameters in the regression model and its time series components are set to vary across satellite orbits given that the spatial information from the orbits is gradually changing throughout every year in the chosen GSM coordinate frame and temporal information such as space weather condition is also changing over the orbits. Hence for each orbit of an individual satellite the statistical model has orbit-indexed parameters. Letting the model parameters vary over the orbits allows us to relate the orbit-indexed regression parameters to the orbital information, i.e. the spatial and the temporal information associated with the orbits, and the orbital information can be used to understand variations in the regression parameters. The regression model is fitted individually to the x-, y- and z-components of the magnetic field vectors of the four Cluster satellites and their corresponding computer model outputs, and as a result, the different satellites and the field strength components might have effects on the time-series based regression model.

This chapter develops a statistical model that quantifies the biases and uncertainties in the magnetic field data of four satellites in three components. The time-series-based regression modelling is motivated by our attempts to calibrate the two computer models,

namely the IGRF and the T96 model, and to explain the variations in the magnetic field strength, the knowledge of which can be used for change point detection of magnetic storms in Chapter 5. Statistical models in this chapter include time-series based regression models and mixed-effects models. The aim in this chapter is to calibrate the computer models of the near-Earth magnetic field through estimating and making inference of parameters in the statistical model, and to explore factors that affect the calibration results using the mixed-effects model. The chapter is organized as follows. Section 4.1 provides an overview of the time-series based regression and the mixed-effects modelling. Section 4.2 describes the statistical methods used in the time-series-based regression modelling of the magnetic field data and the mixed-effects modelling of the estimates of the orbital regression model parameters. Section 4.3.1 applies the methods to the modelling of the magnetic field data and Section 4.4 concludes this chapter with a discussion of the modelling results.

4.1 Introduction

The regression model with time series errors that describes the relationship between the observed and simulated magnetic field data is given in Equation 4.1. For any Cluster satellite C, $C \in \{C_1, C_2, C_3, C_4\}$, and a given component d, $d \in \{x, y, z\}$,

$$S_t = \mu_{o(t)} + \alpha_{o(t)} I_t + \beta_{o(t)} T_t + \epsilon_t, \tag{4.1}$$

where S_t, I_t, and T_t denote, respectively, the satellite measurement, IGRF output and T96 output of the magnetic field strength in the component d at time t and position of Satellite C at time t. $o(.)$ is an orbital function and $o(t)$ maps the time t to an orbital number o. $\mu_{o(t)}$, $\alpha_{o(t)}$, and $\beta_{o(t)}$ are the regression model parameters at orbit o determined by time t, and can be writen as μ_o, α_o, and β_o since the parameters are fixed for time within a single orbit, $\{t : t \in \mathcal{O}_{o(t)}\}$, where $\mathcal{O}_{o(t)}$ denotes the set of times within the orbit o. Equation 4.1 differs from Equation 3.18 in that that orbital function has been included in the regression model.

It was found in the exploratory data analysis that the errors of the regression model ϵ_t are correlated in time. For errors within each orbit $\{\epsilon_t : t \in \mathcal{O}_{o(t)}\}$, an AR(1) model was reasonable to capture dependence in the mean of the errors, and an ARCH (1)

model was reasonable to capture the dependence in the variance in the errors. Thus an AR(1)-ARCH(1) model, i.e. the two time series models in combination, can be fitted to the errors estimated from the regression model over the orbits. The AR(1)-ARCH(1) process for errors within an orbit o can be written as,

$$\begin{aligned} \epsilon_t &= \phi_o \epsilon_{t-1} + z_t, && -1 < \phi < 1 \\ z_t &= \sigma_t \eta_t, && \{\eta_t\} \overset{iid}{\sim} \mathcal{N}(0,1) \\ \sigma_t^2 &= \omega_o + \lambda_o z_{t-1}^2, && \omega_o > 0, \quad \lambda_o \geq 0 \end{aligned}$$

where ϕ_o, ω_o, and λ_o are the time series model parameters which also vary across the satellite orbits. The time series model for the orbital errors account for two components: possible error in the Cluster satellite measurements, and possible uncertainty due to a lack of fit (or mis-calibration) between the computer model outputs and the observed Cluster satellite measurements.

The parameters in the regression model are allowed to vary across satellite orbits, given spatial properties of the orbit that are gradually changing throughout a year in the chosen GSM reference frame. Within each satellite orbit, the models have a time-series-based structure for describing the autocorrelated disturbances and the non-constant variances for the error. Autocorrelation and heteroskedasticity detected in the estimated errors from the OLS fit can be characterized by AR model and ARCH model component. The AR model specifies that the variable depends linearly on its own previous values and on a stochastic term; ARCH is the condition that one or more data points in a series for which the variance of the current error term or innovation is a function of the actual sizes of the previous time periods error terms.

Estimation of AR-ARCH models for the error terms encounters the problem of missing values. The missingness of the error terms comes from the Cluster satellite measurements which were assumed to be missing at random. The missing at random (MAR) assumption made in Chapter 3 states that the observations are missing at random if the probability of missingness does not depend on the unobserved values, i.e.

$$\mathbb{P}(R = r | Y = \mathbf{y}) = \mathbb{P}(R = r | Y = \mathbf{y}_{obs})$$

or equivalently in terms of the likelihood function f,

$$f_{R|Y}(r|\mathbf{y},\theta) = f_{R|Y_{obs}}(r|\mathbf{y}_{obs},\theta),$$

where Y denotes a variable that has a sequence of independent and identically distributed (iid) observations $\mathbf{y} = \{y_1, \cdots, y_n\}$ and follows a known distribution $P_\theta$with parameter θ. The likelihood function of $\mathbf{y}$ can be written as

$$f_Y(\mathbf{y}|\theta) = \prod_{i=1}^{n} f_Y(y_i|\theta),$$

where $f_Y(.|\theta)$ is the density of P_θ. If the observations have missing values, the variable can be written as $Y = (\mathbf{y}_{obs}, \mathbf{y}_{mis})$, where $\mathbf{y}_{obs}$ are the observed values and $\mathbf{y}_{mis}$ are the missing values. Let r_i be an indicator variable R that has values

$$r_i = \begin{cases} 1 & \text{if} \quad y_i \quad \text{is observed} \\ 0 & \text{if} \quad y_i \quad \text{is missing} \end{cases},$$

This is saying that R and Y_{mis} are conditionally independent given Y_{obs}. In the presence of missing values, MAR has been assumed for estimating the time series model parameters with MLE or QMLE, which searches for the parameter values that maximize the likelihood of obtaining the data given the parameters. MLE is the most commonly used estimation procedure for AR and ARCH models when data are missing. Berkes and Horváth (2004), Francq et al. (2004), Straumann et al. (2006) studied the asymptotic properties of QMLE for ARCH models. Other approaches for dealing with missing data in time series modelling include least square methods and Expectation-Maximization algorithm and Bootstrap approach (EMB). Bondon and Bahamonde (2012) addressed the problem of estimating an ARCH model in the presence of missing values by proposing a two-stage least square estimation which generalizes the estimator proposed by Bose and Mukherjee (2003) for estimating the ARCH parameters by solving linear equations. The EMB algorithm combines the classic EM algorithm with a bootstrap approach to take draws from the posterior. For each draw, Honaker and King (2010) bootstrap the data to simulate estimation uncertainty and then run the EM algorithm to find the mode of the posterior for the bootstrapped data, which gives the fundamental uncertainty.

The time series parameters characterize the temporal structures in the errors of each

orbit and need to be estimated for constructing the variance-covariance matrix of the regression errors and are important for making inference on the regression parameters, namely the intercept μ_o, the IGRF model coefficient α_o, and the T96 model coefficient β_o. Estimates of the regression parameters quantify the relationship between the satellite measurements and two models outputs over orbits and the two model coefficients inform on how close the IGRF and T96 model outputs match with the Cluster satellite measurements. Section 4.2 describes the theory and method used for estimating the regression parameters over the orbits while accounting for the time series errors.

The estimates of $\{\mu_o, \alpha_o, \beta_o : o \in n_o\}$, where n_o denotes the total number of the orbits in the magnetic field data, form new time series indexed by the orbit o. By examining the estimated time series parameters from the regression model again over the orbit, we can assess whether there are effects in the regression errors that are due to other factors. On this note, the mixed-effects model is used to explore how the various parameters in the regression model are associated with other factors as either fixed or random effects. By definition, *fixed effects* refers to parameters associated with an entire population; *random effects* are associated with individual units drawn at random from a population (Pinero and Bates, 2000). In our analysis of the magnetic field data, the factors that we consider as fixed effects in the mixed model include the storm levels, i.e. space weather conditions, and the orbital features, and for random effects we consider the four Cluster satellites and their measurements in the three components in the GSM frame. The inclusion of fixed and random effects, estimation and selection of the mixed-effects model will be elaborated again in Section 4.2.

4.2 Statistical methodology

This section describes statistical methods used for calibrating the IGRF and the T96 models against the Cluster satellite measurements in the time-series-based regression model, and explaining the calibration results with relevant factors.

The regression model in Equation 4.1 has a matrix form, $\mathbf{y} = \mathbf{X}\boldsymbol{\beta} + \boldsymbol{\epsilon}$,where $\mathbf{y}$ and $\mathbf{X}$ represent the response and explanatory variables, $\boldsymbol{\beta}$ denotes the unknown parameters, and $\boldsymbol{\epsilon}$ is the error term. Estimation of the unknown parameters quantifies the relationship between the response and explanatory variables, and assumptions must hold

for estimation methods to be applicable. Ordinary least squares (OLS) is a commonly used method for estimating the unknown parameters in a linear regression model, with the goal of minimizing the sum of the squares of the differences between the observed responses in the given dataset and those predicted by a linear function of a set of explanatory variables. One OLS assumption that the error term has constant variance, i.e. $Var(\boldsymbol{\epsilon}|\mathbf{X}) = \sigma^2\mathbf{I}_n$, where $\mathbf{I}_n$ is the identity matrix in dimension n, and σ^2 is a parameter which determines the variance of each observation, is violated by the fact that the error term has changing variances. If this assumption is violated then the OLS estimates are still valid, but no longer efficient. Therefore, an alternative method need to be considered to enhance the efficiency of parameter estimation in the regression model of the magnetic field data. Generalized least squares (GLS) relaxes the assumptions in OLS by stating that the conditional mean of $\mathbf{y}$ given $\mathbf{X}$ is a linear function of $\mathbf{X}$, whereas the conditional variance of the error term given $\boldsymbol{\epsilon}$ is a known non-singular matrix $\boldsymbol{\Sigma}$. This usually written as

$$\mathbf{y} = \mathbf{X}\boldsymbol{\beta} + \boldsymbol{\epsilon}, \qquad E(\boldsymbol{\epsilon}|\mathbf{X}) = \mathbf{0} \quad \text{and} \quad Var(\boldsymbol{\epsilon}|\mathbf{X}) = \boldsymbol{\Sigma}. \tag{4.2}$$

In practice the covariance matrix $\boldsymbol{\Sigma}$ is unknown and we use feasible GLS (FGLS) to estimate the structure of $\boldsymbol{\Sigma}$ from the OLS residuals.

Fitting the regression AR-ARCH errors provides estimates of the regression model parameters. The Maximum-likelihood Estimation (MLE) algorithm has been developed for dealing with missing data problem in FGLS estimation with AR-ARCH structure. The estimated parameters with their confidence intervals calibrate the IGRF model and the T96 model with the Cluster satellite measurements. Performance of the two computer models can be evaluated through analysing the estimated parameters together with other factors that might affect the calibration results.

The estimated model parameters quantify the relationship between the satellite measurements and the two computer model outputs and can be used to explore how the relationship varies across satellite orbits. In the mixed-effects modelling, we consider orbital factors such as mean orbital distance, storm level (as indicated by the maximum of the Kp index over the orbit), the missing proportion (number of orbital observations divided by hours of the orbital period), etc. Mixed-effects models that take both fixed

effects and random effects into account can be used to explain the calibration or mis-calibration of the computer model simulations. In the mixed-effects analysis, whether treating a factor as fixed or random depends on the questions of interest and how the data is gathered. Our primary interest in assessing the calibration of the computer model is to understand how the models perform under different space weather condition across the satellite orbits. Hence factors of the storm levels and the satellite orbits are considered as fixed effects. Random factors include satellites and components of which the magnetic field data are collected. The factor of satellites has four levels for C1-4 and can be regarded as a random sample of satellites in near-Earth space. Instead of estimating the effect of each of the Cluster satellite, estimating the variability caused by the satellite factor would make more sense. The component factor nested in the satellite factor should also be considered random.

4.2.1 GLS estimation with an AR-ARCH structure

GLS considers a more general variance covariance matrix for the disturbances, in which case $\boldsymbol{\epsilon} \sim \mathcal{N}(0, \sigma^2 \mathbf{I}_n)$ is relaxed to $\boldsymbol{\epsilon} \sim \mathcal{N}(0, \sigma^2 \boldsymbol{\Sigma})$, where $\boldsymbol{\Sigma}$ is a positive definite matrix of dimension $(n \times n)$. For every positive definite matrix $\boldsymbol{\Sigma}$, there exists a non-singular matrix $\mathbf{P}$ such that $\mathbf{P}\mathbf{P}^T = \boldsymbol{\Sigma}$. The original model can be transformed into

$$\mathbf{P}^{-1}\mathbf{y} = \mathbf{P}^{-1}\mathbf{X}\boldsymbol{\beta} + \mathbf{P}^{-1}\boldsymbol{\epsilon}$$

by pre-multiplying $\mathbf{P}^{-1}$. Then

$$\text{Var}(\mathbf{P}^{-1}\boldsymbol{\epsilon}) = \mathbf{P}^{-1}\text{Var}(\boldsymbol{\epsilon})\mathbf{P}_{T-1} = \sigma^2\mathbf{P}^{-1}\boldsymbol{\Sigma}\mathbf{P}_{T-1} = \sigma^2\mathbf{P}^{-1}\mathbf{P}\mathbf{P}^T\mathbf{P}_{T-1} = \sigma^2\mathbf{I}_n$$

Hence the variance-covariance of the transformed errors of the model becomes a scalar times the identity matrix. Using this transformation allows us to obtain the GLS estimator of $\boldsymbol{\beta}$

The regression model given in Equation 4.1 can be expressed in a matrix form as shown in Equation 4.2. The heterogeneous variance of the error term is taken into account in the GLS estimation of the regression parameters $\hat{\boldsymbol{\beta}}$ and the standard errors of $\hat{\boldsymbol{\beta}}$,

$$\hat{\boldsymbol{\beta}}_{GLS} = (\mathbf{X}^T\boldsymbol{\Sigma}^{-1}\mathbf{X})^{-1}\mathbf{X}^T\boldsymbol{\Sigma}^{-1}\mathbf{y}, \qquad \text{Var}(\hat{\boldsymbol{\beta}}_{GLS}) = (\mathbf{X}^T\boldsymbol{\Sigma}^{-1}\mathbf{X})^{-1} \tag{4.3}$$

where the structure of $\mathbf{\Sigma}$ is unknown. Instead of assuming the structure of $\mathbf{\Sigma}$, we usually obtain the estimated error $\hat{\boldsymbol{\epsilon}}$ from OLS and estimate its variance-covariance structure,$\hat{\mathbf{\Sigma}}$, and use $\hat{\mathbf{\Sigma}}$ instead of $\mathbf{\Sigma}$.

Assuming time-dependent error within an orbit o, $\{\epsilon_t : t \in \mathcal{O}_{o(t)}\}$, to follow an AR(1)-ARCH(1) process,

$$\epsilon_t = \phi\epsilon_{t-1} + z_t, \qquad -1 < \phi < 1 \tag{4.4}$$

$$z_t = \sigma_t\eta_t, \qquad \{\eta_t\} \overset{iid}{\sim} \mathcal{N}(0,1) \tag{4.5}$$

$$\sigma_t^2 = \omega + \lambda z_{t-1}^2, \qquad \omega > 0, \quad \lambda \geq 0. \tag{4.6}$$

The unconditional variance of ϵ_t is invariant to t and can be obtained through Equation 4.4 given $\mathrm{Var}(z_t)$. Equation 4.5 relates z_t to σ_t and η_t, which follows a standard normal distribution. Hence z_t has mean zero and its variance can be obtained from Equation 4.6.

It can be derived, for $t = 1$,

$$\epsilon_1 \sim \mathcal{N}\left(0, \frac{\omega}{(1-\lambda)(1-\phi^2)}\right), \tag{4.7}$$

for $t = 2$,

$$\epsilon_2|\epsilon_1 \sim \mathcal{N}\left(\phi\epsilon_1, \frac{\omega}{1-\lambda}\right), \tag{4.8}$$

and for $t \geq 3$,

$$\epsilon_t|\epsilon_{t-1}, \epsilon_{t-2} \sim \mathcal{N}\left(\phi\epsilon_{t-1}, \omega + \lambda z_{t-1}^2\right). \tag{4.9}$$

Since $z_{t-1} = \epsilon_{t-1} - \phi\epsilon_{t-2}$, the conditional probability of ϵ_t given its past values can be written as

$$\epsilon_t|\epsilon_{t-1}, \epsilon_{t-2} \sim \mathcal{N}\left(\phi\epsilon_{t-1}, \omega + \lambda(\epsilon_{t-1} - \phi\epsilon_{t-2})^2\right), \quad t \geq 3. \tag{4.10}$$

Equations of the AR-ARCH model give the variance-covariance matrix,

$$\mathrm{Cov}(\epsilon_t, \epsilon_{t+\tau}) = \mathrm{Cov}(\epsilon_t, \underbrace{\phi\{\ldots(\phi(\phi}_{\tau}\epsilon_t + z_{t+1}) + z_{t+2}) + \ldots\} + z_{t+\tau}) \tag{4.11}$$

$$= \phi^\tau \mathrm{Var}(\epsilon_t), \tag{4.12}$$

since for any positive integer τ, $\mathrm{Cov}(\epsilon_t, z_{t+\tau}) = 0$, and

$$\mathrm{Var}(\epsilon_t) = \frac{\mathrm{Var}(z_t)}{1-\phi^2} = \frac{1}{1-\phi^2}\frac{\omega}{1-\lambda}$$

the variance-covariance matrix becomes

$$\mathrm{Cov}(\epsilon_t, \epsilon_{t+\tau}) = \phi^\tau \frac{1}{1-\phi^2}\frac{\omega}{1-\lambda}$$

R functions were implemented to estimate the model parameters for ϵ_t using maximum likelihood estimation. The vector of parameters is

$$\boldsymbol{\theta} = (\phi, \omega, \lambda)^T \tag{4.13}$$

and the following conditions hold so that the error process is stationary:

$$|\phi| < 1, \quad \omega > 0, \quad 0 \leq \lambda < 1.$$

To find the MLEs numerically, exponential and logit inverse transformations were used for α_0 and α_1. The logit of a number p between 0 and 1 is given by $\mathrm{logit}(p) = \log(\frac{p}{1-p})$.

Let $\{\epsilon_t\}$ be a realization of length n to the AR(1)-ARCH(1) model. Conditional on initial values, the overall likelihood $\mathcal{L}_n$ is given by

$$\mathcal{L}_n(\boldsymbol{\theta}; \epsilon_1, \cdots, \epsilon_n) = P(\epsilon_1) \cdot P(\epsilon_2|\epsilon_1) \cdot \prod_{t=2}^{n} P(\epsilon_t|\epsilon_{t-1}, \epsilon_{t-2}). \tag{4.14}$$

Through an iterative process, we find the measurable solution $\hat{\theta}_n$ of

$$\hat{\theta}_n = \arg\max_{\theta \in \Theta} L_n(\theta) \tag{4.15}$$

The error variance-covariance matrix takes the form $\hat{\boldsymbol{\Sigma}} = (\sigma_{ij}) \in R^{n \times n}$ with

$$\sigma_{ij} = \hat{\phi}^{|i-j|}\frac{1}{(1-\hat{\phi}^2)}\frac{\hat{\omega}}{1-\hat{\lambda}} \tag{4.16}$$

where $\hat{\phi}, \hat{\alpha}_0, \hat{\alpha}_1$ are the estimates of the AR-ARCH model.

The GLS estimator $\hat{\boldsymbol{\beta}}_{GLS}$ and its variances can be obtained using Equation 4.3, replacing $\boldsymbol{\Sigma}$ with $\hat{\boldsymbol{\Sigma}}$.

4.2.2 Mixed effects model

This section provides an overview of linear mixed-effects model (LME) in terms of its theoretical and computational aspects, covering a general formulation of LME models and estimation methods for LME models. A comprehensive description of the theory of LME models can be found in McCulloch (1997), and detailed examples of the applications of LME models are available in Pinero and Bates (2000).

A two nested levels of random effects, the cross-satellite and the cross-component effects, are considered in the mixed-effects model. The first grouping factor divides the observations into M groups and the response vectors can be written as $\mathbf{y}_{ij}$, $i = 1, \cdots, M$, $j = 1, \cdots, M_i$, where M is the number of first-level groups and M_i is the number of second-level groups nested within the first-level group i. $\mathbf{y}_{ij}$ has the length n_{ij}.

Let $\mathbf{X}_{ij}$ denote the fixed-effects model matrices that have size $n_{ij} \times p$, $\mathbf{b}_i$ of length q_1 be the first-level random effects, $\mathbf{b}_{ij}$ of length q_2 be the second-level random effects, $\mathbf{Z}_{i,j}$ of size $n_i \times q_1$ denote the model matrices corresponding to $\mathbf{b}_i$, and $\mathbf{Z}_{ij}$ of size $n_i \times q_2$ denotes the model matrices corresponding to $\mathbf{b}_{ij}$. Hence the LME model of two nested levels of random effects can be written as

$$\begin{aligned} \mathbf{y}_{ij} = \mathbf{X}_{ij}\beta + \mathbf{Z}_{i,j}\mathbf{b}_i + \mathbf{Z}_{ij}\mathbf{b}_{ij} + \boldsymbol{\epsilon}_{ij}, \quad i = 1, \cdots, M \quad j = 1, \cdots, M_i, \\ \mathbf{b_i} \sim \mathcal{N}(\mathbf{0}, \boldsymbol{\Psi}_1), \qquad \mathbf{b_{ij}} \sim \mathcal{N}(\mathbf{0}, \boldsymbol{\Psi}_2), \qquad \boldsymbol{\epsilon_{ij}} \sim \mathcal{N}(\mathbf{0}, \sigma^2\mathbf{I}). \end{aligned} \tag{4.17}$$

The first-level random effects $\mathbf{b}_i$ are assumed to be independent for different i, the second-level random effects $\mathbf{b}_{ij}$ are assumed to be independent of $\mathbf{b}_i$ and for different i or j, and the within-group errors $\boldsymbol{\epsilon}_{ij}$ are assumed to be independent of $\mathbf{b}_i$ and $\mathbf{b}_{ij}$ and for different i or j.

The two variance-covariance matrices $\boldsymbol{\Psi}_1$ and $\boldsymbol{\Psi}_2$ are written in terms of relative precision factors $\boldsymbol{\Delta}_1$ and $\boldsymbol{\Delta}_2$, parametrized by unconstrained parameter vectors $\boldsymbol{\theta}_1$ and $\boldsymbol{\theta}_2$. The profiled log-likelihood or the profiled log-restricted-likelihood, a function of $\boldsymbol{\theta}_1$ and $\boldsymbol{\theta}_2$ only, is maximized to produce the estimates $\widehat{\boldsymbol{\beta}}$, $\widehat{\sigma}^2$, $\widehat{\boldsymbol{\Psi}}_1$, and $\widehat{\boldsymbol{\Psi}}_2$.

4.3 Application to the magnetic field data

This section calibrates the IGRF and T96 models with satellite measurement using a time-varying coefficients model. The estimated model coefficients that quantify the relationship of between the satellite measurements and the computer models are analysed in a linear mixed effects model with the satellite numbers, C1-4, and the components, x, y, and z, as random effects, for evaluating the overall performance of the computer model. The mixed-effect model assumes the same amount of variance between observations within each group, i.e. the satellite group or the component group, but the observations do not vary consistently across these groups.

4.3.1 Calibrating the computer models with the Cluster data

We apply the methods given in subsection 4.2.1 to the magnetic field datasets of the four Cluster satellites in the three components of 11-years.

Steps in the time-series based modelling can be summarized as follows:

1. obtain $\{\hat{\epsilon}_t : t \in \mathcal{O}_{o(t)}\}$ the estimated regression errors using OLS;
2. estimate the AR-ARCH model parameters, $\{\hat{\phi}_o, \hat{\omega}_o, \hat{\lambda}_o\}$, using the regression residuals of each orbit o;
3. construct $\hat{\mathbf{\Sigma}}$ the variance-covariance matrix of the regression errors using the estimated AR-ARCH model parameters;
4. estimate the regression model parameters, $\{\hat{\alpha}_o, \hat{\beta}_o, \hat{\mu}_o\}$, construct confidence intervals for the estimated regression model parameters using the variance-covariance information of the regression error.

The work provides a calibration of the magnetic field models with the four Cluster satellite data in the three components through estimating the time-varying regression model parameters. Figure 4.1, 4.2, 4.3, 4.4, 4.5, 4.6, and 4.7 provide time plots of the estimates of model coefficients $\{\hat{\alpha}_o\}$, $\{\hat{\beta}_o\}$, and $\{\hat{\mu}_o\}$, against orbits in the year 2003, 2004, 2007, 2009, 2010, 2011 and 2012. $\{\hat{\alpha}_o\}$ and $\{\hat{\beta}_o\}$ are the coefficients for the IGRF and the T96 model outputs. $\{\hat{\mu}_o\}$ are the intercepts in the regression model. Each figure

presents, from the top to the bottom panels, the estimates of the three parameters from the magnetic field strengths in the x-, y- and z- component. The parameter estimates across orbits are indicated by the black line, and the confidence intervals for the estimates are shown by the grey regions around the black line. The red lines represent the mean features of the estimated parameters using B-splines for smoothing.

The regression parameter estimated across the satellite orbits form new time series. The temporal features of the estimated parameters can be summarized as:

- $\{\hat{\alpha}_o\}$ are centred around 1 and range from 0.5 to 1.5. The $\{\hat{\alpha}_o\}$ of the x-component has higher variability in June and December, when the orbits of the satellite are most elongated in the plane perpendicular to the x-component (see Figure 3.1); The $\{\hat{\alpha}_o\}$ of the y-component has higher variability in March and September, when the orbits of satellite are most elongated in the plane perpendicular to the y-component.
- $\{\hat{\beta}_o\}$ ranges from 0 to 2 and have larger variances $\{\hat{\alpha}_o\}$. Trends of each component appear different.
- $\{\hat{\mu}_o\}$ ranges from -20 to 20 and have value 0 included in most of their confidence intervals.

The temporal features of the three estimated parameters, especially $\{\hat{\alpha}_o\}$, also differs in years. The $\{\hat{\alpha}_o\}$ obtained after 2007 become noisier for certain time periods in the following years. The time series of the estimated IGRF coefficient is stationary and has smaller variance than the time series of the estimated T96 coefficient, which has changing volatility and a trend that can be removed by taking its first order difference.

If, for example, $\{\alpha_{o(t)} : t \in \mathbb{Z}\}$ follows a distribution that centred around the value 1 with a small variance, we would conclude that the IGRF model calibrates the internal magnetic field well with the satellite data. If the mean value estimated from $\{\alpha_{o(t)} : t \in \mathbb{Z}\}$ deviates significantly from 1, we would conclude that the IGRF model overestimates or underestimates the internal magnetic field with an uncertainty depending on the size of the variance.

The results show that the estimated parameter $\hat{\beta}_o$ for T96, the external model, has more variability than the estimated parameter $\hat{\alpha}_o$ for IGRF, the internal model. This is

consistent with the fact that the external field contributed by the current system is more uncertain than the internal field generated by the Earth's dynamo. Therefore, given the complex nature of the external field, the T96 model is less reliable in predicting the external field than the IGRF model for the internal field. Temporal analysis of $\{\hat{\alpha}_o : o \in \mathcal{O}\}$ and $\{\hat{\beta}_o : o \in \mathcal{O}\}$ suggest that $\hat{\alpha}_o$ has no trend while $\hat{\beta}_o$ has a trend that can be removed by taking its first order difference.

It has also been observed that $\hat{\alpha}_o$ seems to have a mean value of 1 with outliers occurring at the same orbits in a few years while $\hat{\beta}_o$ has a clear cyclic pattern that repeats every year from 2003 to 2006, before the satellite maneuver took place in 2007. The time plot of $\hat{\beta}_o$ in 2003 shows the mean value of the parameter is close to 1 in the first half of the year, when the satellite spent most of its time in the magnetopause, i.e. the head of the magnetosphere, but drops below 1 in the second half of the year, when the satellite were mainly investigating the magnetotail region. The changes in the $\hat{beta}$ and $\hat{miu}$ from 2009 onwards is associated with the changes in the satellite trajectories, as discussed in Chapter 3. This suggests the reliability of the T96 model varies across space. The T96 model provides less reliable estimates in the years when $\hat{beta}$ and $\hat{miu}$ have larger confidence interval and larger variability. All this evidence is pointing to the fact that the calibration results are somehow associated with the properties of the orbits, to be exact, the region in space that the satellite travels through.

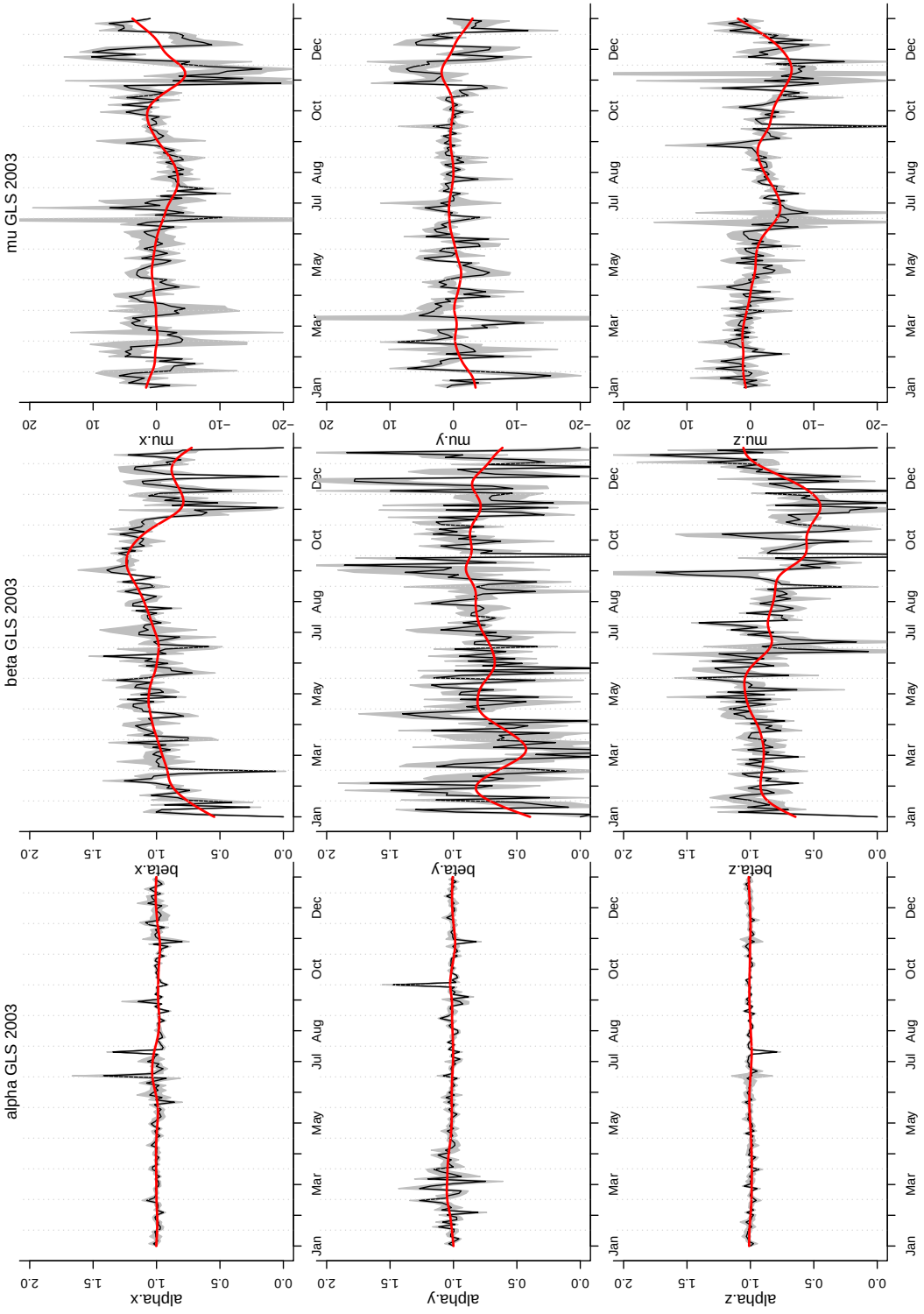

FIGURE 4.1: Estimates of regression parameters in 2003. The black lines represent the estimated values of the parameters; the grey shaded regions denote the 95 percent confidence interval constructed for the estimated parameters; The red curves are the smoothing splines fitted to the estimates.

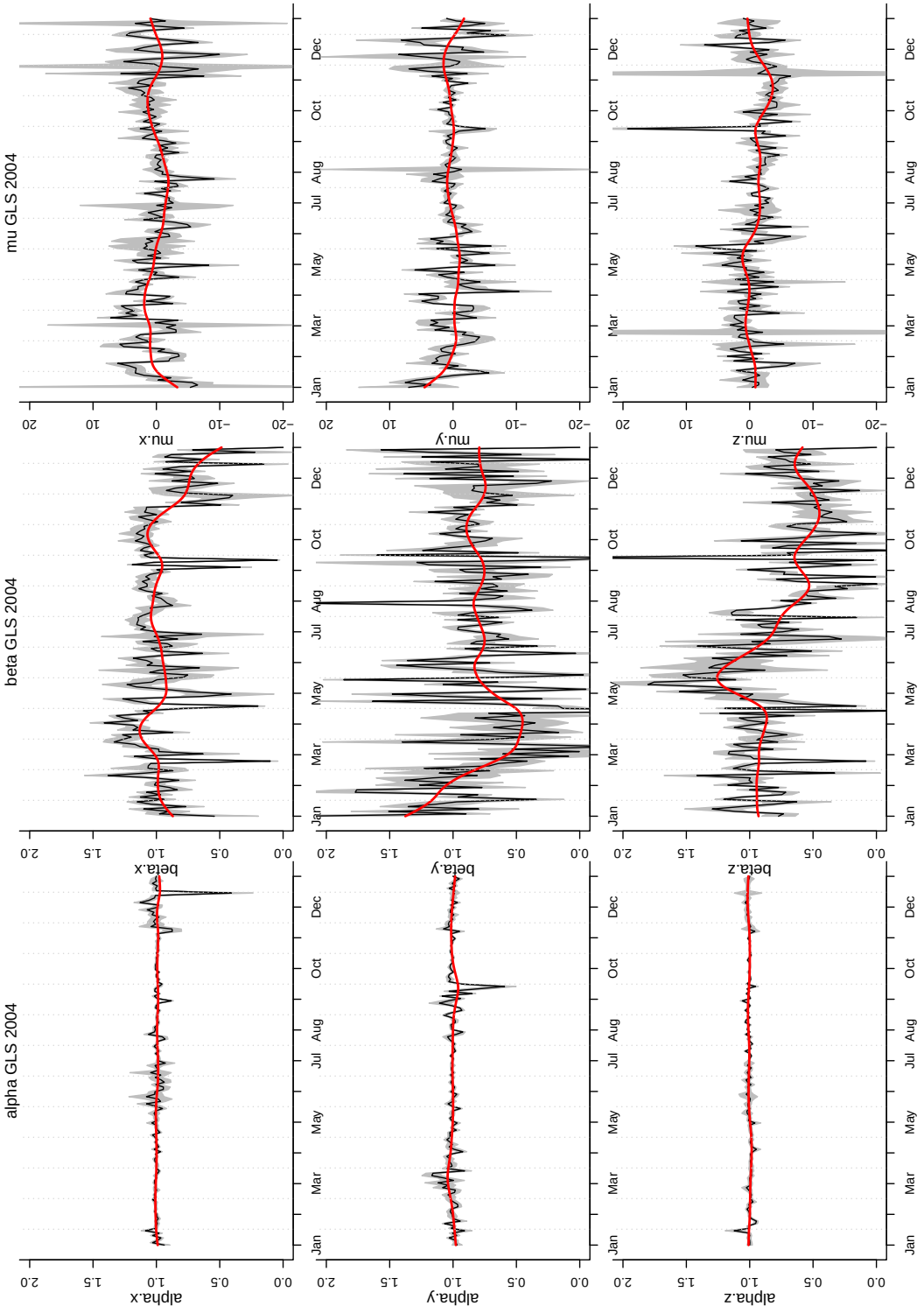

FIGURE 4.2: Estimates of regression parameters in 2004, Lines have the same meaning as in Figure 4.1.

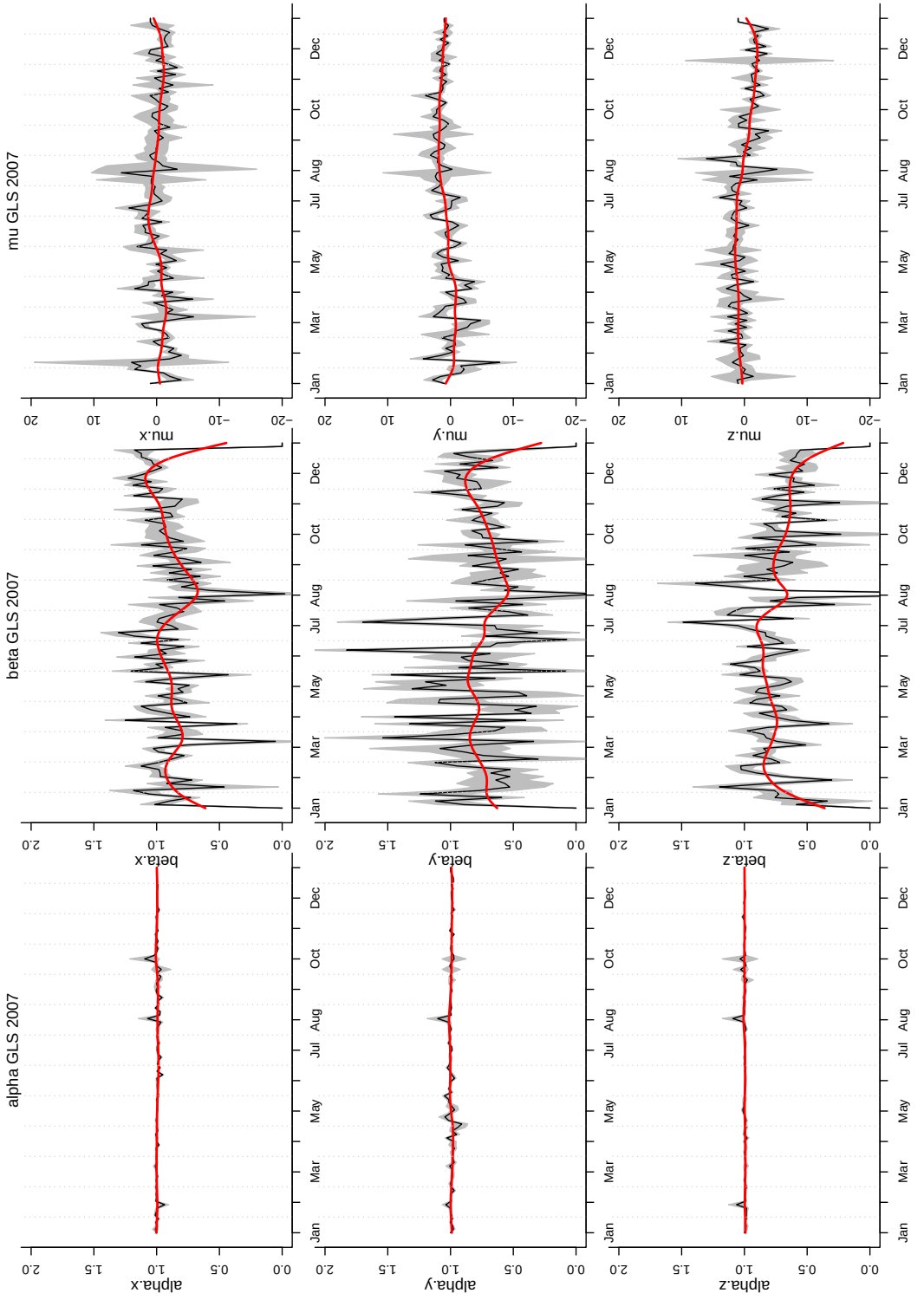

FIGURE 4.3: Estimates of regression parameters in 2007

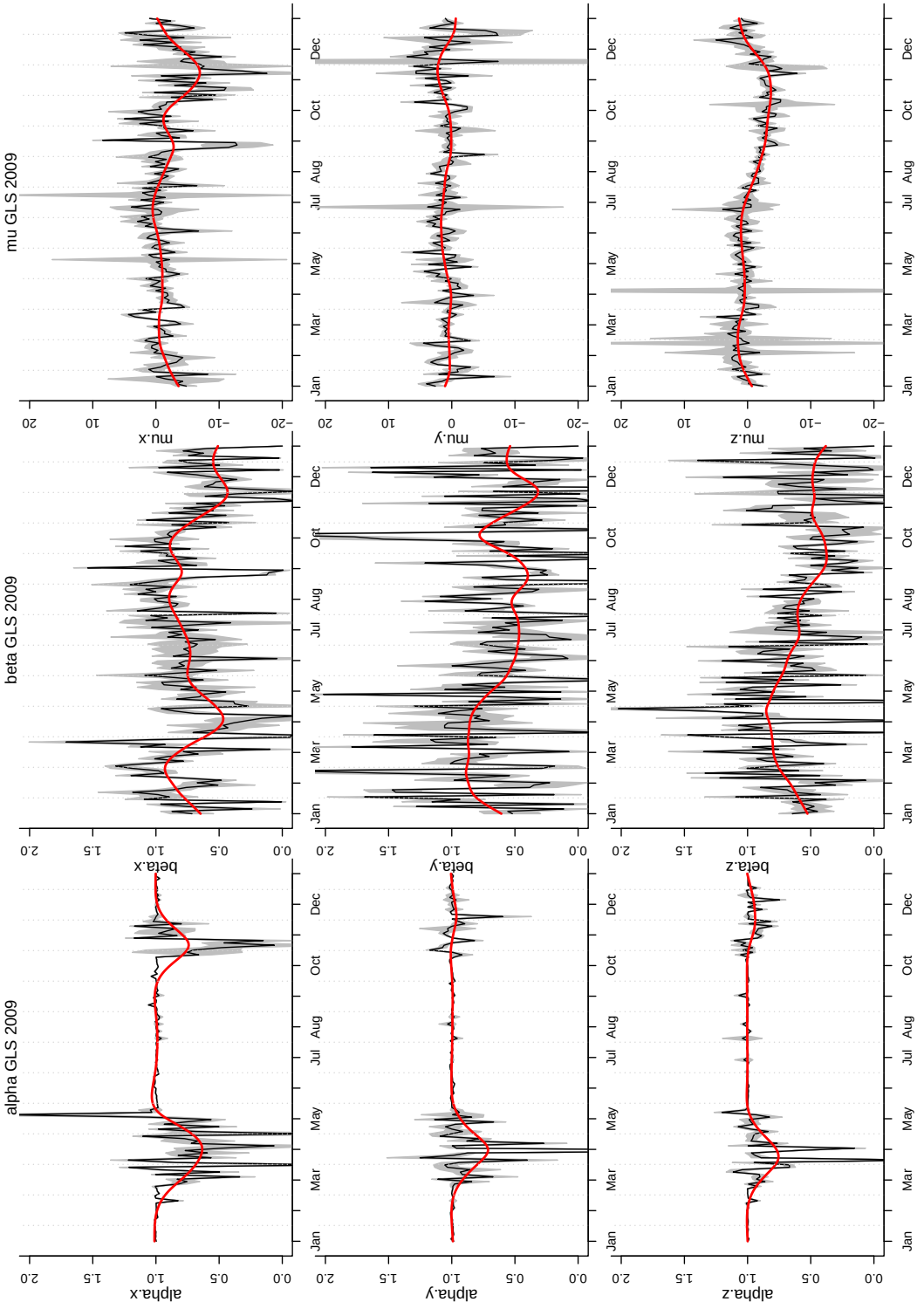

FIGURE 4.4: Estimates of regression parameters in 2009

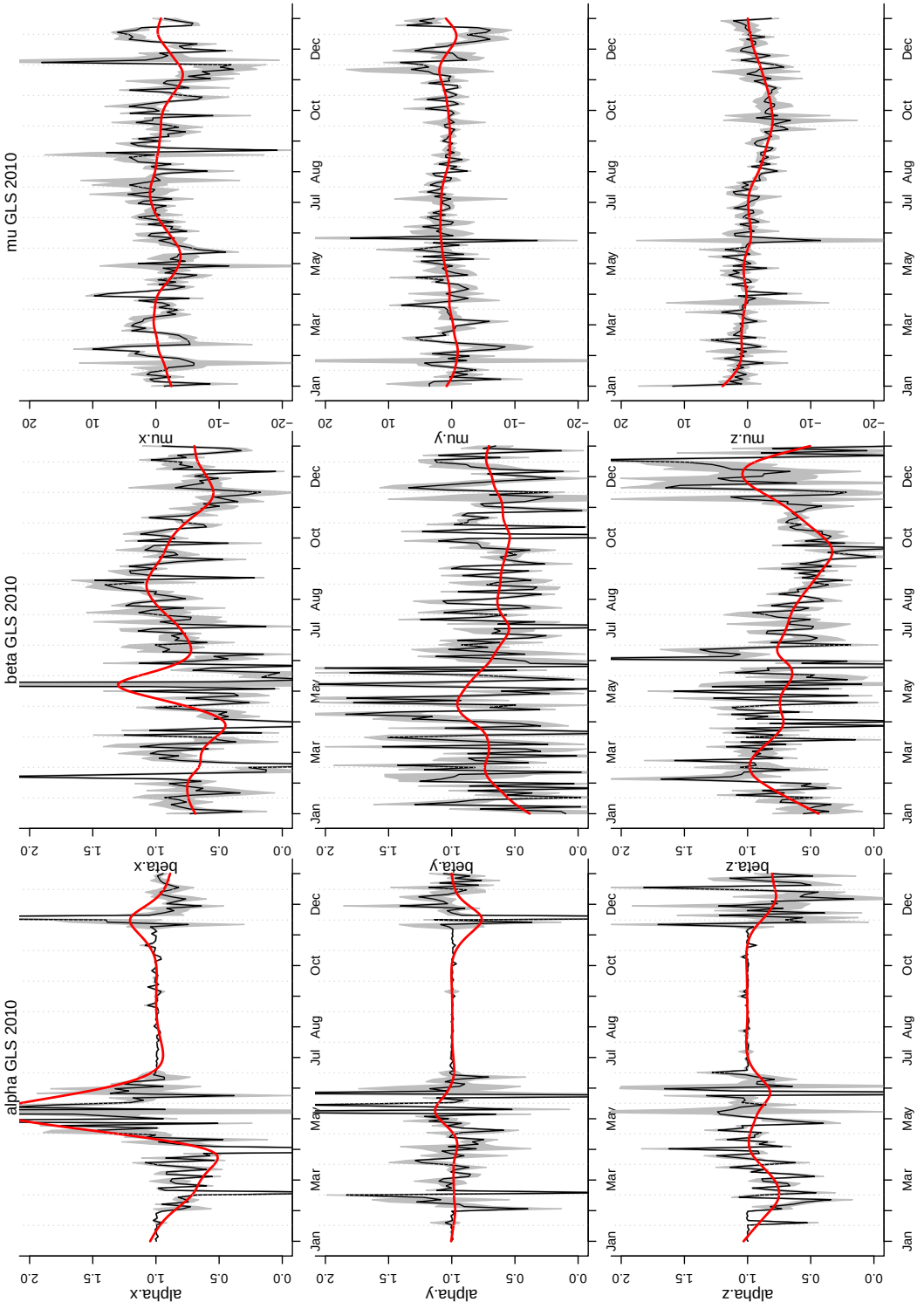

FIGURE 4.5: Estimates of regression parameters in 2010

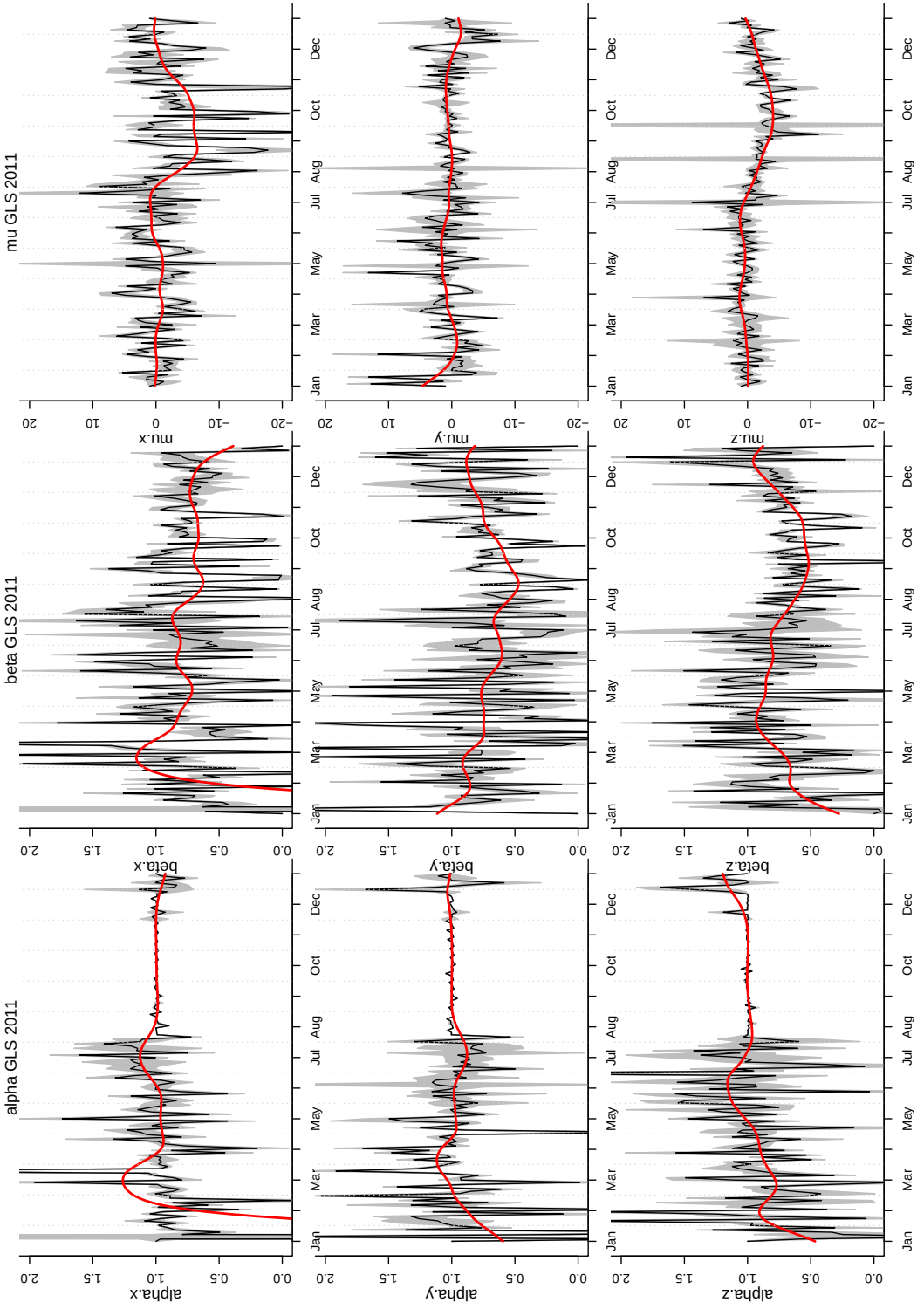

FIGURE 4.6: Estimates of regression parameters in 2011

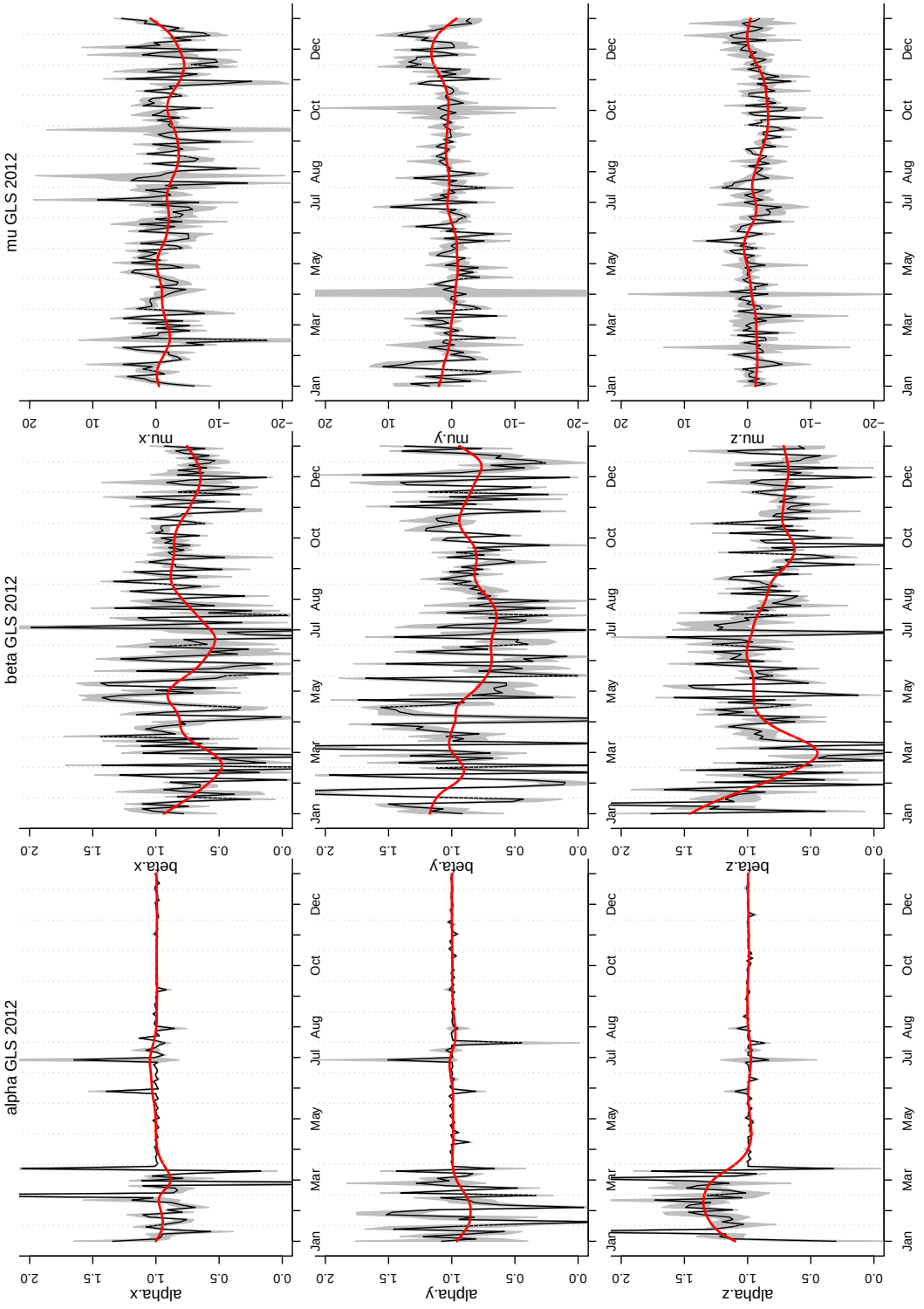

FIGURE 4.7: Estimates of regression parameters in 2012

The calibration results, based on $\hat{\alpha}_o$ and $\hat{\beta}_o$ the estimated coefficients correspond to the IGRF and the T96 model, differ in years, shown in Figure 4.8, as a result of the Cluster satellite investigating different regions in space.

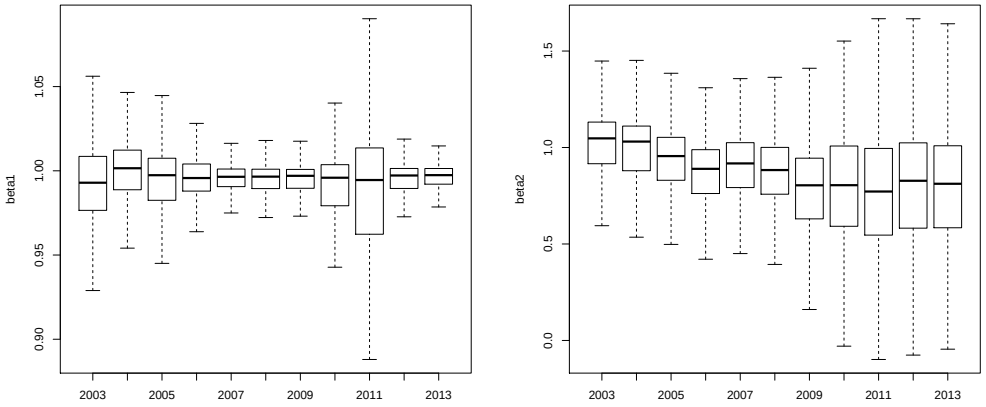

FIGURE 4.8: Boxplot of $\hat{\alpha}_o$, the estimated coefficients for the IGRF model, and $\hat{\beta}_o$, the estimated coefficients for the T96 model.

Estimates of the AR-ARCH model parameters, $\{\phi_o\}$, $\{\omega_o\}$, and $\{\lambda_o\}$, are provided in Figure 4.9, 4.10, 4.11, 4.12,4.13,4.14,4.15,4.16,4.17, and 4.18. These plot suggest the yearly patterns in the three estimated parameters. The values of the estimated parameters confirm the existence of autocorrelation and conditional variances in the regression model residuals.

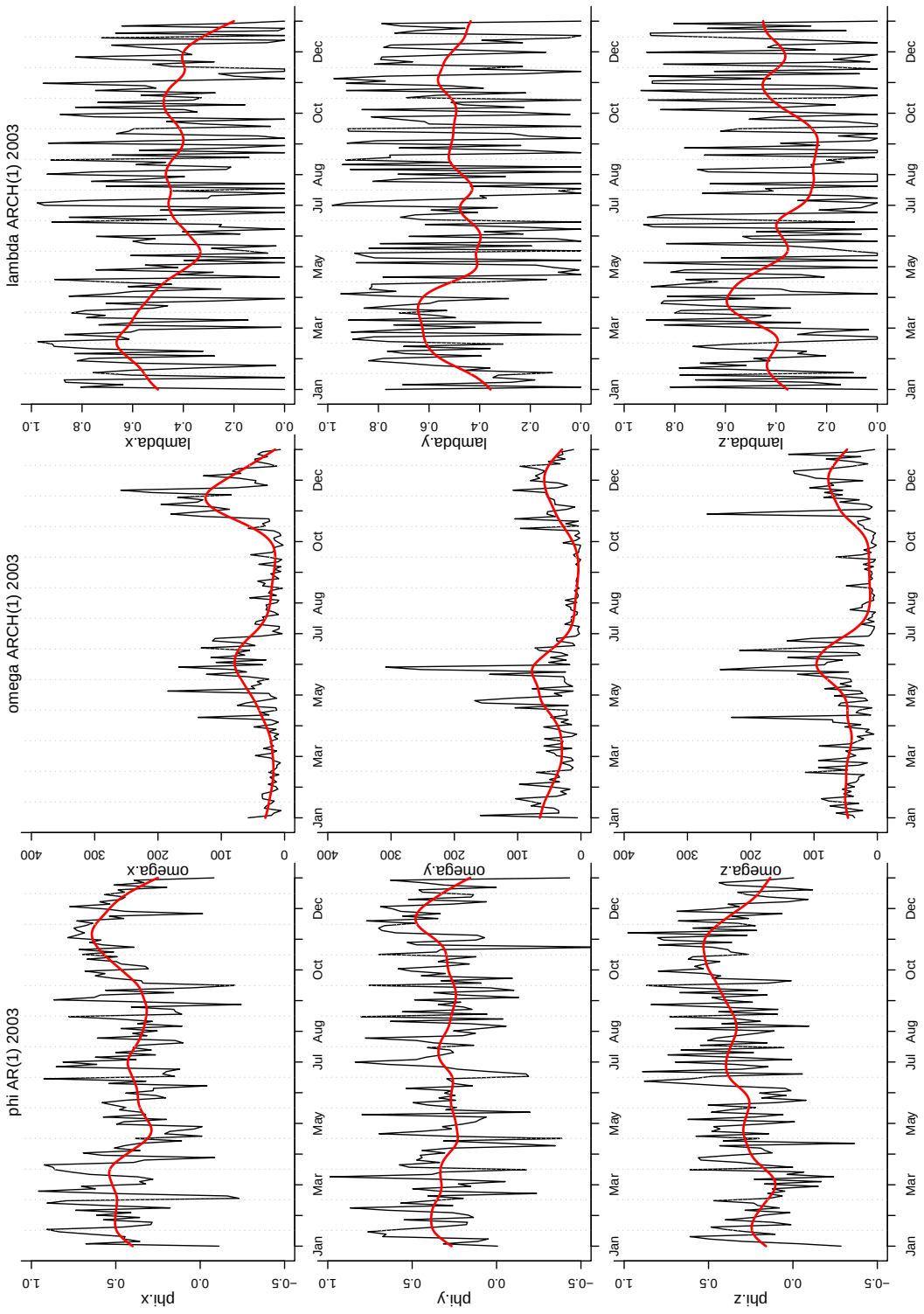

FIGURE 4.9: Time plots of parameters in the AR-ARCH model, $\{\hat{\phi}_o\}$, $\{\hat{\omega}_o\}$, and $\{\hat{\lambda}_o\}$ (from left to right), estimated from the x-, y- and z-components (from top to bottom) of the 2003 magnetic field data. The red curves in each plot are the smoothing splines showing the mean features.

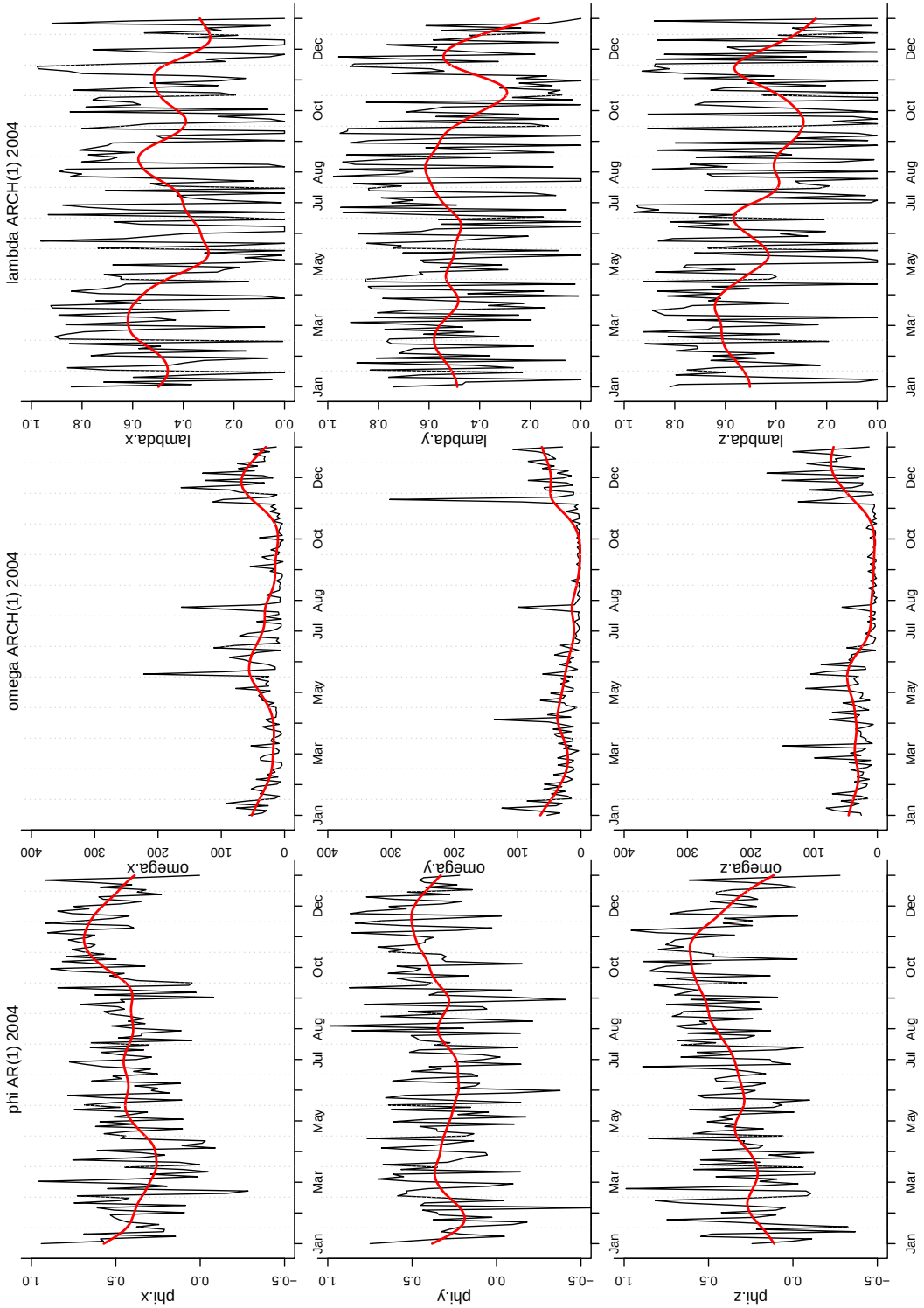

FIGURE 4.10: est ar arch 2004

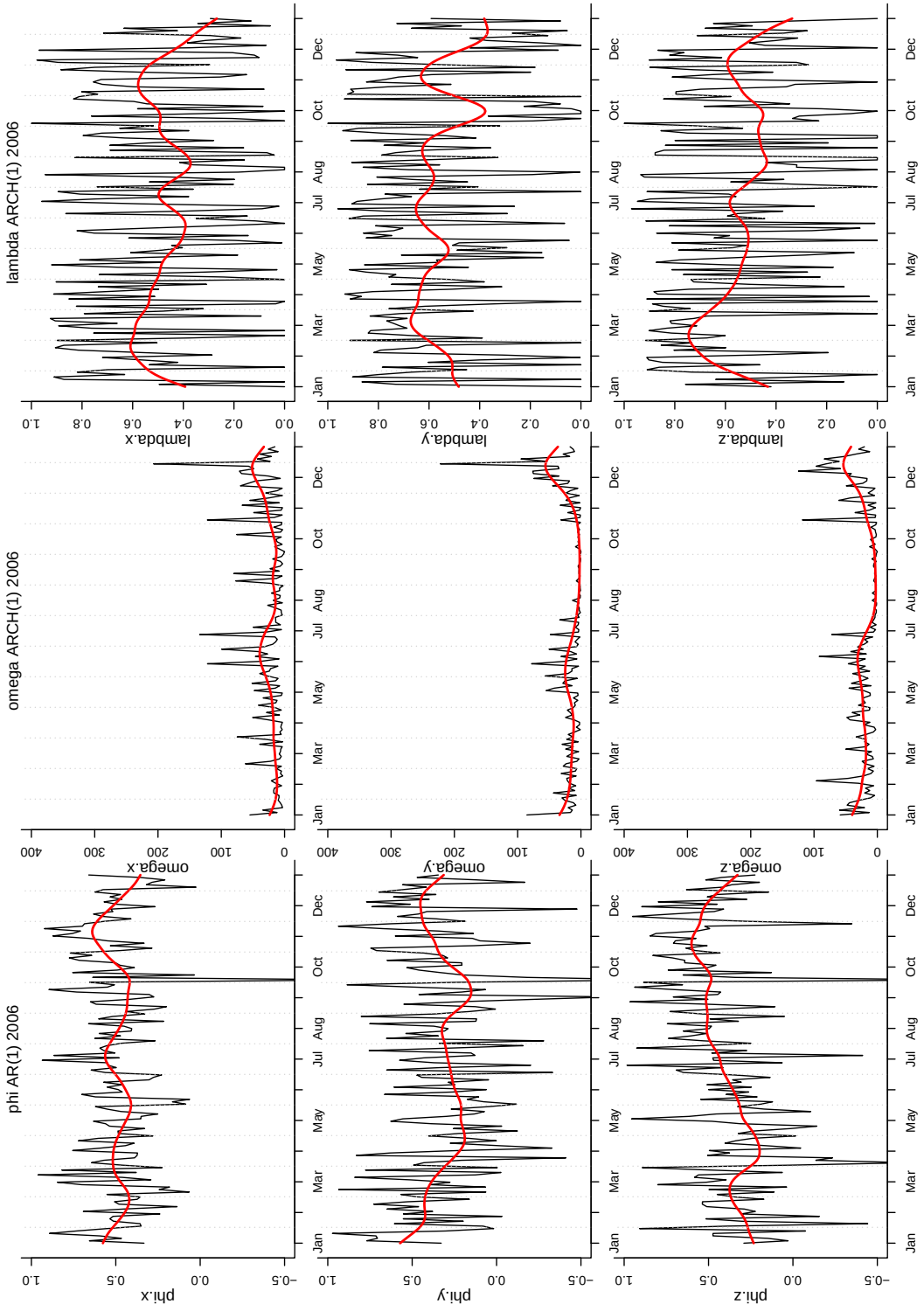

FIGURE 4.11: est ar arch 2006

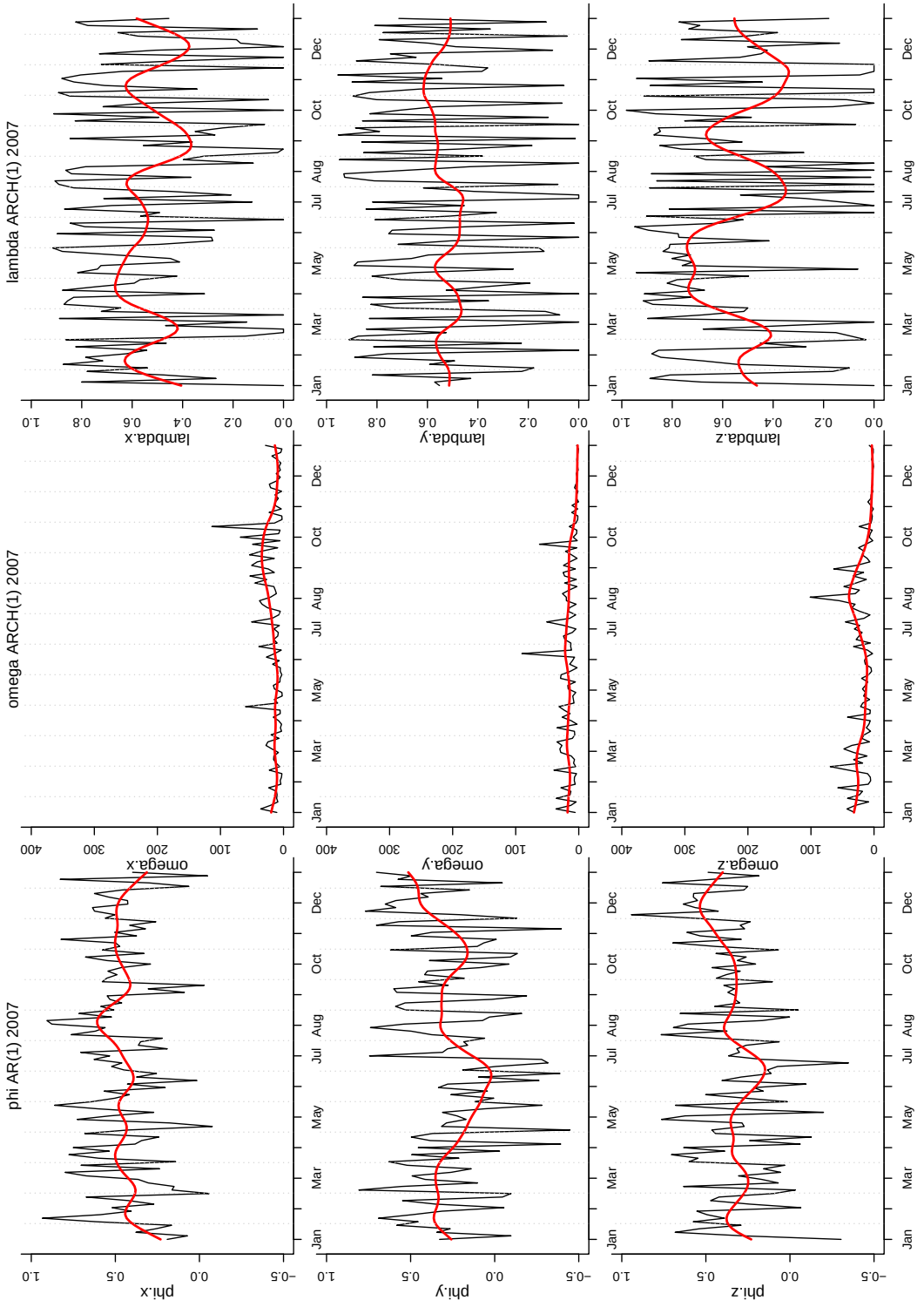

FIGURE 4.12: est ar arch 2007

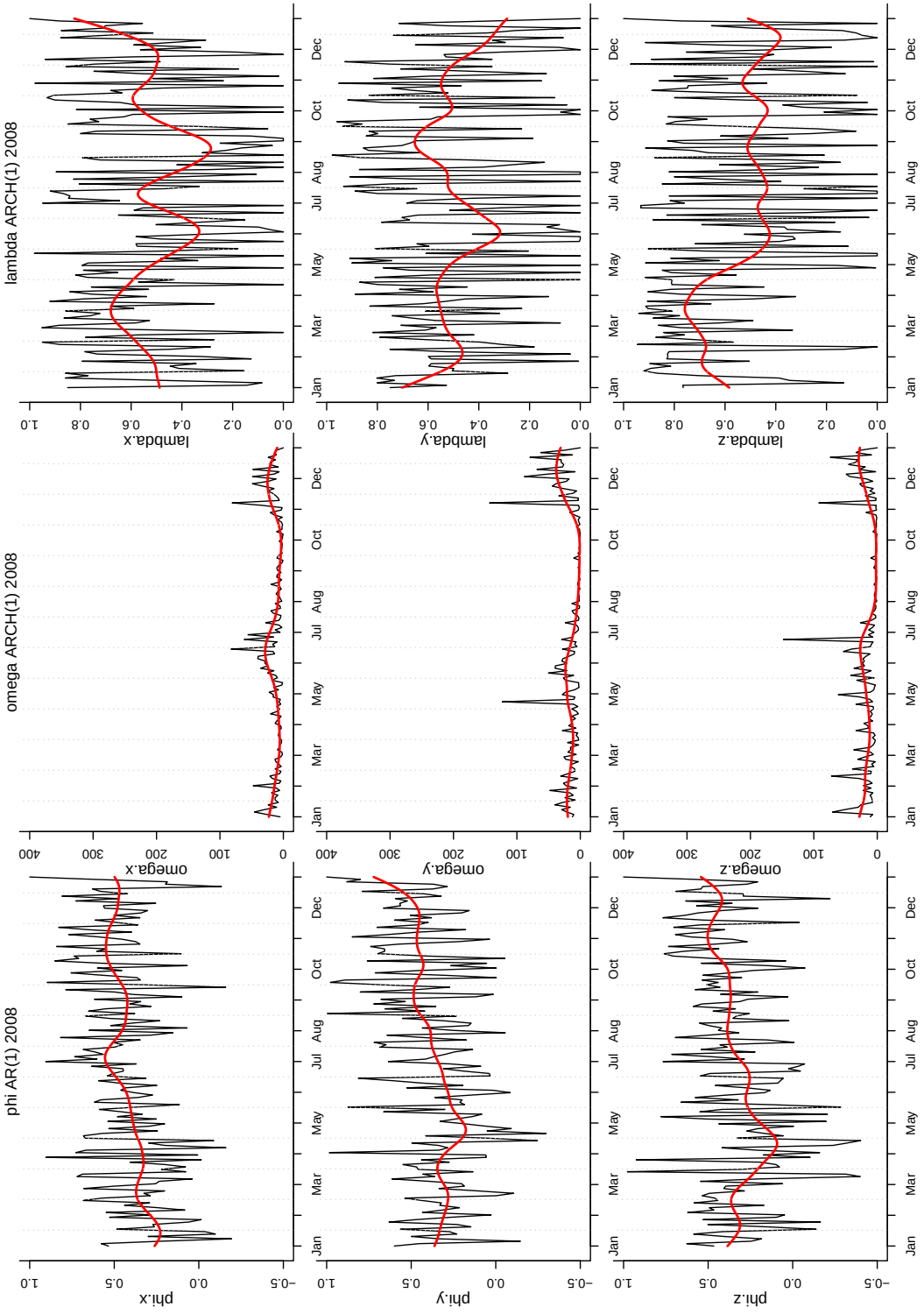

FIGURE 4.13: est ar arch 2008

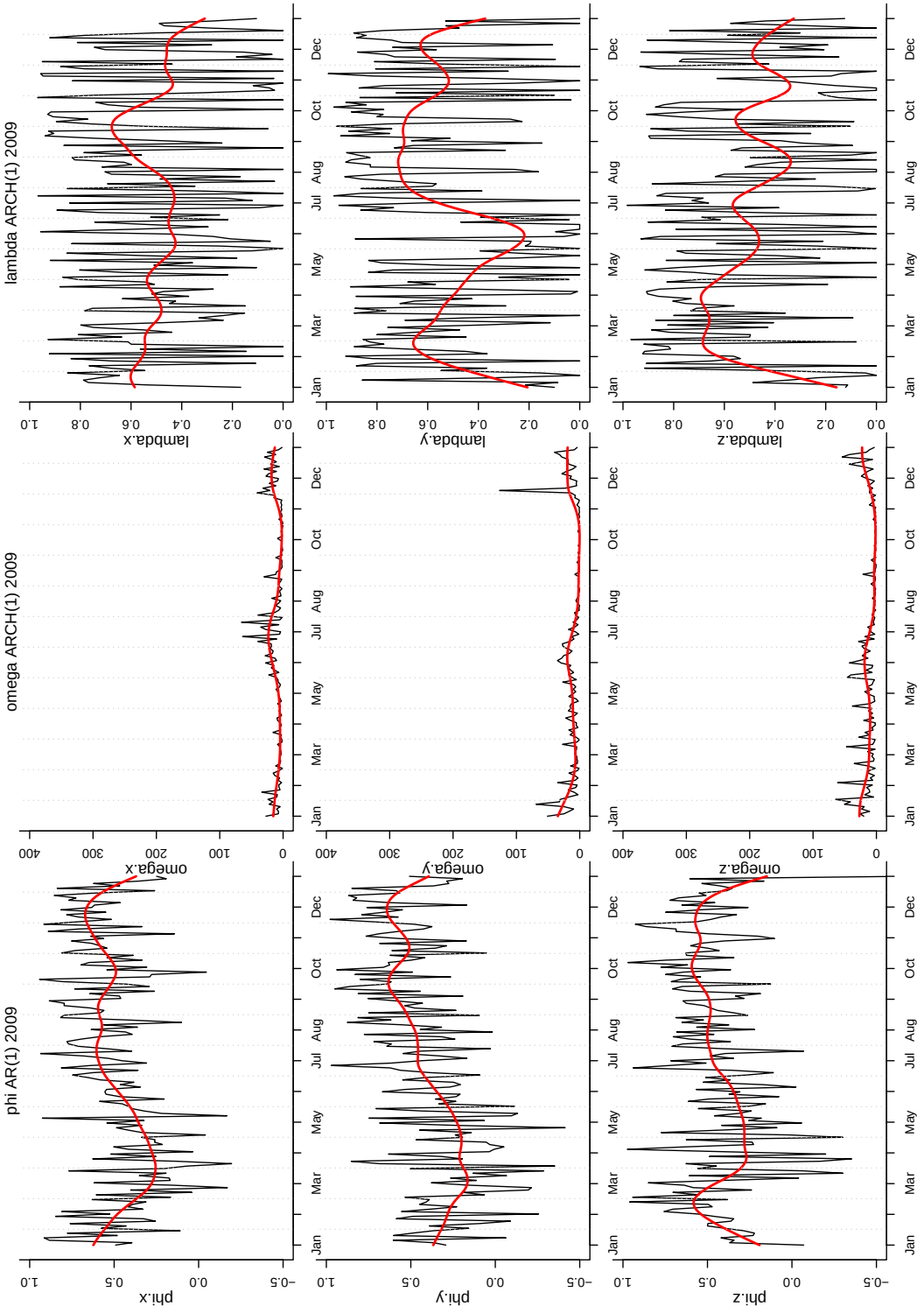

FIGURE 4.14: est ar arch 2009

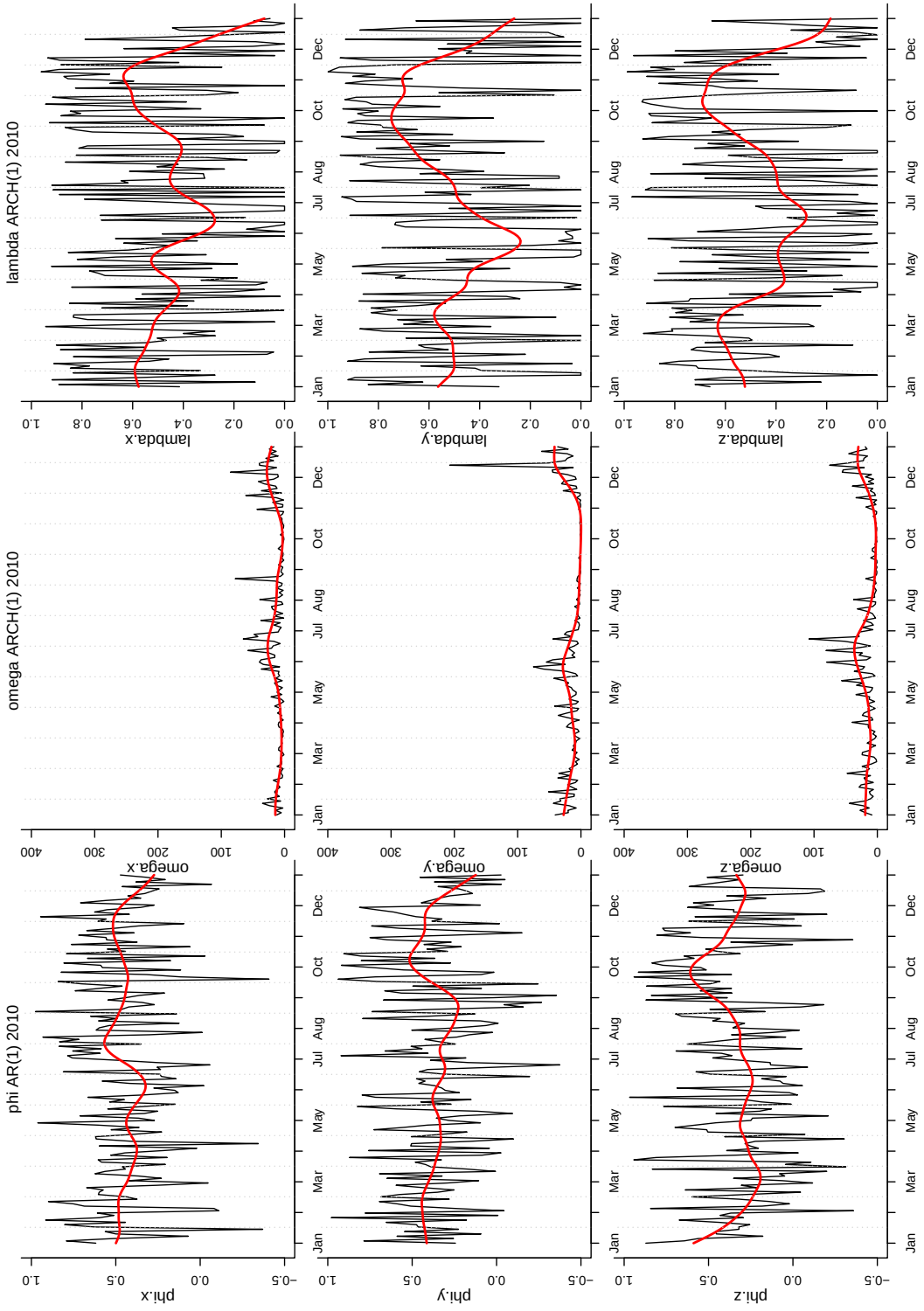

FIGURE 4.15: est ar arch 2010

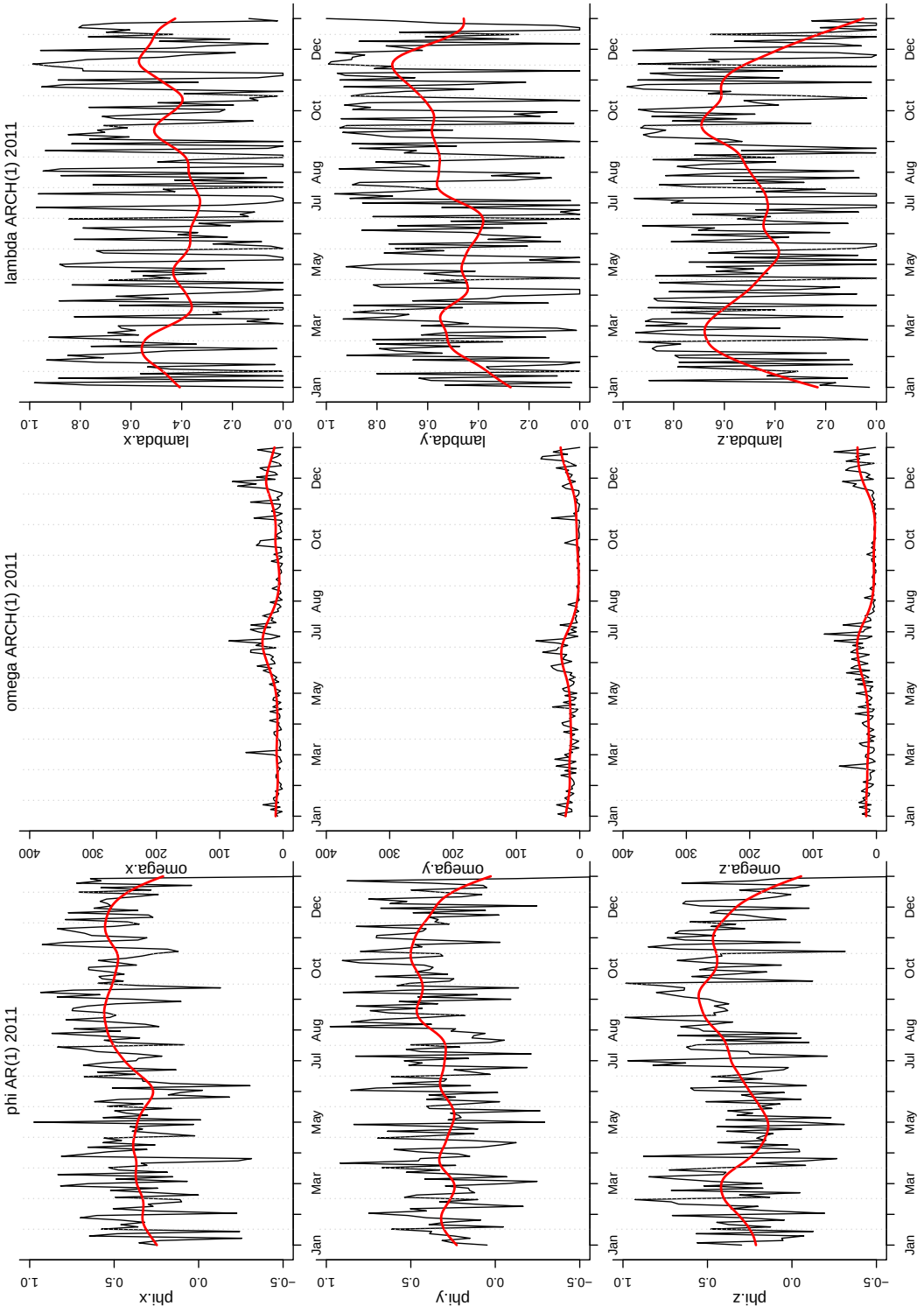

FIGURE 4.16: est ar arch 2011

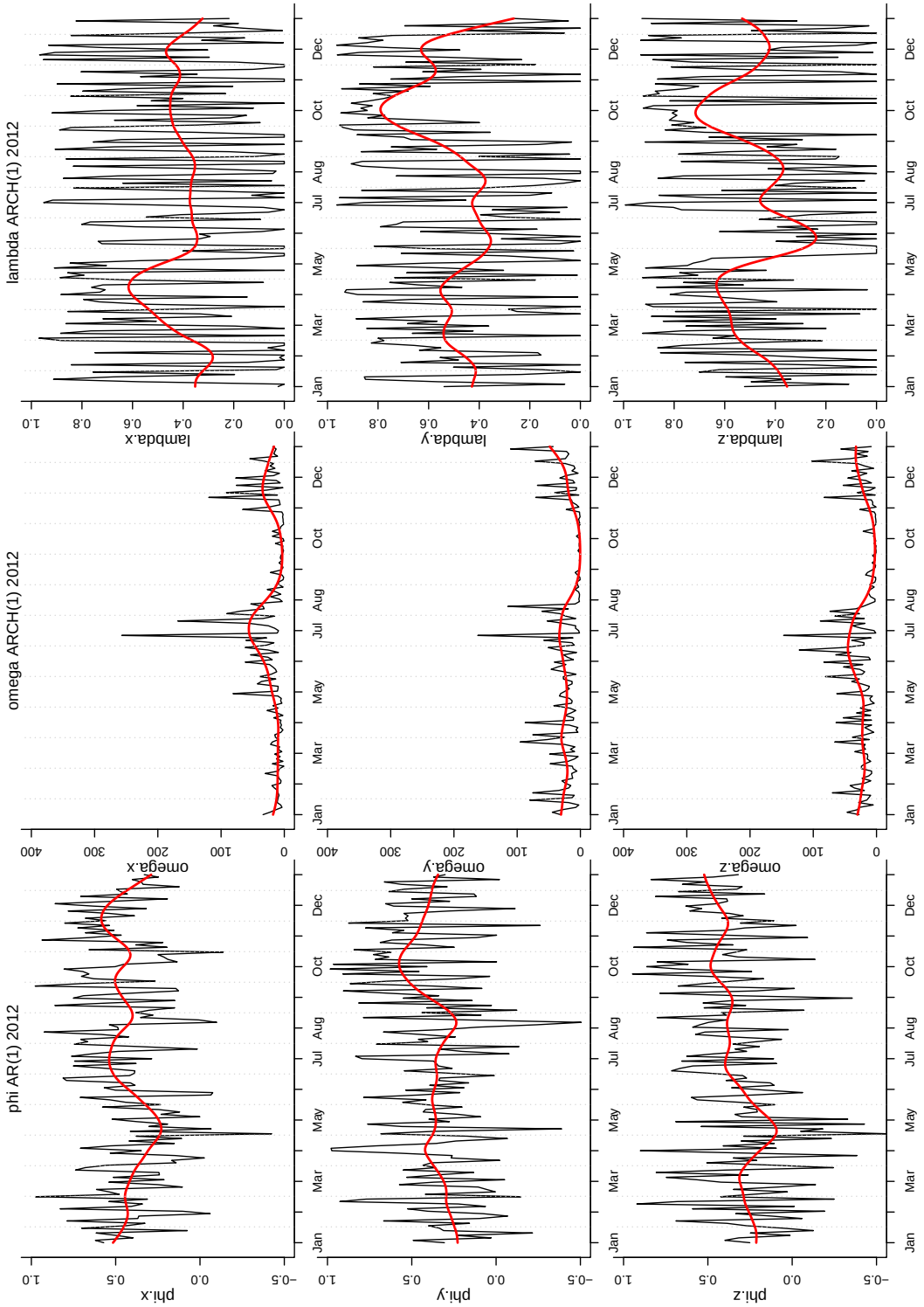

FIGURE 4.17: est ar arch 2012

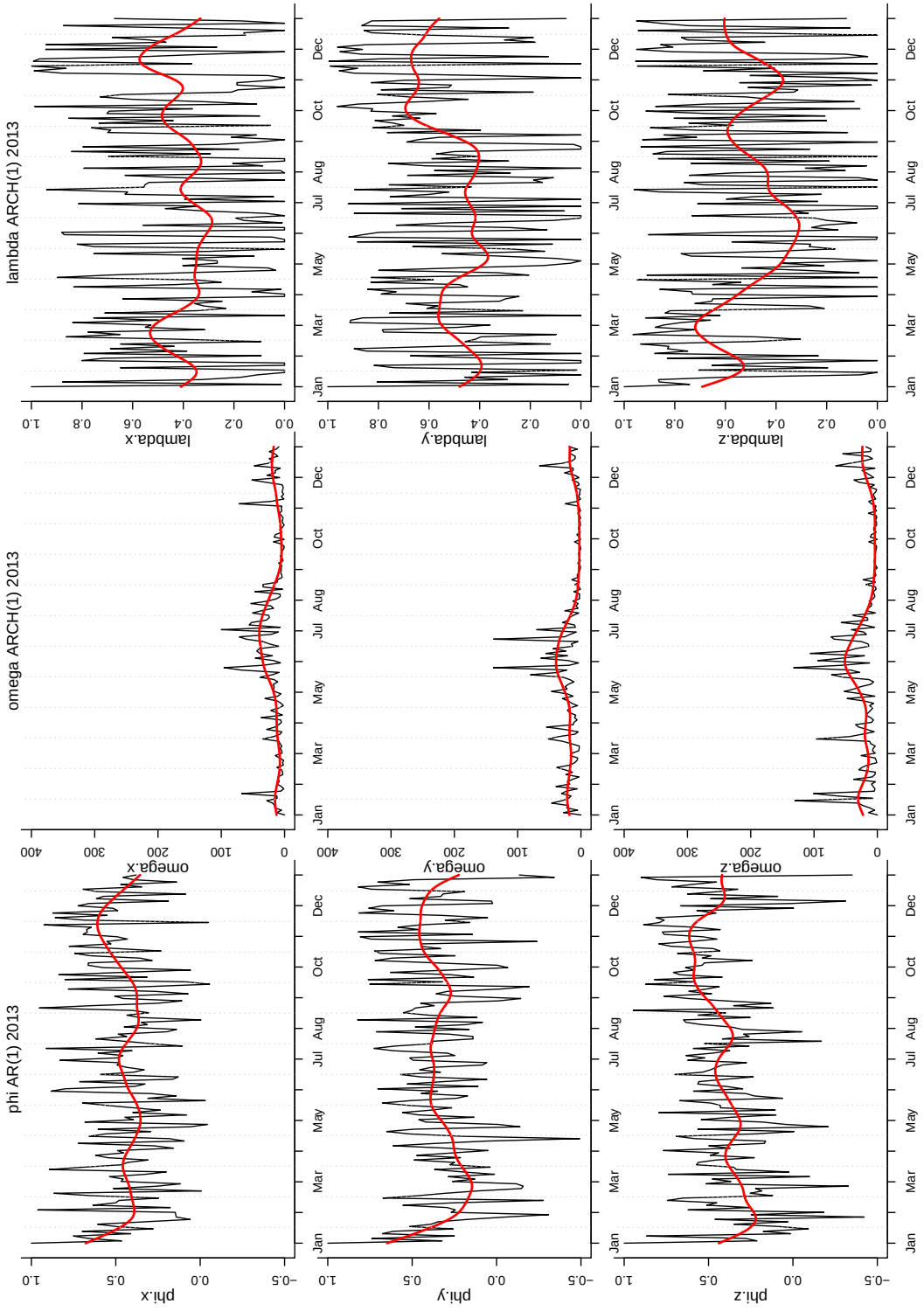

FIGURE 4.18: est ar arch 2013

4.3.2 Understanding the uncertainties in the model calibration

In the previous analysis, we obtain $\{\hat{\mu}_o, \hat{\alpha}_o, \hat{\beta}_o o \in \mathcal{O}\}$, for a single satellite $C \in \{C1, C2, C3, C4\}$ in the component d, $d \in \{x, y, z\}$. To explain the variability in the orbital coefficients and comprehensively assess the calibration of the IGRF and T96 model, we fit mixed-effects models (Pinheiro and Bates, 2000) to $\{\hat{\alpha}_o\}$ and $\{\hat{\beta}_o\}$. Potential fixed effects are the space weather condition, indicated by the orbital max Kp index, i.e. the highest storm level in each orbit, and orbit properties, such as the mean distance from the satellite to the Earth. The satellites and the components are included as random factors.

4.4 Results and discussion

We have developed spatio-temporal statistical models of the near-Earth magnetic field utilising in-situ magnetic field data and physical model outputs. Statistical approaches used include B-spline smoothing to capture the complex mean features, and AR-ARCH models to capture the stochastic model components due to the non-stationary properties of the time series. The physical models, the IGRF and the T96 models representing the internal and external magnetic field, calibrate the observed magnetic field well, however, the statistical properties of the time-series models change across the satellite orbits and the variations in the estimated time-series model parameters have a seasonal pattern. This could be a result of the satellite investigating different regions though out the year.

In the current work, the calibration of the models and measurements as a function of time has been examined. In the first stage, a time-series-based regression model has been developed for the magnetic field data, linking them to the computer model outputs. The parameters in the regression model are estimated using GLS with an unknown variance-covariance matrix. It is assumed that the error term in the regression model has an AR-ARCH structure given the presence of serial correlation and heteroscedasticity in the time-dependent errors. A first order AR-ARCH model has been identified for the error term. Because of missing data in the satellite observations, a maximum likelihood approach is used to deal with the missing data problem. Based on the estimation of AR-ARCH parameters, the variance-covariance matrix of the error term is constructed combining the serial correlation and heteroscedasticity. The GLS estimation then provides the estimates of the regression model parameters and their standard

errors. In the second stage, these estimated regression parameters are then modelled in the mixed-effects models to evaluate the overall performance of the IGRF and the T96 models, based on the time-series-based modelling results. The calibration results show that the reliability of the two models are invariant to satellite and components and the performance of the T96 model the external magnetic field model don't seem to be affected by space weather conditions which are indicated by the Kp indices. Spatial information contained in the satellite orbits are not significant in the mixed-effects model. The internal field is invariant to space weather.

In general, the two models, IGRF and T96, calibrate well with Cluster satellite measurements. IGRF provides more precise prediction for the internal field than T96 does for the external field. However, if one miscalibrates, the other tends to miscalibrate at the same time. The performance of the two physical models appears to be consistent when calibrated with measurements in different components or from different satellites. The calibration of the physical models is affected by where the satellite travels through space and is weakly associated with storm conditions. The T96 model, though not being tested under extreme conditions separately, has been calibrated under time-varying space weather conditions from 2003 to 2013, the time period of which includes a few extreme storm events.

Chapter 5

Detecting magnetic storms in space

The near-Earth magnetic field is being investigated by sensors carried on Earth-orbiting satellites and these satellites provide in-situ observations at regular time-intervals and locations along their trajectory. Real-time magnetic field data provided by the satellite-based sensors, however, are not sufficient for studying the global behaviour of the magnetic field during storm periods, since the current satellite investigations of the near-Earth magnetic field have a limited spatial coverage. This limits our ability to detect storms using satellite data. For studying the behaviour of the near-Earth magnetic field in response to space weather, the data sparsity issue can be addressed by using the T96 model to generate estimates of the external magnetic field at desired times and locations with appropriate space weather parameters. It is reasonable to use the T96 model because the calibration of T96 model against the Cluster satellite measurements in Chapter 4 has proved that the T96 model provides fairly reliable and accurate estimates of the external magnetic field regardless of the space weather condition. The time points and the location vectors input into the T96 model can be constructed so that the process of simulating data from the T96 model mimics the process of collecting data along a satellite orbit. Hence simulating the magnetic field at time-varying locations along arbitrarily defined satellite orbits compensates for the limitation by the space-time constraints in current-flying satellites.

Towards the aim of real-time monitoring of space weather from space-based platforms, we investigate how satellites can be placed in near-Earth space so that the in-situ satellite measurements, i.e. the real-time observations of the magnetic field along the satellite orbits, capture spatio-temporal changes that are relevant to magnetic storms in the near-Earth magnetic field. Large magnetic disturbances as a result of magnetic reconnection and ring current intensification are expected in certain regions of the space during a magnetic storm (see details in Chapter 1). A simulation study is designed and implemented in this chapter to identify probable locations at which magnetic storm features are likely to occur. Given the constraint that satellites are in orbit, and therefore the sampling locations for the near-Earth magnetic field change in time along a prescribed orbital path, we search for satellite orbits along which the magnetic field data obtained as a time series exhibits changes in its statistical properties. For stationary time series, it is common to look for change in mean, variance, or both. This chapter considers the use of online change-point detection methods for recognizing both such changes. Using physical positional constraints that Earth-orbiting satellites must follow, and the characterisation of detectability of storms, we are able to propose network design considerations, which will be included in Chapter 6, for space weather monitoring in terms of early magnetic storm detection.

The chapter begins with an introduction to the magnetic storm detection problem in Section 5.1, and then describes the process of the simulation study for exploring the magnetic storm features along imaginary satellite orbits in Section 5.2. A literature review of change-point detection is provided in Section 5.3 and the methods appropriate for near-Earth magnetic storm detection are given in Section 5.4. Application of the change-point methods on the magnetic field data collected along satellite orbits is included in Section 5.5. Results of the applications are summarized and discussed in Section 5.6.

5.1 Introduction

As introduced in Chapter 1, space weather describes the environmental conditions in space determined by plasma physics and solar process, Magnetic storms are one of the most important space weather phenomena and characterized as large-scale electromagnetic disturbances in the near-Earth space environment. Magnetic storms may damage

satellites and sensitive technology systems, so early detection is an important step in mitigating their effects.

The aim in this chapter is to extract storm patterns from time series magnetic field data generated from the T96 model and to apply appropriate change-point detection methods for recognizing the storms in the near-Earth magnetic field. We first simulate the near-Earth magnetic field under storm and quiet conditions using the T96 model, given that the T96 model provides reliable estimates of the external magnetic field under both conditions. It has been understood that the dynamic processes in the external magnetic field are associated with space weather conditions, and the external magnetic field would become highly disturbed at specified and localized regions, such as in the magnetotail, at the boundary of the magnetosphere, and in the ring current regions, when a magnetic storm happens. Earth-orbiting satellites sample the near-Earth magnetic field along their trajectories, and provide sensor-based monitoring of the near-Earth magnetic field environment. Time series magnetic field data from satellites can be used to identify if a magnetic storm is in progress. Satellite orbits that cross different regions of space are emulated through manipulating orbital parameters, and in-situ magnetic field data are obtained from T96 model estimates of the external magnetic field along these satellite orbits, under quiet and storm space weather conditions. We process the model magnetic field data under storm and quiet conditions, extracting time series magnetic field data that contain space weather information, and consider magnetic storms, the episodes when the magnetic field behaviour changes considerably over time, as qualitatively significant change in space weather. Thus the problem is to identity the time points at which magnetic storm behaviour occurs and whether the changes are significant. Such kind of problem has been referred to as the *change-point detection* problem in the statistics literature (Antoch and Jarušková, 2000, Guralnik and Srivastava, 1999). Specifically speaking, our problem is to detect magnetic storms that evolve in the near-Earth space environment, from time series magnetic field data sampled sparsely from restricted locations.

The storm detection problem can be decomposed into three questions,

1. to understand the dynamics of the magnetic storms in the external magnetic field and to identify orbits along which, when sampling the magnetic field along these orbits, we can pick up the magnetic storm signal;

2. to summarize the changes in the time series magnetic field data generated along selected satellite orbits and to consider appropriate change-point detection methods for recognizing the changes in the near-Earth magnetic field along the satellite orbits;

3. to apply prospective detection algorithms to the simulated spatio-temporal magnetic field data with the goal of identifying the storm onset as accurately and quickly as possible.

Each of the above question will be addressed in the following sections accordingly. Question 1 will be answered in the simulation study of the external magnetic field in Section 5.2. Question 2 will be discussed in Section 5.4, preceded by a review of change-point methods in Section 5.3. The review provides a statistical framework for performing change-point detection in two settings, namely using the *batch* detection method and the *sequential* detection method. In batch detection, the dataset for the entire observational time period is available whereas in sequential detection, new observations will be received one at a time. Question 3 will be investigated in Section 5.5 through comparing the results of change-point detection with different approaches based on sensible criteria. Summary of the chapter in Section 5.6 will include:

1. types of satellite orbits that are likely to capture the storm-time behaviour in the external magnetic field;

2. typical features of the storm-time behaviours as observed along the satellite orbits;

3. a discussion of detection methods for recognizing the changes in the external magnetic field along the satellite orbits and their application on simulated and real magnetic field data.

5.2 Simulation study on the external magnetic field

It has been explained in Chapter 2 that the magnetic field in near-Earth space can be viewed as the sum of an internal magnetic field and an external magnetic field, with the former being invariant to solar sources and the latter answering to the solar-terrestrial interaction. Space weather is engendered by the solar-terrestrial interaction

in the external magnetic field and conditions of space weather, either being stormy or quiet, can be characterized through the behaviour of the external magnetic field. Hence understanding the storm-time behaviour of the external magnetic field is a crucial step in detecting magnetic storms in near-Earth space.

This section focuses on extracting the storm patterns of the external magnetic field using the T96 model. The T96 model, as introduced and calibrated in Chapter 2 and 4, is a physics-based empirical model that produces reliable estimates of the external magnetic field given real-time space weather parameters. The space weather parameters used in the T96 model include observations of the solar wind and the magnetic field in interplanetary space and the storm-disturbance level on the surface of the Earth. The solar-wind ram pressures and the y- and the z-components of the IMF, measured by satellites, together with the Dst index derived from ground-based observatories, parametrize the T96 model for constructing the external magnetic field based on physical equations and past observations in near-Earth space. We reconstruct the external magnetic field under selected magnetic storm events to visualise the spatio-temporal variations in the external magnetic field.

5.2.1 Global simulation

We start with a global simulation of the T96 model under five pre-defined storm events on a global scale; i.e. near-Earth space encompassing most of the Earth's magnetosphere. The five events are major magnetic storms that occurred from 2003 to 2005. In 2003, there were two storms in May and October, lasting from 4 to 8 days. The simulation results of all these events look similar in terms of the external magnetic field variations and an example of the 2003 May storm is presented in Figure 5.1 and 5.2. These figures provide the magnetospheric configurations at different time points, i.e. by displaying time-varying contour plots of the z-component of the external magnetic field on the x-y plane in the GSM coordinates frame.

Figure 5.1 shows the contrast between the field configuration at one time point before the onset of the storm (bottom left panel) and the field configuration at another time point when the storm is in progress (bottom right panel). The time points at which the two field were simulated are indicated by the vertical lines in the time plots of the space weather parameters shown on the top panels. The top three panels on the left

and right columns show the time plots of the T96 model input parameters, the Dst index, the y- and z- components of the IMF, and the solar wind ram pressure. These parameters become disturbed and the Dst index in the top panels drops below -100 when the main phase of the magnetic storm starts. Figure 5.2 shows the gradual changes in the field configuration over the x-y plane throughout the entire storm period. Each panel corresponds to a time point and the time point increases by hour. The panels are arranged in time order from left to right and then top to bottom.

The contour plots in Figure 5.1 and 5.2 have the same resolution and scale. The x-axis ranges from -35 to 15 r_E and the y-axis ranges from -25 to 25 r_E. The x-y plane was chosen to cover the magnetopause and part of the magnetotail, and the magnetotail extends to over 100 r_E. The Earth, which is not shown on the plots, should sit at the place where the vertical and horizontal dashed lines intersect. The boundary of the magnetosphere is visible in each panel, and the magnetospheric configuration changes throughout the storm periods. The stand-off position, i.e. the distance between the boundary at the magnetopause on the day-side and the centre of the Earth, ranges from about 6 to 10 r_E. The magnetopause stand-off distance is important as it determines the size of the magnetosphere. The problem of identifying the location of the magnetopause was briefly reviewed by Pudovkin et al. (1998). The T96 model attributed the Earthward displacement of the magnetopause to variations of magnetospheric currents rather than simply the solar wind pressure and the southward IMF, which trigger magnetic reconnection at the magnetopause and subsequently erode the magnetic field on the day-side (Tsyganenko and Sibeck, 1994, Tsyganenko and Stern, 1996b).

The comparison of the before-storm and the storm-time configurations in Figure 5.1 shows that the magnetosphere gets compressed and the ring current region, as indicated by the blue area between 3 and 5 r_E, becomes distinct, during the magnetic storms. The hourly configuration in Figure 5.1 reveals the spatial variations of the storm process. Similar patterns have been obtain for other storm periods, and hence the description given above is considered as typical storm-behaviours in the external magnetic field. This suggests that magnetic storms are more likely to be recognized in the ring current regions.

We also investigated what happens in the external magnetic field when the space weather condition is absolutely quiet. The absolute quiet condition is defined as when the space

weather parameters have constant values close to those of the average quiet condition over a time period. We fix the space weather input parameters in the T96 model to their annual average, since storms rarely occur and the space weather condition is quiet for most of the year, and simulate the external magnetic field with these fixed parameters for an extended time period. The external magnetic field appears steady in the GSM coordinate frame under absolute quiet conditions, since fixed input parameters generate fixed output from the T96 model. In other words, the only magnetic field variation in simulation study that we present in this chapter come from the variation in the space weather parameters.

Running the T96 model simulation with real-time space weather parameters for extended time periods shows that there are variations in the external magnetic field during time periods which are not characterized as major storms. Major storms, as mentioned in Chapter 1, are indicated by the Kp index greater than 8 or the Dst index less than -100. These two selection criteria (Kp or Dst index) can be used interchangeably as they identify the same major storms. The non-storm variations in the external magnetic field do not appear to be as distinct as storm-time variations, i.e. there are no strong variations in the ring current regions, but the regions are still recognizable from the changing boundary of the magnetosphere. All these external field variations are responses to the input space weather parameters and so the minor variation are probably related to substorms rather than major geomagnetic storms, since disturbances in the field have multi-scale features. The occurrence of sub-storms is thought to be independent from the occurrence of magnetic storm, however, the substorms are more frequent and stronger during the main phase of magnetic storms.

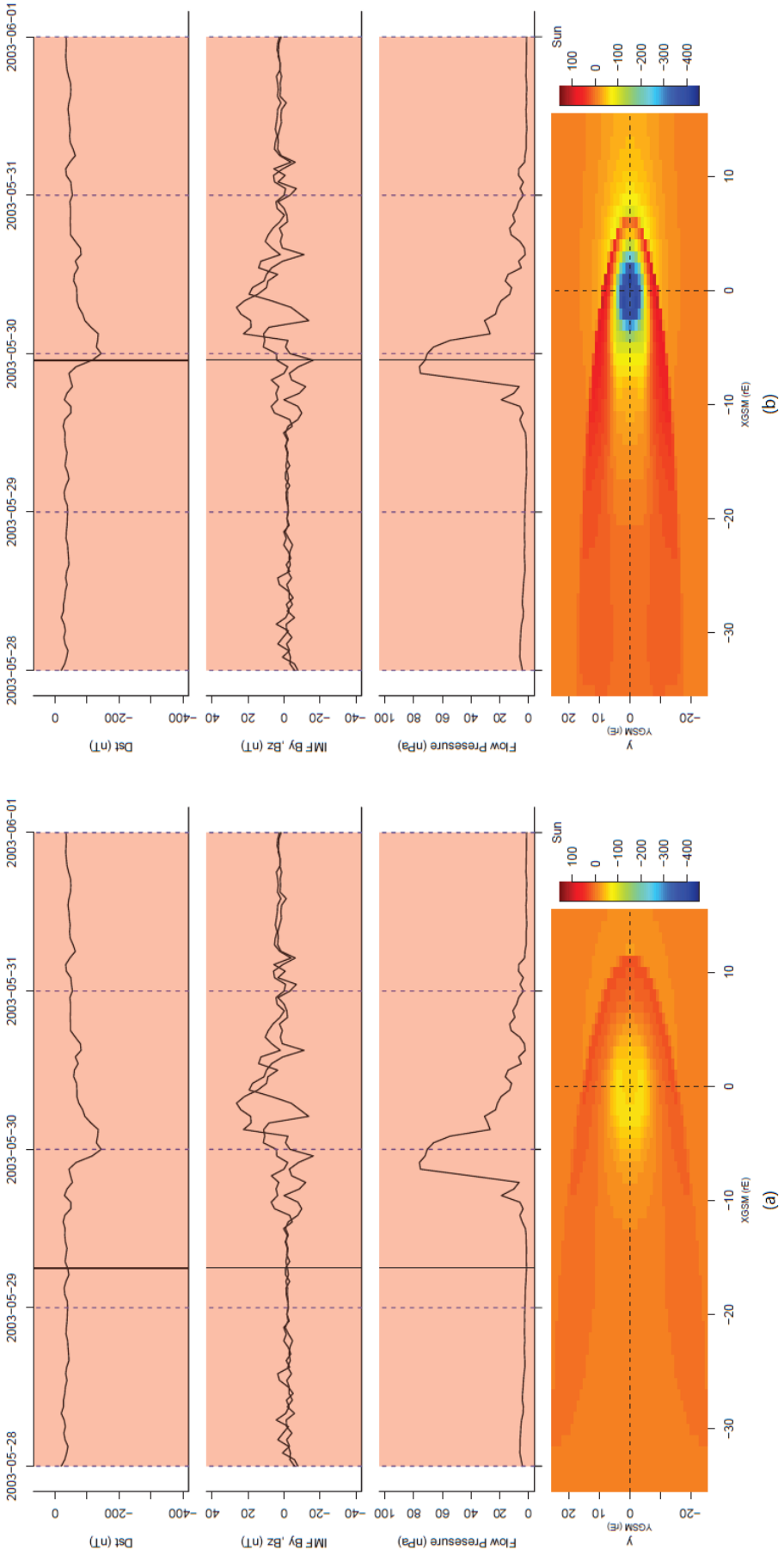

FIGURE 5.1: T96 model simulation during the May 2003 storm, contrasting of the magnetospheric configurations at two time points corresponding to the vertical black lines. The colour scale in the lower panels in the strength of the external magnetic field in the z-component (nT).

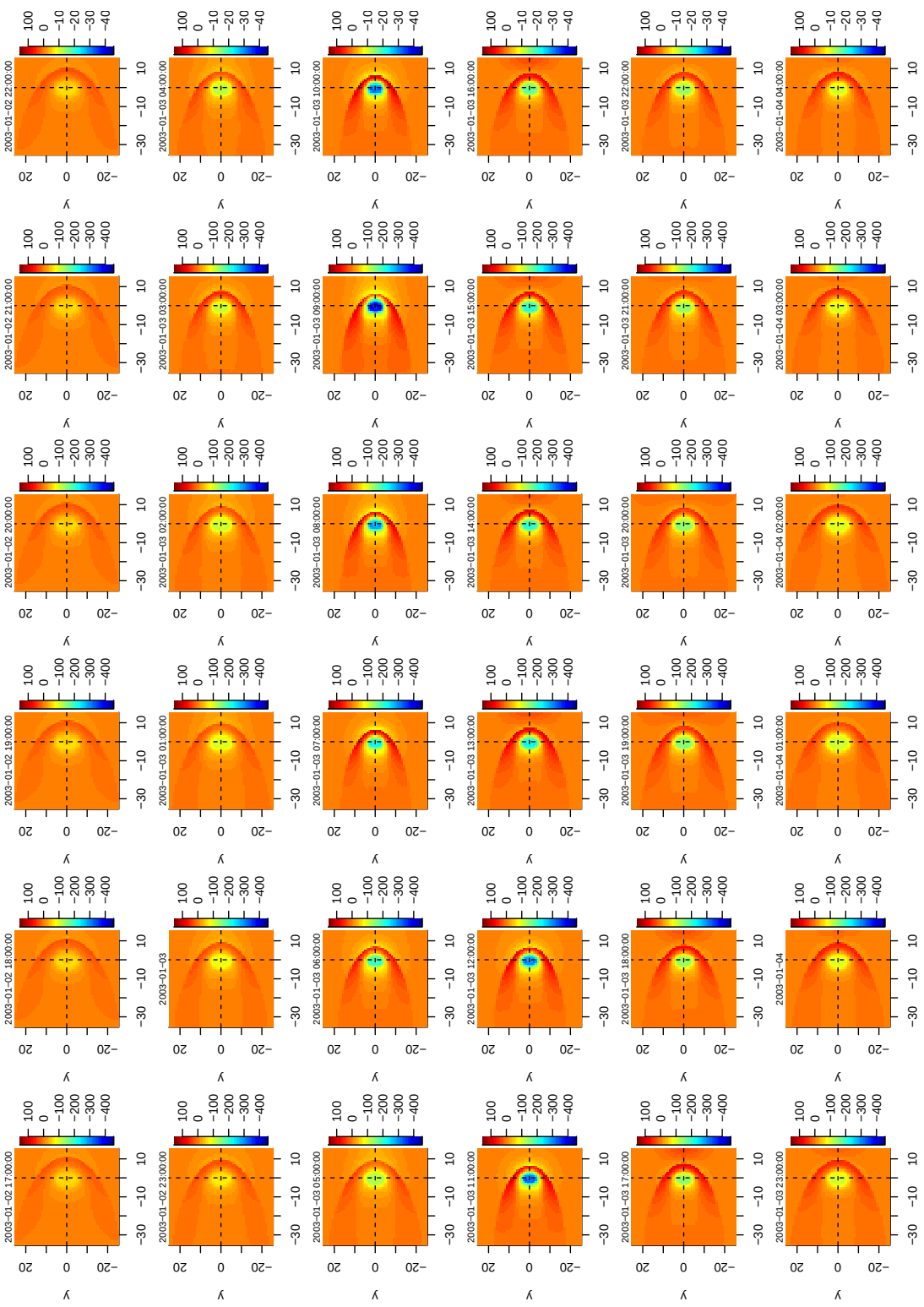

FIGURE 5.2: T96 model simulation during the May 2003 storm, showing gradual changes in the spatial distribution of the external magnetic field throughout the storm period.

5.2.2 Orbital simulation

Space weather monitoring differs from other environmental monitoring problems in that the magnetic field monitoring sensors, instead of being placed at fixed locations, are carried by Earth-orbiting satellites. So far there are a limited number of satellites that carry magnetic field sensors and the satellites are investigating a small fraction of space, hence the time series arising from the in-situ satellite measurements of the magnetic field are not enough for us to study in any detail the time-varying behaviour of the magnetic field across different regions of space. Therefore estimates of the external magnetic field, produced along various satellite orbits from the T96 model, substitute for real-time satellite observations. Generating T96 model outputs along feasible satellite orbits under pre-defined magnetic storm periods allows us to extract storm patterns along these orbits.

An elliptical satellite orbit can be determined by five orbital parameters, a the semi-major axis, e the eccentricity, and three angular parameters that define the orientation of the orbital plane in the reference frame, namely i inclination, Ω longitude of the ascending node, and ω argument of periapsis. We first use the a and e to determine the size and shape of the orbits in a 2-D plane, with the restriction $0 < e < 1$ and then through a rotation matrix with the angular parameters we convert the 2-D orbit to 3-D orbit in the Geocentric Inertial GEI system. The position vector of a satellite at time t within an orbit parametrized by the five orbital elements can be derived from a set of equations. These equations define a position along an orbit through three anomalies.

The three anomalies include the *true anomaly* θ denoting the angle between the position vector of the satellite and the position vector at perigee, the *mean anomaly* M given by the constant angular speed, and an auxiliary parameter referred to as the *eccentricity anomaly* E (Tsui, 2005). The mean anomaly M can be calculated by the formula $M = n(t - t_0)$, where n denotes the angular speed required for a satellite to complete one orbit ($n = \frac{2\pi}{T}$ where T is the orbital period) and t_0 denotes the initial time. Kepler's Equation 5.1 relates the mean anomaly M to the eccentric anomaly E,

$$M = E - e \sin E, \tag{5.1}$$

where e is the eccentricity. Since this equation does not have a closed-form solution for E given M, the eccentric anomaly E is usually solved by numerical methods such as the Newton-Raphson method (Curtis, 2013). The true anomaly θ and the eccentric anomaly E are related in Equation 5.2,

$$\cos\theta = \frac{\cos E - e}{1 - e\cos E}. \tag{5.2}$$

Figure 5.3 shows an example of the relationship among the three anomalies, as a function of the time in hours from the perigee, in a particular orbit.

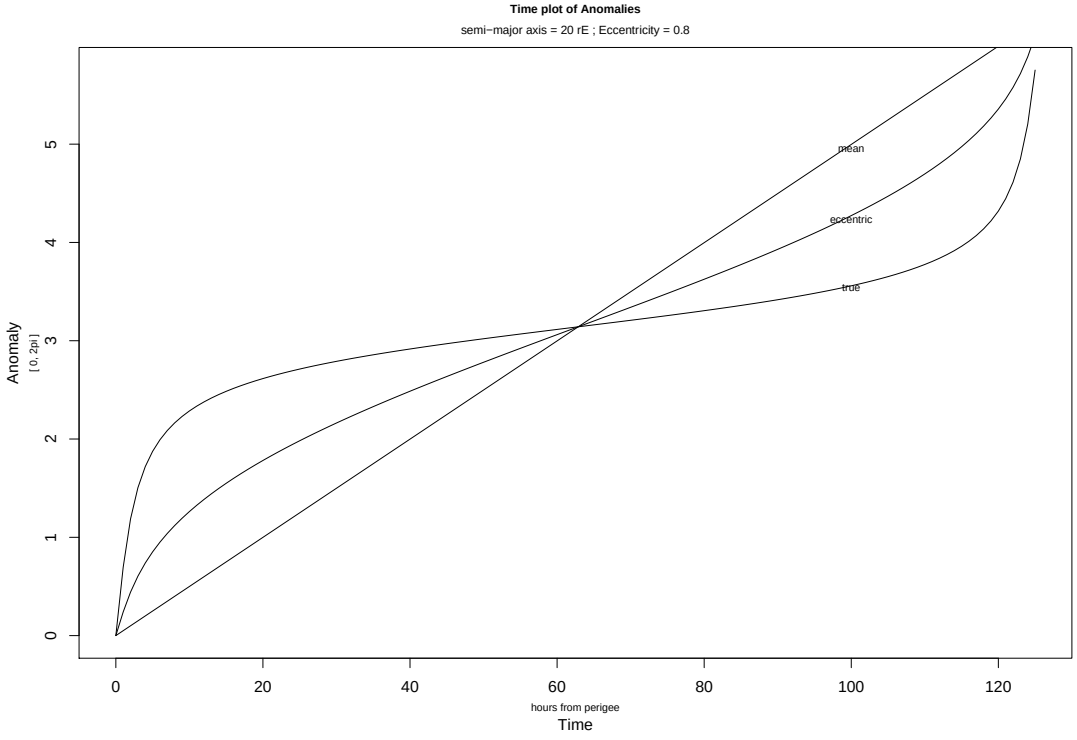

FIGURE 5.3: Time plots of the anomalies

An orbit must have a perigee altitude greater than the Earth radius plus the atmosphere (7380 km) and an apogee altitude less the Earth-Moon distance (384, 000 km), thus constraining the values of a and e. In the emulation, we choose a from (1.16, 60) r_E, with the interval of 3 r_E, and e from (0, 1) in steps of 0.1, then run the test for orbital constraints with all possible combination of a and e, and finally end up with 127 2-D orbits. Figure 5.5 shows an example of 16 orbits with different a and e. The black dots represent the positions at a time interval of one hour and the red dots track the position

of the satellites in these orbits. Panel (a) shows the initial positions, as indicated by the red dots, of 16 satellites in the 16 orbits and Panel (b) shows the satellite positions after several hours. The two panels confirm that satellites are moving on different path in different orbits. The bottom panel of each plot with high eccentricities, $e = 0.6$ or 0.8, shows that the hourly sampling is more sparse in space around the perigee, as satellite moves faster at perigee.

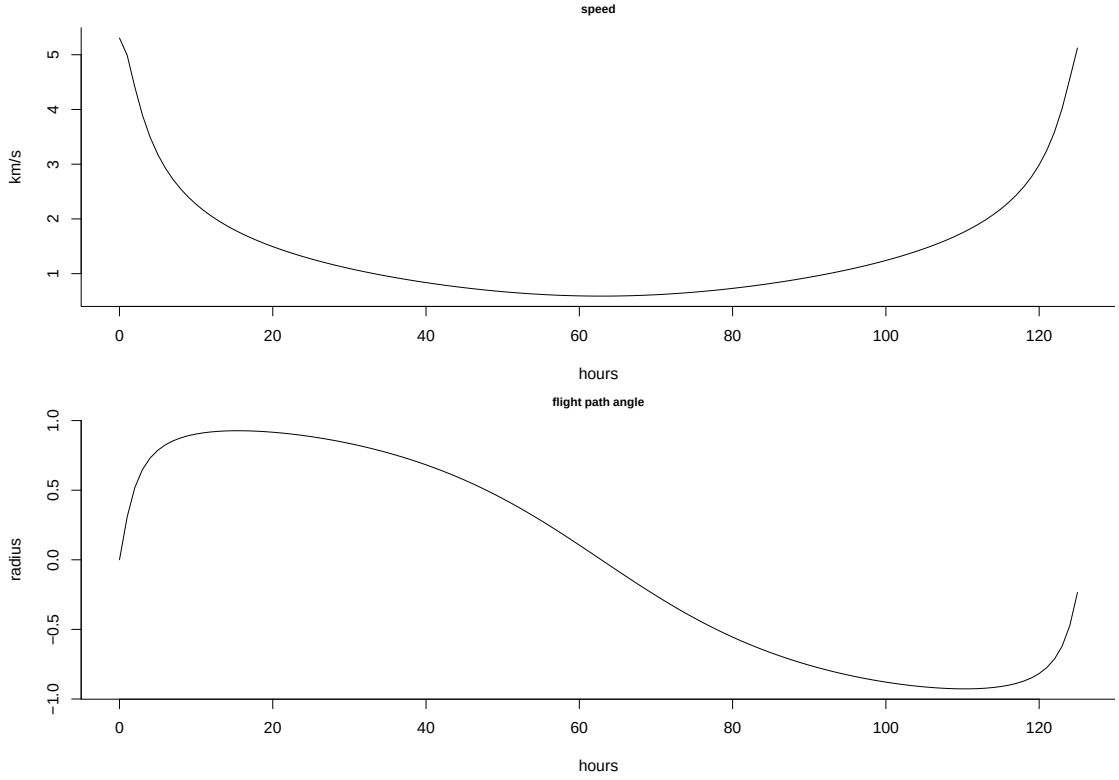

FIGURE 5.4: Plots of the speed and the flight path angle of a satellite with a particular satellite orbit with $a = 20r_E$ and $e = 0.8$ as a function of time.

Figure 5.4 plots the speed and the flight path angle, (i.e. the angle between horizontal and the velocity vector for describing whether the satellite is ascending or descending), of a single satellite with $a = 20r_E$ and $e = 0.8$ against time for over an orbital period. This demonstrates that the speed and the flight path angle are not constant in time.

The 127 orbits are converted into 3-D GEI system by a rotation matrix. The three angular parameters can vary from (0, 2π) and each takes the values of 0, $\frac{2\pi}{3}$, $\frac{4\pi}{3}$. The selection of angular parameters roughly split the space into a few quadrants. Further analysis will take more values in quadrant of interests. With the rotation, there are $127 \times 27 = 3429$ different orbits.

Given time, position, and space weather parameters, we simulate the magnetic field along each orbit in the GSM system. T96 model outputs are obtained as time series data for each orbit. The T96 model is simulated under both real storm condition with time-varying space-weather input parameters and averaged quiet condition with fixed space-weather input parameters to allow comparison of storm and non-storm conditions. The internal field IGRF model is not in use for analysing magnetic storm features since the IGRF model is invariant to space weather condition. If given real-time satellite observations, this invariance can be handled by subtracting the IGRF outputs the from the observed magnetic field data, since Chapter 4 showed that IGRF model provides accurate and reliable estimates of the internal magnetic field. Hence removing the contribution from the internal magnetic field from the total magnetic field allows us to focus on variations in the external magnetic field for the detection of magnetic storms.

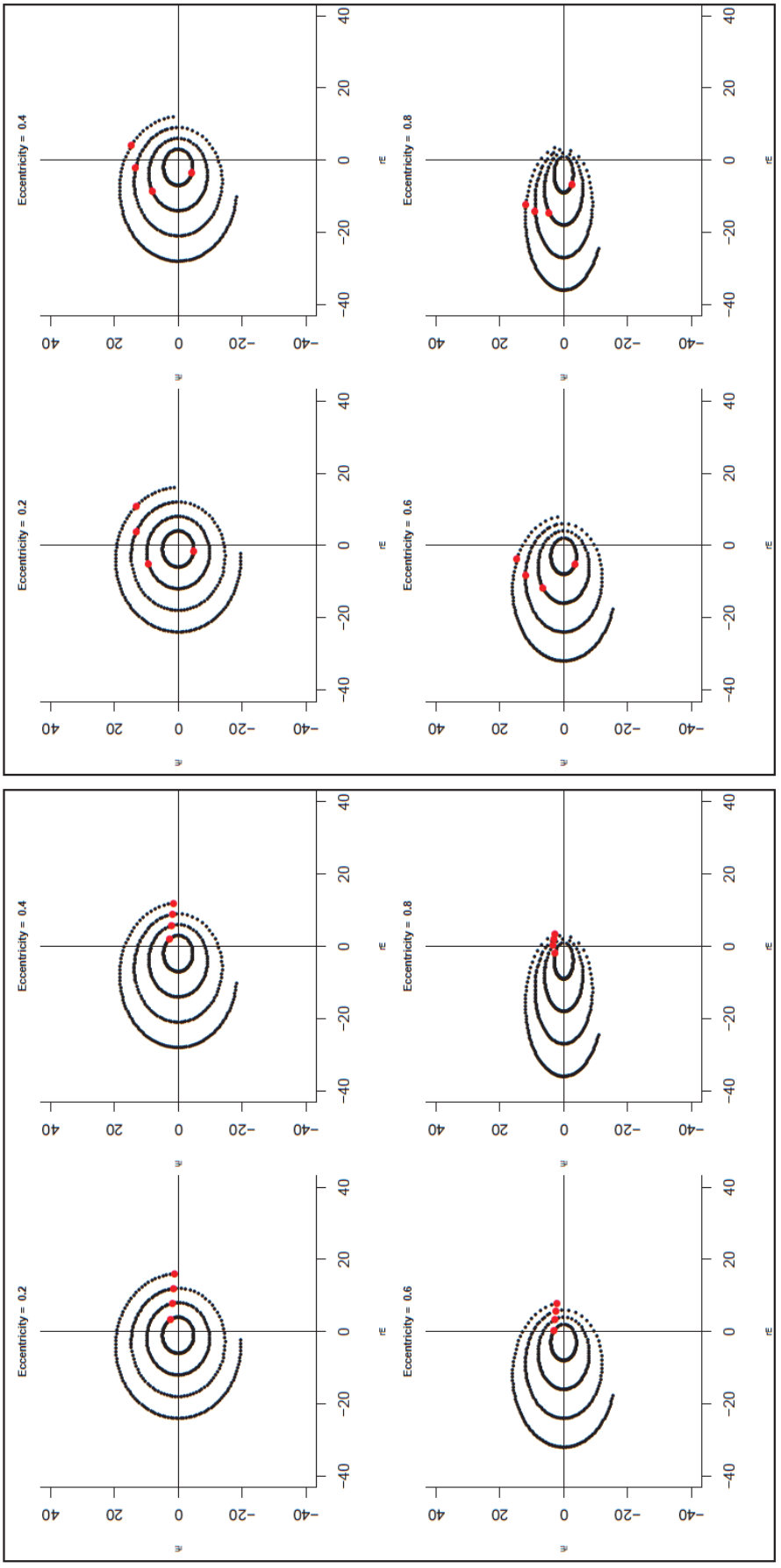

FIGURE 5.5: Some example orbits in 2-D space for different values of eccentricity and semi-major axis. Panel (a) and (b) show positions of satellites as indicated by red dots along each orbit at the initial and the other time points.

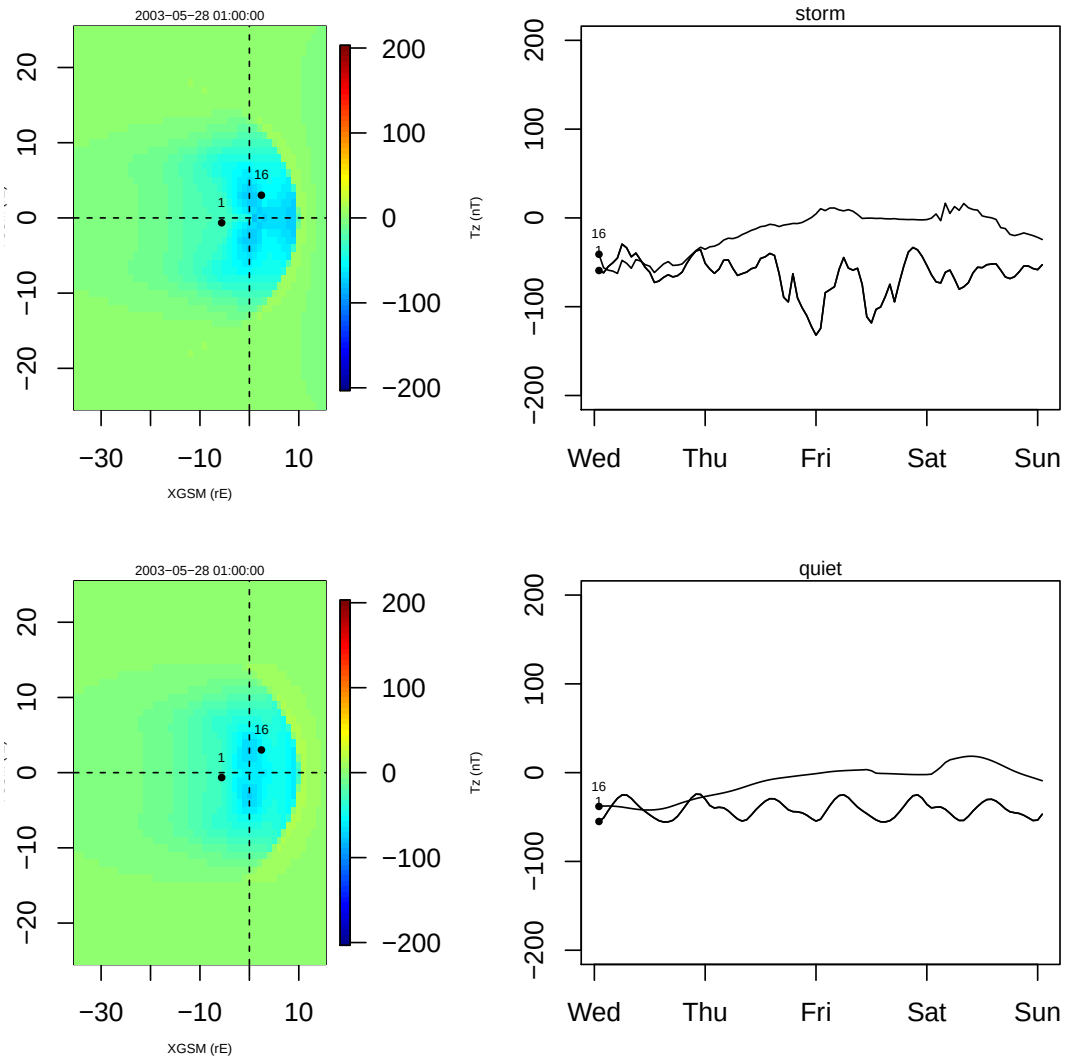

FIGURE 5.6: T96 model simulation along satellite orbits. The left panels provide contour plots of the magnetic field strength of the z-component on the GSM x-y plane. The right panels provide time plots of the z-component field strength as obtained along two orbits labelled as 1 and 16. The starting positions of the two orbits are indicated by the black dots in the contour plots. The top and the bottom panels contrast the T96 outputs, in both the contour and the time plots, generated under storm and quiet conditions.

Figure 5.6 left panels show snapshots of T96 model z-component under real storm (top) and quiet (bottom) conditions and right panels give time plots of T96 z-component along two orbits, with real on top and quiet at the bottom. It can be observed that under quiet condition (bottom panels), there are cyclic patterns in the time series of the z-component of the T96 model outputs as introduced by the motion of sampling. The data simulated under the real storm condition (top panels) is more disturbed compared to the data simulated under the averaged quiet condition.

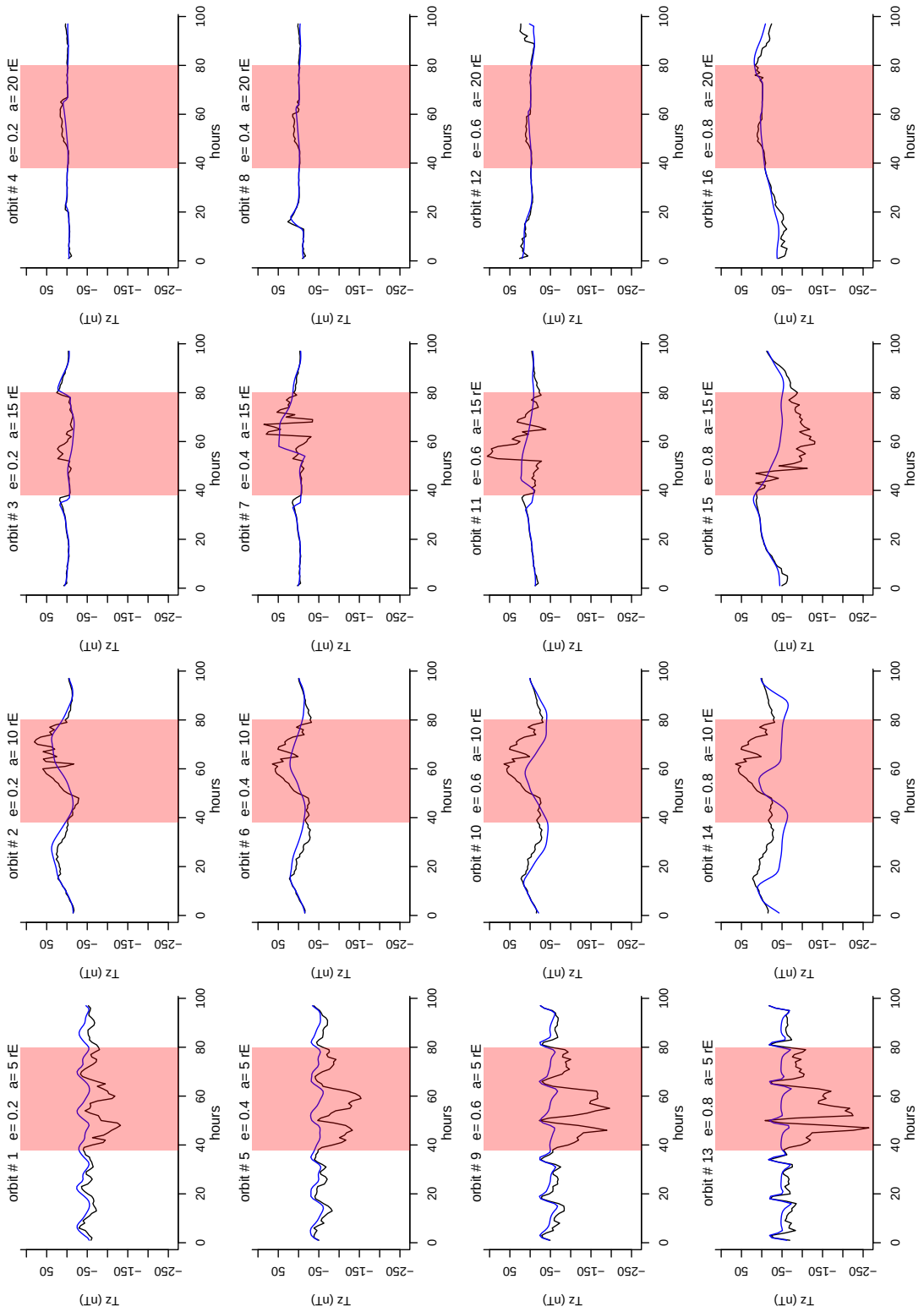

FIGURE 5.7: Time series magnetic field data (the z-component) simulated along orbits with different sizes and shape. The black and blue curves show the T96 outputs under real storm and averaged quiet conditions. The shaded areas denote the time the storm being observed on Earth.

Figure 5.7 shows more time plots of the magnetic field data simulated along different satellite orbits under the real storm and averaged quiet condition. The black line represents the magnetic field data under the real storm condition and the blue line represents the magnetic field data under the quiet condition. The shaded regions show the time span of the magnetic storm, as defined by the geomagnetic indices Kp and Dst. The sixteen orbits have the same angular parameters but different size and shapes. The values of the eccentricity e and the semi-major axis a are added on top of each plot. In the right column when $a = 20r_E$, the black lines and the blue lines overlap. This suggest the storm data does not deviate significantly from the quiet data along these orbits. In other columns when $a = 5, 10, 15r_E$, the black lines deviate from the blue lines in the shadowed regions, however, the pattern differs when the distance from the satellite to the Earth increases. In the left column when $a = 5r_E$, there are cyclic patterns in the magnetic field data. This is because when the semi-major axis of the orbit is small the orbital period that depends on the semi-major axis shortens so that the satellite orbits around the same regions repeatedly during the storm time. The eccentricity e also has a slight effect on the magnetic field data comparing the time series patterns in each rows.

Figure 5.8 provides the time plots of the difference between the storm magnetic field data and the quiet magnetic field data. The time series represents the deviation of the magnetic field from its quiet status as sampled along the orbits.

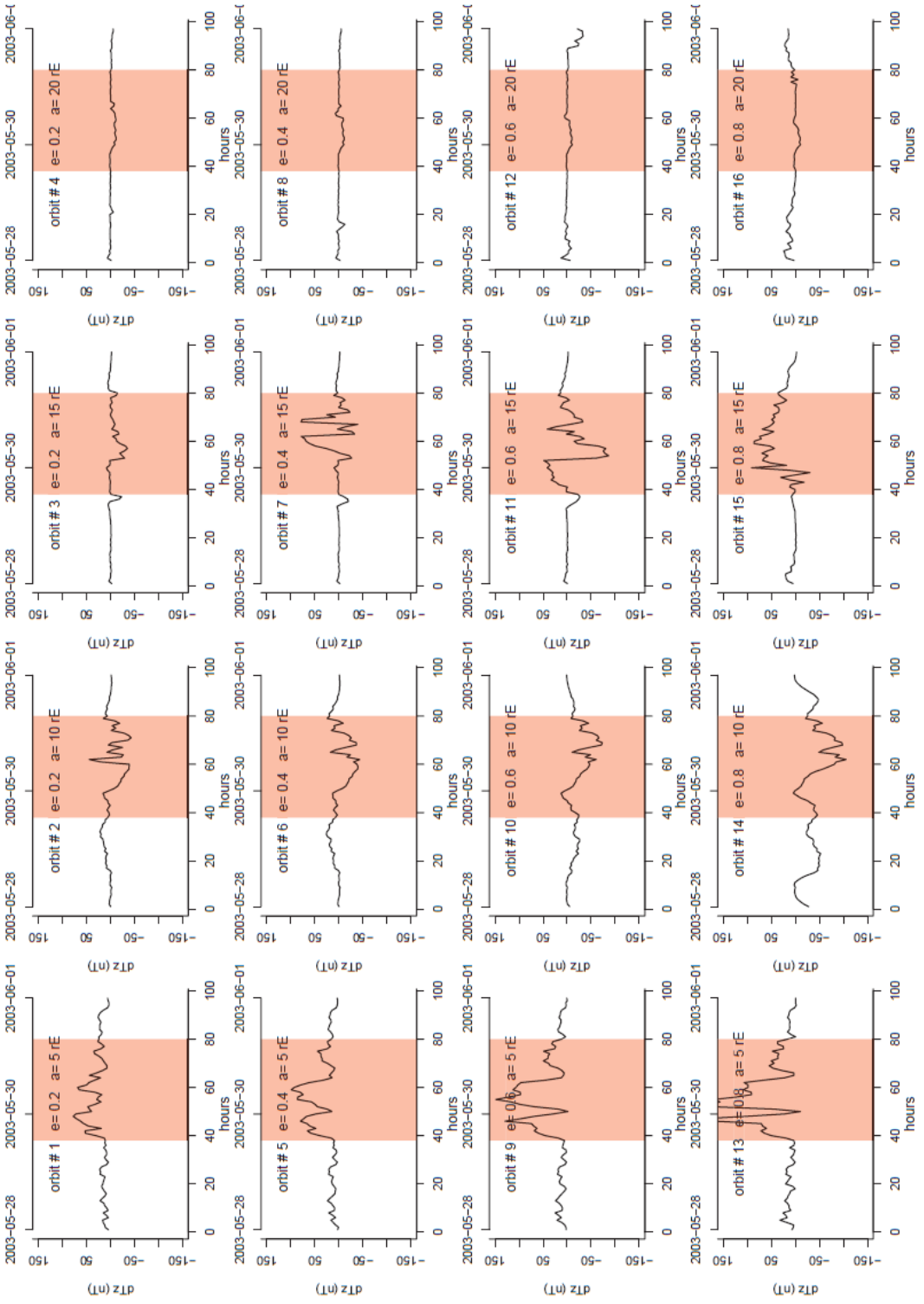

FIGURE 5.8: The difference between the storm and the quiet magnetic field data in the z-component along satellite orbits with different values of the semi-major axis a and the eccentricity e as a function of time.

We extend our study of the time series patterns to the magnetic field data along the satellite orbits with different angular parameters, and then summarize the storm features along different orbits. It has been found that the magnetic storm pattern along equatorial satellites orbits, i.e. orbits whose inclination with respect to the equatorial plane is nearly zero, is more obvious than the polar orbits, i.e. orbits in which a satellite passes above or nearly above both poles of the Earth. This could be explained by the facts that the ring current sits in the equatorial region and the storm effects on the magnetic field mostly comes from the intensification of the ring current. Hence sampling along equatorial orbits capture the storm signal better than sampling along the polar orbits.

5.2.3 Summary of storm features in the external field

We now summarize the simulation process from the T96 model. Estimates of the external magnetic field can be generated by the T96 model given a time point, a location vector and a collection of input space weather parameters. In our simulation, we take the annual average of the space weather parameters as the inputs for the T96 model to generated estimates of the external field under quiet space weather condition.

Since the external magnetic field $\mathbf{B}_E$ responds to the time-varying space weather conditions and appears steady in the GSM frame under quiet conditions, we expect to see disturbances in $\mathbf{B}_E$ that reflect changes in the space weather condition. It is known that disturbances in $\mathbf{B}_E$ have multi-scale features and are direct results of global magnetic reconnection and the ring current intensification, which happens both in magnetic storms and sub-storm. Estimates of $\mathbf{B}_E$ can be produced from the Tsyganenko model given a number of parameters. Let t denote the time in hours, $\mathbf{s}$ denote the position vector in the GSM frame, and $\mathcal{O}$ denote the orbital function that governs the motion of the sampling and maps the time to the space, $\mathbf{s} = \mathcal{O}(t)$. The two sets of space weather parameters are the real-time condition $\boldsymbol{\theta}_t$ and the average-quiet condition $\bar{\boldsymbol{\theta}}$.

Along each orbit $\mathcal{O}$ at time t, we obtain

$$d\mathbf{B}_t = \mathbf{B}_E(t, \mathcal{O}(t), \boldsymbol{\theta}_t) - \mathbf{B}_E(t, \mathcal{O}(t), \bar{\boldsymbol{\theta}}),$$

where $d\mathbf{B}_t$ denotes the deviation of the external magnetic field under real condition from the field under averaged quiet condition at time t and at location $\mathcal{O}(t)$. $d\mathbf{B}_t =$

$\{dBx_t, dBy_t, dBz_t\}$ the magnetic field data are vectors that have three components in the GSM frame, and each component is a univariate time series of magnetic field strengths deviations in the x-, y- or z-components.

We manipulate the orbital function $\mathcal{O}$ through changing the orbital parameters in the trajectory equation so that the external magnetic field is sampled along the orbits in various different regions. The angular parameters in the orbital function were chosen to attain equatorial orbits, and the eccentricity is set to be around 0.8 so that the orbits are not highly elliptical. Then we compare storm features along satellite orbits that have different semi-major axes. Figure 5.9 shows the typical behaviour of the orbital storm features when sampling along relatively low orbits ($a = 5\ r_E$). Time plots of dBx, dBy, dBz are given for two storm periods. The left column shows the plots in the 2003 May storm and the right column shows the plots in the 2003 Oct storm. Figure 5.10 shows the orbital storm features when $a = 10\ r_E$ and Figure 5.11 shows the the features when $a = 15\ r_E$.

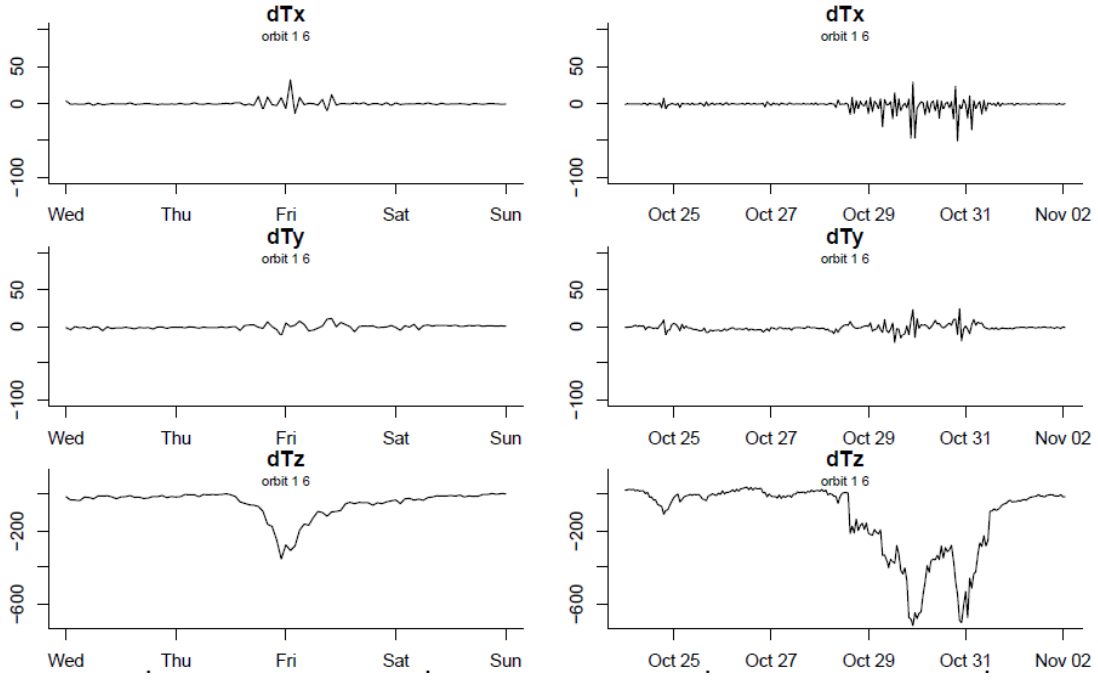

FIGURE 5.9: Time plot of dBx, dBy, dBz in two storm periods along orbits with $a = 5$ r_E. Units of the y-axis are nT.

These plots suggest that the storm features of the two storms are along the same orbits in the same components. The level of disturbances in the 2003 Oct storm is higher than that of the 2003 May storm, and the changes in the 2003 Oct storm time series signals

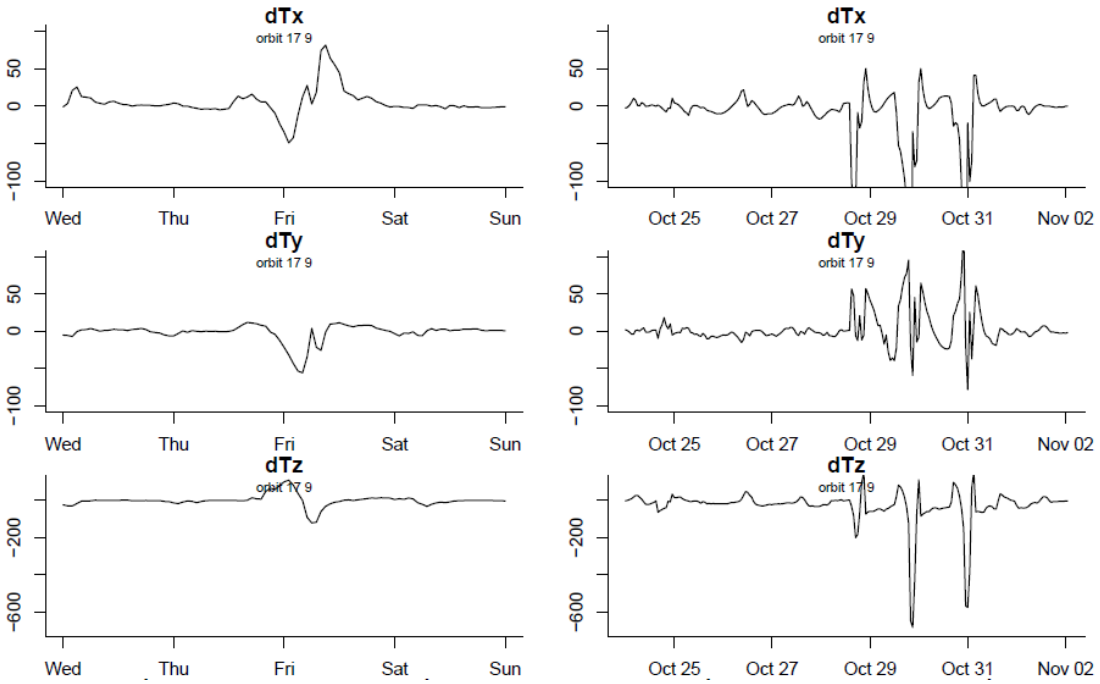

FIGURE 5.10: Time plot of dBx, dBy, dBz in two storm periods along orbits with $a = 10\ r_E$

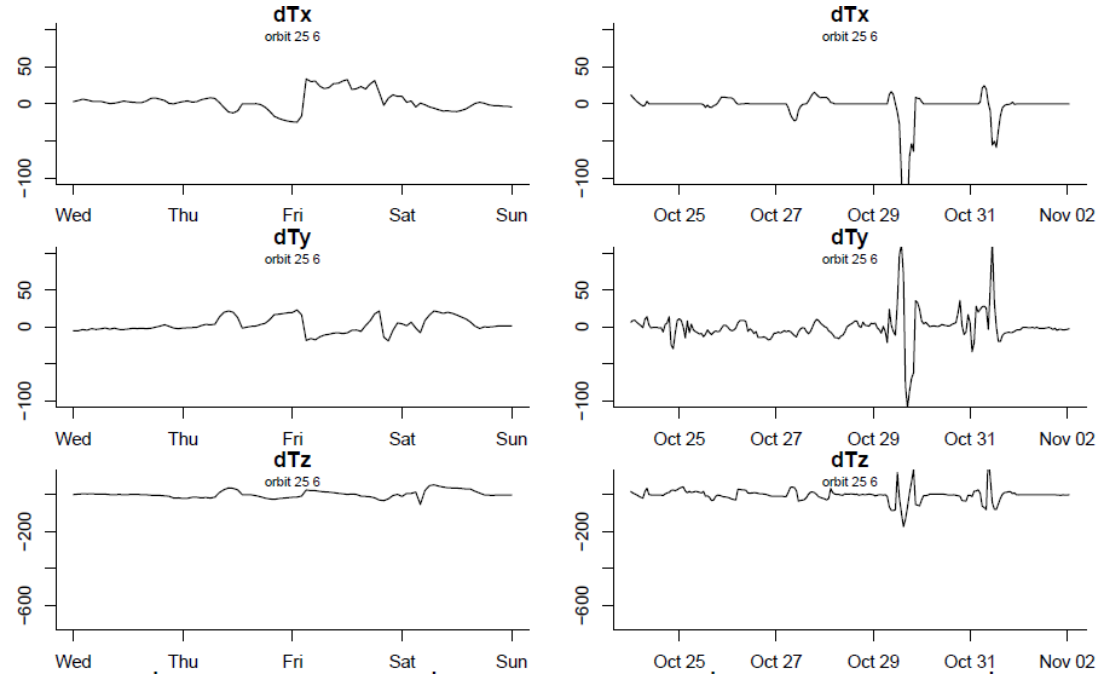

FIGURE 5.11: Time plot of dBx, dBy, dBz in two storm periods along orbits with $a = 15\ r_E$

have larger scale and are more obvious than the changes in the 2003 May storm signals, especially in the high orbit with $a = 15\ r_E$. As for cross-orbit comparison, the low orbits with $a = 5\ r_E$ displays the patterns that are different from those of high orbits.

Figure 5.9 shows that along the low orbits the x- and y- components have mean zero and change in variance, and the z-components have values that drop below zero and than recover to their original levels. Figure 5.10 and Figure 5.11 show that along the higher orbits, there are peaks and troughs in all three components, and that the pattern differs in the two storm periods. The right column of the 2003 Oct storm exhibit repetitive patterns whereas the left column of the 2003 May storm only has a single pattern. Since these high orbits are not passing through the ring current region that has a distance of 3-5 rE from the Earth, the signals picked up by these orbits are possibly signatures of magnetic reconnection which was happening in a broad region. The repetitive patterns in the October 2003 storm could be the results of multiple substorms within the major magnetic storm, as substorms tend to be more frequent and stronger during the main phase of magnetic storms.

Based on the typical features observed along satellite orbits during magnetic storms, we now consider detection methods that recognize the changes in the magnetic signal along the orbits. A review of change-point detection methods follows in the next subsection.

5.3 Review of change-point detection

Time series data describes temporal variations in a system or an environment, and such variations can be systematic and non-systematic. In environmental science, systematic change mostly comes from the intrinsic behaviours environment while non-systematic change comes from effects external to the environment. Change-point detection has been developed to recognize non-systematic changes in time series. The times at which non-systematic changes occur are regarded as *change points* and the change points, once detected, then can be associated with external events. In our study of space weather, we obtained the deviation of the external magnetic field from its quiet state as a time series and explored the magnetic storm patterns that are present in these time series. We aim to look for changes in the magnetic field time series signals for detecting magnetic storms as early and quickly as possible. This requires the use of change-point analysis. In this section, we provide a review of change-point detection methods relevant to our problem.

5.3.1 The problem settings

Change-point detection problem first appeared in quality control for detecting a change from the in-control to the out-of-control state given time-indexed observations. The early problem is originated in the work of Page (1955), Shiryaev (1963), and Lorden (1971). Change point detection in a sequence of random variables was first proposed by Page (1954). Subsequent investigations are in Hinkley (1970). More generally complete theoretical optimality results about the likelihood approach to change detection are obtained in Deshayes and Picard (1985). Csörgö and Horváth (1997) provided a review of the earlier probabilistic methods for detecting various types of possible changes in the distribution of time-dependent observations.

Methods of change-point detection have been developed for different purposes, e.g. analysing, monitoring, and forecasting, in various disciplines, such as finance, engineering, genetics, and environmental sciences. The general problem of change point is to investigate whether the pattern of a time series change over time. In discrete time series, the problem can be formulated as follows: Let $\{x_1, x_2, \cdots, x_n\}$ be a sequence of variables with probability distribution $\{F_1, F_2, \cdots, F_n\}$, respectively. The change point problem tests the null hypothesis H_0 "no change points" versus the alternative hypothesis H_1: "there exists a change point", by testing more formally

- $H_0 : F_1 = F_2 = \cdots = F_n$, versus
- $H_1 : F_1 = \cdots = F_k \neq F_{k+1} = \cdots = F_n$

where k $(1 < k < n)$ is the location at which the change point occurs. The change-point k is often assumed to be unknown and various statistical tests of the null hypothesis H_0 against the alternative H_1 for some $k > 1$ have been suggested. In this framework, the problem is to evaluate if probability distributions from which data in the two intervals are generated differ from each other and to estimate the time point k if the two distributions are significantly different.

In the case where there is more than one change point, the problem becomes the following: Let $\{x_1, x_2, \cdots, x_n\}$ be a sequence of variables with probability distribution $\{F_1, F_2, \cdots, F_n\}$, respectively. The change point problem tests the null hypothesis H_0 "no change points" versus the alternative hypothesis H_1: "there exist m change points"

- $H_0 : F_1 = F_2 = \cdots = F_n$, versus
- $H_1 : F_1 = \cdots = F_{k_1} \neq F_{k_1+1} = \cdots = F_{k_2} \neq F_{k_2+1} = \cdots = F_{k_q} \neq F_{k_q+1} = \cdots = F_n$

where $1 < k_1 < k_2 < \cdots < k_m < n$, and m is the unknown number of change points and $k_1, k_2, \cdots, k_m$ are the respective unknown locations at which change points occur.

The change-point detection methods that involve testing and estimation procedures in statistics can be classified in different ways. The problem can be split further into single change-point or multiple change-point detection as illustrated above. There are classical and Bayesian approaches for dealing with data that are discrete or continuous in time. Also different assumptions such as the time series being stationary or non-stationary can be made for detecting change-points in the time series. Furthermore, the problem can be expressed as a parametric or non-parametric statistical problem. More importantly, the analysis of change-points can include *retrospective analysis* in which cases all observations are given at one time and *sequential analysis* when observations are given one at a time.

- Retrospective analysis is also called *batch or offline detection*. Given a fixed number n of observations, we test the hypotheses for θ_i the unknown parameters,

$$\begin{aligned} H_0 : X_i &\sim F_0(x;\theta_0), \quad i = 1, \cdots, n, \quad \text{versus} \\ H_1 : X_i &\sim \begin{cases} F_0(x;\theta_0), & i = 1, \cdots, k \\ F_1(x;\theta_1), & i = k+1, \cdots, n \end{cases} \end{aligned}$$

- Sequential analysis, also named *online detection*, is as follows. When new observations are received, x_t for $t \in \{1, 2, \cdots\}$, we obtain D_t, the test statistics, for $\{x_1, \cdots, x_t\}$ and choose h_t the threshold. If $D_t > h_t$, a change-point is detected; if not, D_{t+1} is computed with a new observation x_{t+1} and is then compared with the threshold h_{t+1}. The threshold is chosen to guarantee a constant false positive detection rate. Hence under the null hypothesis that there is no change-point in $\{x_1, \cdots, x_t\}$, the threshold h_t satisfies the following

$$\begin{aligned} P(D_1 > h_1) &= \alpha \\ P(D_t > h_t | D_{t-1} \leq h_{t-1}, \cdots, D_1 \leq h_1) &= \alpha, \quad t > 1. \end{aligned}$$

where α is the probability of false positive detection. This means that, on average, a number of $1/\alpha$ observations will be received before the detection method falsely rejecting a true null hypothesis. The quantity $1/\alpha$ is known as the *average run length* (Ross, 2014).

Offline algorithms consider the entire data set at once, and look back in time to recognize where the change occurred, without constraint on the run time. Online detection algorithms run concurrently with the process they are monitoring, processing each data point as it becomes available, with a goal of detecting a change point as soon as possible after it occurs, ideally before the next data point arrives (Downey, 2008). In both cases, the aims of change-point detection are detecting true change-points (sensitivity) and avoiding false detection (specificity). Online change point problems have been presented in statistical quality control, public health surveillance, and signal processing (Mei, 2006). The problem is well understood and has been solved under a variety of criteria. Some popular schemes are Shewhart's control charts (Shewhart, 1931), moving average control charts, Page's cumulative sums of squares (CUSUM) procedure (Page, 1954) and the Shiryayev-Roberts procedure (Shiryaev, 1963). Inclan and Tiao (1994) used the CUSUM for retrospective detection of changes of variance under the assumption of independent normal distribution.

Recent contributions to the change-point problem are summarized as follows. Kawahara and Sugiyama (2012) presented a non-parametric approach to detecting the change of probability distributions of sequence data, estimating the ratio of probability densities. Adams and MacKay (2007) implemented a Bayesian online approach. Aminikhanghahi and Cook (2016) reviewed recent advances in online detection methods, including parametric, non-parametric, Bayesian, and non-Bayesian, and categorized the methods into supervised and non-supervised. In a multi-sensor situation, there are structured and unstructured problems. For structured problems there exists a profile determining the relative magnitudes of the changes observed by different sensors, according to their distance from the location of a signal. Mei (2006) proposed a multi-sensor procedure based on sums of the CUSUM statistic from individual sensors. The procedure fails to be asymptotically optimal when the specified distributions are incorrect. Tartakovsky

and Veeravalli (2008) proposed a different procedure that sums the local likelihood ratio statistics before forming CUSUM statistics, assuming that the change-point is observed by all sensors. Xie and Siegmund (2013) develops a mixture procedure using the generalized likelihood ratio in the case of an unknown subset of affected sensors and incompletely specified post-change distributions, under the assumption the individual observations are independent and normally distributed with unit variance, and that the changes occur in their mean values.

5.3.2 Change-point problem in environmental science

In environmental sciences, Jaruskova (1997) provides a review of change-point methodology with a discussion of typical features in environmental data, including seasonality. For finding systematic changes in the mean under the assumptions of independent normal distribution, Jaruskova argued that seasonality and skewed distribution can be reduced by averaging or taking the quotient or difference of the reference series, and dependence in the form of an ARMA model can be dealt with by incorporating the spectral density of the corresponding ARMA process in the test statistics for change-point detection. Kim (2000) derived a statistics for testing changes in ARMA model parameters.

Reeves et al. (2007) compares methods for detecting undocumented change points in climate data series under the same assumptions that the series are homogeneous and can be adequately described by a regression equation with i.i.d. Gaussian errors, or that the series has at most one change point. The *standard normal homogeneity* (SNH) test and its parametric and non-parametric variants were compared. The non-parametric variants of the SNH test remove the effects of outliers by applying parametric procedures to the relative ranks of the data rather than directly to the observed data. *Two-phase regression* (TPR) models and their two recent versions were introduced. The original form of TPR proposed by Hinkley (1970) then applied by Solow (1987) has the drawback that the model allows change in slope, i.e. the coefficient parameter in the TPR, but fixes the mean with a continuity constraint, causing inaccuracy of the percentiles of the test statistics under null hypothesis. Lund and Reeves (2002) improved the model by allowing change in both mean and slope and presented simulated critical values of the test statistics that enable one to reach statistically valid conclusions. Wang (2003) noted the likelihood ratio model may be unrealistic in climate setting and modified the

model by assuming no trend. Two hierarchical methods and two information approaches were also mentioned in the review. The study used four measures of model adequacy to compare the detection methods. Reeves concluded that incorporating a good reference series, when available, can boost change point detection power, non-parametric and parametric change point procedures can be used in tandem for dealing with outliers, periodicities can be easy to remove but autocorrelation would result in false detection. According to Reeves et al. (2007), the common trend TPR and and Sawa's Bayes criteria procedures seen optimal for most climate time series, whereas the SNH procedure and its non-parametric variant are probably best when trend and periodic effects can be diminished by using homogeneous reference series.

Lund et al. (2007) modified classical change-point test to take into account autocorrelations and periodicities for testing undocumented change-point (mean change) in climate data. Methods started with detecting changes in the mean of a sequence of independent random variables and were then extended to dependent sequences. Gombay (2008) used test statistics based on the efficient score vector for detecting changes in AR model parameters. Spokoiny (2009), based on the assumption of local homogeneity, offered a new approach to modelling and forecasting of non-stationary time series with applications to volatility modelling for financial data. Verbesselt et al. (2010) demonstrated the phenological change detection ability of a method that integrates the decomposition of time series into trend, seasonal, and remainder components for detecting change. Beaulieu et al. (2012) reviewed the detection methods for climate science and gave a detailed explanation of change-point methodology based on the information approach and provided an extension to take into account mth-order autocorrelation in the detection of a shift in the mean and of a shift in the coefficients of a simple linear regression, and to detect a shift in the mean and in the autocorrelation.

5.4 Prospective methods for storm detection

Various change-point detection algorithms have been implemented in different R packages. The R package **changepoint** by Killick and Eckley (2014) provides methods for retrospectively detecting multiple and single change points using different search methods in a likelihood based framework. The **cpm** package by Ross et al. (2013) includes parametric and non-parametric methods for both batch and sequential detection

of changes in mean or variance. The framework of the change point model used in the package is based on the work of Hawkins et al. (2003), Hawkins and Zamba (2005), Hawkins and Deng (2010), Ross et al. (2012), and Ross (2014). The parametric methods in the package are for sequences with a known distribution, including Caussian, Bernoulli, and Exponential distribution. Non-parametric change detection is for non-Gaussian sequences or sequences whose distributional forms are unknown. The **bcp** package by Erdman et al. (2007) implemented a Bayesian approach for change point problem. The difference between Bayesian and frequentist procedures for change point analysis was that frequentist approaches estimate specific locations of change points and Bayesian approaches estimate the probability of a change point at each data point in a time series.

Our analysis of the time series magnetic signal involve the use of the **changepoint** package and the **cpm** package. We start with a retrospective single change-point detection using the general likelihood ratio based approach implemented in **changepoint** and then move on to online detection using various different approaches in **cpm**. These methods will be presented in this section.

5.4.1 Batch detection methods

In the **changepoint** package, the *general likelihood ratio* (GLR) tests were implemented for batch detection of change in mean, variance, and both.

Let $\{x_1, x_2, \cdots, x_n\}$ denote a sequence of variables. Assuming there is a single change-point τ, $\tau \in \{1, 2, \cdots, n-1\}$, that divides the sequence into two segments, $\{x_1, \cdots, x_\tau\}$ and $\{x_{\tau+1}, \cdots x_n\}$, let θ_0 and θ_1 denote the parameters for the two segments. If there is no such change-points, let θ denote the parameter for the original sequence.

The maximum log-likelihood for a given τ can be written as

$$ML(\tau) = \log p(x_1, \cdots, x_\tau|\hat{\theta}_1) + \log p(x_{\tau+1}, \cdots x_n|\hat{\theta}_2),$$

where $p(.)$ is the probability density function and $\hat{\theta}_1$ and $\hat{\theta}_2$ are the two estimated parameters. The test statistic is given by

$$\lambda = 2\big[\max_{\tau_1} ML(\tau) - \log p(x_1, x_2, \cdots, x_n|\hat{\theta})\big],$$

where $\max_{\tau_1} ML(\tau_1)$ is the maximum evaluated at all possible change-point locations. For a chosen threshold c, we reject the null hypothesis if $\lambda > c$ and estimate $\hat{\tau_1}$ that maximizes $ML(\tau_1)$ as the detected change-point.

Hinkley (1970) first proposed this GLR-based approach and derived the asymptotic distribution of the likelihood ratio test statistics for a change in the mean for time series data that follows a normal distribution. Gupta and Tang (1984) extended the approach to detect change in variance for normally distributed data. Eckley et al. (2011), Silva and Teixeira (2008) provided more comprehensive review of this approach. Discussion of the choice of c can be found in Birgé and Massart (2007), Chen and Gupta (2011), Guyon and Yao (1999), Lavielle (2005).

5.4.2 Sequential detection methods

In the **cpm** package, parametric and non-parametric tests were implemented for sequential detection. The parametric methods for data with Gaussian distribution, i.e. normally distributed data, include the following. The GLR can be used detect both change in mean and variance. The *Student-t* test is for detecting change in mean and the *Bartlett's* test (Sokal and Rohlf, 1969) for detecting change in variance. Non-parametric methods come into use when no assumption are made about the distribution of the data. These include the *Mann-Whitney*, *Mood*, and *Lepage* statistics for detecting location changes, scale changes, and location and scale changes (Hawkins and Deng, 2010, Ross et al., 2011).

Here we present the parametric Bartlett's test under Gaussian assumption and its non-parametric equivalence Mood test. The Bartlett's test was first proposed to test if k samples have equal variances. Let $\{X_1, \cdots, X_k\}$ denote the k samples that follow normal distribution and have the variances $\{\sigma_1^2, \sigma_2^2, \cdots, \sigma_k^2\}$

$$
\begin{aligned}
H_0 &: \sigma_1^2 = \sigma_2^2 = \cdots = \sigma_k^2 \\
H_1 &: \sigma_i^2 \neq \sigma_j^2 \quad i, j \in \{1, 2, \cdots, k\}
\end{aligned}
$$

The test statistic is given as

$$
T = \frac{(N-k)\ln s_p^2 - \sum_{i=1}^{k}(N_i - 1)\ln s_i^2}{1 + (1/(3(k-1)))((\sum_{i=1}^{k} 1/(N_i - 1)) - 1/(N-k))} \tag{5.3}
$$

where s_i^2 is the variance of the ith group, N is the total sample size, N_i is the sample size of the $i$the group, k is the number of groups, and s_p^2 is the pooled variance, $s_p^2 = \sum_{i=1}^{k}(N_i - 1)s_i^2/(N-k)$.

The Mood test statistic for a sequence of variables $\{X_1, X_2, \cdots, X_t\}$ can be written as

$$D_{k,t} = \sum_{i=1}^{k}(R_i - (n+1)/2)^2, \tag{5.4}$$

where R_i is the rank of X_i within $X_1, X_2, \cdots, X_t$.

The *Kolmogorov-Smirnov* (KS) and *Cramer-von-Mises* (CvM) statistics are for detecting arbitrary changes (Ross and Adams, 2012). Data are partitioned into $S_1 = \{X_1, \cdots, X_k\}$ and $S_1 = \{X_{k+1}, \cdots, X_t\}$ if there is a change-point at k and have the empirical distributions,

$$\hat{F}_{S_1} = \frac{1}{k}\sum_{i=1}^{k} I(X_i \leq x)$$
$$\hat{F}_{S_2} = \frac{1}{t-k}\sum_{i=k+1}^{t} I(X_i \leq x)$$

where $I(X_i \leq x)$ is the indicator function that has the following form,

$$I(X_i \leq x) = \begin{cases} 1 & \text{if} \quad X_i < x \\ 0 & \text{otherwise.} \end{cases}$$

The KS statistics can be written as

$$D_{k,t} = \sup_x |\hat{F}_{S_1}(x) - \hat{F}_{S_2}(x)|, \tag{5.5}$$

and the CvM statistics is given by

$$W_{k,t} = \int_{-\infty}^{\infty} |\hat{F}_{S_1} - \hat{F}_{S_1}|^2 dF_t(x). \tag{5.6}$$

5.5 Application to the magnetic data

Our initial impression from the T96 model simulation was that the orbital time series magnetic field data exhibit different storm pattern in its x-, y- and z-components. The x-components, $\{dBx_t\}$ for $t \in \{1, 2, \cdots\}$, have constant mean zero and change in variance during the selected storm period; the y-components $\{dBy_t\}$ also have change in variance but variation in their mean values throughout the storm period; the z-components $\{dBz_t\}$ display a pattern that resembles the variations in the Dst index, which behaves like a sharp decrease followed by a slow recovery and could be regarded as an arbitrary change or a change in both mean and variance.

In this section, we starts with retrospective analysis using the GLR approach for detecting the changes in mean, variance, and mean and variance of the data in the three components. The detection results would give information on the type of changes in $\{dBx_t\}$, $\{dBy_t\}$ and $\{dBz_t\}$. Then we perform sequential analysis for the types of changes determined for data of each component. Comparison of different detection methods will be made in the sequential analysis.

5.5.1 Identifying types of changes in the data of the three components

Assuming the three sets of time series data $\{dBx_t, dBy_t, dBz_t\}$ are Gaussian, we apply the retrospective single detection method with GLR from the **changepoint** package to the time series data of each storm period. The storm periods are determined by the ground monitoring based on the Kp and the Dst index. Since the detection methods look for a single change-point, we expect to see one change-point detected either at the beginning or the end of each storm period if the change at the beginning is not significant. Figure 5.12, 5.13, and 5.14 show examples of applying the detection methods for change in mean, variance, and mean variance for $\{dBx_t, dBy_t, dBz_t\}$ of the 2003 May and the 2003 Oct storms. The figure gives the time plots of the data against the time in hour and the estimated change-points. The shadowed regions in each plot marked the storm periods as defined by the geomagnetic indices. The left column in each figure plots $\{dBx_t, dBy_t, dBz_t\}$ of the 2003 May storm from top to bottom and the right column plots the data of of the 2003 Oct.

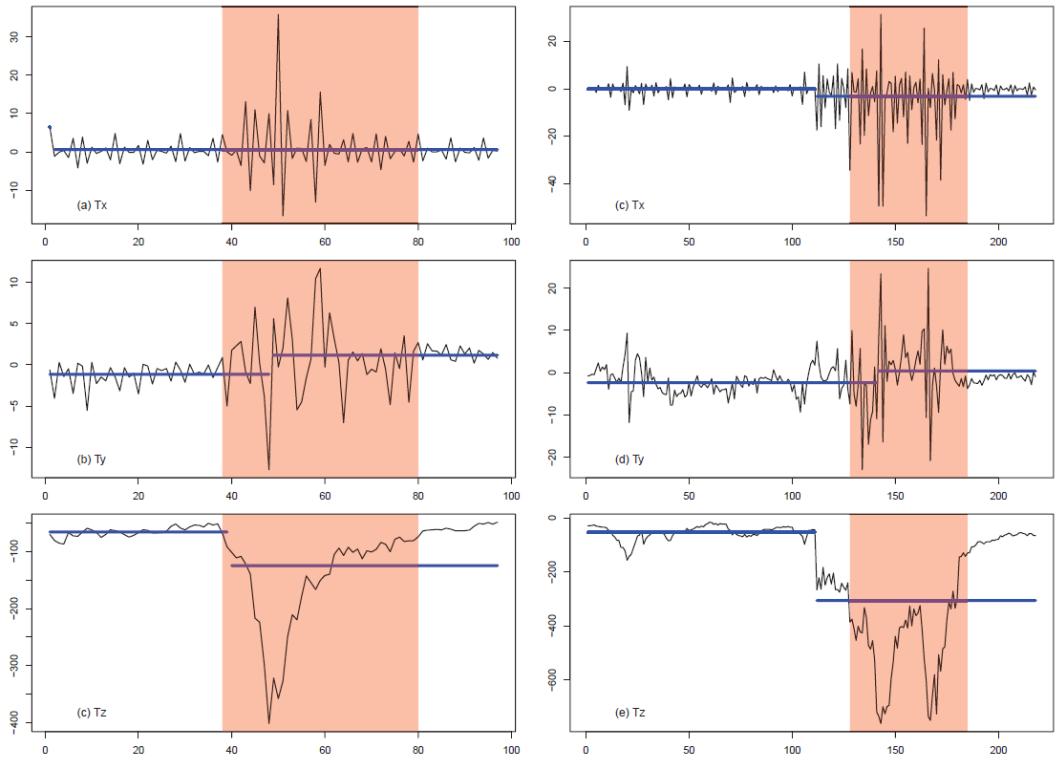

FIGURE 5.12: GLR detection for change in mean. The curves represent the time series magnetic signal of the x-, y-, and z-components (from top to bottom) obtained along selected orbits during two magnetic storms (left and right). The horizontal lines indicate the estimated mean values. The shaded regions show the storm periods

Figure 5.12 shows the detected change in the mean assuming there exists a single change-point in the time series. The horizontal blue lines fitted to each time plot represent the mean values estimated in each segment. The break points in the blue line indicate where the changes occur. As shown by the plots on the top panels, there are no changes in the x-components. The plots on the middle panel suggest there exists a change point in the y-component during the two storms. The changes were detected about 10 hours after the onset of the storm. The plots on the bottom panel suggest that changes in mean were detected in the z-component. The changes take place a few hours quicker in the z-components than in the y-components, as the z-components reflect the decrease in the equatorial ring current regions along the particular orbit. The left plot for the May storm suggests the change was detected just after the onset of the storm, or the observation of the storm on the ground of the Earth. The right plot for the Oct storm suggests the change in mean was detected a few hours before the observation of storm on the ground.

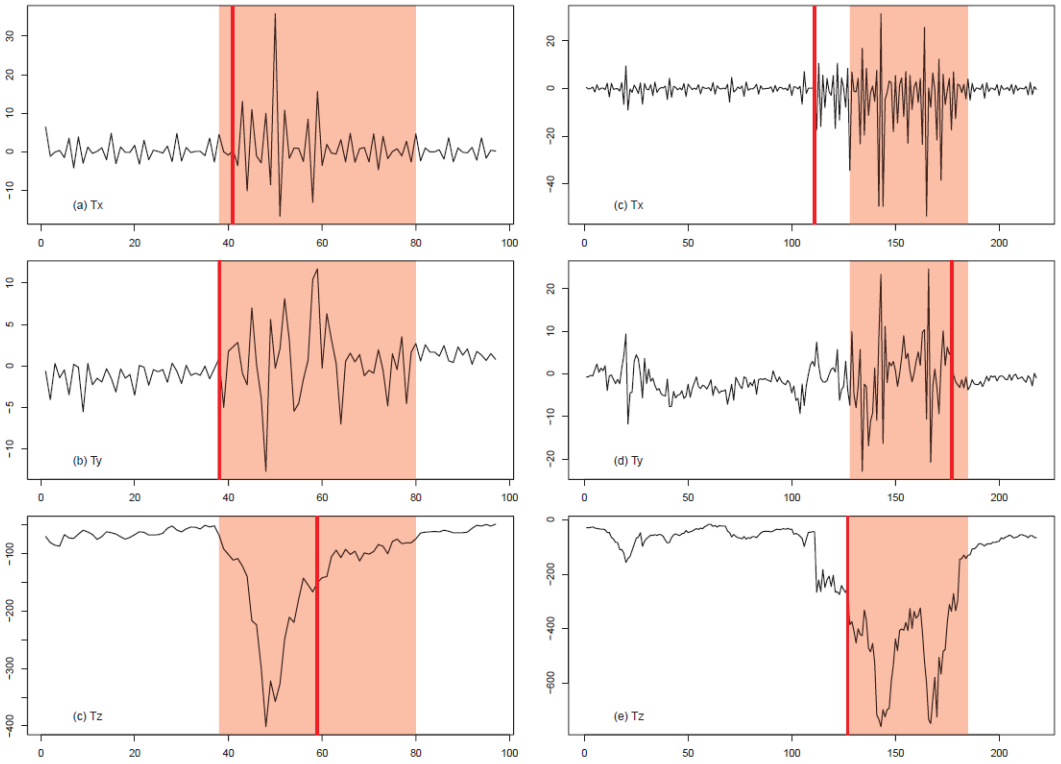

FIGURE 5.13: GLR detection for change in variance

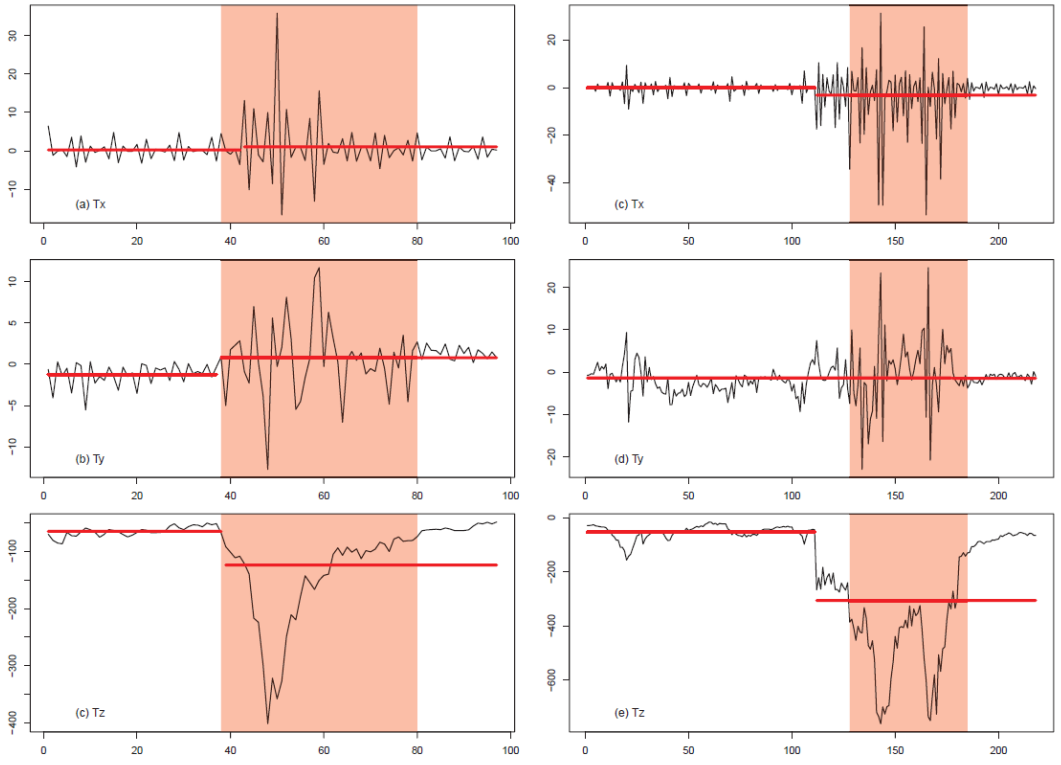

FIGURE 5.14: GLR detection for change in mean and variance

Figure 5.13 shows the detected change in the variance assuming a single change-point exists. The vertical red lines indicate the time at which detected changes occur. The top left plot, the middle left plot, and the bottom right plot of the dBx_t, dBy_t in the May storm and the dBz_t in the Oct storm suggest that the times at which changes occur in near-Earth space coincide with the time at which storms were observed on the ground. The top right plot of the dBx_t in the Oct storm has change detected before the observation was made on the ground. In dBz_t in the May storm (bottom left) and dBy_t in the Oct storm (middle right), the changes were detected more than 20 hours later the storms happened.

Figure 5.14 shows the detected change in both mean and variance, again with the same single change-point assumption. Except for the time plot of dBy_t in the Oct storm (middle left) in which no change was detected, other time plots suggested a change was detected at times close to the onset of the storms.

To investigate how the time of detection differs in components, we produce box-plots of the time of detection in the x-, y-, and z- components of the two storms in Figure 5.15. The results are obtained from the application of the single change-point detection to all the orbits emulated in the previous section. The y-axes show the hours in the selected time periods and the interval between the two red lines in each plot indicates the time span of the storm. For the May storm, as shown by the plot on the left panel, most of the change-point detected falls in the time range of the storm but the results differ in the x-component and the other two components. The plot of the Oct storm on the right panel suggests there is not much difference across the three components and half of the change-points detected are prior to the storm onset as observed on the Earth.

Given that the Oct 2003 storm was larger in magnitude and lasted longer than the May 2003 storm, it is reasonable to deduce that the near-Earth magnetic field environment was more disturbed in the time period when the Oct 2003 storm was about to impact on Earth than the environment was prior to the May 2003 storm. This might explain why the changes for the onset of the Oct storm, in general, was recognized earlier in the time series of the near-Earth magnetic field signals than the changes for the onset of the May storm.

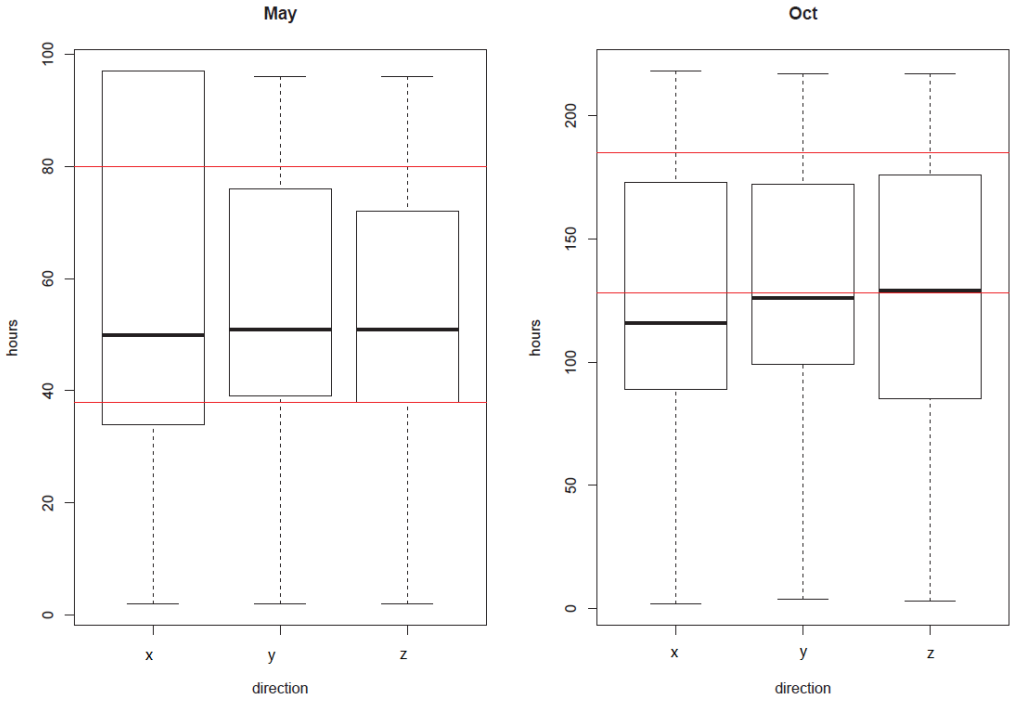

FIGURE 5.15: Boxplots of the time of the detection for the May and Oct storm in 2003

5.5.2 Detecting changes in variance online for data of the x-component

It has been identified in the retrospective analysis that $\{dBx_t\}$, the time series magnetic signal in the x-component, has constant mean and change in variance. Here we apply both the parametric and the non-parametric tests, namely Bartlett's test and Mood test, for change in variance to $\{dBx_t\}$ and compare the online detection results.

Figure 5.16 shows the results of the non-parametric Mood test on $\{dBx_t\}$ during the 2003 Oct storm. The test statistic measures the extent to which the rank of each points deviates from its expected value. Figure 5.17 shows the results of Bartlett test, the parametric test that assumes equal variance under normality, on the time series data. The top panel of each figure has the time plot of $\{dBx_t\}$ on the left and the time plot of the estimate of variance on the left. The bottom panel has the the time plot of the Kp index. Red vertical lines shown on every plot indicate the change-points detected from $\{dBx_t\}$ using the two tests. The results suggest a few change-points were detected during one storm period using the two tests and more change-points are detected using the parametric test.

In Figure 5.16, the Kp index time plot shows one out of the six change-points was detected when the Kp index was high. The space weather condition is considered to be highly disturbed when Kp > 8. The time plots of the estimate of variance on the top right panel shows that the first and the second change-points capture a minor increase in variance, the third and the fourth change-points both mark a sudden increase in the variance, and the fifth and sixth change-points capture a minor decrease in the variance.

In Figure 5.17, the three time plots of $\{dBx_t\}$, the estimate of variance, and the Kp index suggest some of the change-points detected $\{dBx_t\}$ do not correspond to significant change in either the estimated variance or the storm level observed on the Earth. The *Average Run Length* (ARL), the expected time between false positive detections, is set to be the same with the value of 500, in the two tests. This means a false detection in every 500 observations. In sequential analysis, false detection rate can be reduced by increasing the ARL. However, this does not provide an immediate solution to our problem.

Comparison of the detection results from the parametric Bartlett's test and the non-parametric Mood test suggests that the Mood test outperforms the Bartlett's test in the online detection of changes in variances for the time series magnetic signals, since some change-points identified by the Bartlett's test do not correspond to either a substantial change in the estimated variance, i.e. change observed in near-Earth space, or a high Kp value for change observed on Earth, and can thus be regarded as false detections. As previously mentioned the false positive rate was set to be the same in the two tests, hence the unsatisfactory results from the Bartlett's test can be attributed to the fact that Bartlett's test is sensitive to departures from normality. This implies that normality might be a dubious assumption to hold for the time series magnetic data.

As for the results from the Mood test, the beginning and the end of a major disturbance in $\{dBx_t\}$ seem to be picked up well by two of the detected change-points. However, minor fluctuations other than the major disturbance have also been identified by the Mood test. These fluctuations in the time series magnetic signals correspond to small but noticeable changes in the estimates of the variances and relatively high Kp values ($Kp >$ 6). Therefore, the minor disturbances detected by the online Mood test, though remain unclear as to identifying the magnetic storm, are considered as non-trivial changes.

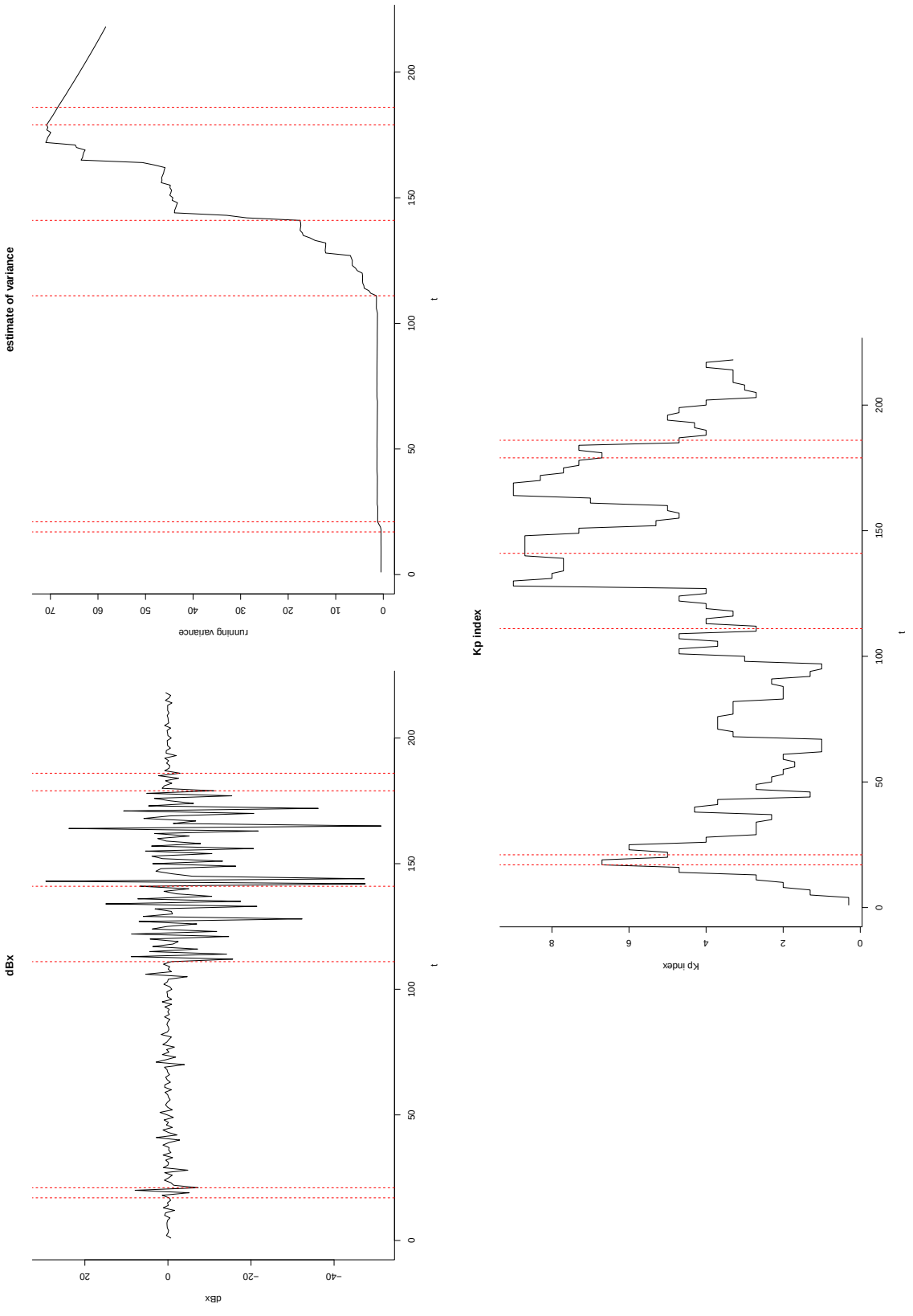

FIGURE 5.16: Online detection results from Mood Test for $\{dBx_t\}$. The red vertical lines indicate the changes in variance detected in $\{dBx_t\}$ using the non-parametric Mood test.

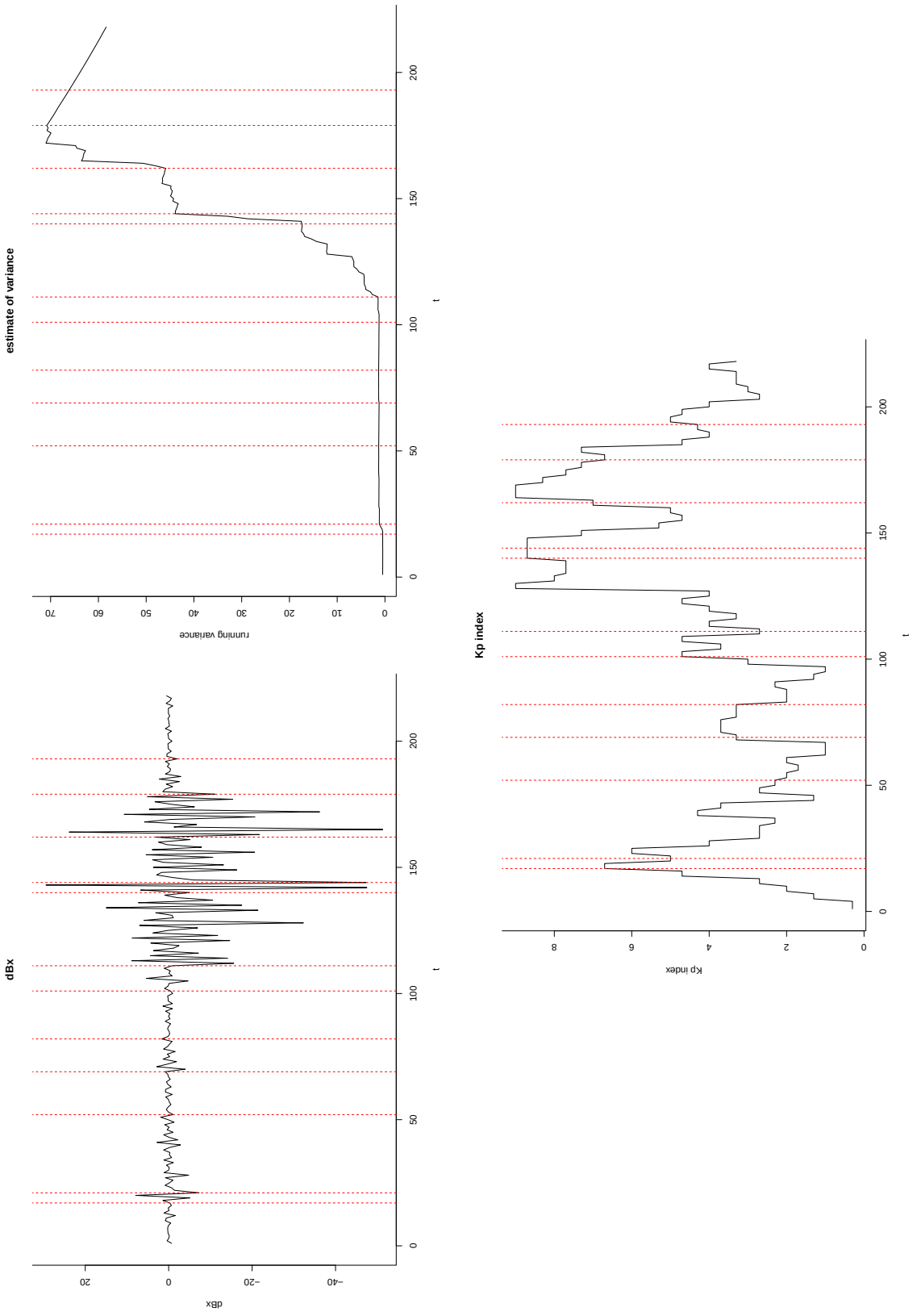

FIGURE 5.17: Online detection results from Bartlett's Test for $\{dBx_t\}$. The red vertical lines indicate the changes in variance detected in $\{dBx_t\}$ using the parametric Bartlett's test.

5.5.3 Detecting arbitrary changes online for data of the three components

The time series of the magnetic signal in the y- and z-components, do not appear to have structural pattern, hence we consider the KS and CvM tests for detecting arbitrary change in the $\{dBy_t\}$ and $\{dBz_t\}$. The arbitrary change tests can also be used for $\{dBx_t\}$ which clearly has a change in variance.

Figure 5.18 and 5.19 show the online detection results of the CvM test and the KS test on $\{dBx_t\}$, $\{dBy_t\}$, and $\{dBz_t\}$ under the Oct storm. Time plots of $\{dBx_t\}$, $\{dBy_t\}$, and $\{dBz_t\}$ are given from top to bottom in each figure. The red dashed lines in each plot indicate the change-points that were detected and the black solid lines indicate the time points at which the change-points were detected. The space between the each pair of the dashed and the solid lines represent the time delay of detection. The ARL was set to be 500 in the two tests.

The tests performs well on $\{dBx_t\}$, the magnetic signal on the x-component. Two change-points corresponding to the start and the end of the storm were detected. Detection with the CvM test has a longer delay than detection with the KS test. For $\{dBy_t\}$, and $\{dBz_t\}$ there are too many change-points detected and it is hard to associate the change-points with the storm period. Therefore $\{dBx_t\}$ seems to be more appropriate for recognizing changes related to the main storm periods. The online detection with the KS algorithm is considered to be better as it produces more timely detection than the CvM algorithm.

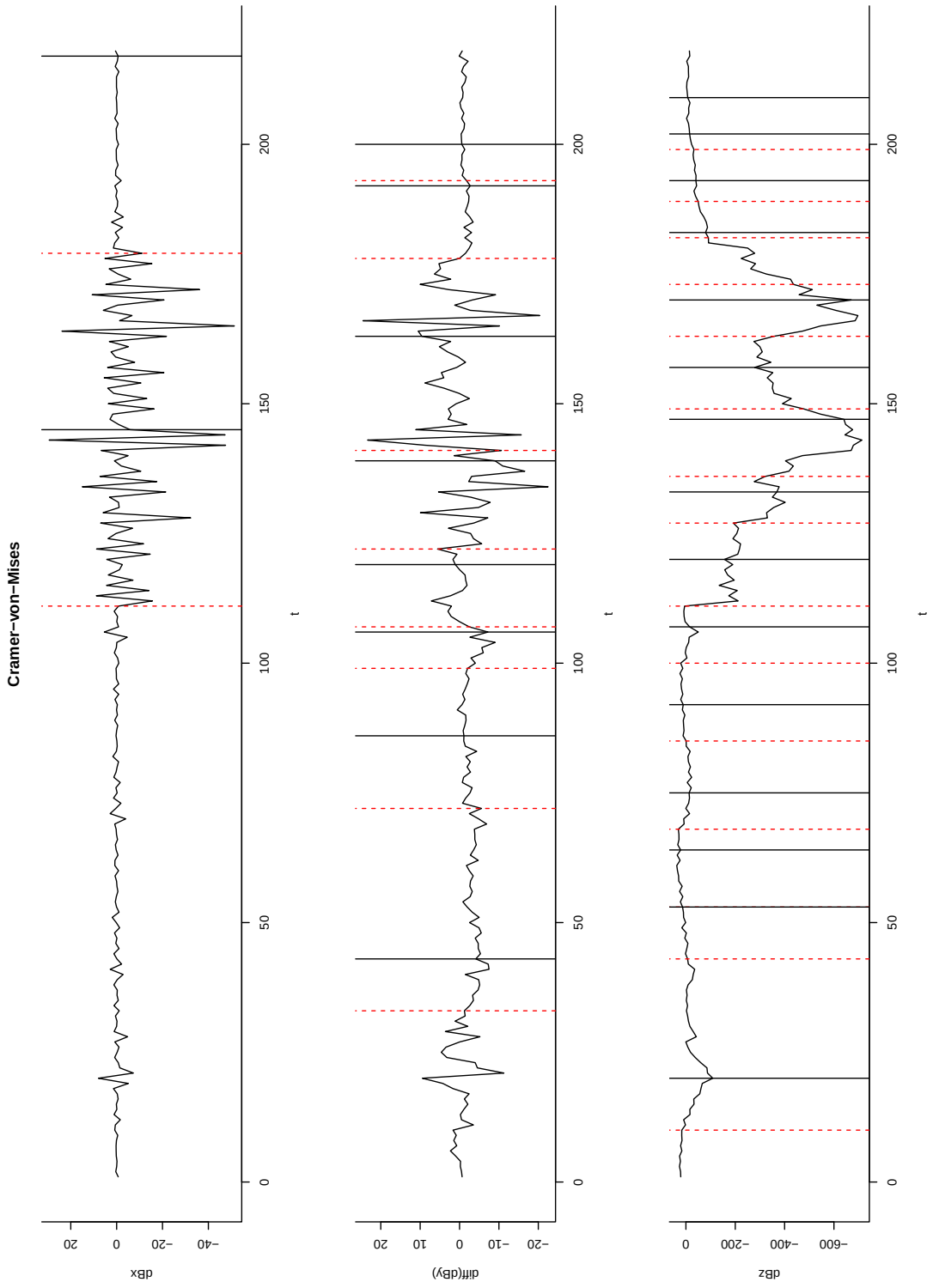

FIGURE 5.18: Cramer-von-Mises test for arbitrary changes in $\{dBx_t\}$, $\{dBy_t\}$, and $\{dBz_t\}$ under the 2003 Oct storm

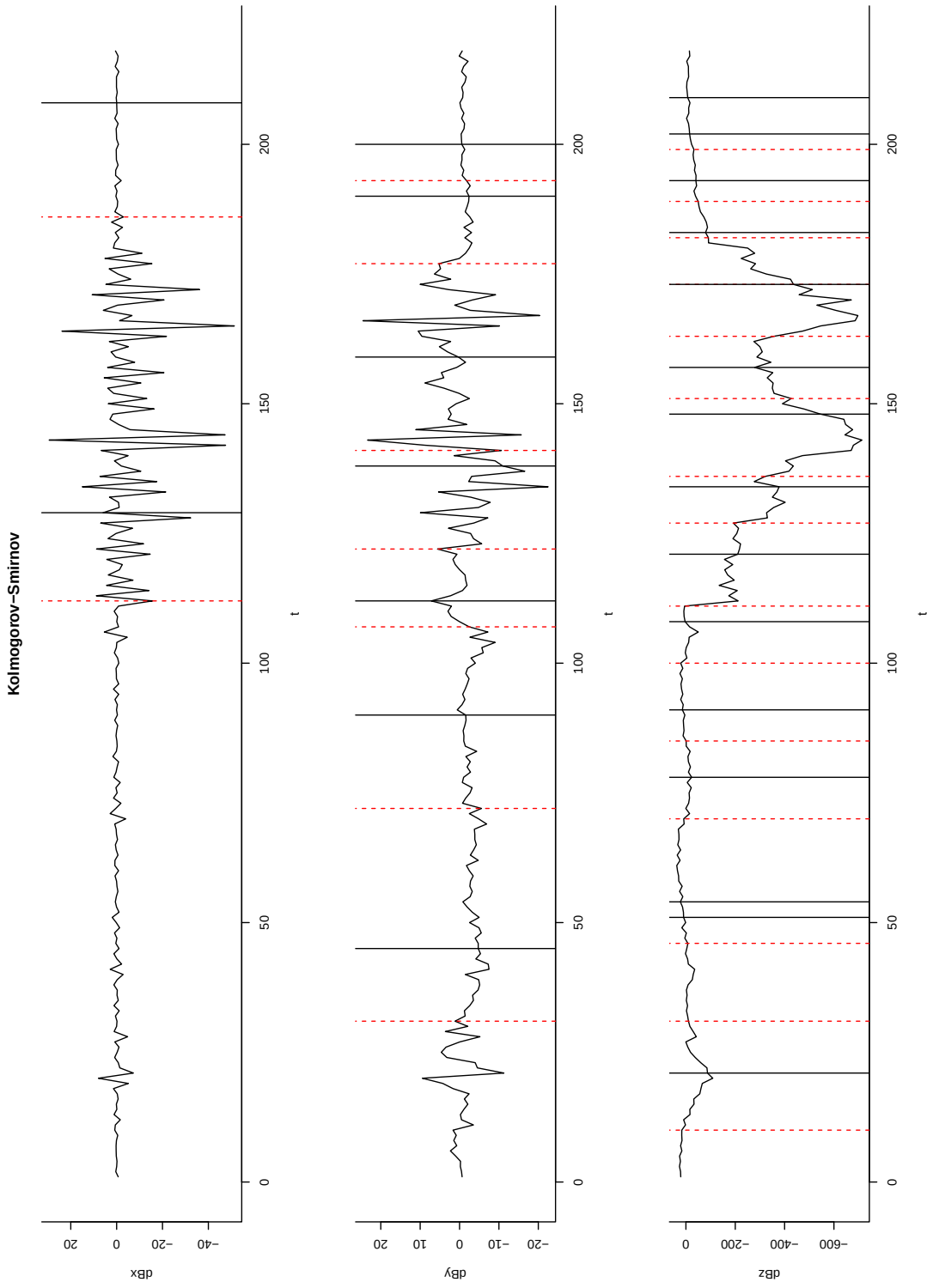

FIGURE 5.19: Kolmogorov-Smirnov test for arbitrary changes in $\{dBx_t\}$, $\{dBy_t\}$, and $\{dBz_t\}$ under the 2003 Oct storm

5.6 Results and discussion

In this chapter, the T96 model is used to generate estimates of the external field under storm and non-storm conditions for extracting the storm patterns in the near-Earth magnetic field. Real-time space weather parameters during five storm periods in 2003-2005 are input into the T96 model for generating the storm-time magnetic field data. The five storm periods are all major storms but differ in magnitude. The 2003 October storm is the most severe and the longest among the five storms. Annual averages of these space weather parameters are used to produce the quiet-time magnetic field data. Comparison of the storm-time and quiet-time over near-Earth space shows distinct storm patterns in the equatorial ring current regions during all of the five storm periods. Time series data are sampled from the storm-time and the quiet-time magnetic fields along different sets of satellite orbit trajectories. Taking the difference between the sampled time series data gives time series of external magnetic field deviations along the orbit trajectories. Visualization of these time series magnetic field deviations suggest storm patterns are most obvious along orbits that travel through the equatorial ring current regions. The time series of external magnetic field deviation obtained from T96 model simulation along satellite orbits exhibit different storm features in its x-, y- and z-components. Typical features from the ring current crossing orbits can be summarized as follows. The x-component has a constant mean and change in variance. The y-, and z- components seem to have patterns other than simply change in mean or variance.

Change-point methods are considered for recognizing magnetic storms in these time series magnetic field signals in two scenarios for batch detection and online detection. The batch approach processes data all at once and searchs for single or multiple changes-points. The online approach possesses data in a sequential manner with the aim of identifying storm onset as accurately and quickly as possible. In the retrospective analysis, GLR test is used for detecting single change in mean, variance, or mean and variance of the time series signals of the x-, y- and z-components. The batch detection with GLR works the best for detecting changes in variance of the x-component magnetic signal, since the detected change-points correspond to the time of the magnetic storm onset as determined by the geomagnetic indices. Comparison of the detection results in the five storm periods suggests that the detection of the 2003 October storm, which is the largest among the five storms, works the best, since along most of the select orbits

the change-points are detected prior to the arrival of the storm onto Earth. In the sequential analysis, the parametric Bartlett's test and the non-parametric Mood test for detecting changes in variance of the x-components, and two non-parametric tests for arbitrary changes are applied to the time series magnetic field signal of the all three components. The online detection for change in variance of the x-component suggests the non-parametric test outperforms the parametric test, making the assumption of the parametric test dubious. For arbitrary changes in the x-, y- and z-components, more change-points are detected in the y-, and z- components than the x-component. Comparisons of the two test (KS and CvM) results shows that the online KS test detects the change-points about 10 hours after the change occurs and the CvM detects the changes with a longer delay. This is because the CvM test uses a smoothing in the computation of the test statistics.

To sum up, this chapter tested online detection algorithms that recognise changes associated with storms in spatio-temporal magnetic field data. The data are obtained as numerical values of the near-Earth field under different space weather conditions using a physically-based semi-empirical model, given satellite trajectory data as time and position inputs. The x-components of the magnetic field data are ideal for recognizing the major storm periods. The results of detection on the x-components indicates that for detecting change in scale Mood the non-parametric test outperforms its parametric equivalence Bartlett test under Gaussian assumption. However, the online Mood test on the x-components also picked up changes irrelevant to the storm periods. Non-parametric tests for detecting such as Kolmogorov-Smirnov and Cramer-von-Mises for arbitrary changes perform well on the x-components as the major storms periods are picked up by the detected change-points. Two criteria for comparing the detection methods are the average run length and the mean delay. The average run length is associated with the false positive rate and is set to be the same in all the tests. Based on the criteria of the mean delay, we conclude that the Kolmogorov-Simrnov test performs better than the Cramer-von-Mises test. Based on the detection results, we would be able to consider physical constraints for optimizing the design of a monitoring network that consists of a reasonable number of Earth-orbiting satellites in future.

Chapter 6

Conclusion

Space weather describes the changing environment in the Sun-Earth system and has been characterized as electromagnetic disturbances in near-Earth space. Severe space weather events such as magnetic storms pose growing risk to our modern society, as they have the potential of disrupting a variety of technologies that rely on a stable magnetic field environment. Space weather monitoring and early magnetic storm detection can be used to mitigate risk in sensitive technological systems.

Magnetic storms, as introduced in Chapter 1, are driven by solar activity such as coronal mass ejections or corotating interaction regions. A general description of magnetic storms has been given as an intensification of the equatorial ring current, at a distance of 3-5 r_E from Earth, in the magnetosphere. The magnetosphere is formed by the interaction between the solar wind and the Earth's magnetic field and the principle mechanism that controls the dynamics of the magnetosphere is magnetic reconnection happening at both the magnetopause, where the terrestrial magnetic field is compressed by the solar wind on the day-side, and the magnetotail, where the terrestrial magnetic field is stretched in to hundreds of r_E on the night-side. The rate at which magnetic reconnection occurs in the magnetosphere is closely related to magnetic storms and substorms. When solar wind drives the interplanetary magnetic field southward, substorm activity will be enhanced by magnetic reconnection and, if the solar wind last for a prolonged time period, the substorms can develop into a magnetic storm, during which a noticeable change in the magnetic field strength occurs in the near-Earth equatorial regions as a

result of ring current intensification. A quantitative statistical approach has been considered for studying the spatio-temporal behaviour of the near-Earth magnetic field for the purpose of monitoring space weather and forecasting magnetic storms. The overall aim of this thesis has been to develop and use statistical methodologies to investigate the detectability of magnetic storms in near-Earth space, the environment of which responds to the time-varying space weather condition.

Data of the near-Earth magnetic field were collected as time- and space-dependent vectors in the GSM coordinate systems, and each vector has three magnetic field strengths measured in the x-, y- and z-directions of the GSM system. The data were sampled from the in-situ satellite measurements and the computer model outputs. The Cluster II mission directed by ESA and NASA launched four identical satellites into similar elliptical polar orbits in 2001. The initial orbits had perigees around $4r_E$ and apogees around $19.6r_E$. These orbits were changing throughout the years, and the four Cluster satellite provide in-situ measurements of the near-Earth magnetic field at time-varying locations along their orbit trajectories. The computer model consists of an internal part that calculates the magnetic field sourced from Earth itself and an external part that estimates the magnetic field resulted from the Sun-Earth interaction. These magnetic fields, termed as the internal field and the external field, add up to the total magnetic field. Numerical estimates of the internal field and the external field are obtained from the IGRF-11 model and the Tysganenko-96 (T96) model given the times and the locations as inputs. The IGRF model based on Gauss's harmonic expansion of a magnetic scalar potential serves as a seasonal approximation of the internal field in near-Earth space. A series of semi-empirical Tsyganenko models, including T96, calculate the magnetic field contribution from the magnetospheric currents in near-Earth space and are considered as the best-fit representations for the external field. The IGRF model outputs are invariant to space weather conditions whereas the T96 model outputs change with the input space weather parameters. The time-varying space weather parameters for T96 model include the solar wind ram pressure, the y and the z-components of the IMF, and the Dst index. These parameters are the estimated time series of the solar wind conditions at the magnetopause, i.e. the boundary of the magnetosphere on the day-side. A detailed description of space weather data sources and the process of collecting magnetic field data from the Cluster satellite measurements, the IGRF model, and the T96 model for our study of the near-Earth magnetic field was documented in

Chapter 2.

In this thesis, our work has been devoted to (*i*) statistical modelling of the near-Earth magnetic field utilizing the in-situ satellite measurements and the computer model outputs for charactering the magnetic field variations and quantifying the biases and uncertainties in the satellite measurements and computer models; (*ii*) investigation of satellite-based sampling strategies for recognizing magnetic storm signals in the near-Earth space using change-point detection methods for time series data generated along feasible satellite orbits. This chapter summarizes the main finding of the work shown in the thesis and their implication for (*iii*) the construction for a magnetic storm warning system, i.e. the optimization of the sampling strategies in the near-Earth space given the physical constraints and the design of satellite-based sensor network to detect and predict magnetic storm events in space weather.

6.1 Understanding variations in the near-Earth magnetic field

An exploratory analysis of the in-situ satellite magnetic field observations was conducted in Chapter 3, in which regression analysis and time series analysis were used to understand the variations in the hourly magnetic field data sampled at time-varying locations along the Cluster satellite orbits. The trajectories of the Cluster satellite have been visualized in the GSM coordinate system, in which the satellite orbits have a wobbling effect and sweep through the space completing a full scan every year. Letting an orbital function specify the movement of the satellite in space and time, we converted the spatio-temporal magnetic field into time series data with the spatial information incorporated into time-varying covariates. The time series of the magnetic field strengths in the x-, y- and z-directions, observed in the GSM spatial frame, displayed seasonal and cyclic variations mainly due to the changes in sampling locations over space. Even though the distances between the Cluster satellites vary over the study period, the magnetic field measurements from the four different satellites have similar statistical features.

Regression analysis has been applied to the time series of magnetic field strengths for each direction from the four satellites. We related the satellite measurements to the internal field IGRF and the external field T96 model outputs in a regression model.

Results from the regression analysis have suggested that the computer model outputs explain most of the variability in the observed magnetic field but the residuals from the regression model appears to be dependent locally in time, indicating that there are small scale features of the magnetic field that are not captured by the large scale computer models.

This suggest the use of time series analysis on the residuals to understand the discrepancies between the observed magnetic field strengths and the model outputs. Two distinctive features in the residuals series is temporal autocorrelation, i.e. the errors are correlated with their past values, and changing variance. Time series methods for dealing with autocorrelation and changing variance often require the assumption that the time series being stationary. Segmenting the regression residuals into orbital residuals, i.e. residuals within each satellite orbit, generates time series which are piecewise stationary. ARMA models have been considered for the temporal autocorrelation and ARCH/GARCH models for the changing-variance. The sample ac.f and p.ac.f of the orbital residuals have suggested an AR(1) model for capturing the autocorrelation and the sample ac.f and p.ac.f of squared AR(1) model residuals have suggested an ARCH(1) for accounting the changing variance. In the presence of missing values, the AR(1) model for the regression residuals and the ARCH(1) model for the AR(1) model were both estimated using a ML approach. The AR(1)-ARCH(1) structure for the regression errors within each satellite orbits means that the error term is correlated with its past (hourly) value and has a conditional variance that is also dependent on this past value.

Challenges in the exploratory analysis thus dealt with the space-time dependence and multi-dimensional structure of the magnetic field data. The temporal resolution of the magnetic field data is limited by the availability of the space weather parameters for the T96 model. The multi-dimensional structure refers to the magnetic field vectors having three field strength components in the x-, y-, and z-directions. Analysing the time series of the magnetic field strengths in isolation could be limiting since in this case the field strength of one direction was not allowed to propagate to field strengths of other directions. In the future, a vector autoregression model could be used to link the time-series variables together and examine the contemporaneous relationship among the three time series. This would allow for a more comprehensive comparison between the observed satellite measurements and the computer model output.

6.2 Calibrating magnetic field models with satellite measurements

Following the results from Chapter 3, a time-series-based regression model was proposed in Chapter 4 for quantifying the relationship between the in-situ magnetic field measurements and the magnetic field model outputs. The regression model has an AR(1)-ARCH(1) structure for its error term, and the AR(1)-ARCH(1) model parameters were obtained simultaneously using maximum likelihood estimation in the presence of missing data. The variance-covariance structure of the error term were then parametrized with the estimated AR(1)-ARCH(1) model parameters. General least square theory was applied to deal with the autocorrelation and the changing variance identied in the error term. This method was then used to provide estimates of the regression model parameters and to construct the confidence interval for the estimates given the variance-covariance structure of the error term. This time-series-based regression model was fitted to the magnetic field data of the three directions and across the four Cluster satellites.

The time series of model parameter estimates, by orbit, were then analysed to examine any long term patterns, variations and associations to storm indices using a mixed-effects model. In calibrating the computer models against in-situ satellite measurements across orbits, our primary interest has been to investigate if the reliability of the two computer model outputs vary across space and if the performance of T96 the external field model differs under the time-varying space weather conditions. It would be natural to analyse the regression model parameters estimated from the satellite orbits with proxy variables for the spatial information contained in the satellite orbits and the space weather conditions during the time periods of the orbits. For this reason, the spatial coverage of the satellite orbits were converted into a continuous variable in terms of the mean orbital distances, and the space weather conditions were categorized into a factor variable of quiet, moderate, and storm levels based on the geomagnetic indices. Since the parameter estimates were obtained from the regression models for magnetic field strengths sampled along four Cluster satellite in three directions, the estimates were grouped by the satellite numbers, $1 - 4$, and the direction labels, x, y, z. These grouping effects, though not of primary interest, should also be examined in the analysis of the estimated regression model parameters. Mixed-effects models that includes the spatial information and the space weather condition as fixed effects and the satellite and

direction effects as random effects were fitted to the estimates of the regression model parameters. The random effects were included to accounted for the possible correlation in error within the groups, which include the four-level satellite groups and the three-level direction groups nested within each of the satellite groups. In the mixed-effect models, fixed effect parameters inform on the means given the spatial information and the space weather conditions while the random effect parameters suggest the general variability among the satellite groups and the direction groups.

The calibration results have suggested that the IGRF and the T96 model provide reliable estimates of the internal and the external magnetic fields in general. The performance of the $T96$ model did not seem to be affected by the space weather conditions. Hence we infer that the T96 model can be used to produce reliable estimates of the external magnetic field at potentially unobserved times and locations. This is critical to understanding the general behaviour of the external magnetic field for different space weather conditions, under different satellite paths than the ones taken by the Cluster mission.

6.3 Detecting magnetic storms in the near-Earth space

Chapter 5 investigated the patterns of magnetic storms in the near-Earth magnetic field and explored various change-point detection methods for recognizing the occurrence of a (major) magnetic storm in time series measurements along feasible satellite orbits. As described in Chapter 4, we explored magnetic storms using a proxy for the external magnetic field – the T96 model output. Five major storm periods in 2003-2005 has been identified using the geomagnetic indices Kp and Dst. These storms, though differing in magnitude, have similar spatio-temporal patterns based on visual analysis of the external magnetic field from the T96 model run. The storm patterns have been summarized as gradual changes in the magnetospheric boundary and distinctive variations in equatorial regions. We emulated satellite orbits along which magnetic field data were sample from the T96 model under the magnetic storms and the averaged space weather conditions. This allowed us to make comparison of the storm and non-storm behaviours of the external magnetic field as observed by satellite at time-varying locations. The results suggested that time series magnetic field data generated along the same orbits under both storm and non-storm condition have similar cyclic patterns as a result of the orbital effects and the time series under storm condition appears to be noisier than the time

series under non-storm condition. Taking the difference between the storm series and the non-storm series produced a series that represents the deviation of the external magnetic field from its quiet status along pre-dened orbits. Change-point statistical procedures were performed on these deviation series.

The orbits were manipulated so that the external magnetic field could be sampled across different regions of space. Results of the orbital sampling showed that the storm signals can be captured by equatorial orbits with a reasonable size and shape. In x-, y- and z-directions the deviation series captured the storm features differently. In the x- and y- directions, storms were expressed as changes in the variance, but not in the mean of the series. In the z-direction both the mean and variance of the deviation series tended to change when a storm was present. Retrospective and sequential analysis have been performed using various detection methods on the time series magnetic signals. In the retrospective analysis where the full time series were given at one time, the detection of a change in the variance of the x-component outperformed the detection on the y- and z- components, since the change-points detected from the x-components in the storm periods corresponded to the onset of the magnetic storms as observed on Earth well in comparison with the change-points detected from the y- and z-components. In the sequential detection where new observations were received one hour at a time, change-points in the x-components were detected in correspondence to magnetic storms. The detection on the x-component still outperformed the detection on the y- and z-components in the sense that the change-points detected in the x-components picked up non-trivial changes for the major storm periods. However, with a delay of about 10 hours, the time of online detection was considered to be a bit late for immediate storm recognition. Hence further development of detecting algorithm or higher resolution of magnetic field data would be considered in future work for online detection of magnetic storms in near-Earth space.

Work in this chapter identified the ring current crossing orbits as the trajectories along which storm can be easily detected, the x-component as the direction which display clear storm patterns, and the Kolmogorov-Smirnov test as the detection method most suitable for recognizing the storms along the selected orbit trajectories. Another important finding for the change-point detection results was that for some orbits, usually for high-orbits under severe storm, there exist repetitive patterns within one storm period. The repetitive patterns were believed to be associated with the multiple occurrences of

substorms with a single storm. This conjecture can be validated through comparing the multiple change-points with substorm indices.

6.4 Discussions and Future work

Contradicting to the conventional idea of focusing the z-component (in the GSM) of the magnetic field in the study of magnetic storms and substorms, our work has identified the possibility of recognizing magnetic storms in the x-component of the deviated external field, given time series data collected along equatorial orbits passing through the ring current regions. Possible extensions to this project include developing detection algorithm for achieving faster detection, given the orbital storm patterns found in our study, and a design of satellite network to allow multi-sensor monitoring of the near-Earth magnetic field along multiple satellite orbits. Faster detection of magnetic storms would greatly help mitigating the risks of magnetic storms in sensitive technologies, and can be achieved by refining the detection algorithm, using real-time data of higher resolution, or considering multivariable methods that take all magnetic field components into account. The required network parameters must then be set against what is achievable in terms of sensor quality and satellite numbers, satellite orbits and formations and satellite communication restrictions to arrive at an optimal sensor network solution. This can be investigated following the methods present in Chapter 5, by generating time series external magnetic field signals along simultaneous multi-orbits and optimizing the online detection of change-points. For application onto real-time satellite data, the discrepancy between the T96 model and the satellite measurement must be dealt with. As Chapter 3 and 4 suggested, there exists temporal autocorrelation and volatility in the residuals of the regression model which relates the satellite data to the T96 model outputs. Therefore the detection methods need to be modified for detecting changes in the presence of temporal autocorrelation and volatility.

The novelty of thesis lies in the application of change-point methods to spatio-temporal magnetic field data for magnetic storm detection, which necessitates the statistical calibration of magnetic field models under time-varying space weather conditions. The next stage of work would consider how, as technology of cube-satellite develops, the knowledge of this thesis could inform design of a network of cube-satellites to efficiently, and in a likely manner, detect magnetic storms. A very brief review of traditional network

design follows. Banjevic and Switzer (2004) considered network design of observation and locations in a spatial domain and presented an example of optimal network design for measuring maximum temperatures in Mojave desert. Design strategies based on simultaneous simulated annealing and sequential point selection algorithms are compared by using criteria such as minimum estimation variance, maximum conditional variance and maximum entropy. The process is modelled by a spatial random field, incorporating prior knowledge and selecting the best subset of points of desired cardinality to best represent the field in question. Volkmann et al. (2010) showed an example of optimizing the network in a multi-objective setting using radiation monitoring stations in the Netherlands and parts of Germany. The network is designed to monitor both routine and emergency conditions, which requires minimizing prediction error under routine conditions and maximizing calamity detection capability in emergency cases. The objective function combined two criteria, namely average kriging prediction error variance and network detection capability. The study implemented spatial simulated annealing (SSA) to optimize the monitoring design by iteratively moving stations around and accepting all designs that improved a weighted sum of average spatial prediction error and calamity detection capability. The probability with which the worse design were accepted decreases to zero as iteration goes on. Networks were optimized using a combined variance-based and simulation approach. Melles et al. (2011) considered the problem of optimal sensor network design for monitoring precipitation and predicting flash flood in semiarid region. A small number of rain gauges are used to acquire data on rainfall depth and spatio-temporal variability of intensity during storm events. Optimizing the placement of rain gauges by using a multi-criteria strategy consists of three simultaneous steps: minimize the residual percent bias, maximize the coefficient of correlation between the estimated and true mean areal rainfall and minimize the normalized spatial mean squared error between the estimated and true spatio-temporal rainfall distribution. By comparing the performance of the optimized rain gauge network against randomly designed network, the paper concludes that the multi-criteria strategy provide a robust design.

Overall these classical designs deal with fixed monitoring locations, however, the magnetic storm problem must address sensor moving in 3-D space and time, adding considerable additional complexity. The work constitutes the early knowledge concerns the volatility in the measurements and fusion of measurements and computer models, which

will form part of any future design criteria.

Appendix A

Coordinate Transformations

Different coordinate systems are used in studies of the geomagnetic field and Sun-Earth connections. Geocentric solar magnetospheric (GSM) system, which has its X axis towards the Sun and its Z axis is the projection of the Earth's magnetic dipole axis on to the plane perpendicular to the X axis, is considered the best system to use when studying the effects of solar wind, in particular, the orientation and strength of the interplanetary magnetic field interplanetary magnetic field components, on magnetospheric and ionospheric phenomena.

The measurements from Cluster are recorded in Geocentric solar ecliptic (GSE) system. Therefore coordinates transformations are required to put the data in the appropriate system. Four geocentric coordinates systems are introduced and the possible conversions among them are defined based on Kivelson and Russell (1995).

TABLE A.1: Geocentric Coordinate Systems

System		Definition of axes
Geocentric equatorial inertial	GEI	X = First Point of Aries Z = Geographic North Pole
Geographic	GEO	X = Intersection of Greenwich meridian and geographic equator Z = Geographic North Pole
Geocentric solar ecliptic	GSE	X = Earth-Sun line Z = Ecliptic North Pole
Geocentric solar magnetospheric	GSM	X = Earth-Sun line Z = Projection of the magnetic dipole on the GSE YZ plane

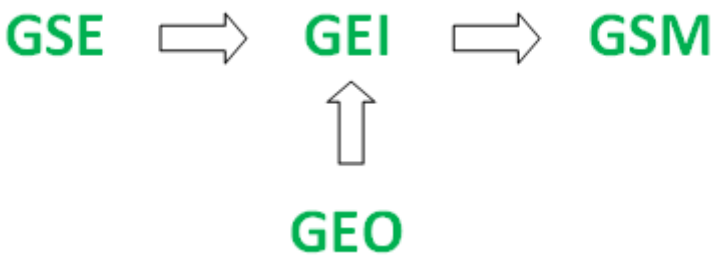

A.1 GSE to GSM

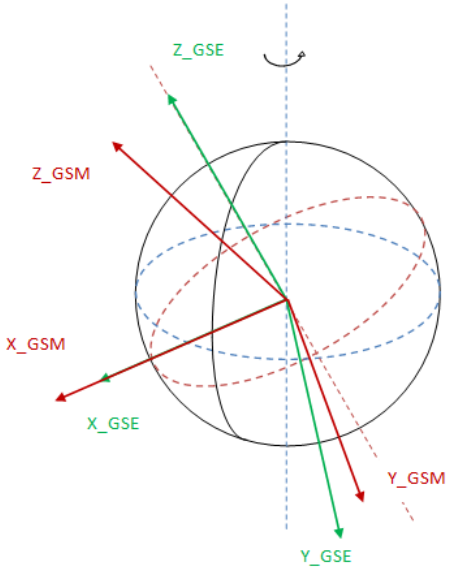

The geocentric solar magnetospheric (GSM) system, like the GSE system, has its x-axis from the earth to the sun. The transformation from GSE to GSM is a rotation around x-axis, and the transformation matrix is of the form,

$$\begin{pmatrix} 1 & 0 & 0 \\ 0 & \cos\psi & -\sin\psi \\ 0 & \sin\psi & \cos\psi \end{pmatrix}$$

where ψ is the angle between the GSE z-axis and projection of the magnetic dipole axis on the GSE YZ plane (the GSM z-axis). Since ψ is not easily derivable, we decompose GSE to GSM into two steps: GSE to GEI and GEI to GSM. And the transformation from GEO to GEI is needed for GEI to GSM.

A.2 GEO to GEI

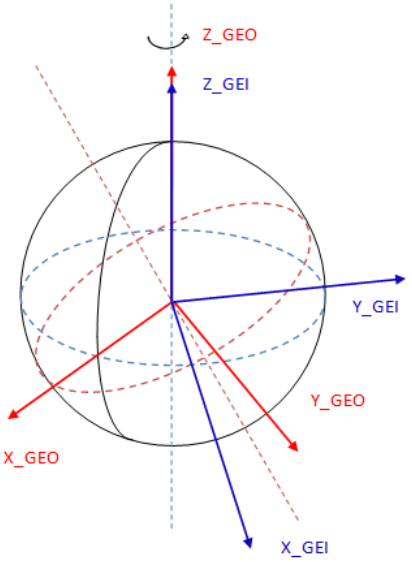

Because the GEO and GEI coordinate systems have the z-axis in common, the transformation matrix from GEO to GEI corresponds to a rotation around z-axis. $V_{GEI} = R_z(\theta) \cdot V_{GEO}$, i.e.

$$\begin{pmatrix} V_x \\ V_y \\ V_z \end{pmatrix}_{GEI} = \begin{pmatrix} \cos\theta & -\sin\theta & 0 \\ \sin\theta & \cos\theta & 0 \\ 0 & 0 & 1 \end{pmatrix} \cdot \begin{pmatrix} V_x \\ V_y \\ V_z \end{pmatrix}_{GEO}$$

The rotation angle θ, called *Greenwich mean sidereal time* (GMST), is the angle between the Greenwich meridian (the x-axis of GEO) and the first point of Aries (the x-axis of GEI). This can be calculated in hours (0h to 24h) then converted to degrees using the following formula:

$$\theta = \mathrm{mod}(6.697374558 + 0.06570982441908 \cdot D0 + 1.00273790935 \cdot H + ... 0.000026 \cdot (T^2), 24) \cdot 15$$

where T is the number of centuries since 12:00 UT on 1 January (J2000), $D0$ is the number of days since J2000, and H is time in hours past previous midnight.

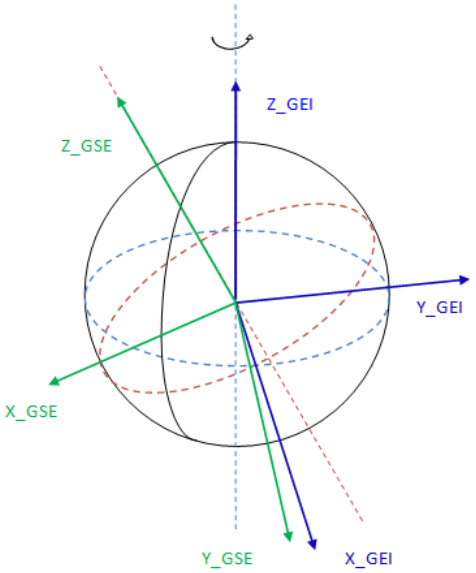

A.3 GSE to GEI

The transformation matrix from GEI to GSE has x-axis, y-axis, z-axis of GSE in GEI systems as row vectors.

- The x-axis of GSE is pointing the direction of the sun, and can be obtained in GEI as (S_1, S_2, S_3).
- The direction of the ecliptic pole, same as the z-axis of GSE, is constant in GEI $(0, 0.3978, 0.9175)$.
- Then the y-axis of GSE in GEI is $(y_1, y_2, y_3) = (0, 0.3978, 0.9175) \times (S_1, S_2, S_3)$.

So the transformation from GEI to GSE is

$$\begin{pmatrix} V_x \\ V_y \\ V_z \end{pmatrix}_{GSE} = \begin{pmatrix} S_1 & S_2 & S_3 \\ y_1 & y_2 & y_3 \\ 0 & -0.3978 & 0.9175 \end{pmatrix} \cdot \begin{pmatrix} V_x \\ V_y \\ V_z \end{pmatrix}_{GEI}$$

And the inverse transformation is

$$\begin{pmatrix} V_x \\ V_y \\ V_z \end{pmatrix}_{GEI} = \begin{pmatrix} S_1 & S_2 & S_3 \\ y_1 & y_2 & y_3 \\ 0 & -0.3978 & 0.9175 \end{pmatrix}^{-1} \cdot \begin{pmatrix} V_x \\ V_y \\ V_z \end{pmatrix}_{GSE}$$

A.4 GEI to GSM

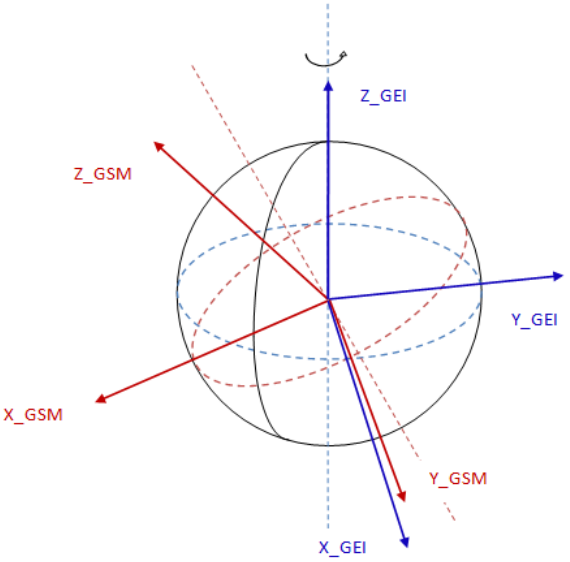

The transformation matrix from GEI to GSM has x-axis, y-axis, z-axis of GSM in GEI systems as row vectors.

- The x-axis of GSM is pointing the direction of the sun, and can be obtained in GEI as (S_1, S_2, S_3).
- The y-axis of GSM in GEI can be obtained as follow:

$$y = \frac{D\prime \times S}{|D\prime \times S|}$$

  where $D\prime$ is $D = (0.06252, -0.18060, 0.98157)$, the direction of dipole in GEO, transformed into GEI.
- Then the z-axis of GSM in GEI is $(z_1, z_2, z_3) = (S_1, S_2, S_3) \times (y_1, y_2, y_3)$.

Thus the transformation from GEI to GSM is

$$\begin{pmatrix} V_x \\ V_y \\ V_z \end{pmatrix}_{GSM} = \begin{pmatrix} S_1 & S_2 & S_3 \\ y_1 & y_2 & y_3 \\ z_1 & z_2 & z_3 \end{pmatrix} \cdot \begin{pmatrix} V_x \\ V_y \\ V_z \end{pmatrix}_{GEI}$$

Bibliography

Adams, R. P. and MacKay, D. J. (2007). Bayesian online changepoint detection. *arXiv preprint arXiv:0710.3742*.

Akaike, H. (1973). Maximum likelihood identification of Gaussian autoregressive moving average models. *Biometrika*, 60:255–265.

Akasofu, S.-I. and Chapman, S. (1961). The ring current, geomagnetic disturbance, and the Van Allen radiation belts. *Journal of Geophysical Research*, 66:1321–1350.

Alconcel, L., Fox, P., Brown, P., Oddy, T., Lucek, E., and Carr, C. (2014). An initial investigation of the long-term trends in the fluxgate magnetometer (FGM) calibration parameters on the four Cluster spacecraft. *Geoscientific Instrumentation, Methods and Data Systems*, 3:95.

Alfvén, H. (1942). Existence of electromagnetic-hydrodynamic waves. *Nature*, 150:405–406.

Aminikhanghahi, S. and Cook, D. J. (2016). A survey of methods for time series change point detection. *Knowledge and Information Systems*, pages 1–29.

Angelopoulos, V., Carlson, C., Curtis, D., Harvey, P., Lin, R., Mozer, F., Pankow, D., Raeder, J., and Russell, C. (1998). On the necessity and feasibility of an equatorial magnetospheric constellation. *Science Closure and Enabling Technologies for Constellation Class Missions*, page 14.

Antoch, J. and Jarušková, D. (2000). Change point detection. In *Forum Statisticum Slovacum*, page 2.

Baker, D., Kanekal, S., Li, X., Monk, S., Goldstein, J., and Burch, J. (2004). An extreme distortion of the Van Allen belt arising from the halloween solar storm in 2003. *Nature*, 432(7019):878–881.

Baker, D., Li, X., Pulkkinen, A., Ngwira, C., Mays, M., Galvin, A., and Simunac, K. (2013). A major solar eruptive event in July 2012: Defining extreme space weather scenarios. *Space Weather*, 11:585–591.

Baker, D. N., Pulkkinen, T., Angelopoulos, V., Baumjohann, W., and McPherron, R. (1996). Neutral line model of substorms: Past results and present view. *Journal of Geophysical Research: Space Physics*, 101:12975–13010.

Balogh, A., Carr, C. M., Acuña, M. H., Dunlop, M. W., Beek, T. J., Brown, P., Fornacon, K.-H., Georgescu, E., Glassmeier, K.-H., Harris, J., Musmann, G., Oddy, T., and Schwingenschuh, K. (2001). The Cluster magnetic field investigation: overview of in-flight performance and initial results. *Annales Geophysicae*, 19(10/12).

Balogh, A., Dunlop, M., Cowley, S., Southwood, D., Thomlinson, J., Glassmeier, K., Musmann, G., LHR, H., Buchert, S., AcuA, M., Fairfield, D., Slavin, J., Riedler, W., Schwingenschuh, K., and Kivelson, M. (1997). The Cluster magnetic field investigation. *Space Science Reviews*, 79:65–91.

Banjevic, M. and Switzer, P. (2004). Optimal network designs in spatial statistics. *Department of Statistics, Stanford University*, 114.

Bartels, J., Heck, N., and Johnston, H. (1939). The three-hour-range index measuring geomagnetic activity. *Terrestrial Magnetism and Atmospheric Electricity*, 44:411–454.

Beaulieu, C., Chen, J., and Sarmiento, J. L. (2012). Change-point analysis as a tool to detect abrupt climate variations. *Philosophical Transactions of the Royal Society of London A: Mathematical, Physical and Engineering Sciences*, 370:1228–1249.

Belehaki, A., Stanislawska, I., and Lilensten, J. (2009). An overview of ionospherethermosphere models available for space weather purposes. *Space Science Reviews*, 147:271–313.

Berkes, I. and Horváth, L. (2004). The efficiency of the estimators of the parameters in GARCH processes. *The Annals of Statistics*, 32:633–655.

Birgé, L. and Massart, P. (2007). Minimal penalties for Gaussian model selection. *Probability theory and related fields*, 138:33–73.

Bollerslev, T. (1986). Generalized autoregressive conditional heteroskedasticity. *Journal of Econometrics*, 31:307–327.

Bondon, P. and Bahamonde, N. (2012). Least squares estimation of ARCH models with missing observations. *Journal of Time Series Analysis*, 33:880–891.

Bose, A. and Mukherjee, K. (2003). Estimating the ARCH parameters by solving linear equations. *Journal of Time Series Analysis*, 24:127–136.

Bothmer, V. and Daglis, I. A. (2007). *Space weather: physics and effects*. Springer Science, UK.

Bowe, J. and McCulloch, S. (2007). The value of real-time geomagnetic reference data to the oil and gas industry. In *Space Weather*, pages 289–298. Springer, New York.

Box, G. E., Jenkins, G. M., and Reinsel, G. (1970). Forecasting and control. *Time Series Analysis*, 3:75.

Box, G. E., Jenkins, G. M., Reinsel, G. C., and Ljung, G. M. (2015). *Time series analysis: forecasting and control*. John Wiley & Sons.

Burch, J., Russell, C., Ergun, R., Phan, T., Hesse, M., Eastwood, J., Giles, B., Moore, T., Chen, L.-J., Torbert, R., et al. (2016). Investigation of magnetic reconnection at the Earth's magnetopause using data from the magnetospheric multiscale mission. In *41st COSPAR Scientific Assembly*, volume 41.

Cabinet Office (2015). *The National Risk Register (NRR) of Civil Emergencies*.

Chapman, S. and Bartels, J. (1940). *Geomagnetism*, volume 1. Clarendon Press Oxford.

Chatfield, C. (2016). *The analysis of time series: an introduction*. CRC press.

Chen, J. and Gupta, A. K. (2011). *Parametric statistical change point analysis: with applications to genetics, medicine, and finance*. Springer Science & Business Media.

Cliver, E. W. and Dietrich, W. F. (2013). The 1859 space weather event revisited: limits of extreme activity. *Journal of Space Weather and Space Climate*, 3:A31.

Cliver, E. W. and Svalgaard, L. (2004). The 1859 solar–terrestrial disturbance and the current limits of extreme space weather activity. *Solar Physics*, 224:407–422.

Connor, H., Zesta, E., Ober, D., and Raeder, J. (2014). The relation between transpolar potential and reconnection rates during sudden enhancement of solar wind dynamic pressure: OpenGGCM-CTIM results. *Journal of Geophysical Research: Space Physics*, 119:3411–3429.

Cowley, S. (1982). The causes of convection in the Earth's magnetosphere: A review of developments during the IMS. *Reviews of Geophysics*, 20:531–565.

Cramer, W. D., Turner, N. E., Fok, M.-C., and Buzulukova, N. Y. (2013). Effects of different geomagnetic storm drivers on the ring current: CRCM results. *Journal of Geophysical Research: Space Physics*, 118:1062–1073.

Cressie, N. and Wikle, C. K. (2015). *Statistics for spatio-temporal data*. John Wiley & Sons.

Csörgö, M. and Horváth, L. (1997). *Limit theorems in change-point analysis*, volume 18. John Wiley & Sons Inc.

Curtis, H. D. (2013). *Orbital mechanics for engineering students*. Butterworth-Heinemann.

Daglis, I. A. (2001). Space storms, ring current and space-atmosphere coupling. In *Space storms and space weather hazards*, pages 1–42. Springer.

Davis, T. N. and Sugiura, M. (1966). Auroral electrojet activity index AE and its universal time variations. *Journal of Geophysical Research*, 71:785–801.

De Michelis, P., Tozzi, R., and Meloni, A. (2005). Geomagnetic jerks: observation and theoretical modeling. *Memorie della Società Astronomica Italiana*.

De Pater, I. and Lissauer, J. J. (2015). *Planetary sciences*. Cambridge University Press, New York.

DeJong, A., Ridley, A., and Clauer, C. (2008). Balanced reconnection intervals: Four case studies.

Deshayes, J. and Picard, D. (1985). Off-line statistical analysis of change-point models using non parametric and likelihood methods. In *Detection of Abrupt Changes in Signals and Dynamical Systems*, pages 103–168. Springer.

Downey, A. B. (2008). A novel changepoint detection algorithm. *arXiv preprint arXiv:0812.1237*.

Dungey, J. W. (1961). Interplanetary magnetic field and the auroral zones. *Phys. Rev. Lett.*, 6:47–48.

Eastwood, J. (2008). The science of space weather. *Philosophical Transactions of the Royal Society A-Mathematical Physical and Engineering Sciences*, 366:4489–4500.

Eastwood, J. P. (2015). Observing magnetic reconnection: The influence of Jim Dungey. In *Magnetospheric Plasma Physics: The Impact of Jim Dungeys Research*, pages 181–197. Springer.

Eastwood, J. P., Biffis, E., Hapgood, M. A., Green, L., Bisi, M. M., Bentley, R. D., Wicks, R., McKinnell, L.-A., Gibbs, M., and Burnett, C. (2017). The economic impact of space weather: Where do we stand? *Risk Analysis*, 37(2):206–218.

Echer, E., Gonzalez, W., Tsurutani, B., and Gonzalez, A. (2008). Interplanetary conditions causing intense geomagnetic storms (Dst- 100 nt) during solar cycle 23 (1996–2006). *Journal of Geophysical Research: Space Physics*, 113(A5).

Eckley, I. A., Fearnhead, P., and Killick, R. (2011). Analysis of changepoint models. *Bayesian Time Series Models*, pages 205–224.

Engle, R. (2001). Garch 101: The use of ARCH/GARCH models in applied econometrics. *The Journal of Economic Perspectives*, 15:157–168.

Engle, R. F. (1982). Autoregressive conditional heteroscedasticity with estimates of the variance of United Kingdom inflation. *Econometrica: Journal of the Econometric Society*, pages 987–1007.

Engle, R. F. (1984). Wald, likelihood ratio, and Lagrange multiplier tests in econometrics. *Handbook of econometrics*, 2:775–826.

Erdman, C., Emerson, J. W., et al. (2007). bcp: an R package for performing a Bayesian analysis of change point problems. *Journal of Statistical Software*, 23:1–13.

Escoubet, C., Fehringer, M., and Goldstein, M. (2001a). Introduction the Cluster mission. In *Annales Geophysicae*, volume 19, pages 1197–1200.

Escoubet, C., Schmidt, R., and Goldstein, M. (1997). Cluster–science and mission overview. *Space Science Reviews*, 79:11–32.

Escoubet, C. P., Fehringer, M., and Goldstein, M. (2001b). Introduction the Cluster mission. *Annales Geophysicae*, 19(10/12):1197–1200.

Finlay, C., Maus, S., Beggan, C., Bondar, T., Chambodut, A., Chernova, T., Chulliat, A., Golovkov, V., Hamilton, B., Hamoudi, M., et al. (2010). International geomagnetic reference field: the eleventh generation. *Geophysical Journal International*, 183:1216–1230.

Francq, C., Zakoïan, J.-M., et al. (2004). Maximum likelihood estimation of pure GARCH and ARMA-GARCH processes. *Bernoulli*, 10:605–637.

Frey, H., Phan, T., Fuselier, S., and Mende, S. (2003). Continuous magnetic reconnection at Earth's magnetopause. *Nature*, 426:533–537.

Friis-Christensen, E., Lühr, H., Knudsen, D., and Haagmans, R. (2008). Swarm–an Earth observation mission investigating geospace. *Advances in Space Research*, 41:210–216.

Gauss, C. F., Sabine, M., and Herschel, S. J. F. W. (1839). *General theory of terrestrial magnetism*. R and J.E.Taylor, London.

Gjerloev, J., Hoffman, R., Friel, M., Frank, L., and Sigwarth, J. (2004). Substorm behavior of the auroral electrojet indices. In *Annales Geophysicae*, volume 22, pages 2135–2149.

Gloag, J., Lucek, E., Alconcel, L.-N., Balogh, A., Brown, P., Carr, C., Dunford, C., Oddy, T., and Soucek, J. (2010). FGM data products in the CAA. In *The Cluster Active Archive*, pages 109–128. Springer, The Netherlands.

Gombay, E. (2008). Change detection in autoregressive time series. *Journal of Multivariate Analysis*, 99:451–464.

Gonzalez, W., Joselyn, J., Kamide, Y., Kroehl, H., Rostoker, G., Tsurutani, B., and Vasyliunas, V. (1994). What is a geomagnetic storm? *Journal of Geophysical Research: Space Physics*, 99(A4):5771–5792.

Gopalswamy, N., Yashiro, S., Michalek, G., Xie, H., Lepping, R., and Howard, R. (2005). Solar source of the largest geomagnetic storm of cycle 23. *Geophysical research letters*, 32(12).

Gunnarsdóttir, E. L. (2012). The Earth's magnetic field.

Gupta, A. and Tang, J. (1984). Distribution of likelihood ratio statistic for testing equality of covariance matrices of multivariate Gaussian models. *Biometrika*, 71:555–559.

Guralnik, V. and Srivastava, J. (1999). Event detection from time series data. In *Proceedings of the fifth ACM SIGKDD international conference on Knowledge discovery and data mining*, pages 33–42. ACM.

Guyon, X. and Yao, J.-f. (1999). On the underfitting and overfitting sets of models chosen by order selection criteria. *Journal of Multivariate Analysis*, 70:221–249.

Häkkinen, L. V., Pulkkinen, T. I., Pirjola, R. J., Nevanlinna, H., Tanskanen, E. I., and Turner, N. E. (2003). Seasonal and diurnal variation of geomagnetic activity: Revised Dst versus external drivers. *Journal of Geophysical Research: Space Physics*, 108.

Hapgood, M. (2012). Astrophysics: Prepare for the coming space weather storm. *Nature*, 484:311–313.

Hapgood, M. (2017). *Space Weather*. 2399-2891. IOP Publishing.

Hargreaves, J. K. (1992). *The solar-terrestrial environment: an introduction to geospace-the science of the terrestrial upper atmosphere, ionosphere, and magnetosphere*. Cambridge University Press, UK.

Hawkins, D. M. and Deng, Q. (2010). A nonparametric change-point control chart. *Journal of Quality Technology*, 42:165.

Hawkins, D. M., Qiu, P., and Kang, C. W. (2003). The changepoint model for statistical process control. *Journal of Quality Technology*, 35:355.

Hawkins, D. M. and Zamba, K. (2005). Statistical process control for shifts in mean or variance using a changepoint formulation. *Technometrics*, 47:164–173.

Helsel, D. R. (2012). Computing summary statistics and totals. *Statistics for Censored Environmental Data Using Minitab® and R, Second Edition*, pages 62–98.

Hinkley, D. V. (1970). Inference about the change-point in a sequence of random variables. *Biometrika*, pages 1–17.

Honaker, J. and King, G. (2010). What to do about missing values in time-series cross-section data. *American Journal of Political Science*, 54:561–581.

Hughes, W. (1995). The magnetopause, magnetotail, and magnetic reconnection. *Introduction to Space Physics*, pages 227–287.

Hultqvist, M. Øieroset, G. P. and Treumann, R. (1999). Magnetospheric plasma sources and losses. *Space Sciences Series of ISSI*, 6.

Hurvich, C. M., Simonoff, J. S., and Tsai, C.-L. (1998). Smoothing parameter selection in nonparametric regression using an improved Akaike information criterion. *Journal of the Royal Statistical Society: Series B (Statistical Methodology)*, 60:271–293.

Inclan, C. and Tiao, G. C. (1994). Use of cumulative sums of squares for retrospective detection of changes of variance. *Journal of the American Statistical Association*, 89:913–923.

Jaruskova, D. (1997). Some problems with application of change-point detection methods to environmental data. *Environmetrics*, 8:469–484.

Kamide, Y. (1992). Is substorm occurrence a necessary condition for a magnetic storm? *Journal of geomagnetism and geoelectricity*, 44:109–117.

Kamide, Y. and Akasofu, S.-I. (1983). Notes on the auroral electrojet indices. *Reviews of Geophysics*, 21:1647–1656.

Kawahara, Y. and Sugiyama, M. (2012). Sequential change-point detection based on direct density-ratio estimation. *Statistical Analysis and Data Mining*, 5:114–127.

Killick, R. and Eckley, I. (2014). changepoint: An R package for changepoint analysis. *Journal of Statistical Software*, 58(3):1–19.

Kim, J.-Y. (2000). Detection of change in persistence of a linear time series. *Journal of Econometrics*, 95:97–116.

Kivelson, M. G. and Russell, C. T. (1995). *Introduction to space physics*. Cambridge university press, UK.

Koskinen, H. (2011). *Physics of Space Storms: From the Solar Surface to the Earth*. Springer Science, UK.

Kuijpers, J., Frey, H. U., and Fletcher, L. (2015). Electric current circuits in astrophysics. *Space Science Reviews*, 188:3–57.

Lanza, R., Meloni, A., et al. (2006). *The Earth's magnetism*. Springer, New York.

Lavielle, M. (2005). Using penalized contrasts for the change-point problem. *Signal processing*, 85:1501–1510.

Little, R. J. and Rubin, D. B. (2014). *Statistical analysis with missing data*. John Wiley & Sons.

Ljung, G. M. and Box, G. E. (1978). On a measure of lack of fit in time series models. *Biometrika*, 65:297–303.

Loewe, C. and Prölss, G. (1997). Classification and mean behavior of magnetic storms. *Journal of Geophysical Research: Space Physics*, 102(A7):14209–14213.

Lopez, R., Lyon, J., Wiltberger, M., and Goodrich, C. (2001). Comparison of global MHD simulation results with actual storm and substorm events. *Advances in Space Research*, 28:1701–1706.

Lorden, G. (1971). Procedures for reacting to a change in distribution. *The Annals of Mathematical Statistics*, pages 1897–1908.

Love, J. J. and Remick, K. (2007). Magnetic indices. In *Encyclopedia of Geomagnetism and Paleomagnetism*, pages 509–512. Springer.

Lui, A. (2002). Multiscale phenomena in the near-Earth magnetosphere. *Journal of Atmospheric and Solar-Terrestrial Physics*, 64:125–143.

Lund, R. and Reeves, J. (2002). Detection of undocumented changepoints: A revision of the two-phase regression model. *Journal of Climate*, 15:2547–2554.

Lund, R., Wang, X. L., Lu, Q. Q., Reeves, J., Gallagher, C., and Feng, Y. (2007). Changepoint detection in periodic and autocorrelated time series. *Journal of Climate*, 20:5178–5190.

Macmillan, S. and Finlay, C. (2011). The international geomagnetic reference field. In *Geomagnetic observations and models*, pages 265–276. Springer.

Macmillan, S. and Olsen, N. (2013). Observatory data and the Swarm mission. *Earth, Planets and Space*, 65:15.

Matzka, J., Chulliat, A., Mandea, M., Finlay, C., and Qamili, E. (2010). Geomagnetic observations for main field studies: from ground to space. *Space science reviews*, 155:29–64.

Maus, S. and Lühr, H. (2005). Signature of the quiet-time magnetospheric magnetic field and its electromagnetic induction in the rotating Earth. *Geophysical Journal International*, 162:755–763.

McCulloch, C. E. (1997). Maximum likelihood algorithms for generalized linear mixed models. *Journal of the American statistical Association*, 92:162–170.

McPherron, R. (1997). The role of substorms in the generation of magnetic storms. *Magnetic Storms*, pages 131–147.

McWilliams, K., Pfeifer, J., and McPherron, R. (2008). Steady magnetospheric convection selection criteria: Implications of global superdarn convection measurements. *Geophysical Research Letters*, 35.

Mei, Y. (2006). Sequential change-point detection when unknown parameters are present in the pre-change distribution. *The Annals of Statistics*, pages 92–122.

Melles, S., Heuvelink, G. B., Twenhöfel, C. J., van Dijk, A., Hiemstra, P. H., Baume, O., and Stöhlker, U. (2011). Optimizing the spatial pattern of networks for monitoring radioactive releases. *Computers & Geosciences*, 37:280–288.

Menvielle, M. and Berthelier, A. (1991). The k-derived planetary indices: Description and availability. *Reviews of Geophysics*, 29:415–432.

Menvielle, M. and Marchaudon, A. (2007). Geomagnetic indices in solar-terrestrial physics and space weather. In *Space weather*, pages 277–288. Springer, New York.

Messerotti, M., Zuccarello, F., Guglielmino, S. L., Bothmer, V., Lilensten, J., Noci, G., Storini, M., and Lundstedt, H. (2009). Solar weather event modelling and prediction. *Space Science Reviews*, 147:121–185.

Milan, S., Provan, G., and Hubert, B. (2007). Magnetic flux transport in the Dungey cycle: A survey of dayside and nightside reconnection rates. *Journal of Geophysical Research: Space Physics*, 112(A1).

Moldwin, M. (2008). *An Introduction to Space Weather*.

NASA/SOHO (2008). *Halloween Storms of 2003 Still the Scariest.*

Ngwira, C. M., Pulkkinen, A., Leila Mays, M., Kuznetsova, M. M., Galvin, A., Simunac, K., Baker, D. N., Li, X., Zheng, Y., and Glocer, A. (2013). Simulation of the 23 July 2012 extreme space weather event: What if this extremely rare CME was earth directed? *Space Weather*, 11:671–679.

Odenwald, S. (2012). Space weather–impacts, mitigation and forecasting. *Visiting Scientists Program, University Corporation for Atmospheric Research, Boulder, Colorado*, page 14.

Olsen, N., Glassmeier, K.-H., and Jia, X. (2010). Separation of the magnetic field into external and internal parts. *Space science reviews*, 152:135–157.

Page, E. (1954). Continuous inspection schemes. *Biometrika*, 41(1/2):100–115.

Page, E. (1955). A test for a change in a parameter occurring at an unknown point. *Biometrika*, 42:523–527.

Parker, E. (1962). Dynamics of the geomagnetic storm. *Space Science Reviews*, 1(1):62–99.

Parker, E. (1965). Dynamical theory of the solar wind. *Space Science Reviews*, 4:666–708.

Parks, G. K. (1991). Physics of space plasmas-an introduction.

Pinero, J. and Bates, D. (2000). *Mixed-effects models in S and S-PLUS (statistics and computing)*. Springer, New York.

Pinheiro, J. C. and Bates, D. M. (2000). Linear mixed-effects models: basic concepts and examples. *Mixed-effects models in S and S-Plus*, pages 3–56.

Pudovkin, M., Besser, B., and Zaitseva, S. (1998). Magnetopause stand-off distance in dependence on the magnetosheath and solar wind parameters. In *Annales Geophysicae*, volume 16, pages 388–396. Springer.

Pulkkinen, A. (2007). Spatiotemporal characteristics of the ground electromagnetic field fluctuations in the auroral region and implications on the predictability of geomagnetically induced currents. In *Space Weather*, pages 299–310. Springer.

Rathore, B. S., Kaushik, S. C., Firoz, K., Gupta, D., Shrivastava, A., Parashar, K. K., and Bhaduriya, R. M. (2011). A correlative study of geomagnetic storms associated with solar wind and IMF features during solar cycle 23. *International Journal of applied physics and mathematics*, 1:149.

Reeves, J., Chen, J., Wang, X. L., Lund, R., and Lu, Q. Q. (2007). A review and comparison of changepoint detection techniques for climate data. *Journal of Applied Meteorology and Climatology*, 46:900–915.

Richardson, I., Cliver, E., and Cane, H. (2000). Sources of geomagnetic activity over the solar cycle: Relative importance of coronal mass ejections, high-speed streams, and slow solar wind. *Journal of Geophysical Research: Space Physics*, 105:18203–18213.

Ross, G. J. (2014). Sequential change detection in the presence of unknown parameters. *Statistics and Computing*, 24:1017–1030.

Ross, G. J. and Adams, N. M. (2012). Two nonparametric control charts for detecting arbitrary distribution changes. *Journal of Quality Technology*, 44:102.

Ross, G. J., Adams, N. M., Tasoulis, D. K., and Hand, D. J. (2012). Exponentially weighted moving average charts for detecting concept drift. *Pattern Recognition Letters*, 33:191–198.

Ross, G. J. et al. (2013). Parametric and nonparametric sequential change detection in r: The cpm package. *Journal of Statistical Software*, 78.

Ross, G. J., Tasoulis, D. K., and Adams, N. M. (2011). Nonparametric monitoring of data streams for changes in location and scale. *Technometrics*, 53:379–389.

Russell, C. (1991). The magnetosphere. *Annual Review of Earth and Planetary Sciences*, 19:169–182.

Russell, C. and McPherron, R. (1973). The magnetotail and substorms. *Space Science Reviews*, 15:205–266.

Russell, C. T. (1971). Geophysical coordinate transformations. *Cosmic Electrodynamics*, 2:184–196.

Russell, C. T. (2007). The coupling of the solar wind to the Earth's magnetosphere. In *Space Weather-Physics and Effects*, pages 103–130. Springer.

Saiz, E., Cerrato, Y., Cid, C., Dobrica, V., Hejda, P., Nenovski, P., Stauning, P., Bochnicek, J., Danov, D., Demetrescu, C., et al. (2013). Geomagnetic response to solar and interplanetary disturbances. *Journal of Space Weather and Space Climate*, 3:A26.

Schwarz, G. et al. (1978). Estimating the dimension of a model. *The Annals of Statistics*, 6:461–464.

Seki, K., Nagy, A., Jackman, C., Crary, F., Fontaine, D., Zarka, P., Wurz, P., Milillo, A., Slavin, J., Delcourt, D., et al. (2015). A review of general physical and chemical processes related to plasma sources and losses for solar system magnetospheres. *Space science reviews*, 192:27–89.

Sergeev, V., Angelopoulos, V., and Nakamura, R. (2012). Recent advances in understanding substorm dynamics. *Geophysical Research Letters*, 39.

Shewhart, W. A. (1931). *Economic control of quality of manufactured product*. ASQ Quality Press.

Shiryaev, A. N. (1963). On optimum methods in quickest detection problems. *Theory of Probability & Its Applications*, 8:22–46.

Shumway, R. H. and Stoffer, D. S. (2010). *Time series analysis and its applications: with R examples*. Springer Science & Business Media.

Silva, E. G. and Teixeira, A. A. (2008). Surveying structural change: Seminal contributions and a bibliometric account. *Structural Change and Economic Dynamics*, 19:273–300.

Smith, C. W., L'Heureux, J., Ness, N. F., Acuña, M. H., Burlaga, L. F., and Scheifele, J. (1998). The ACE magnetic fields experiment. *Space Science Reviews*, 86:613–632.

Sokal, R. and Rohlf, F. (1969). Bartlett's test of homogeneity of variances.

Solow, A. R. (1987). Testing for climate change: An application of the two-phase regression model. *Journal of Climate and Applied Meteorology*, 26:1401–1405.

Sotirelis, T., Keller, M. R., Liou, K., Smith, D., Barnes, R. J., Talaat, E., and Baker, J. B. (2017). Testing the expanding-contracting polar cap (ECPC) paradigm. *Journal of Geophysical Research: Space Physics*.

Spokoiny, V. (2009). Multiscale local change point detection with applications to value-at-risk. *The Annals of Statistics*, pages 1405–1436.

Stern, D. P. (1989). A brief history of magnetospheric physics before the spaceflight era. *Reviews of Geophysics*, 27:103–114.

Straumann, D., Mikosch, T., et al. (2006). Quasi-maximum-likelihood estimation in conditionally heteroscedastic time series: A stochastic recurrence equations approach. *The Annals of Statistics*, 34:2449–2495.

Tartakovsky, A. G. and Veeravalli, V. V. (2008). Asymptotically optimal quickest change detection in distributed sensor systems. *Sequential Analysis*, 27:441–475.

Thomson, A. W. (2014). Geomagnetic observatories: monitoring the Earth's magnetic and space weather environment. *Weather*, 69:234–237.

Thomson, A. W., Dawson, E. B., and Reay, S. J. (2011). Quantifying extreme behavior in geomagnetic activity. *Space Weather*, 9(10).

Tocaci, E. (2012). *Relativistic mechanics, time and inertia*, volume 8. Springer Science & Business Media.

Tsagouri, I., Belehaki, A., Bergeot, N., Cid, C., Delouille, V., Egorova, T., Jakowski, N., Kutiev, I., Mikhailov, A., Núñez, M., et al. (2013). Progress in space weather modeling in an operational environment. *Journal of Space Weather and Space Climate*, 3:A17.

Tsui, J. B.-Y. (2005). *Fundamentals of global positioning system receivers: a software approach*, volume 173. John Wiley & Sons.

Tsurutani, B. T., Gonzalez, W. D., Tang, F., Akasofu, S. I., and Smith, E. J. (1988). Origin of interplanetary southward magnetic fields responsible for major magnetic storms near solar maximum (1978 - 1979). *Journal of Geophysical Research: Space Physics*, 93(A8):8519–8531.

Tsyganenko, N. (1989). A magnetospheric magnetic field model with a warped tail current sheet. *Planetary and Space Science*, 37:5–20.

Tsyganenko, N. (2008). Geopack: a set of fortran subroutines for computations of the geomagnetic field in the Earth's magnetosphere.

Tsyganenko, N. (2013). Data-based modelling of the Earth's dynamic magnetosphere: A review. In *Annales Geophysicae*, volume 31, pages 1745–1772. Copernicus GmbH.

Tsyganenko, N. and Sibeck, D. (1994). Concerning flux erosion from the dayside magnetosphere. *Journal of Geophysical Research: Space Physics*, 99:13425–13436.

Tsyganenko, N. and Stern, D. (1996a). A new-generation global magnetosphere field model, based on spacecraft magnetometer data. *ISTP newsletter*, 6:21.

Tsyganenko, N. A. and Sitnov, M. I. (2007). Magnetospheric configurations from a high-resolution data-based magnetic field model. *Journal of Geophysical Research: Space Physics*, 112.

Tsyganenko, N. A. and Stern, D. P. (1996b). Modeling the global magnetic field of the large-scale birkeland current systems. *Journal of Geophysical Research: Space Physics*, 101:27187–27198.

Turner, N. E., Baker, D., Pulkkinen, T., and McPherron, R. (2000). Evaluation of the tail current contribution to Dst. *Journal of Geophysical Research: Space Physics*, 105:5431–5439.

United States Geological Survey: Science Features (2013). *The Magnetic Storm of Halloween 2003*.

US National Space Weather Program Strategic Plan (2010). National space weather program strategic plan.

Vainio, R., Desorgher, L., Heynderickx, D., Storini, M., Flückiger, E., Horne, R. B., Kovaltsov, G. A., Kudela, K., Laurenza, M., McKenna-Lawlor, S., et al. (2009). Dynamics of the Earth's particle radiation environment. *Space Science Reviews*, 147:187–231.

Van Allen, J. A., McIlwain, C. E., and Ludwig, G. H. (1959). Satellite observations of electrons artificially injected into the geomagnetic field. *Proceedings of the National Academy of Sciences*, 45(8):1152–1171.

Vasyliūnas, V. M. (2011). Physics of magnetospheric variability. *Space Science Reviews*, 158:91–118.

Verbesselt, J., Hyndman, R., Zeileis, A., and Culvenor, D. (2010). Phenological change detection while accounting for abrupt and gradual trends in satellite image time series. *Remote Sensing of Environment*, 114:2970–2980.

Viljanen, A., Nevanlinna, H., Pajunpää, K., and Pulkkinen, A. (2001). Time derivative of the horizontal geomagnetic field as an activity indicator. In *Annales Geophysicae*, volume 19, pages 1107–1118.

Volkmann, T. H., Lyon, S. W., Gupta, H. V., and Troch, P. A. (2010). Multicriteria design of rain gauge networks for flash flood prediction in semiarid catchments with complex terrain. *Water resources research*, 46(11).

Wang, X. L. (2003). Comments on detection of undocumented changepoints: a revision of the two-phase regression model. *Journal of Climate*, 16:3383–3385.

Watermann, J. (2007). The magnetic environment–GIC and other ground effects. In *Space weather*, pages 269–275. Springer, New York.

Watermann, J., Vainio, R., Lilensten, J., Belehaki, A., and Messerotti, M. (2009). The state of space weather scientific modeling - an introduction. *Space Science Reviews*, 147:111–120.

Welling, D. T., Andre, M., Dandouras, I., Delcourt, D., Fazakerley, A., Fontaine, D., Foster, J., Ilie, R., Kistler, L., Lee, J. H., et al. (2015). The Earth: Plasma sources, losses, and transport processes. *Space Science Reviews*, 192:145–208.

White, H. (1980). A heteroskedasticity-consistent covariance matrix estimator and a direct test for heteroskedasticity. *Econometrica: Journal of the Econometric Society*, pages 817–838.

Winch, D., Ivers, D., Turner, J., and Stening, R. (2005). Geomagnetism and schmidt quasi-normalization. *Geophysical Journal International*, 160:487–504.

Woellert, K., Ehrenfreund, P., Ricco, A. J., and Hertzfeld, H. (2011). Cubesats: Cost-effective science and technology platforms for emerging and developing nations. *Advances in Space Research*, 47(4):663–684.

Woodfield, E., Dunlop, M., Holme, R., Davies, J., and Hapgood, M. (2007). A comparison of Cluster magnetic data with the Tsyganenko 2001 model. *Journal of Geophysical Research: Space Physics*, 112.

Xie, Y. and Siegmund, D. (2013). Sequential multi-sensor change-point detection. In *Information Theory and Applications Workshop (ITA), 2013*, pages 1–20. IEEE.

You-Qiu, H., Xiao-Cheng, G., Guo-Qiang, L., Chi, W., and Zhao-Hui, H. (2005). Oscillation of quasi-steady Earth's magnetosphere. *Chinese Physics Letters*, 22:2723.

Zhang, Q.-H., Dunlop, M. W., Holme, R., and Woodfield, E. E. (2010). Comparison of eight years magnetic field data from Cluster with Tsyganenko models in the inner magnetosphere. *Annales Geophysicae*, 28:309–326.